Conversion of Cellulose-based Papers into Functional Ceramic Papers

TECHNISCHE
UNIVERSITÄT
DARMSTADT

Disperse
Feststoffe

Conversion of Cellulose-based Papers into Functional Ceramic Papers

vom Fachbereich Material- und Geowissenschaften

der Technischen Universität Darmstadt

im Fachgebiet Disperse Feststoffe

zur Erlangung des akademischen Grades

Doktor der Ingenieurwissenschaften

(Dr.-Ing.)

Dissertation

von

M.Sc. Alexander Ott

Erklärungen zur Dissertation gemäß § 22 Abs. 7 APB TU Darmstadt

Hiermit versichere ich, die vorliegende Dissertation ohne Hilfe Dritter nur mit den angegebenen Quellen und Hilfsmitteln angefertigt zu haben. Alle Stellen, die aus Quellen entnommen wurden, sind als solche kenntlich gemacht. Diese Arbeit hat in gleicher oder ähnlicher Form noch keiner Prüfungsbehörde vorgelegen.

Ort und Datum: Unterschrift:

_____   _____

                                                  (Alexander Ott)

Acknowledgments

Abstract

Paper has been used for thousands of years, be it as a writing utensil like Papyrus or in different applications, for example as cellulose-based nanogenerators, as shape memory polymers, or as membranes for wound healing. Its microstructure shows randomly arranged fibers consisting of cellulose. Furthermore, it represents a good alternative as a template material due to its unique intrinsic properties and versatile modification potential as a functional material.

The main characteristic of functional materials is their tunability towards the desired electronic, magnetic, or optical properties. This dissertation introduces the synthesis of functional ceramic papers and focuses on the understanding of occurring processes during functionalization. The ceramic papers were produced using a so-called "One-Pot" synthesis approach by dipping different types of cellulose-based papers (Sartorius, Linters and Eucalyptus) into a solution, consisting of different transition metals and polysilazanes. After vacuum drying the impregnated pre-ceramic papers, they were pyrolyzed at different atmospheres and temperatures.

The phase composition of the produced ceramic papers and the belonging powders were studied using different characterization techniques. Fourier-transform infrared spectroscopy (FTIR) allowed to investigate the bonding situation of the functional groups, while X-Ray diffraction (XRD) identified the crystalline phases. The carbonization of the cellulose template during pyrolysis was studied using µ-Raman spectroscopy. Thermogravimetric Analysis (TGA) was used to determine the thermal stability of the impregnated papers and their volatile components based on the weight loss that occurs during pyrolysis.

Lastly, electrocatalytic and electromagnetic measurements were performed with the ceramic papers and compared with state-of-the-art compositions.

Kurzfassung

Papier wird schon seit Jahrtausenden genutzt, wie zum Beispiel als Papyrus um darauf zu schreiben oder heutzutage bei verschiedenen Anwendungen, wie zum Beispiel als Formgedächtnispolymer oder bei der Verwendung als Membran für Wundheilung. Seine Mikrostruktur besteht aus zufällig ausgerichteten Zellulosefasern. Aufgrund dieser einzigartigen intrinsischen Eigenschaften und darüber hinaus vielseitiger Modifikationsmöglichkeiten, eignet sich das Papier für die Herstellung funktioneller Materialien.

Funktionelle Materialien lassen sich gezielt für die jeweilige Anwendung, sei es elektronische, magnetische oder optische abstimmen und beeinflussen. Diese Dissertation behandelt die Herstellung funktioneller keramischer Papiere und erforscht die dabei auftretenden Prozesse. Die keramischen Papiere wurden mit Hilfe der sogenannten „Eintopf" Methode hergestellt. Dabei wurden verschiedene Zellulose-basierte Papiere (Sartorius, Linters und Eukalyptus) in Lösungsgemische, welche aus verschiedenen Übergangsmetallen und Polysilazanen bestanden, eingetaucht. Nach der Imprägnierung und Vakuumtrocknung wurden die präkeramischen Papiere in verschiedenen Atmosphären und Temperaturen behandelt.

Die Phasenzusammensetzung der hergestellten keramischen Papieren und den dazugehörigen keramischen Pulvern wurde mit unterschiedlichen Charakterisierungsmethoden untersucht. Mittels Fourier-Transformations-Infrarotspektrometer (FTIR) konnten die verschiedenen funktionellen Gruppen analysiert werden. Röntgenbeugung (XRD) erlaubte es die (kristallinen) Phasen zu bestimmen. Die Karbonisierung der Zellulosefasern während der thermischen Behandlung wurde mit Hilfe der µ-Raman Spektroskopie untersucht. Die thermogravimetrische Analyse (TGA) half die thermische Stabilität der imprägnierten Zellulose und deren Gasentwicklung während der Pyrolyse zu verstehen.

Zum Schluss wurden, mit einem Teil der hergestellten keramischen Papiere, elektrochemische Messungen durchgeführt und des Weiteren die Abschirmungsfähigkeit gegenüber elektromagnetischer Strahlung untersucht. Die dabei erhaltenen Daten wurden dann mit Materialien aus dem jetzigen Stand der Forschung verglichen.

Abbreviations

Dur	*Durazane 1800 (Polysilazane)*	J_0	*Exchange current density*
EMS	*Electromagnetic Shielding*	L_a	*In-plane crystallite size*
Euc	*Eucalyptus cellulose-based Paper*	L_D	*Inter defect distance*
Fe	*Iron*	L_{eq}	*Average continuous graphene length including tortuosity*
FTIR	*Fourier-Transform-Infrared spectroscopy*	n_D	Defect density
HER	*Hydrogen Evolution Reaction*	η	*Overpotential*
Lin	*Linters cellulose-based paper*	SE_A	*Shielding effectiveness of absorption*
Ni	*Nickel*	SE_M	*Shielding effectiveness of multiple reflections*
OER	*Oxygen Evolution Reaction*	SE_R	*Shielding effectiveness of reflection*
PHPS	*Durazane 2250 (Perhydropolysilazane)*	SE_T	*Total shielding effectiveness*
Pd	*Palladium*	T	*Band of sp^3 hybridized carbon structures*
Sar	*Sartorius cellulose-based paper*		
SEM	*Scanning electron microscopy*		
XPS	*X-ray photoelectron spectroscopy*		
XRD	*X-Ray diffraction*		

Symbols

a-c	*Amorphous carbon band in the μ-Raman spectrum*
D	*Defective band*
D´, D+G´, 2D, 2D´	*Overtones in a μ-Raman spectrum produced from two phonon interactions*
E_0	*Potential under standard conditions*
G	*E_{2g} vibrational band in graphene*
J	*Current density*

Content

Figures

Tables

1. Motivation and Aim of the Study

Template-assisted processing has been used over decades to produce materials with interesting micro-/meso-/macro-porous structures, which are suitable for various applications, such as electrode materials for electric double-layer capacitors (EDLCs) [1, 2] or as sensing materials based on nanostructured arrays [3]. A widespread, widely-available template, that can be used in this regard is cellulose-based paper, which is renewable, biodegradable, and abundant. The microstructure of cellulose consists of randomly arranged fibers with a hierarchical structure and contains additionally hydroxyl functional groups. These are predestined for tuneability with various metals and inorganic compounds. After pyrolysis, the produced (ceramic / metal-based) paper usually keeps its structural features and protects the fibers from decomposition. It can exhibit good heat resistance and based on the additional components, is a suitable candidate for a broad field of applications [4]. These include capacitors [5], sensors [6], and the usage in *electrolysis* [7] and *electromagnetic shielding* applications [8, 9].

One way to employ cellulose templates in the production of ceramic compounds is by the usage of *polymer-derived ceramics* (PDCs). They are preparatively accessed from various polymers, such as polysilazanes or polysiloxanes. By annealing these materials at high temperatures, they convert into their respective ceramics.

In this work, polysilazane precursors, such as Durazane 2250 (Perhydropolysilazane (PHPS)) or Durazane 1800 (Dur), are mixed with transition metals (Fe, Pd or Ni), and then cellulose-based templates (Sartorius, Eucalyptus and Linters) are dip-coated in the resulting solution. Further annealing lead to potential functionalized ceramic papers. The aim of this study can be described as:

- Investigation of the bonding situation of the metal-modified preceramic polymers and comparison thereof with the cellulose-based ceramic paper
- Study of the conversion of cellulose-based paper into a potential functionalized ceramic paper
- Examination of the impact of the different precursors and transition metals on the crystalline phases at different temperatures and atmospheres
- Investigation of the carbonization of the cellulose-based template during processing
- Research of possible fields of applications for the potential functionalized ceramic papers, such as electrolysis and electromagnetic shielding

2. Fundamentals and State of the Art

This chapter starts with an introduction to polymer-derived ceramics (PDCs), followed by the processing of materials with macropores. Afterward, the characterization of carbon with the help of µ-Raman spectroscopy is presented. Lastly, an introduction to possible applications, namely hydrogen evolution and oxygen evolution reaction (HER/OER) and electromagnetic shielding (EMS) is given.

2.1 Polymer-Derived Ceramics (PDCs)

Research on p*olymer-derived ceramics (PDCs)* started already in the early 1960s by Ainger and Herbert and also Chantrell and Popper [10, 11], with the successful production of non-oxide Si-based ceramics. Further developments in the 1970s by Veerbeck and Winter, and Yajima enabled the commercial production of silicon nitride (Si_3N_4) and silicon carbide (SiC) fibers by pyrolyzing molecular precursors such as polysilazanes and polycarbosilanes [12–14], which significantly increased the interest of the community to perform further studies on this topic. Over 5 decades later, PDCs are still at the center of many studies, due to their large number of possible applications, tuneability, and relative facile processing. A short overview of the main preceramic precursors, with their respective final ceramic structures after thermal treatment, is shown in Figure 1.
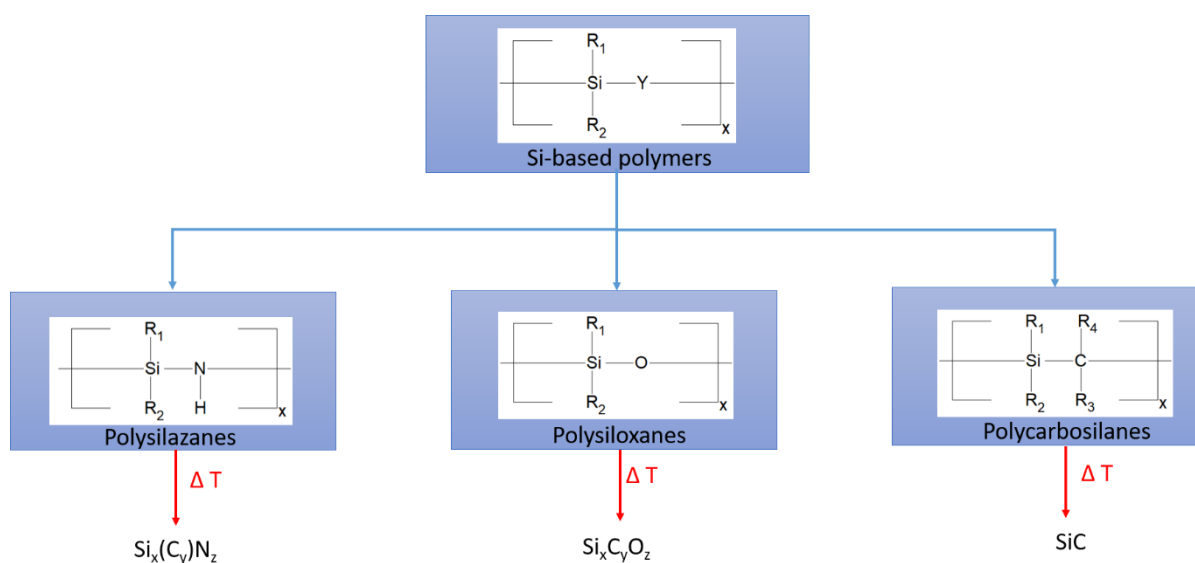
Figure 1. Overview of different preceramic precursors resulting from Si-based polymers

The transformation of polymers into ceramics proceeds in mainly three stages [15, 16]:

I. 100 °C – 400 °C: Crosslinking of the polymer
II. 400 °C – 800 °C: Rearrangement of the polymer, with additional evaporation of organic groups
III. 800 °C – 1000 °C: Conversion into amorphous ceramics
IV. > 1000 °C: Further ceramization (first crystalline phases are produced)

Modification of the Si-based polymers, for instance, the addition of transition metals such as aluminum (Al) into the molecular structure of the polymeric precursor not only improve significantly their properties [17] but can also lead to a reduction of temperatures needed for ceramization of the polymers.

2.2 Processing of Materials with Macropores

This chapter introduces different processing techniques for the synthesis of materials with macropores. There are many techniques, which can incorporate pores into the structure of a ceramic. While some require a sacrificial template, others can be produced via replication of an existing template. In this chapter three different types of processing techniques will be introduced: Template-free processing, sacrificial-template-assisted processing, and template-assisted processing.

2.2.1   Template-Free Processing

In *Direct Foaming,* different gases are used to produce air bubbles inside the (ceramic) suspensions. Additional additives are added to stabilize the formed network and subsequent sintering leads to porous ceramics. The amount of gas, which is incorporated into the (ceramic) suspension, is proportional to the total porosity [18].

In a study by Colombo et al. [19] direct foaming of preceramic polymers, consisting mainly of polysiloxanes and polysilazanes, was used. Those were mixed with a blowing agent, for example pentane. Subsequent annealing led to porous silicon oxycarbide (SiOC) and SiC structures. Du and Yao et. al. [20] successfully synthesized a porous Si_3N_4 ceramic (porosity of 92%-97), by using α-Si_3N_4 powder, with yttrium oxide (Y_2O_3) as a sintering additive. Both were incorporated into a solution of a copolymer, consisting of isobutylene and maleic anhydride. Surfactants helped to stabilize the produced foam, which was inserted into a mold. After drying and sintering, the Si_3N_4 ceramic showed mean pore sizes of 140-240 µm. Other studies have produced SiC [21] and SiO_2-SiC [22] foams. Bauer and Scheffler et al. synthesized Silicoaluminophosphates (SAPO) on a SiC-based foam [23].

Another template-free processing technique is the so-called *Freeze-Casting*, in which (ceramic) suspensions are frozen, by placing them on a cold surface. The resulting temperature gradient initiates the growth of ice dendrites, in which particles are trapped in between. Afterward, the green body is dried and sintered.

Fukasawa and Ando et al. [24] used this processing technique to produce microporous alumina (α-Al_2O_3) ceramic from alumina powder, which was mixed with distilled water and a dispersant. The slurry was then placed inside a container, which bottom part was immersed inside a refrigerator inside an ice bath. After drying and sintering at 1400 °C, the above-mentioned ceramic was produced.

There have been many studies on freeze casting, where other systems like TiO_2 [25] and Si_3N_4 [26] have been synthesized. Yoon and Lee et al. [27] used polycarbosilane to produce highly aligned porous SiC ceramics with well-defined pore structures.

Verma et al. [28] combined both methods by first producing a silica foam, which then was frozen with the help of liquid nitrogen. After drying and sintering, the produced silica ceramic had a porosity of around 85 %.

2.2.2   Replication and Sacrificial-Template-Assisted Processing

In the case of *replication* and *sacrificial* processing, different techniques have been developed. The so-called *replication method* was first introduced by Schwartzwalder and Somers in the 1960s [29], in which a polyurethane sponge was impregnated with different ceramic suspensions. After drying and during the annealing process the template is burned leaving only the microporous ceramic structure behind.

There have been many studies based on polymer foam and ceramic suspensions: Luyten et al. [30] used a polyurethane foam and impregnated it with an Al-Al_2O_3 slurry to produce a light but stable porous Al_2O_3-based ceramic. A similar approach but with magnesium (Mg) and calcium (Ca) stabilized zirconium oxide (ZrO_2) was used by Richardson and Peng et al. [31]. The synthesis of a microporous Si_3N_4 ceramic was performed by Pu and Liu et al. [32] by using β-Si_3N_4 powders with a low percentage of α-Al_2O_3 as additives. Other research on this topic produced microporous SiC and SiO_2 ceramics [33].

Instead of using ceramic suspensions, various studies used preceramic polymers: Nangrejo et al. [34] used polysilane as the preceramic precursor to synthesize, with the addition of Al_2O_3, SiC-Al_2O_3 composite foams. The same author synthesized also SiC-Si_3N_4 and SiC-TiC composites in a similar way [35, 36].

Replication and sacrificial template-assisted processing differ mainly, as in the replication method the structure is replicated resulting in a positive, whereas the sacrificial method leads to a structure displaying a negative morphology of the original template. Various studies used natural templates, like natural rubber [37], cellulose [38, 39], or wood [40, 41] to produce a negative replica. The latter was used to synthesize porous titania, alumina, and zirconia ceramic woods with wood-like microstructures.

The biggest advantages of both methods are the production of complex and porous ceramic structures, where additionally catalytic active materials can be incorporated, leading to promising candidates for various applications.

2.2.3   Template-Assisted Processing

In *template-assisted processing*, a modified and formative template is used to produce the desired structure, which possesses interesting properties due to its reduced dimensionality. Yi and Schwarzacher [42] produced superconducting Pb nanowires in a commercially available track-etched polycarbonate membrane using electrodeposition. Tishkevitch et al. [43] used a similar approach, where alumina membranes were used to produce honeycomb-like ordered Ni nanowires. Other approaches, for example the fabrication of hierarchical porous carbon particles with the help of a hollow polymer microsphere as a template, were also studied [44].

This processing method, compared to the others above, allows for the generation of controlled hierarchical structures and the addition of different transition metals makes it a valuable technique for various applications.

2.3 Characterization of Carbon with µ-Raman Spectroscopy

µ-Raman spectroscopy is a non-destructive characterization method, which allows to analyze the different vibration modes and therefore the structure of molecules. It is mainly used, but not limited to analyzing carbon and carbon-based materials, more precisely amorphous (highly disordered) and graphitic (highly ordered) carbon [45, 46]. Figure 2 (a) shows an exemplary spectrum of a partially amorphous and (b) a graphitic carbon sample. The characteristic bands of the Raman spectra are: T band (1190 cm-1), D band (1350 cm-1), a-c band (1500 cm-1), G band (1590 cm-1) and D´ (1620 cm-1 - not visible here) [45, 46]. Those bands have different derivations: the D and D´ band originates from defects of the carbon structure and is produced by first-order phonons, and the G band arises from the so-called E_{2g} vibration, which is a characteristic vibration mode for graphene, emerging from the Γ point in the Brillouin zone [45, 47, 48]. T band and the a-c band derive from sp^3 hybridized carbon structures and amorphous carbon respectively [46].

(a)

(b)
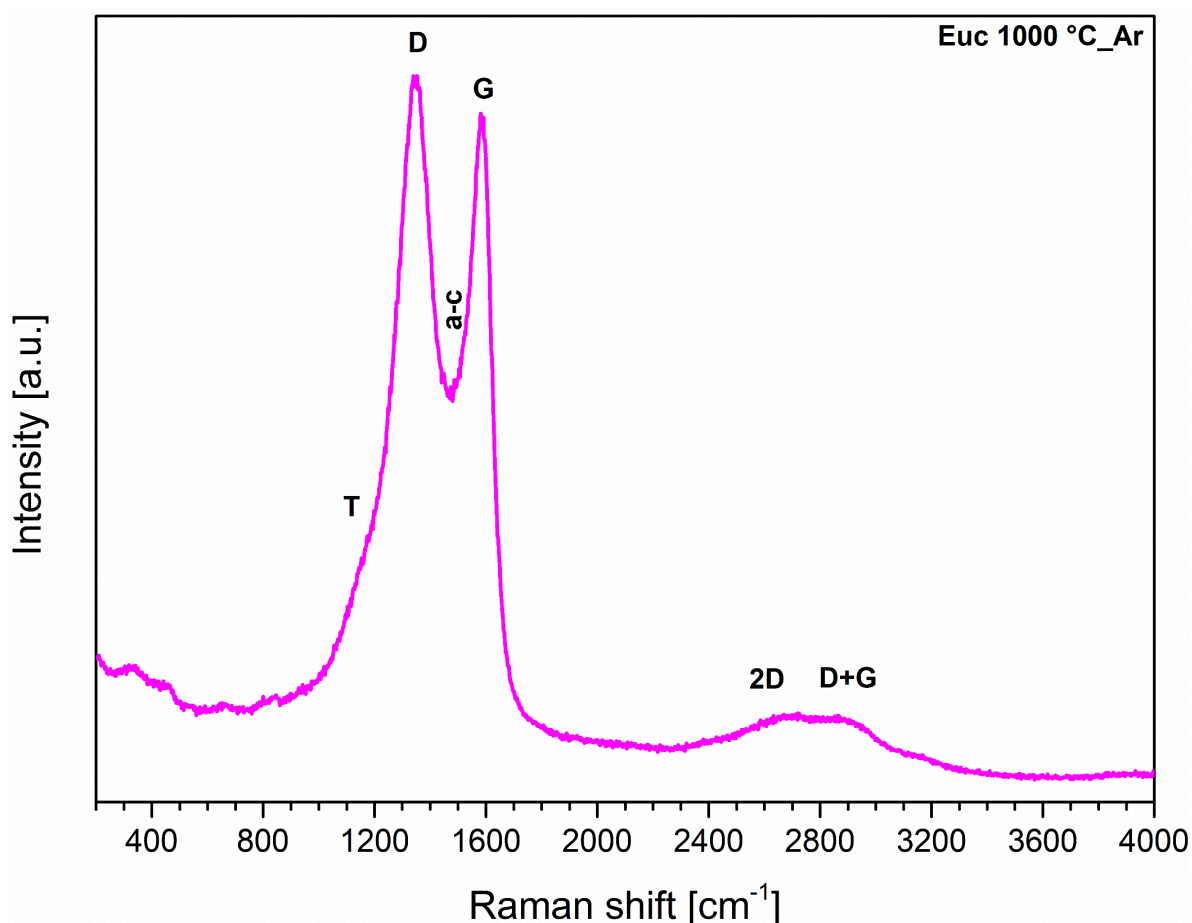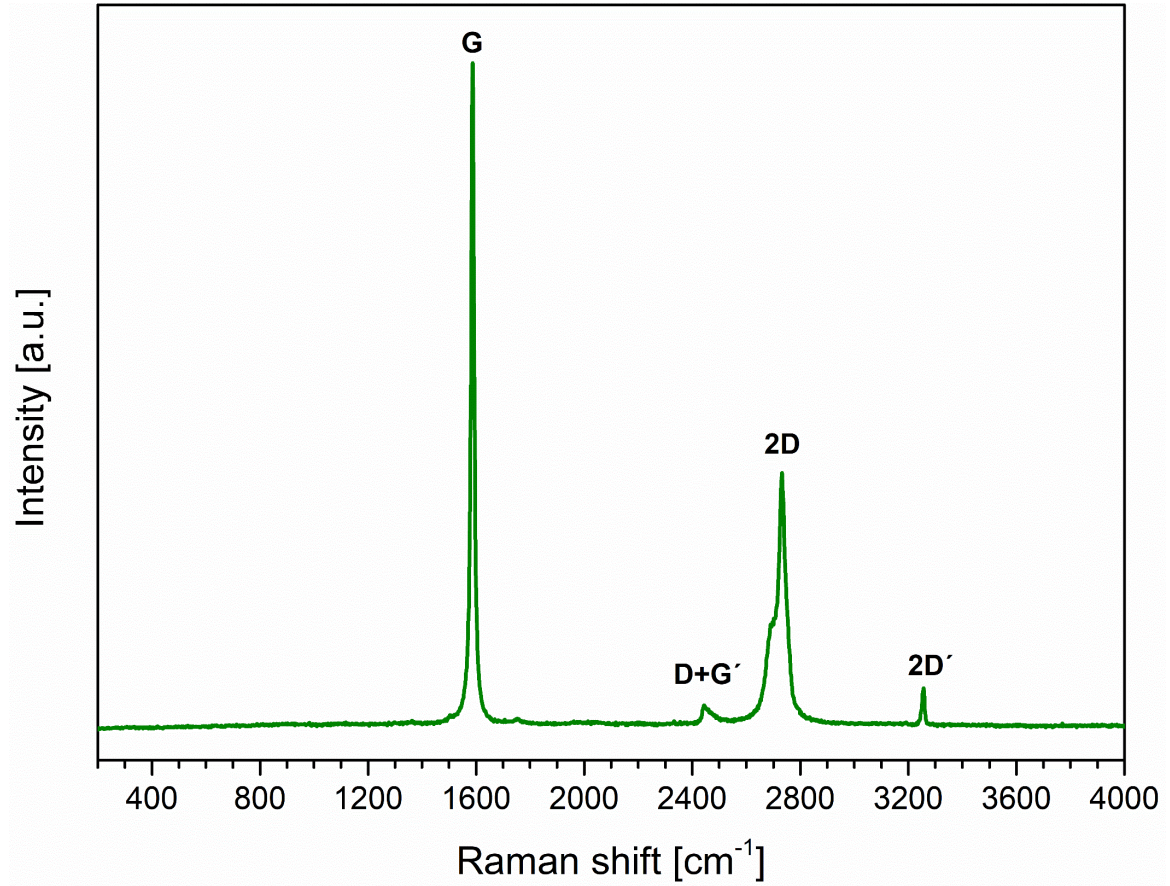
Figure 2. μ-Raman spectra of an (a) partially amorphous carbon sample (Eucalyptus pyrolyzed at 1000 °C in Ar) and (b) a highly graphitic sample (Graphite rock)

Higher bands are called overtones of the respective bands, like 2D (2650 cm^{-1}) from the D band, D+G (2900 cm^{-1}) from D and G band, and mainly arise due to double resonance mechanism originating from two phonon processes [45, 49, 50]. The disappearance of the D band and the sharper 2D band of the Raman spectrum in Figure 2 (b) indicates that graphite is present, consisting of multiple layers of graphene, while in (a) the additional bands (T, a-c, D, the broad 2D, and D+G band) points to highly amorphous carbon structure [45, 49].

The Raman spectrum not only allows to qualify the state of carbon inside the sample but also to quantify it. Tuinstra and König [51, 52] showed that the in-plane crystallite size (L_a) is inversely proportional to the ratio of the D and G band intensities: $L_a \propto (\frac{I_D}{I_G})^{-1}$. This equation was later extended by Knight and White [53], taking the wavelength of the Raman laser ($\lambda = 514.5$ nm) into account and deriving an empirical equation. Further studies suggested using instead of the maximal intensities of the D and G band the integrated intensities (A_D and A_G) [54, 55]. Cançado et al. later suggested equation Eq. 1 for L_a, which also considers the wavelength of the laser [56] and calculated other important parameters like the inter defect distance (L_D) and the

defect density (n_D) [57] (equations Eq. 2 and Eq. 3). Larouche et. al. [58] introduced a fourth parameter L_{eq} (equation Eq. 4), pointing to the average continuous graphene length including tortuosity.

$$L_a = (2.4 \text{ x } 10^{-10})\lambda^4 \left(\frac{A_D}{A_G}\right)^{-1} \quad \textbf{(Eq. 1)}$$

$$L_D^2 = 1.8 \text{ x } 10^{-9}\lambda_L^4 \frac{A_G}{A_D} \quad \textbf{(Eq. 2)}$$

$$n_D = \frac{2.4 \text{ x } 10^{22}}{\lambda_L^4}\frac{A_D}{A_G} \quad \textbf{(Eq. 3)}$$

$$L_{eq} = 77.0648 \frac{A_{2D}}{A_D} \quad \textbf{(Eq. 4)}$$

Typical values for different carbon structures are summarized in Table 1 below.

Table 1. Typical values of crystallite sizes for different carbon structures [46]

Carbon-Type	L_a (nm)
Highly oriented pyrolytic graphite (HOPG)	> 100
Graphite	> 100
Turbostratic carbon	< 10
Glassy carbon	1.5 – 5
Amorphous Carbon	1 - 2

2.4 Applications

The fundamentals of two possible applications are given in this chapter, where the basics of HER/ OER and EMS are introduced.

2.4.1 Hydrogen Evolution Reaction (HER) and Oxygen Evolution Reaction (OER)

An electrochemical reaction can be described as a redox reaction, that either produces electricity (e.g. Battery / Galvanic cell) from a chemical reaction or uses electricity (e.g. Water splitting / Electrolysis) to drive a chemical reaction. Usually, the corresponding half-cell reactions are considered, which can be described as shown in equations Eq. 5 and Eq. 6:

$$\text{Reduction (Cathode): } Ox_2 + ne^- \rightarrow Red_2 \qquad \textbf{(Eq. 5)}$$

$$\text{Oxidation (Anode): } Red_1 \rightarrow Ox_1 + ne^- \qquad \textbf{(Eq. 6)}$$
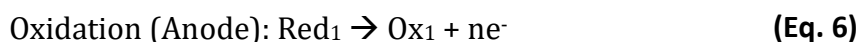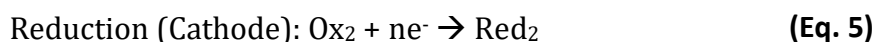
The complete Redox reaction can then be described as a combination of equations Eq. 5 and Eq. 6 and is shown in equation Eq. 7:

$$Ox_2 + ne^- + Red_1 \rightarrow Red_2 + Ox_1 + ne^-$$

$$\Rightarrow \quad Ox_2 + Red_1 \rightarrow Red_2 + Ox_1 \qquad \textbf{(Eq. 7)}$$
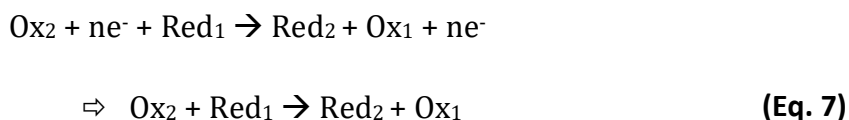
In the case of water splitting two reactions have to be taken into account: The *Hydrogen Evolution Reaction (HER) and the Oxygen Evolution Reaction (OER)*. Both are described in equations Eq. 8 and Eq. 9, under acidic (H^+) and alkaline (OH^-) conditions, respectively:

HER: $\qquad 2H^+ + 2e^- \leftrightarrow H_2 \uparrow \text{ or } 2H_2O + 2e^- \leftrightarrow 2OH^- + H_2 \uparrow$ $\qquad$ **(Eq. 8)**

OER: $\qquad 2H_2O \leftrightarrow O_2 \uparrow + 4H^+ + 4e^- \text{ or } 4OH^- \leftrightarrow 2H_2O + 4e^- + O_2 \uparrow$ $\qquad$ **(Eq. 9)**
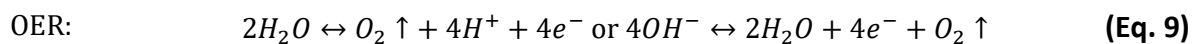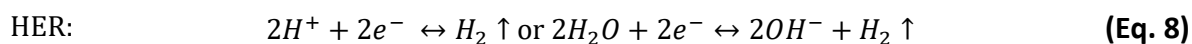
Furthermore, in an OER a multi-electron transfer step can take place, which is described in equations Eq. 10 till Eq. 13, whereas the prefix *ads* denotes the adsorption of the corresponding molecule:

1st step	$O_2 + H^+ + e^- \rightarrow OOH_{ads}$	**(Eq. 10)**
2nd step	$OOH_{ads} + H^+ + e^- \rightarrow 2OH_{ads}$	**(Eq. 11)**
3rd step	$OH_{ads} + H^+ + e^- \rightarrow H_2O$	**(Eq. 12)**
4th step	$OH_{ads} + H^+ + e^- \rightarrow H_2O$	**(Eq. 13)**
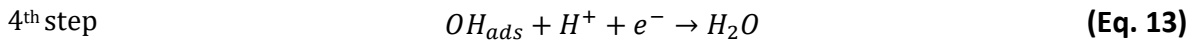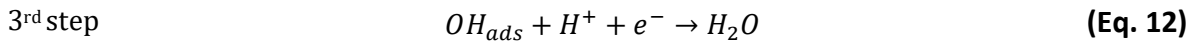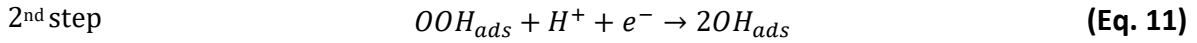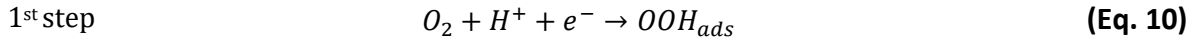
The Nernst equation (Eq. 14) allows to calculate the redox potentials, which deviate from the standard conditions:

$$E = E_0 + \frac{RT}{zF} ln \frac{a_{Ox}}{a_{Red}} \qquad \textbf{(Eq. 14)}$$

E_0 is the potential under standard conditions, R is the gas constant, T is the temperature, z indicates the number of electrons and F is the Faraday constant. a describes the activities of the respective oxidized and reduced species. A minimum of 1.23 V is needed for the water-splitting reaction to occur.

The single half-cell reaction in an electrolysis reaction can be investigated with the help of a three-electrode setup, shown below in Figure 3.
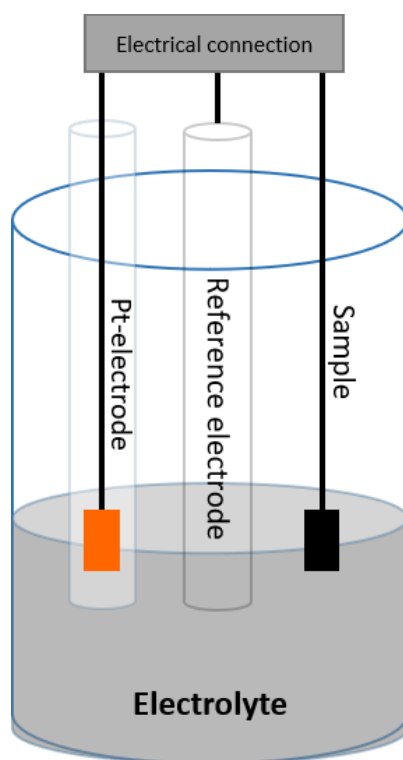
Figure 3. Sketch of the three-electrode setup for the measurement of the single half-cell reaction

Here the current is measured between the counter electrode (Pt-electrode) and the working electrode (Sample), while the potential is measured between the Sample and the reference electrode. The latter derives from specific redox systems (e.g. Hg/HgO) with stable and known potentials.

In general, the activity of a catalyst can be characterized by three different parameters: overpotential, Tafel slope, and exchange current density. These can all be extracted from the polarization curves [59], which are recorded with the above-mentioned method.

Figure 4 shows an exemplary polarization curve of two different samples. As already mentioned before, the occurrence of the water electrolysis requires a minimum potential of 1.23 V (red vertical curve). When the potential produced by the sample exceeds 1.23 V, the difference between the actual potential and the 1.23 V is called Overpotential (η) [59]. In Figure 4 both samples have different η, due to their different catalytic activities. Ideally, a catalytic material possesses a small overpotential and a high current. To evaluate this, the so-called Tafel slope can be calculated from the current density (Δ J, respectively Δ I). If plotted logarithmically (inset), it shows a linear curve.

Then the overpotential can be described with a linear equation, with J_0 being the exchange current density, and can be obtained by extrapolation of the straight line till zero overpotential ($\eta=0$, equals 1.23 V). The slope b describes the catalytic reaction mechanisms [59]. Here, Sample I. has a lower slope and a higher J_0, which shows therefore a better electrocatalytic activity, when compared to Sample II.
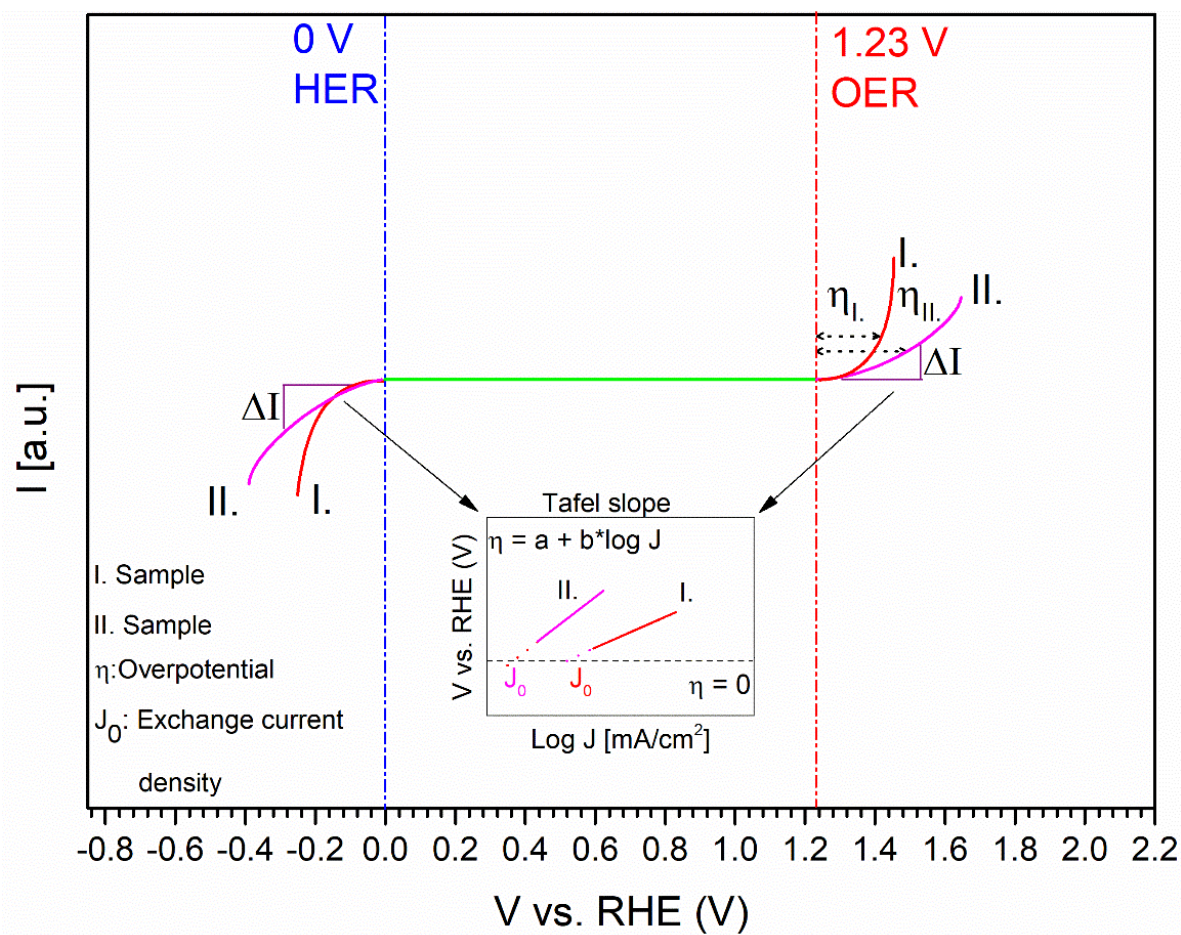
Figure 4. Example of a polarization curve of two different samples, including the resulting Tafel slope, overpotential, and exchange current density. Based on [59] in modified form

There have been many studies of different promising candidates for the electrocatalysis of water splitting, as without a catalytic material the thermodynamic potential (energy barrier) would be too high in both HER and OER. This large thermodynamic barrier can be overcome with some active catalytic materials, which lie on the surface. Nowadays, the two most promising OER catalysts are considered ruthenium (Ru) and iridium (Ir) oxides. In the case of HER, carbon-based platinum (Pt) is the most used catalyst [60–62].

2.4.2   Electromagnetic Shielding (EMS)

Electromagnetic shielding (EMS) helps to minimize interferences between sensitive electronic devices and therefore protects them from damage. In general, an electromagnetic wave consists of two parts, which are perpendicular to each other: an electric and a magnetic part. Reflection and absorption are the main mechanisms of EMS [63]. Figure 5 depicts possible interferences of an electromagnetic wave with a sample. The electromagnetic wave can either be reflected, transmitted, or (partially) absorbed. While the material needs to be conductive for the reflection, the thickness and the availability of electric and magnetic dipoles are important parameters for absorption. Furthermore, an additional mechanism for EMS is to scatter the incoming wave by using multiple surfaces or different phases [63].
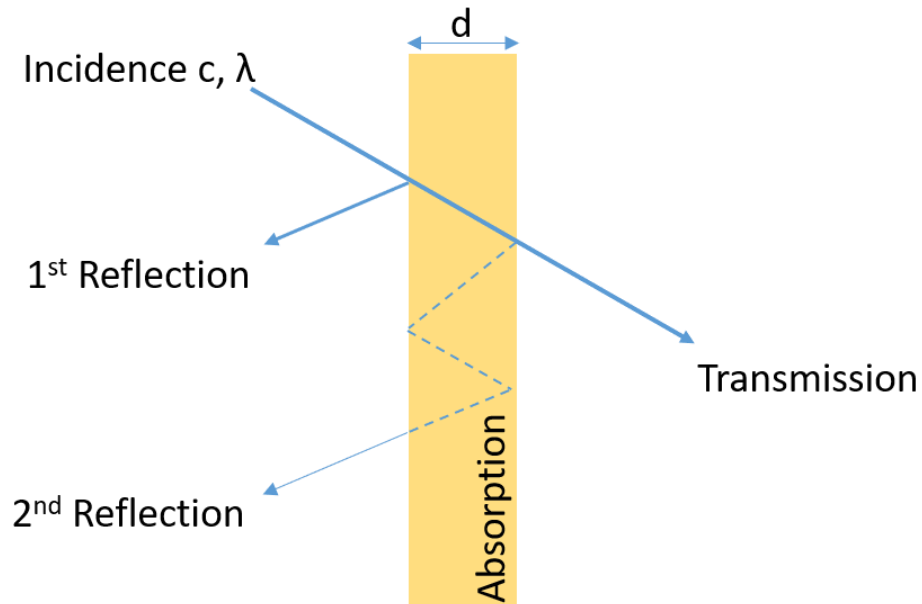
Figure 5. Different mechanisms for electromagnetic shielding upon a sample with a thickness of d

Therefore, promising candidates consist of a mixture of conductive and multiple-phase composites.

SE_T can be calculated from the following equation (Eq. 15) [63–65], whereas SE_A, SE_M, and SE_R are the respective effectiveness of the absorptions, multiple and single reflections:

$$SE_T \text{ (dB)} = SE_A + SE_M + SE_R \qquad \textbf{(Eq. 15)}$$

Liu et al. [64] synthesized a highly flexible and ultrathin Mo_2C film via in-situ growth on graphene oxide, with an estimated thickness of each sub-layer of around 3 μm, which provided average total shielding effectiveness (SE_T) of around 40 dB in the range of 8 GHz – 12.5 GHz.

Table 2 summarizes a few material classes with their respective shield effectiveness.

Table 2. Comparison of EMS performance of different materials. Based on [63–69]

Composite	Thickness [mm]	Frequency range [GHz]	EMS SE_T (dB)
Epoxy/carbon black	1	1 - 10	44
PP/MWNT	1	8 - 12	34.8
PDMS/graphene foam	1	0.03 - 1.5	30
$Ti_3C_2T_x$ carbon black films	-	8 - 12.5	60
Ni/rGO foam	-	2.6 - 26.5	74
Porous SiC ceramic	-	8 - 12	32
FeSiAl/Al_2O_3ceramic	-	8 - 12	36
Cement/graphite	-	3.8 - 6	32
Carbon nanofiber/cellulose	1	8 - 12	24.6

3. Experimental Procedure

In this chapter, a short introduction to the experimental procedure will be described. First, the used chemicals are shown. Afterward, an exemplary procedure to synthesize a Lin_Fe_PHPS ceramic paper is described in detail.

3.1 Synthesis of Cellulose-based Metal-modified Ceramic Papers

The synthesis of the different polymer-derived-ceramic papers (PDCPs) was performed with the help of dip-coating. Depending on the desired system, different precursors and metal-acetylacetonates were used. Table 3 summarizes the used materials and Figure 6 depicts the chemical structure of the preceramic polymers.

Table 3. Used materials for the one-pot-synthesis

System	Metal Precursor	Polymer Precursor	Brand
Si-Fe-O-(N)	Iron(III)acetylacetonate (≥99.9% trace metals basis)	Durazane 2250 (PHPS; 20 wt %)	Sigma Aldrich
Si-Fe-C-O-(N)		Durazane 1800	Sigma Aldrich
Si-Pd-O-(N)	Palladium(II)acetylacetonate (99%)	Durazane 2250 (PHPS; 20 wt %)	Sigma Aldrich
Si-Pd-C-O-(N)		Durazane 1800	Sigma Aldrich
Si-Pd-O-(N)	Nickel(II)acetylacetonate (95 %)	Durazane 2250 (PHPS; 20 wt %)	Sigma Aldrich
Si-Pd-C-O-(N)		Durazane 1800	Sigma Aldrich

(a)   **(b)**
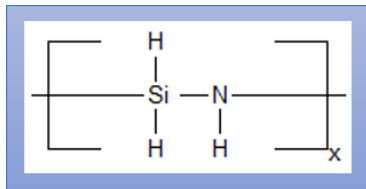
Durazane 2250 (PHPS)   Durazane 1800
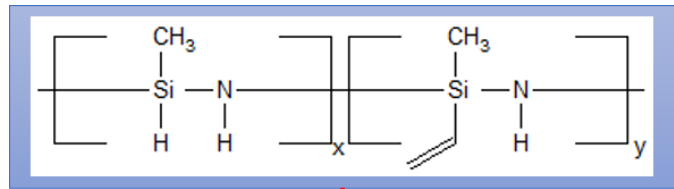
Figure 6. Chemical composition of Perhydropolysilazane in (a) and Durazane 1800 in (b) with their respective ceramic structure after annealing at higher temperatures

As for the cellulose and Eucalyptus paper, different types were used, which are shown in Table 4. Linters and Eucalyptus-based papers were synthesized by Christiane Helbrecht and Andreas Striegel from the Paper Technology and Mechanical Process Engineering (PMV) at TU Darmstadt. The production is shortly described in chapter 3.2.

Table 4. Cellulose-based paper types used in the experiment

Paper-Type	Grammage [g/m²]	Brand
Cellulose-based paper	65	Sartorius (3 hw)
Linters-based paper	65	Self-Made (PMV)
Eucalyptus based paper	65	Self-Made (PMV)

The used masses and volumes are depicted in Table 5. The weight ratios were calculated by taking the respective molar masses into account. As palladium(II)acetylacetonate and nickel(II)acetylacetonate have inferior solubility in toluene compared to iron(III)acetylacetonate, their weights were adjusted. Furthermore, two different Batches, which differ in the concentration of the metal-acetylacetonate, the preceramic precursor, and the amount of solvent, were used. The time during the refluxing process was also varied, to investigate, how the change in parameters influences the results. The solvent of the Perhydropolysilazane precursor was evaporated before mixing it with the other solvent (99,8 % anhydrous Toluene, Merck KGaA). Durazane was used as delivered.

Table 5. Overview of the used molar masses and weights

System	Batch 1	Batch 2
Si-Fe (PHPS and Dur)	1 g (Pure PHPS/Dur) : 1g iron(III)acetylacetonate + 50 ml solvent	0.25 g (Pure PHPS/Dur) : 0.25 g iron(III)acetylacetonate + 25 ml solvent
Si-Pd (PHPS and Dur)	1 g (Pure PHPS/Dur) : 1g palladium(II)acetylacetonate + 30 ml solvent	0.25 g (Pure PHPS/Dur) : 0.215 g palladium(II)acetylacetonate + 25 ml solvent
Si-Ni (PHPS and Dur)	0.5 g (Pure PHPS/Dur) : 0.364 g nickel(II)acetylacetonate + 25 ml solvent	0.25 g (Pure PHPS/Dur) : 0.182 g nickel(II)acetylacetonate + 25 ml solvent
All above (Cooking Time)	12 hours after reaching 100 °C	30 Minutes after reaching 100 °C

3.2 Production of Cellulose-based Papers (Linters and Eucalyptus)

The cellulose-based papers were fabricated from cotton and Eucalyptus respectively. The production was performed with the help of a Rapid Köthen Sheet Machine after DIN EN ISO 5269-2 norm. Round sheets with a grammage of 65 g/m² and an average weight of 1.99 g were produced. The as-produced papers were cut in different sizes [(1.5x1.5) cm² and (5x3) cm²] and before usage dried in an oven at 80 °C for at least 24 hours.

3.2.1 Exemplary Synthesis of a Fe-PHPS-based Ceramic Paper

Exemplary, the synthesis of the Lin_Fe_PHPS (Batch 1) ceramic paper is described here. The other syntheses were performed similarly, with the described amounts of chemicals as shown in Table 5. 5 g of perhydropolysilazane (NN 120-20 (A); 20 wt-% solution of Perhydropolysilazane (PHPS)) was filled into a flask under inert conditions. Using the standard Schlenk technique, di-n-butyl ether was removed by vacuum-drying for 3 hours. After degassing, the pure PHPS was dissolved in 50 ml of anhydrous toluene (99.8%, Merck). Further addition of 1 g of iron(III)-acetylacetonate (≥99.9% trace metals basis, Merck) leads to a red liquid preceramic polymer. Subsequently, the precursor solution was refluxed at 100 °C for 12 hours. The beforehand dried and cut cellulose-based papers (Linters) were dip-coated for approximately 1 second in the preceramic polymer solution in an inert atmosphere. Further vacuum drying of the wet papers led to yellowish/red dry polysilazane-impregnated cellulose papers. The remaining solution was also dried to get the Fe-modified preceramic polymer.

3.2.2 Temperature Programs for the Annealing of the Synthesized Ceramic Papers & Preceramic Precursors

The impregnated and vacuum-dried ceramic papers / preceramic precursors were pyrolyzed at different temperatures and atmospheres. The temperature program is shown in Figure 7.
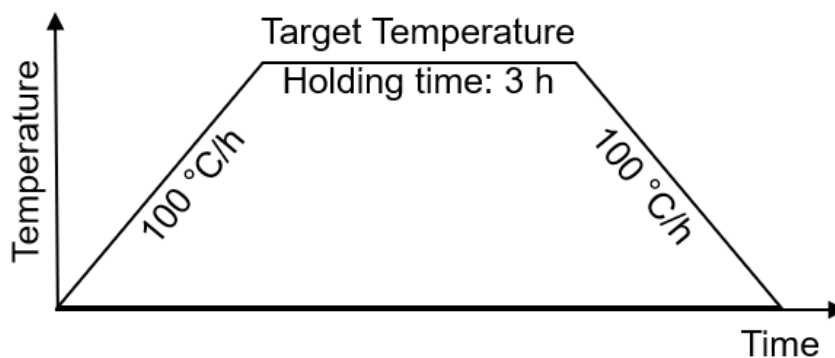
Figure 7. Temperature program

The ammonolysis procedure was performed inside a Schlenk tube in a quartz crucible, which was placed in a high-temperature oven (Gero GmbH & Co., Neuhausen, Germany), where the ammonia flow (purity: 99.999 Vol.%; $H_2O < 5$ ppmv; $O_2 + Ar < 1$ ppmv; Airliquide, Düsseldorf, Germany) was set to 50 sccm (i.e., 0.05 l min^{-1}) and the heating and cooling rates were 100 °C per hour, until the designated temperature was reached.

The pyrolysis at 1000 °C in argon atmosphere was performed also inside a Schlenk tube and a quartz crucible in a tube furnace (Loba, HTM Reetz GmbH, Germany) with the same temperature program as shown in Figure 7. The argon flow was set to 2-3 bubbles per second.

The samples, that were tempered at 1300 °C in either N_2 (purity: 99,999 %, Alphagaz / Airliquide, Düsseldorf, Germany) or Ar atmosphere, were previously annealed at 1000 °C in NH_3 or Ar. For most of the samples, the graphite furnace (GT Advanced Technologies (previous Thermal Technology LLC), California, USA) was used for the annealing at 1300 °C. The samples were placed inside a small graphite crucible, which was then placed inside a larger crucible (Figure 8 (a)) and the temperature program was configured as shown in Figure 8 (b). The N_2 / Ar gas flow rate was set to 80 sccm on the pipes and 40 sccm inside the chamber.

(a)   **(b)**
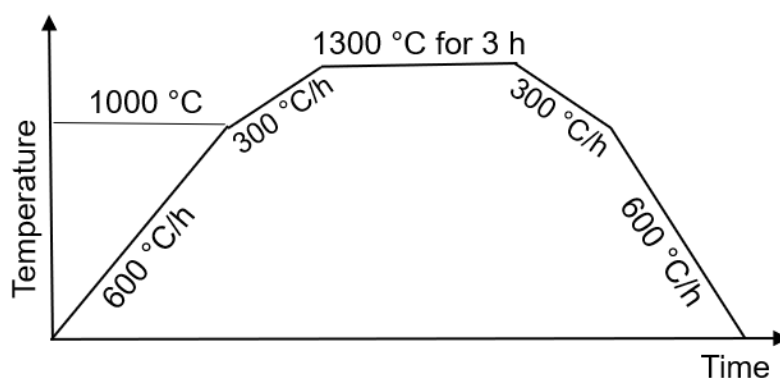
Figure 8. Photograph of samples placed inside a larger graphite crucible with ceramic papers placed on a constructed graphite foil in (a) and (b) used temperature program

For the electrocatalytic and electromagnetic shielding measurements, a bigger piece of ceramic paper was needed. Therefore, the temperature program used at 1000 °C, and the setup was slightly changed, as shown in Figure 9. First, a graphite foil was used to produce flat samples, which were stacked inside the graphite foil. The foil was fixed with SiC fibers so that the preceramic papers remained at their positions. All were performed under an inert atmosphere.

(a)   **(b)**
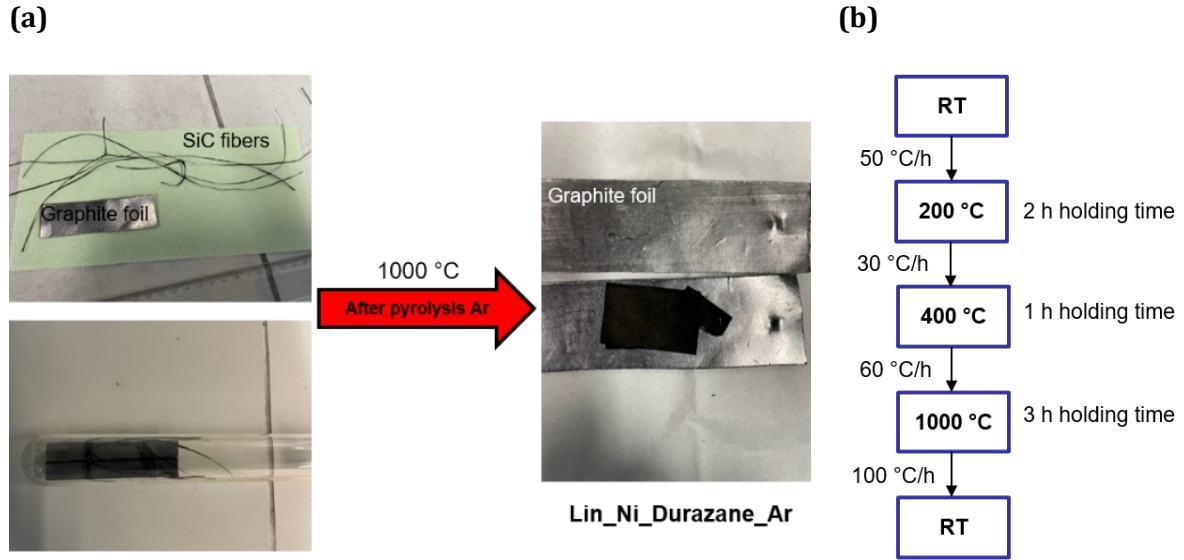
Figure 9. (a) shows the setup for the bigger ceramic papers, which were put inside a graphite foil and wrapped with SiC fibers and (b) depicts the modified temperature program

For the electrocatalytic samples, the annealing at 1300 °C was performed afterward as shown in Figure 8. For the samples produced for the electromagnetic shielding measurements (at 1300 °C) in argon, an Alumina tube furnace (Heraeus, Germany) was used with a heating and cooling rate of 100 °C and a holding time of 3 hours. The samples were previously also put inside a graphite foil.

In the results and discussion part, the samples have been named as follows: Paper-Type_Transition Metal_Polymer Precursor_Temperature_Atmosphere (Previous atmosphere at 1000 °C). Example: Lin_Ni_PHPS-1300 °C N_2 (Ar), means that Linters cellulose-based paper was used as a template with Ni and PHPS as the transition metal and polymer precursor respectively. The sample has been annealed at 1000 °C in Ar before and then further at 1300 °C in N_2.

3.3 Characterization Methods

The following chapter lists the different instruments used for the characterization analysis of the samples.

X-Ray Diffraction (XRD): In order to study the different crystalline phases of the samples, a STOE STADI P diffractometer (STOE & Cie. GmbH, Germany) in transmission mode with monochromatic Mo $K_{\alpha1}$ radiation (λ = 0.70932 Å) was used. The XRD patterns were analyzed using the program "Match" with the Powder Diffraction file 2.0 and Online Databases.

Fourier-Transform-Infrared-Spectroscopy (FTIR): To analyze the different vibration modes the FTIR spectrometer (VARIAN 670-IR, Bruker, Massachusetts, USA) was used in attenuated total reflection (ATR) mode for air-sensitive samples (pre-ceramic precursors) and in transmission geometry mode using Pottasiumbromid (KBr) pellets for all other samples.

μ-Raman Spectroscopy: For the μ-Raman spectroscopy a Horiba HR 800 spectrometer (Horiba Jobin Yvon, Bensheim, Germany) was used. Measurements were performed in the range of 0 cm^{-1} to 4000 cm^{-1} using a green laser (λ = 514.5 nm) combined with a confocal microscope.

Thermogravimetric Analysis (TGA): The thermogravimetric analysis in the argon atmosphere was performed with the help of a TGA device (Netzsch STA 449C Jupiter, Germany) with a heating and cooling rate of 5 °C/min, which was coupled with a quadrupole mass spectrometer (QMS, Netzsch 403C Aëolos, Germany).
For the TGA measurements in ammonia / argon atmosphere (90 % NH_3; 10 % Ar) a Netzsch device (Sel, STA449F3 with Perseus-Coppling) with a 5 °C/min heating and cooling rate in a range from 30 °C to 1350 °C and with a flow of 90 ml/min NH_3 and 10 ml/min Ar was used. Al_2O_3 crucibles were used in the DTA/TG mode.

Scanning Electron Microscopy (SEM): The samples were also investigated via scanning electron microscopy (SEM). To avoid charging under the incident electron beam, the samples were glued to a sample holding stub with a conducting carbon-based glue and lightly sputtered with carbon. A JEOL 7600F microscope (JEOL, Tokyo, Japan) was used for the secondary electron (SE) and backscattered electron (BSE) imaging, being equipped with an energy-dispersive X-ray detector (X-MAX 80; Oxford Instruments, Wiesbaden, Germany).

Hydrogen Evolution Reaction and Oxygen Evolution Reaction (HER/OER): For the electrocatalytic measurements a GAMRY Interface 1000E potentiostat was used. A three-electrode setup, which was custom made and is shown in Figure 10, was utilized. The reference electrode consisted of Hg/HgO and the electrolyte of a 1 M KOH (Carl Roth) solution. The width and the length of the samples were measured before.

After setting everything up, additional measurements were performed to determine the amount of the sample inside the potassium hydroxide (KOH) solution and to calculate the active area afterward.

The measurement was performed following these steps:

I. Open Circuit Potential (OCP) measurement
II. Measurement of the electrochemical impedance spectroscopy (EIS) at the OCP
III. Cyclic voltammetry (CV) measurements between -0.5 V and 1.9 V (calibrated values) with a scan rate of 50 mV s^{-1} for 2 cycles for activation of the (ceramic) paper
IV. Cyclic voltammetry (CV) measurements between -0.5 V and 1.9 V (calibrated values) with a scan rate of 50 mV s^{-1} for 10 cycles

(a)   **(b)**
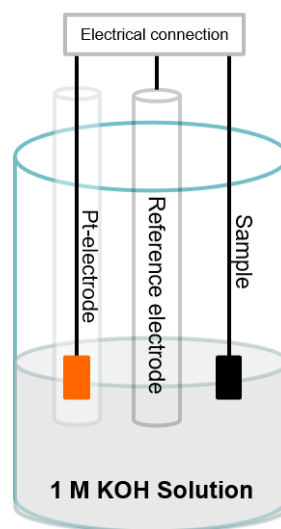
Figure 10. Setup for the HER and OER measurements. (a) Photograph and (b) sketch of the setup

Electromagnetic Shielding (EMS): Electromagnetic shielding was measured with the same setup as described in the paper by Liu et al. [65]. The values of the scattering parameters (S_{11}, S_{12}, S_{21}, and S_{22}) of the ceramic paper-based samples were measured by the so-called waveguide method using a vector network analyzer (VNA, MS4644A; Anritsu, Japan) in the range of 8.2 to 12.4 GHz (X-band).

4. Results and Discussion

This section focuses first on the characteristics of the different cellulose-based templates, which were used (Linters, Eucalyptus, Sartorius). First, the influence of pyrolysis in Ar and NH_3 atmosphere on the paper template is investigated. After impregnation of the cellulose-based template with different transition metals (Fe, Pd, or Ni) and polysilazanes (PHPS or Dur), the impact of the temperature and atmosphere on the ceramic papers are studied with the help of different characterization methods.

4.1.0   Paper Templates - Overview

For this work, three different paper types are used, as described in chapter 3. To get a better understanding, whether the paper types have different surface bonding chemistry, FTIR is used (Figure 11). There are no significant differences between the three paper templates, as the main bands are present in each sample. The characteristic bands are as follows: at 890 cm^{-1} and 1060 cm^{-1} ß-glycosidic linkage of the cellulose unit, 1280 cm^{-1}, 1370 cm^{-1} and 2900 cm^{-1} C-H vibrations. C-H_2 vibrations are visible at 1315 cm^{-1} and 1425 cm^{-1}. The sharp band at 1610 cm^{-1} and the broad one from 2900 to 3400 cm^{-1} are distinct for O-H groups mainly on the surface [70–73].
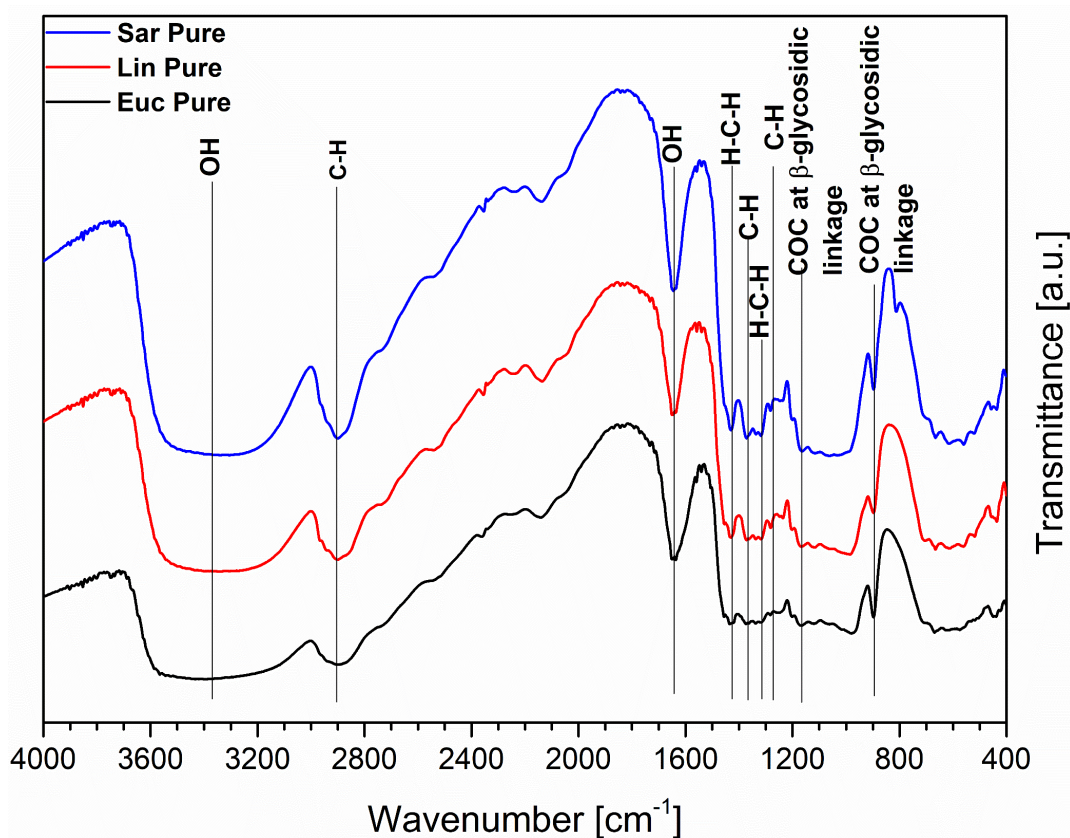
Figure 11. FTIR spectroscopy of the pristine paper templates (as received)

µ-Raman spectroscopy allows to further characterize the bonding situation and the state of carbon of the paper templates (shown in Figure 12). The main bands are summarized in Table 6. Mainly the CCC, COC, CH, and HCC/HCO bands are present, which is in congruence with the FTIR measurements. Comparing those results with a cellulose oligomer (Figure 13), the origin of the vibrations from both µ-Raman spectroscopy and FTIR measurements is evident.
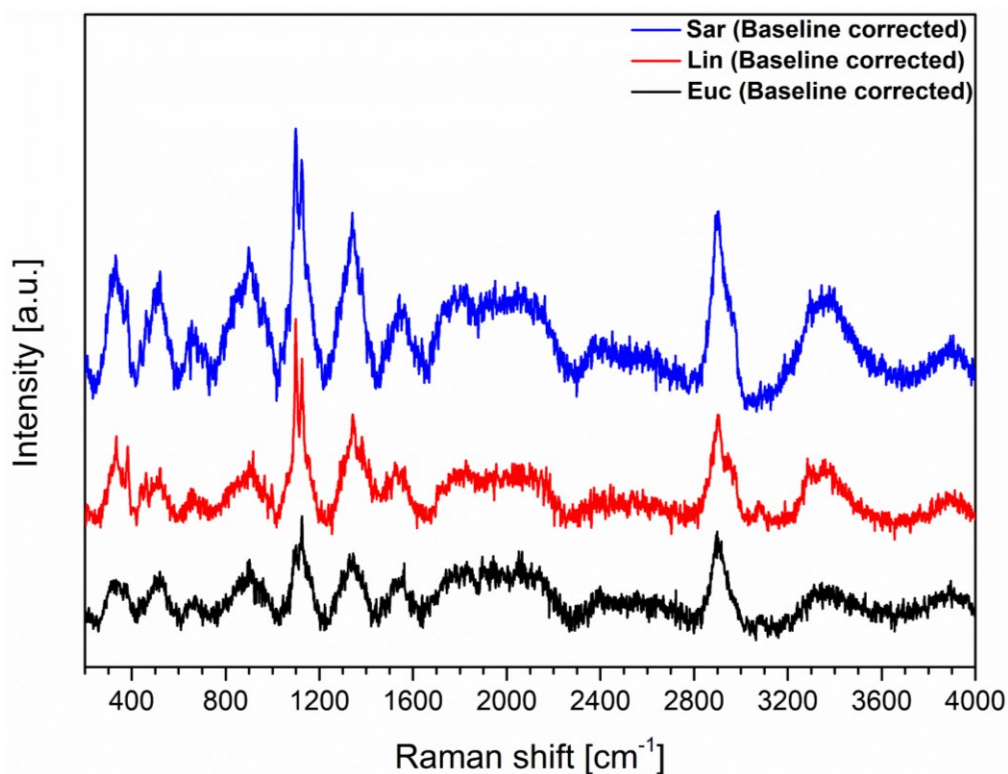
Figure 12. µ-Raman spectroscopy of the different pristine paper templates (as received)

Table 6. Characteristic functional bands from the µ-Raman spectra from Figure 12. Based on [74, 75]

Raman shift [cm^{-1}]	Functional group
330	CCC (ring deformation)
380	CCC (symmetric ring deformation)
520	COC. Glycosidic linkage
895	HCC; HCO;
1098	COC asymmetric, glycosidic, ring breathing, skeletal
1123	COC symmetric, glycosidic, ring breathing, skeletal
1345	C-H
2900	C-H$_3$ (Methyl)

1, 4 β-Gylcosidic bond

Hydrogen bond
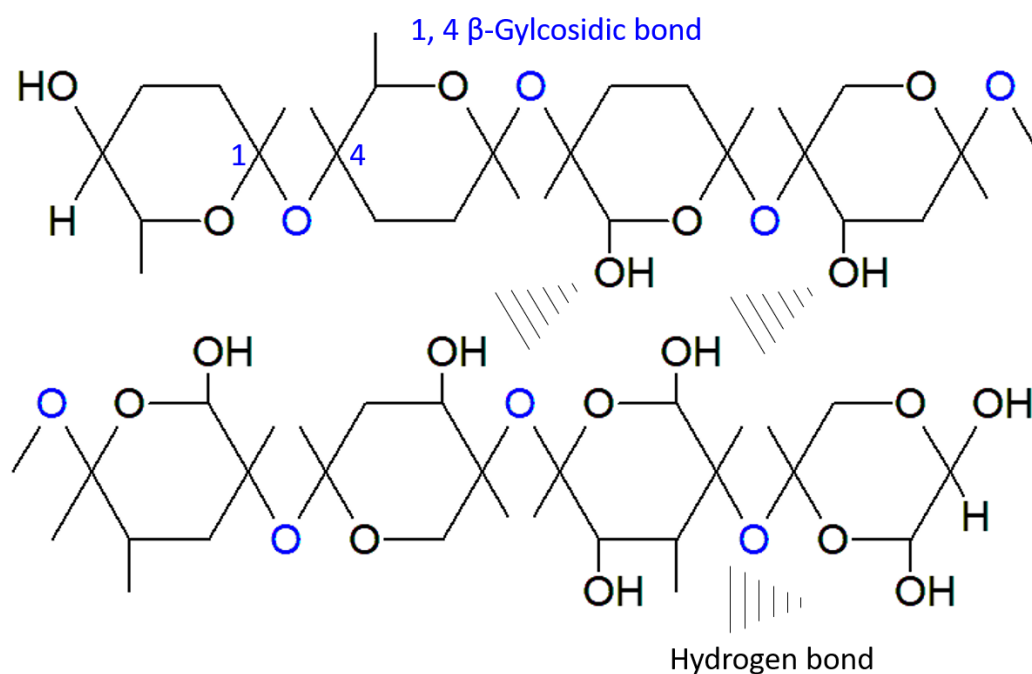
Figure 13. Lewis structure of cellulose. Based on [76, 77]

Secondary electron microscopy (SEM) images of the different paper templates are shown in Figure 14. The paper templates differ mainly in the thickness, length and orientation of the individual fibers. Furthermore, the cellulose-based Linters paper is less dense and appears to have more pore volume in between the fibers, compared to the Sartorius and Eucalyptus-based papers.
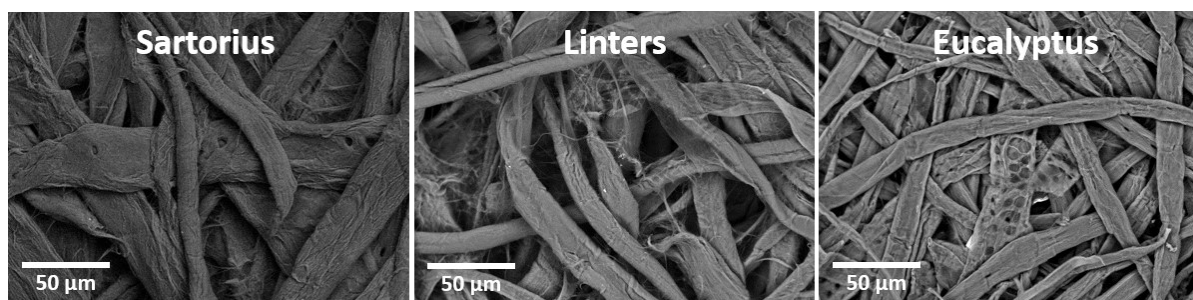
Figure 14. SEM images of the pristine Sartorius, Linters and Eucalyptus paper. Images were taken by Johannes Peter

4.1.1 Paper Templates – Influence of Atmosphere: Ammonolysis at 1000 °C

The untreated paper templates are ammonolyzed at 1000 °C, as described in chapter 3.2.2. At this temperature, a kinetic-driven decomposition of NH_3 occurs, as shown in equation Eq. 16:

$$2\ NH_3\ (g) \rightarrow 3\ H_2\ (g) + N_2\ (g) \qquad \textbf{(Eq. 16)}$$
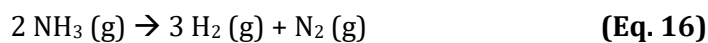
Furthermore, there have been studies [78] on the doping effect of NH_3 atmosphere on cellulose-based paper following the reaction (Eq. 17), whereas nitrogen is incorporated into the cellulose structure:

$$3\ C\ (s) + 4\ NH_3\ (g) \rightarrow 3\ CH_4\ (g) + 2\ N_2\ (g) \qquad \textbf{(Eq. 17)}$$
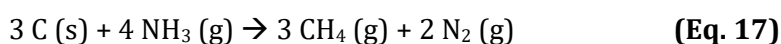
As the atmosphere is not static, the conversion of NH_3 into N_2 and H_2 is partial. The high amount of OH groups on the surface of the cellulose promotes the reaction with H_2 to form H_2O. Both reactions shown in equations Eq. 16 and Eq. 17 lead to a decomposition of the cellulose, which can be partly seen in the photographs (Figure 15). It appears that the Sartorius template has significantly lower shrinkage and decomposition compared with the Linters paper. It is assumed, that during the Sartorius paper production additives are added, which reduce the shrinkage of the paper during ammonolysis.
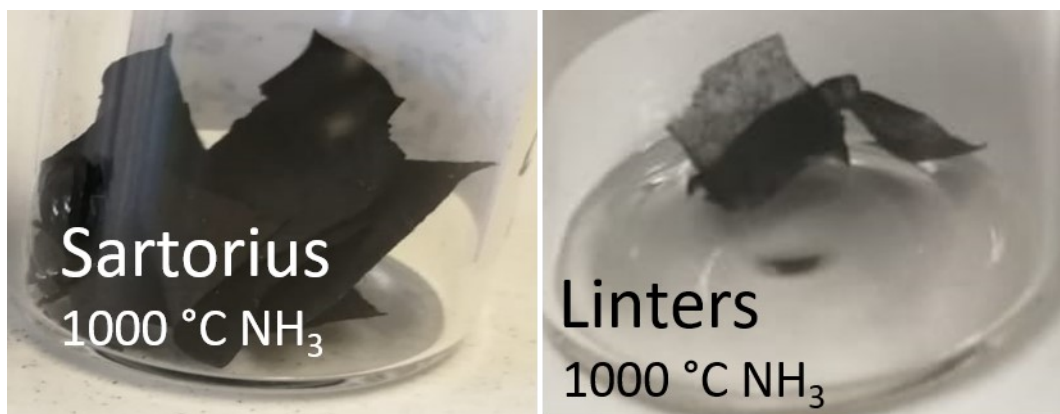
Figure 15. Photographs of the uncoated Sartorius (left) and Linters (right) papers after ammonolysis at 1000 °C

Thermogravimetric analysis (TGA) of the Linters paper was performed to get a better understanding, which processes take place during ammonolysis (shown exemplarily in Figure 16). TGA of the other two templates are in the Appendix (Figure A 1). The progression of the mass loss and DTA curve in regions I. – III. are similar. Only region IV. differs in the Linters template compared to the Sartorius and Eucalyptus template.

The TGA curve can be divided into 4 main regions (I.-IV.). The main evaporating species are summarized in Table 7. In region I. adsorbed water is being evaporated in a temperature range up to 250 °C. In region II., which has the highest mass loss, the decomposition of lignin and carbonyl derivatives, like formic acid (CH_2O_2), takes place. This is caused by the ammonia atmosphere and its partially decomposed parts (comparable to Eq. 16 and Eq. 17) [79, 80]. The produced hydrogen can react with the hydroxyl groups from the cellulose-based template and additionally, the hydroxyl groups can cross-link [81], producing water in both processes. Region III. is dominated by further decomposition of the cellulose into CO and CO_2. At 1000 °C, in region IV., no cellulose remains. After the TGA measurements, residues of calcium, aluminum and oxygen-based compounds remained in the crucible, which could have reacted with the alumina crucible to produce calcium aluminates [82] and therefore produce the strong exothermic peak.
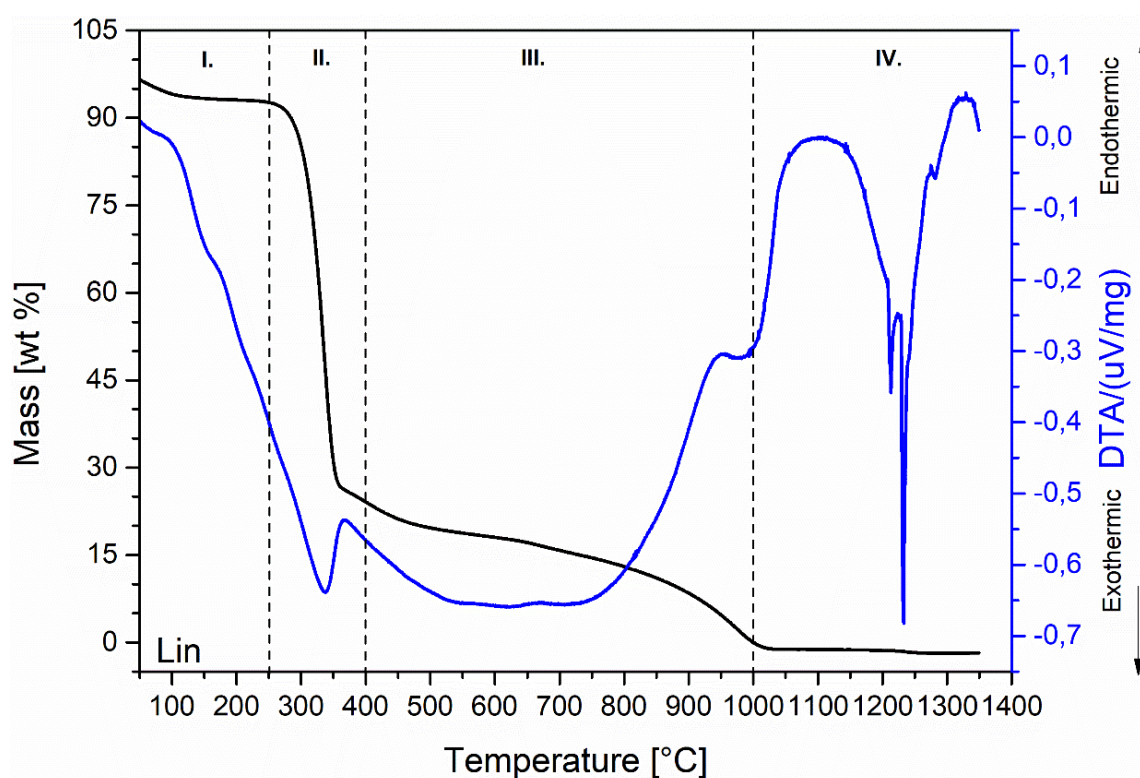
Figure 16. TGA of Linters paper in ammonia/argon (Ratio 90:10) atmosphere

Table 7. Characteristic evaporating species from Figure 16. Based on [79, 80]

Region	Temperature [°C]	Evaporating species
I.	50-250	H_2O;
II.	250-400	H_2O; Carbonyl derivate (CH_2O_2)
III.	400-1000	CO; CO_2;
IV.	1000-1350	-

Moreover, the FTIR spectra of the ammonolyzed samples are similar, independently of the template and are shown in Figure 17. At around 3450 cm^{-1} O-H and/or N-H vibrations from the O-H/N-H groups, which are on the surface of the sample, are visible. The band between 400 and 1200 cm^{-1} is hard to interpret due to its broadness.
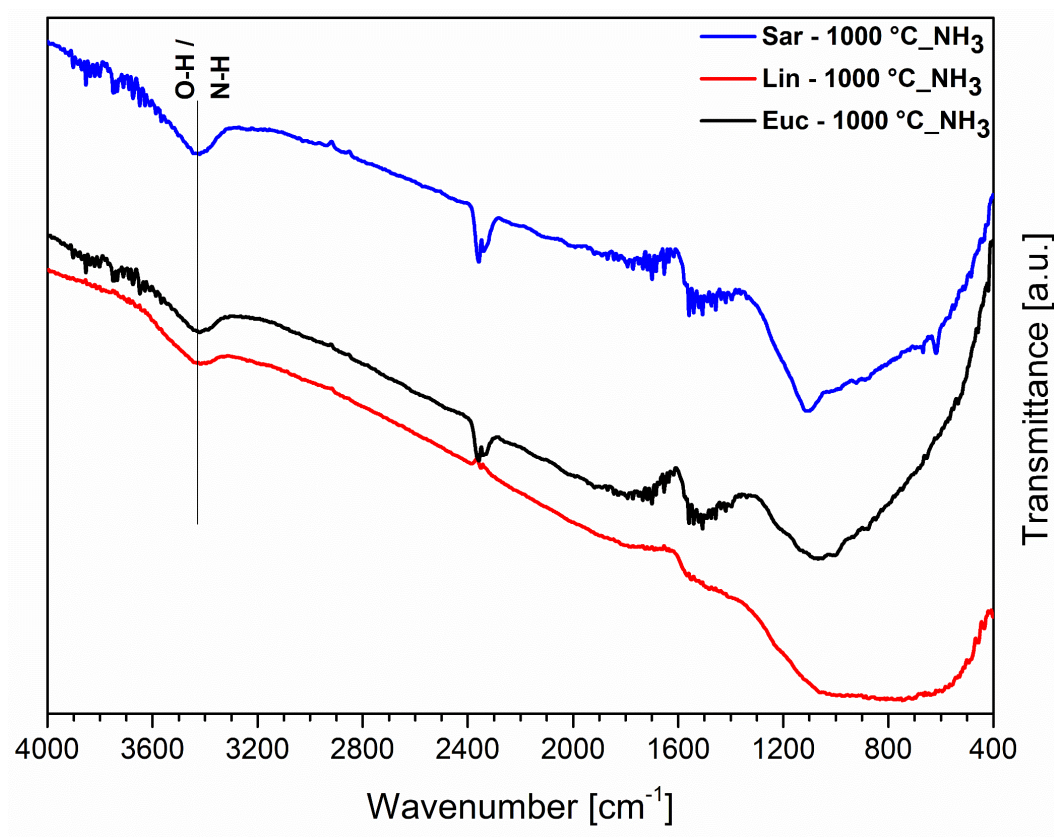
Figure 17. FTIR spectra of the ammonolyzed paper templates at 1000 °C

μ-Raman spectroscopy (Figure 18) reveals the characteristic D (1351 cm^{-1}) and G (1597 cm^{-1}) band, which derivate from the carbon of the cellulose-based paper, the amorphous carbon (a-c) (1508 cm^{-1}) and the T band (1204 cm^{-1}) (designated to sp^3 carbon structures). The influence of the disorder can be seen by the overtones (2D and the D+G bands (2674 cm^{-1} and 2929 cm^{-1})) [83].

The band intensities and structures appear to be similar and reveal a poorly graphitized carbon structure, independent of the paper template. To further characterize this, equations Eq.1 to Eq. 4 were used to calculate the crystallite size L_α, the inter defect distance L_D, the average continuous graphene length including tortuosity (L_{eq}) and the defect density n_D (shown in Table 8). It appears, that the values of all calculated parameters are in the same range. Higher L_{eq} values compared to L_a indicate tortuosity in the sample, which can be attributed to curved (turbostratic) carbon. The poor beforementioned graphitization can also be seen in the small A_{2D}/A_D ratio and the broad 2D band [45, 58].
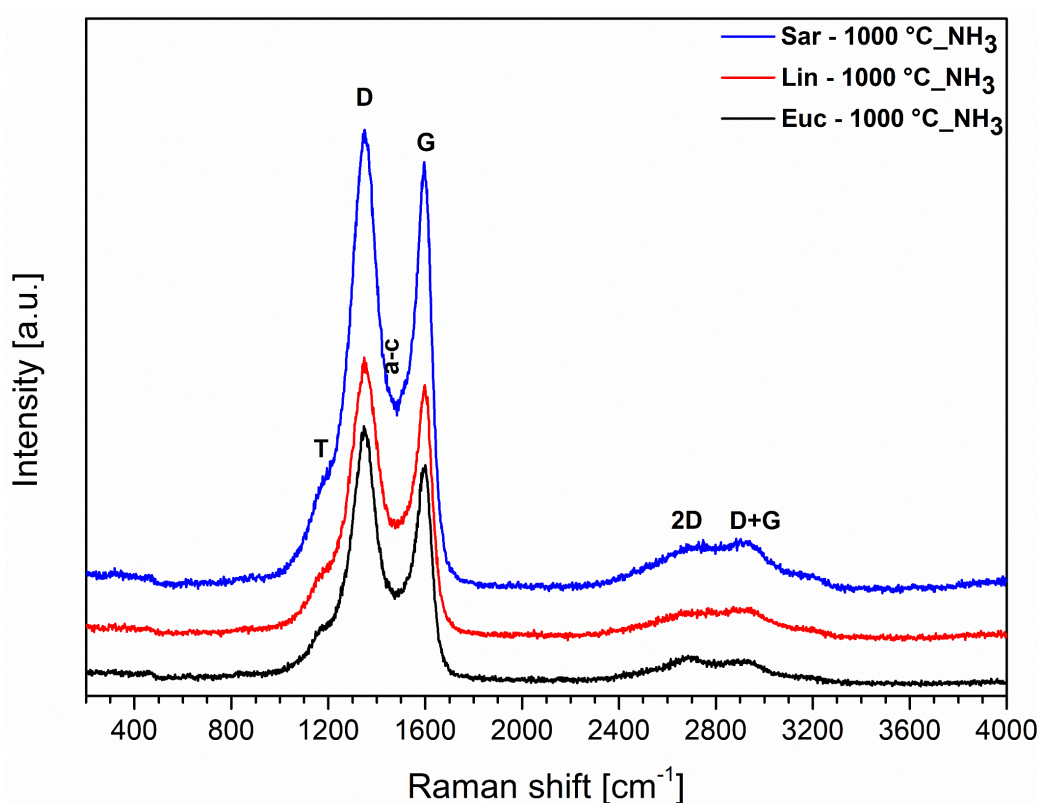
Figure 18. μ-Raman spectra of the ammonolyzed paper templates at 1000 °C

Table 8. Calculated characteristic parameters from μ-Raman spectroscopy (including mean values and standard deviation) of the pristine paper templates in ammonia atmosphere

Sample	A_D/A_G	A_{2D}/A_D	L_a (nm)	L_D (nm)	L_{eq} (nm)	n_D (x 10^{11}, cm^{-3})
Sar – 1000 °C NH$_3$	3.79±0.09	0.15±0.004	4.42±0.11	5.76±0.07	11.38±0.28	13.02±0.31
Lin – 1000 °C NH$_3$	3.26±0,23	0.14±0.03	5.16±0.35	6.22±0,21	10.96±2.23	11.22±0.80
Euc – 1000° C NH$_3$	3.44±0,28	0.12±0.06	4.90±0.41	6.06±0.25	9.42±4.91	11.18±0.95

4.1.2 Paper Templates – Influence of Atmosphere: Argon at 1000 °C

FTIR analysis of the paper templates, which were pyrolyzed in Argon at 1000 °C, are shown in Figure 19. Mainly the OH (3430 cm^{-1}) groups are visible in the spectra, as otherwise, almost all functional groups existing in the pure cellulose-based papers disappeared after the thermal decomposition. Chaiwat et al. [81] suggested, that the O-H band occurs due to incomplete cross-linking of the hydroxyl groups during the pyrolysis process. Another possibility is, that the produced papers adsorped water from the humidity in the air.
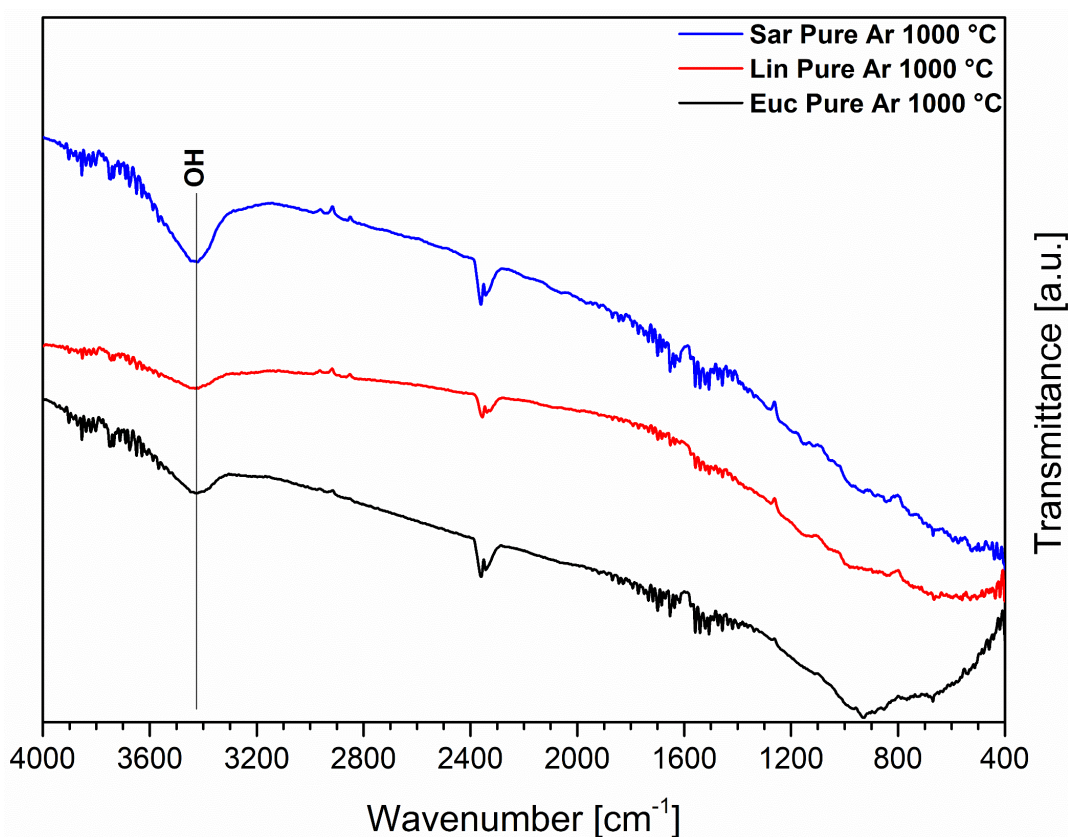
Figure 19. FTIR spectroscopy of the different paper templates pyrolyzed at 1000 °C in Ar

Figure 20 shows the µ-Raman spectroscopy of the pyrolyzed paper templates at 1000 °C in Ar. Comparable to the samples ammonolyzed at 1000 °C, it consists of the characteristic D (1350 cm^{-1}) and G (1590 cm^{-1}) band, the amorphous carbon (a-c) (1504 cm^{-1}) and the T band (1198 cm^{-1}). 2D and the D+G bands (2650 cm^{-1} and 2900 cm^{-1}) are also present. The characteristic parameters are shown in Table 9. Here, the L_{eq} value is again higher than the L_a value, which indicates a curvature of the carbon. Furthermore, the small ratio of A_{2D}/A_D and the broad 2D band indicate partially amorphous carbon with a low degree of graphitization [45, 58].

The Linters paper, which was pyrolyzed at 1000 °C displays the highest L_{eq} value, pointing to a larger graphitic layer, when compared to Sartorius and Eucalyptus.
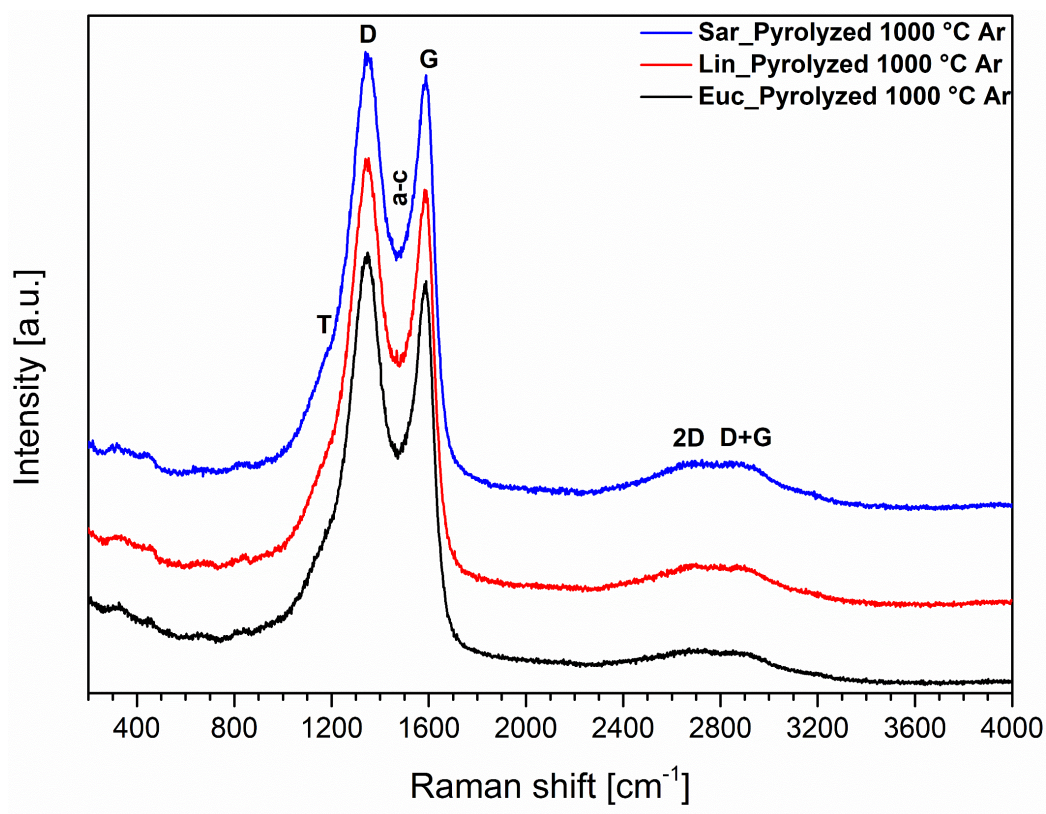
Figure 20. μ-Raman spectroscopy of the different paper templates pyrolyzed at 1000 °C in Ar

Table 9. Calculated characteristic parameters from Raman spectroscopy (including mean values and standard deviation) of the different paper templates in argon atmosphere

Sample	A_D/A_G	A_{2D}/A_D	L_a (nm)	L_D (nm)	L_{eq} (nm)	n_D (x 10^{11}, cm^{-3})
Sar – 1000 °C Ar	3.64±0.07	0.09±0.01	4.61±0.09	5.88±0.06	6.99±1.05	12.50±0.23
Lin – 1000 °C Ar	3.75±0.06	0.12±0.03	4.46±0.07	5.79±0.05	9.06±2.60	12.90±0.21
Euc – 1000 °C Ar	3.63±0.09	0.08±0.03	4.62±0.11	5.88±0.07	6.40±2.33	12.48±0.30

TGA measurements of the pristine Linters paper (Figure 21 (a)) show a considerable mass loss of around 75 % between 290 and 380 °C. Between 380 °C and 1400 °C, the loss is only ∼ 5 %. The DTA analysis shows 4 main endothermic bands at various temperatures, which origins are summarized in Table 10. The evaporating species (Figure 21 (b)) are based on mass spectrometry (MS) and various studies [84–86]. These results coincide with the mass loss, as almost all gases evaporate at around 350 °C. Comparison with literature shows similar results for the decomposition of cellulose [84–86].

Table 10. Summary of the evaporating species during pyrolysis in Argon during TGA measurements. Based on Figure 21 (b) and [84–86]

Region	Temperature [°C]	Evaporating species
I.	95	H_2O
II.	360	Decomposition of cellulose into: H_2O; Acetylaldehyd; Formic Adic; Methanal
III.	450-650	Methane
III.-IV.	700-950	CO; CO_2
IV.	950-1300	CO; CO_2

(a)
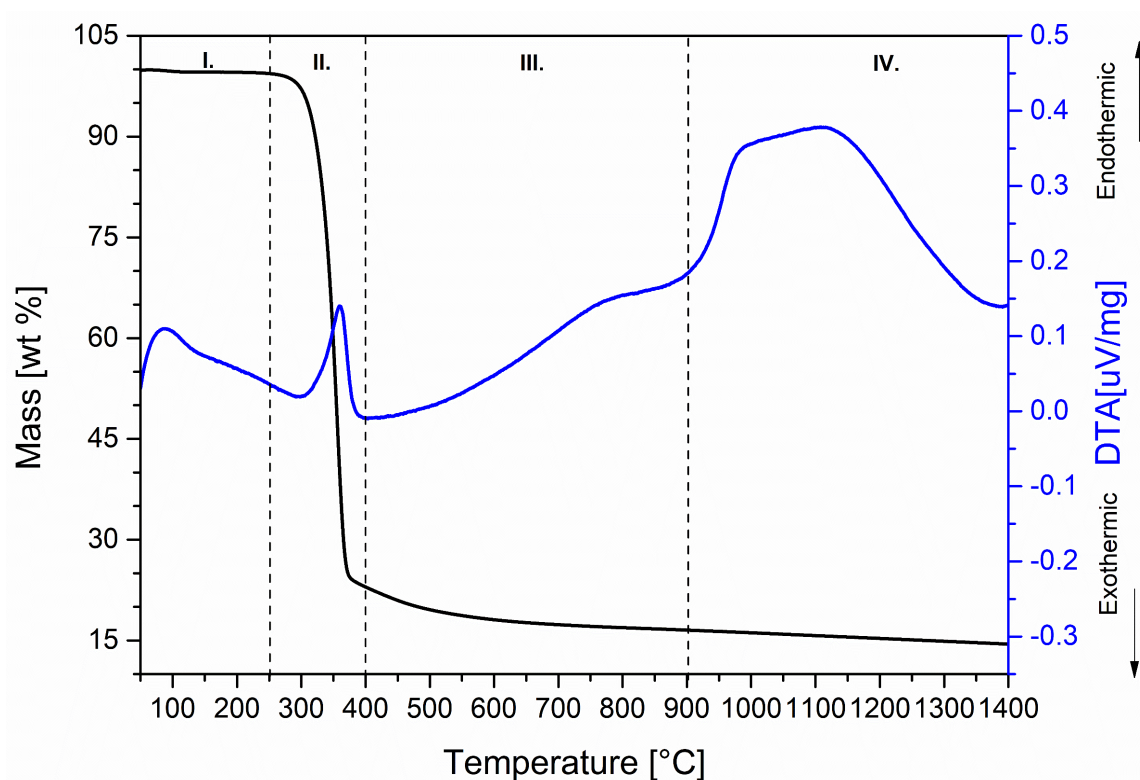
(b)
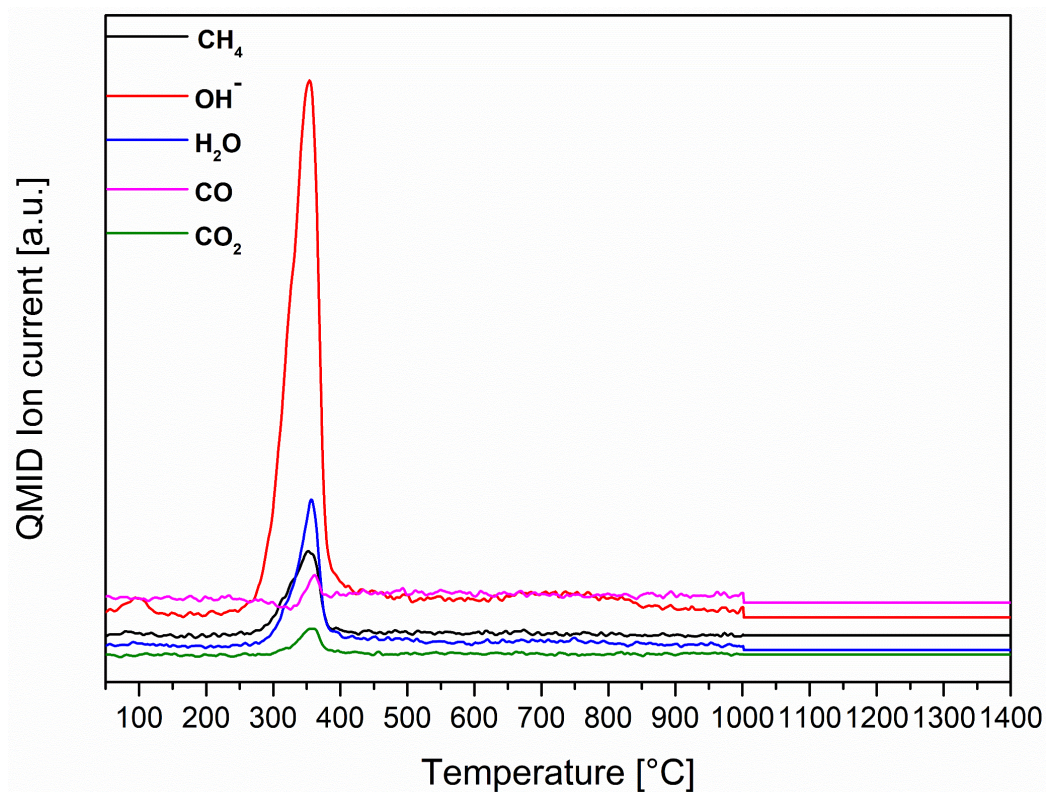
Figure 21. TGA of Linters paper coupled with MS in Argon atmosphere. (a) Mass loss and (b) Mass spectroscopy curve

Pyrolysis in Ar atmosphere of the cellulose-based template (Figure 22) leads to a shrinkage, which is less pronounced than that observed after the ammonolysis (Figure 15).
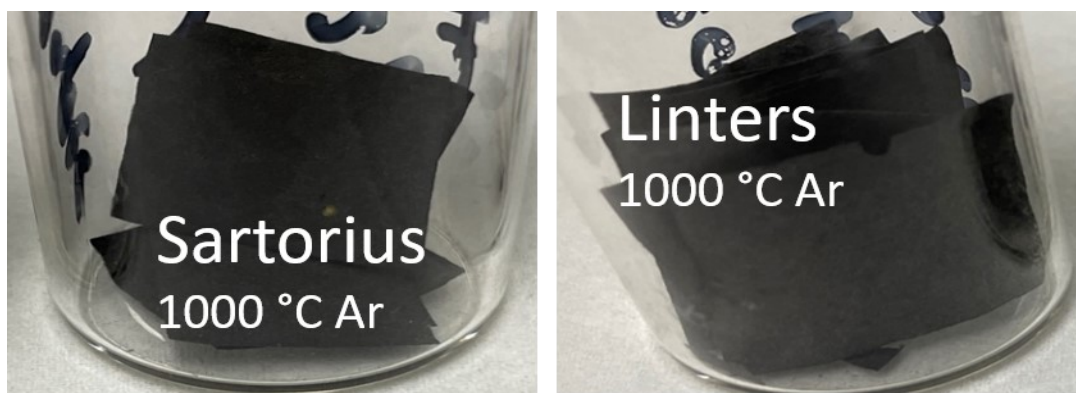
Figure 22. Photographs of the uncoated Sartorius (left) and Linters (right) papers after pyrolysis at 1000 °C in Ar

4.1.3   Summary: Paper Templates

The characterization of the pristine paper templates has shown, that there are insignificant differences between Eucalyptus, Linters, and Sartorius paper. The papers vary only in fiber length, thickness, and orientation (Figure 14). FTIR and Raman spectroscopy showed the different functional groups and linkages, which are similarly present in cellulose-based papers.

After ammonolysis of the papers, it was shown that most of the cellulose-based template is decomposed. Photographs of Sartorius and Eucalyptus paper showed, that there appears to be a difference in the shrinkage and the decomposition of the template. In TGA, almost all of the cellulose-based template is decomposed at 1000 °C. Most of the mass loss of the papers occurs between 250 and 400 °C and mainly H_2O and carbonyl derivates, like formic acid, are being produced in an exothermic reaction. The pyrolysis of the paper templates in Ar atmosphere is less aggressive, compared to the ammonolysis. During the pyrolysis process, the organic compounds of the paper evaporate, leading to a mass loss of around 85 % at 1000 °C, whereas the main mass loss also appears between 250 and 400 °C with the decomposition of the cellulose into H_2O, which is, in this case, an endothermic process ($C_xH_yO_z \rightarrow C_x + H_yO_z$).

In both cases, the FTIR spectra showed almost no surface groups. In NH_3 an additional N-H group is present, compared to only the O-H group in Ar. Ayiania et al. [87] showed the incorporation of nitrogen into a cellulose char, which was then characterized by Raman spectroscopy. Based on these results, the direct comparison of the influence of the atmospheres on the Sartorius template (Figure A 2, normalized values) shows, that in NH_3 the D and G bands are slightly larger, which indicates the incorporation of nitrogen into the cellulose template in the ammonia atmosphere.

Furthermore, this chapter showed bands, which are characteristic of partially graphitized carbon. This can also be seen from the parameters derived from the Raman spectra summarized in Figure 23 (a). The variation of the characteristic parameters is insignificant of the atmosphere and as L_{eq} is higher than L_a, curvature appears inside the carbon phase. The crystallite size (L_a) of all produced samples is between 4 and 5.5 nm and when comparing it to Table 1, it is higher than amorphous carbon (1-2 nm) and in the range of glassy carbon (1.5-5 nm) and turbostratic carbon (<10 nm). L_D and n_D (Figure 23 (b)) are opposed, as a high defect density leads to a lower defect distance and vice versa. The Linters paper pyrolyzed at 1000 °C in Ar and the Sartorius paper ammonolyzed at 1000 °C in NH_3 possess the highest defect densities.

(a)
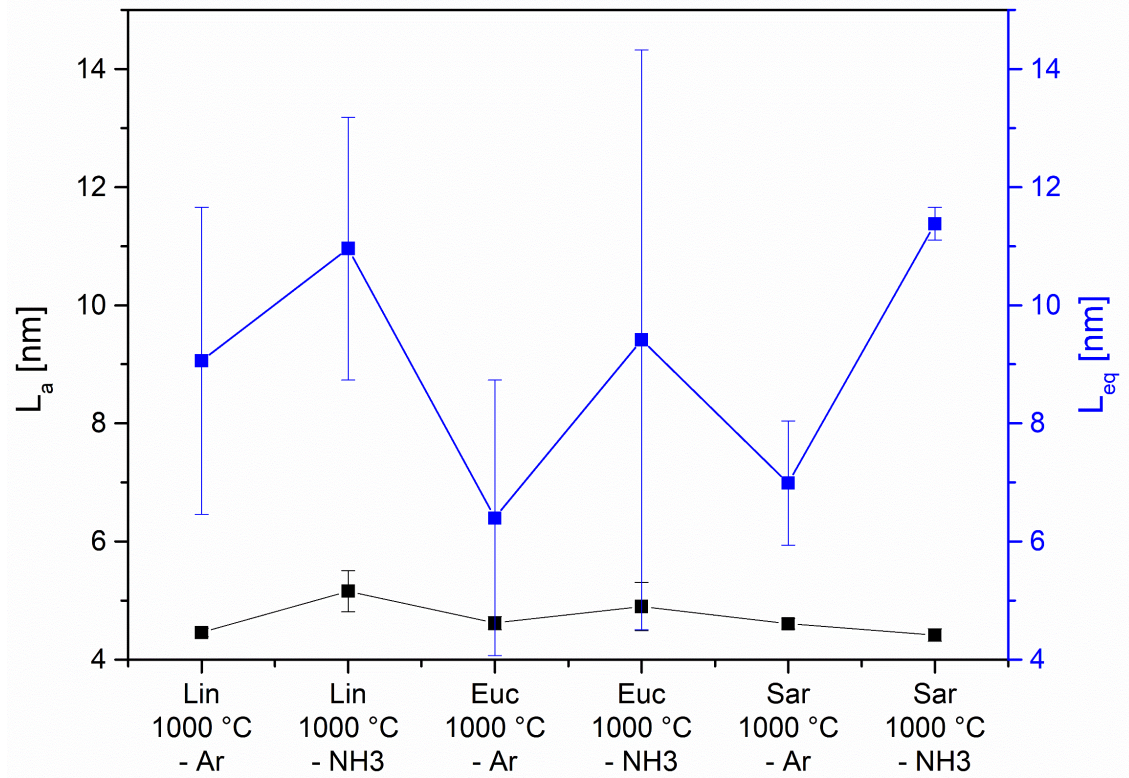
(b)
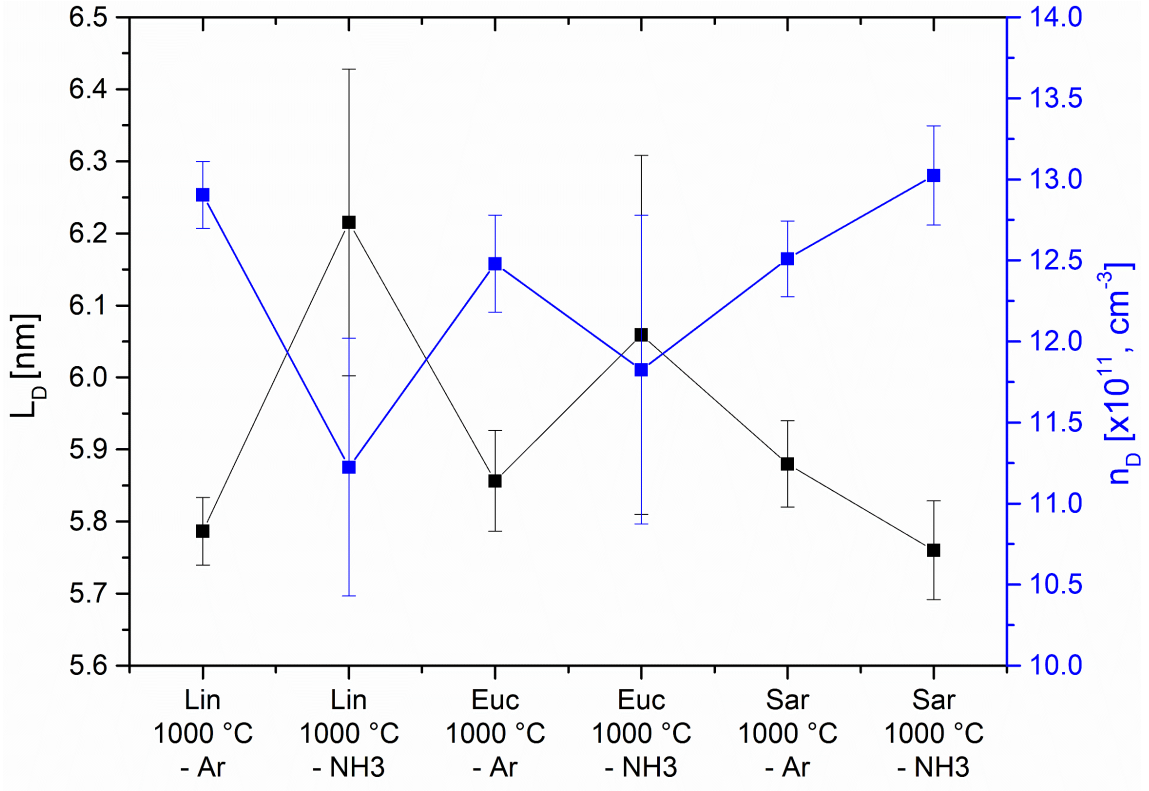
Figure 23. Summary of L_a, L_{eq}, L_D and n_D in dependence of the template type and atmosphere at 1000 °C

4.2.0   Si-Fe-system

In this chapter, the influence of annealing in various atmospheres of the different paper types, which were impregnated with Fe and a polysilazane (PHPS or Dur) are studied with different characterization methods. Firstly, the effect of the ammonia atmosphere and then of the argon atmosphere on the ceramization of the Fe-modified PHPS with and without a cellulose-based template will be discussed. Afterward, similar studies but with Dur will be carried out. The last chapter summarizes the results.

4.2.1   Si-Fe-O-(N) – Influence of Ammonia Atmosphere

The first characterization method, namely FTIR, helps to analyze the different absorptions or emissions, which appear in the samples during measurement. The spectra of the preceramic polymer and the samples resulting from the reaction of iron(III)acetylacetonate (Fe(acac)$_3$) and PHPS after ammonia treatment are shown in Figure 24 (a). Characteristic bands of the preceramic polymer are as follows: Si-H (2176 cm^{-1}), N-H (3371 cm^{-1} and 1169 cm^{-1}), C-O (1267 cm^{-1}), C-H (2855 cm^1, 2922 cm^{-1} and 2962 cm^{-1}), C=O (1571 cm^{-1}) and C=C (1521 cm^{-1}). Upon ammonolysis, at 500 °C the decomposition of the acetylacetonate groups in the preceramic polymers takes place, as indicated by the disappearance of the C-H, C-O, and C=O bands. Due to the disappearance of the Si-H band in the spectrum of the sample ammonolyzed at 500 °C, it is assumed to be consumed during cross-linking reactions. It can be seen that the N-H band is detectable on the surface of the ammonolyzed powders, even after ammonolysis at 900 °C, whereas it vanishes upon ammonolysis at 1000 °C. Si-O-Si (1190 cm^{-1}, 790 cm^{-1}, 1090 cm^{-1}, 460 cm^{-1}) bands indicate the incorporation of oxygen into the PHPS and the formation of these, whereas the Si-O-Fe band at 940 cm^{-1} demonstrates that the iron(III)acetylacetonate-modified polysilazane can be considered as a single-source precursor [88–92].

(a)
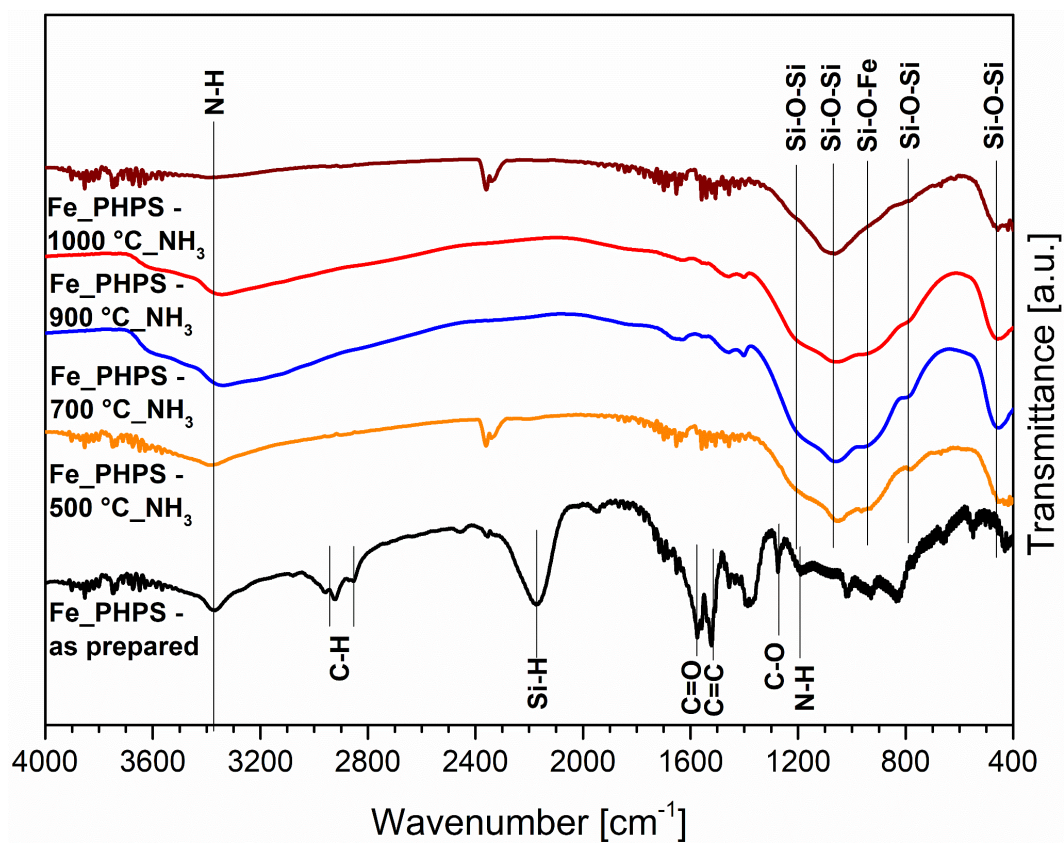
(b)
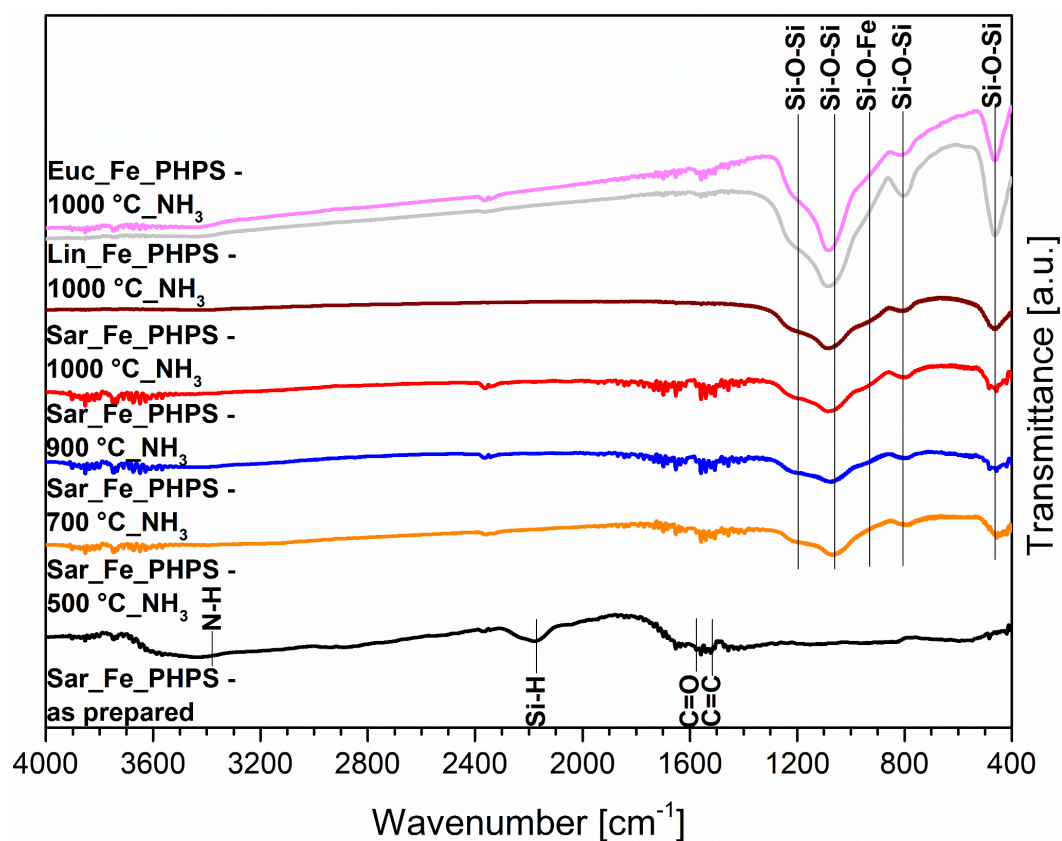
(c)
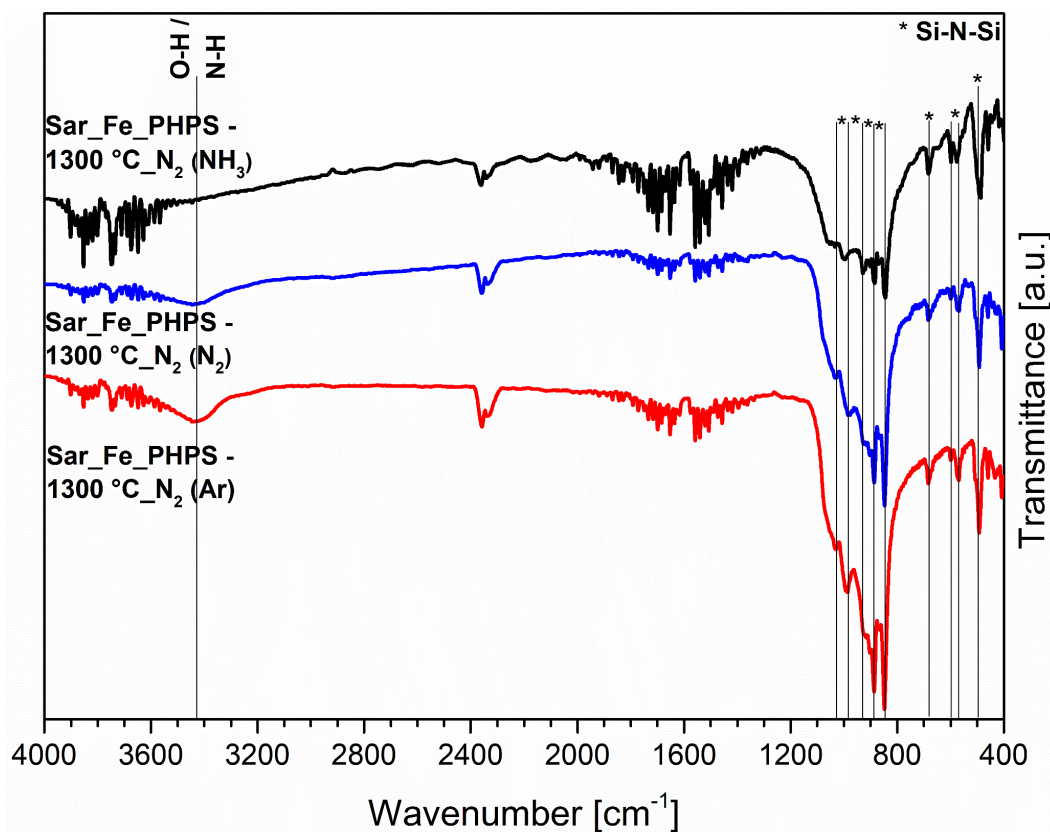
Figure 24. FTIR spectra of the iron(III)acetylacetonate-modified polysilazane (PHPS) powder are shown in (a), the ceramic paper (Sar, Lin, Euc) given in (b), in the as-prepared state and after ammonolysis at different temperatures and (c) depicts the influence of the atmosphere on the functionalization of the ceramic paper

Figure 24 (b) shows the spectra of the related samples, prepared with different cellulose-based templates (Sartorius, Eucalyptus, and Linters). The preceramic polymer-related structural features appear to be insignificantly affected by the presence of the paper template, as the spectra seem to be very similar to those of the preceramic polymer prepared without the templates. For instance, the Si-H band and the acetylacetonate groups are not detectable anymore after ammonolysis at 500 °C, which is in agreement with the results of the template-free precursor. Therefore, the use of the paper templates does not significantly affect the intrinsic bonding in the polymeric precursor itself. Furthermore, the influence of the type of cellulose-based paper templates appears to be also insignificant, as the same bands can be seen in the modified Sartorius, Eucalyptus, and Linters-iron(III)acetylacetonate and polysilazane samples, which were ammonolyzed at 1000 °C.

In Figure 24 (c) the influence of the atmosphere on the functionalization of the pre-treated samples is shown. Those were pyrolyzed in Ar, NH_3, and N_2 at 1000 °C before (FTIR spectra in Figure A 3).

Characteristic bands of the samples are as follows: Si-N-Si (490 cm^{-1} up to 1030 cm^{-1}) and O-H bands (3440 cm^{-1}) [92]. The initial atmosphere, in which the ceramic paper was prepared appears not to matter, as all three samples have similar bands.

Based on the results from Figure 24 (a), two possible reaction paths can be deduced between iron(III)acetylacetonate and polysilazane (PHPS). They are shown in Figure 25, where in (a) it is assumed, that the Si-H group reacts with the iron(III)acetylacetonate, based on the formation of the Si-O-Fe bond. In Figure 25 (b) another possible pathway, is described in the literature as a hydrosilylation of the C=O and groups of acetylacetonate [88–90, 93].
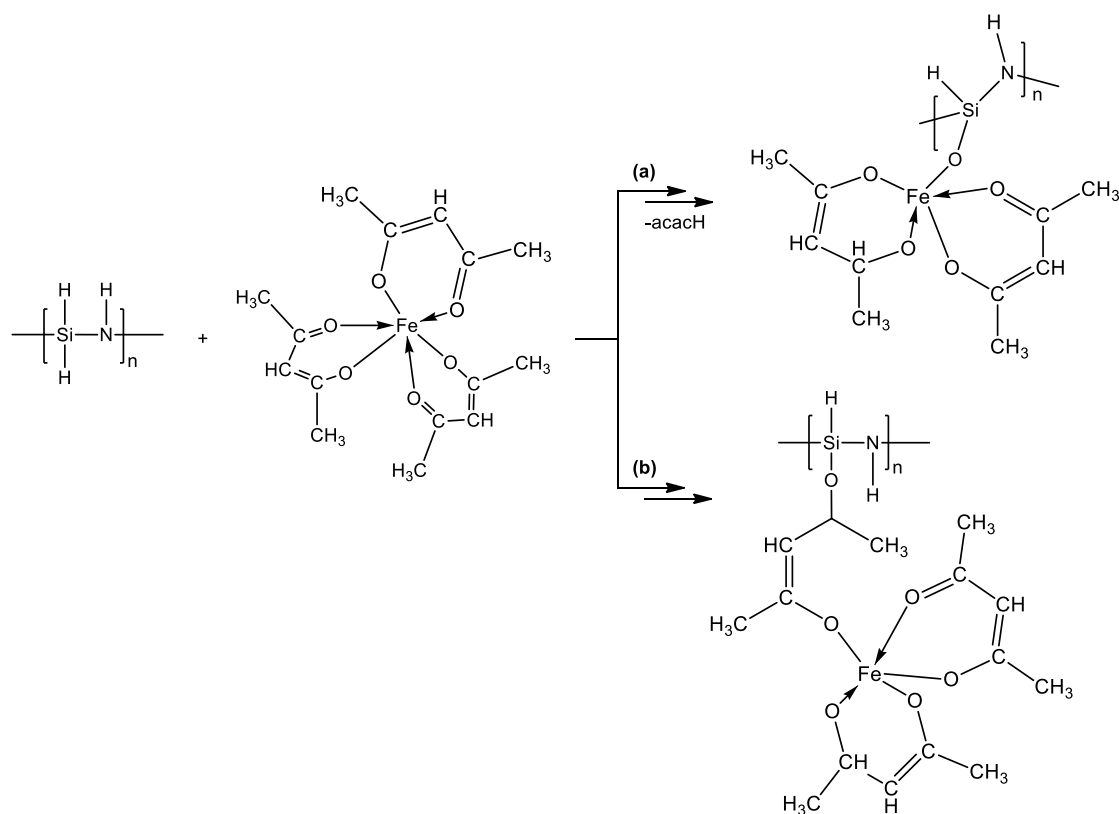
Figure 25. Two possible reaction paths of PHPS with iron(III)acetylacetonate. While in (a) a substitution reaction at the Si-H groups is represented, (b) depicts the hydrosilylation of the C=O groups of acetylacetonate [91]

XRD helps to get a better understanding of the phase evolution of the iron(III)-modified polysilazane during the ammonolysis procedure. Figure 26 (a) shows the XRD patterns of the ceramic powders obtained after ammonolysis at 500, 700, 900, 1000 °C and after annealing at 1300 °C in N$_2$. At ammonolysis temperatures of 500 and 700 °C, only the crystalline ε-Fe$_2$N (space group $P\bar{3}1m$, (162)) phase is present. However, increasing the ammonolysis temperature further to 900 °C and 1000 °C, an additional α-Fe crystalline phase (space group $Im\bar{3}1m$, (229)) appears. Zhou et al. showed [90], that at higher temperatures (1300 °C) Fe$_3$Si (space group $Fm\bar{3}m$, (225)) is formed.

From the XRD spectra in Figure 26 (a) it can be seen, that additional β-Si_3N_4 (space group P31c (159)) and Si_2N_2O (space group Cmc21, (36)) phases are present. According to previous studies [90, 94], this is based on the vapor-liquid-solid process (VLS). That functionalization is accompanied by the formation of ß-Si_3N_4 whiskers, whereas the tip is consisting of Fe_3Si [90]. By comparing the XRD patterns of the iron(III)-modified polysilazane precursor to the cellulose-based ceramic papers, it can be seen, that in general a similar crystallization process occurs, but with a delayed crystallization (Figure 26 (b)). One reason that this occurs, is the presence of cellulose-derived carbon in the ceramic paper. In a previous study, it was shown that the presence of large amounts of segregated carbon in polymer-derived ceramics significantly hinders their crystallization [95].

The atmosphere seems to influence the crystallization process at higher temperatures (1300 °C) (Figure 26 (c)), as the β-Si_3N_4 / Si_2N_2O phase is not present. Furthermore, a graphite phase (space group P63/mmc, (194)) appears in the sample pyrolyzed at 1000 °C in Ar, but disappears after tempering at 1300 °C in N_2. The comparison of the influence of the template on the phase evolution at 1300 °C in N_2 can be seen in Figure 26 (d). Despite the different paper templates a similar phase evolution occurs, which is in congruence with the results from the FTIR measurements shown before.

(a)
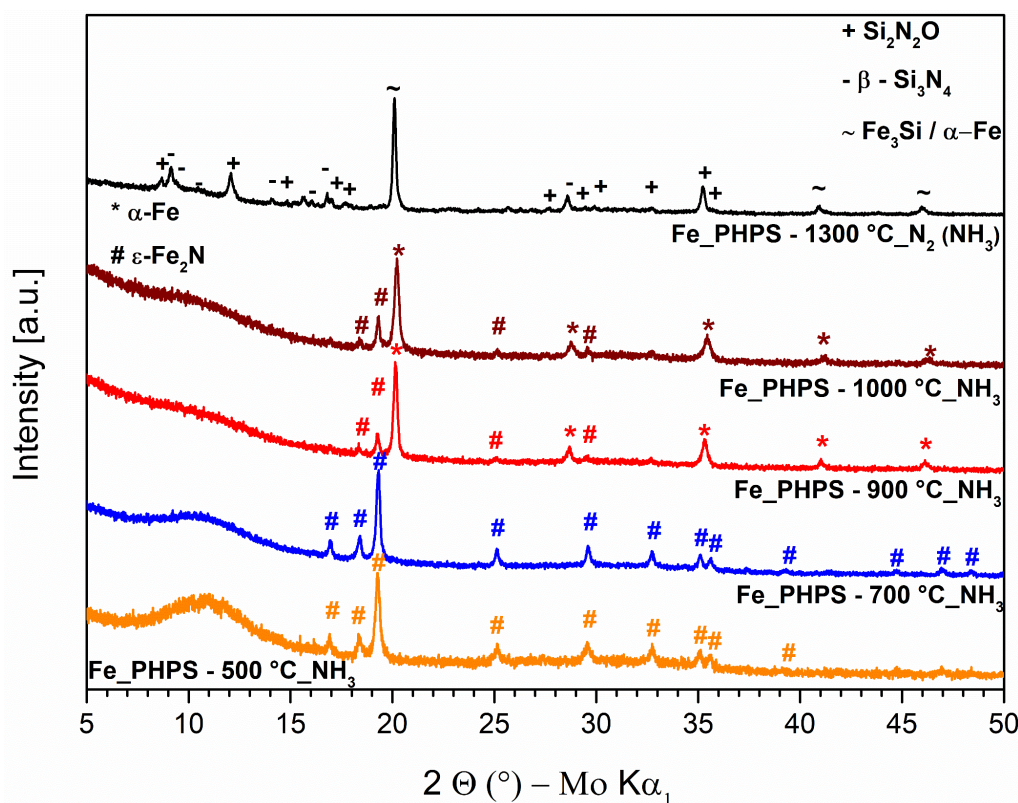
(b)
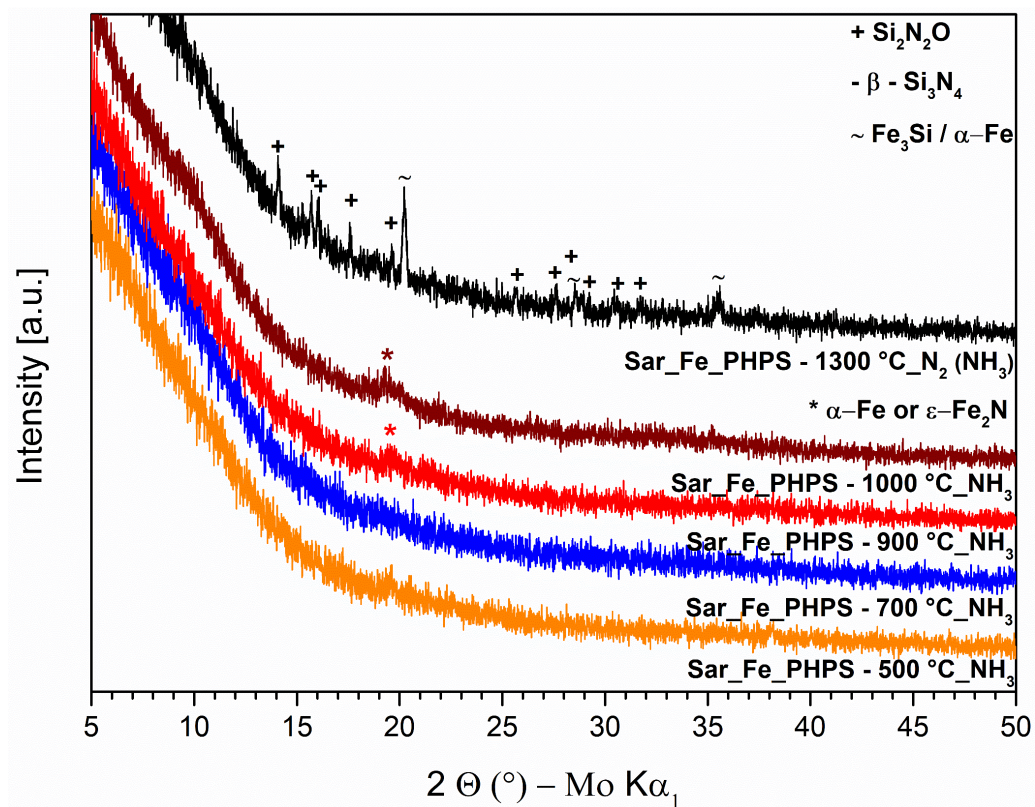
(c)
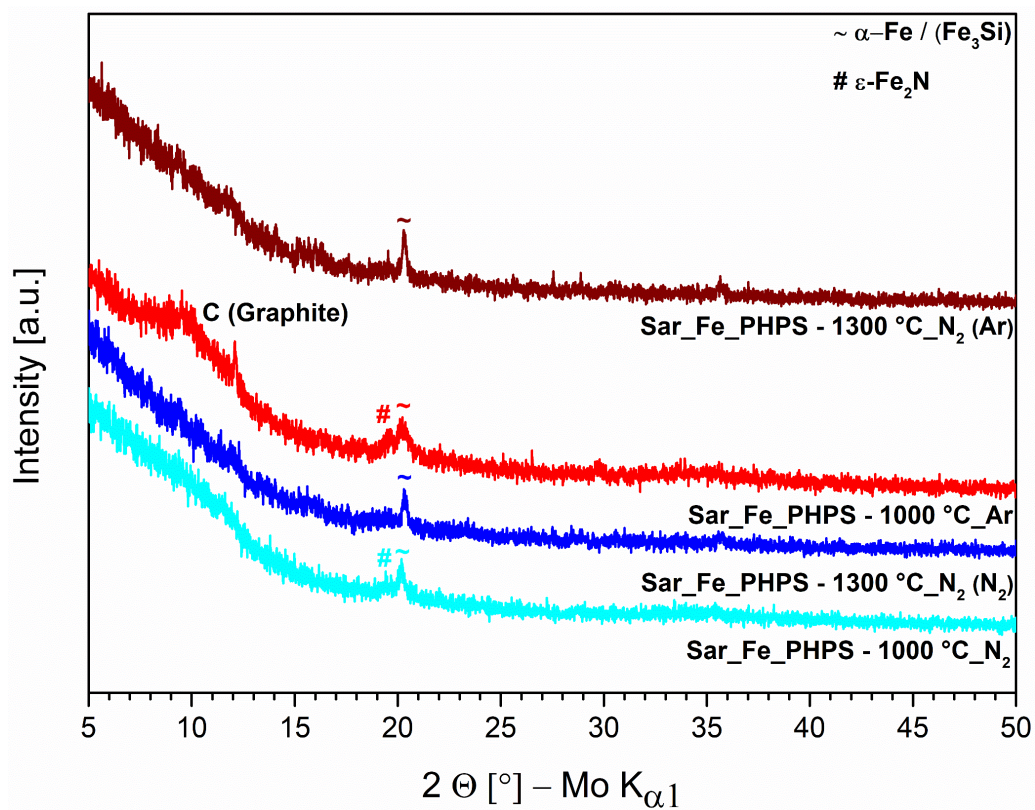
(d)
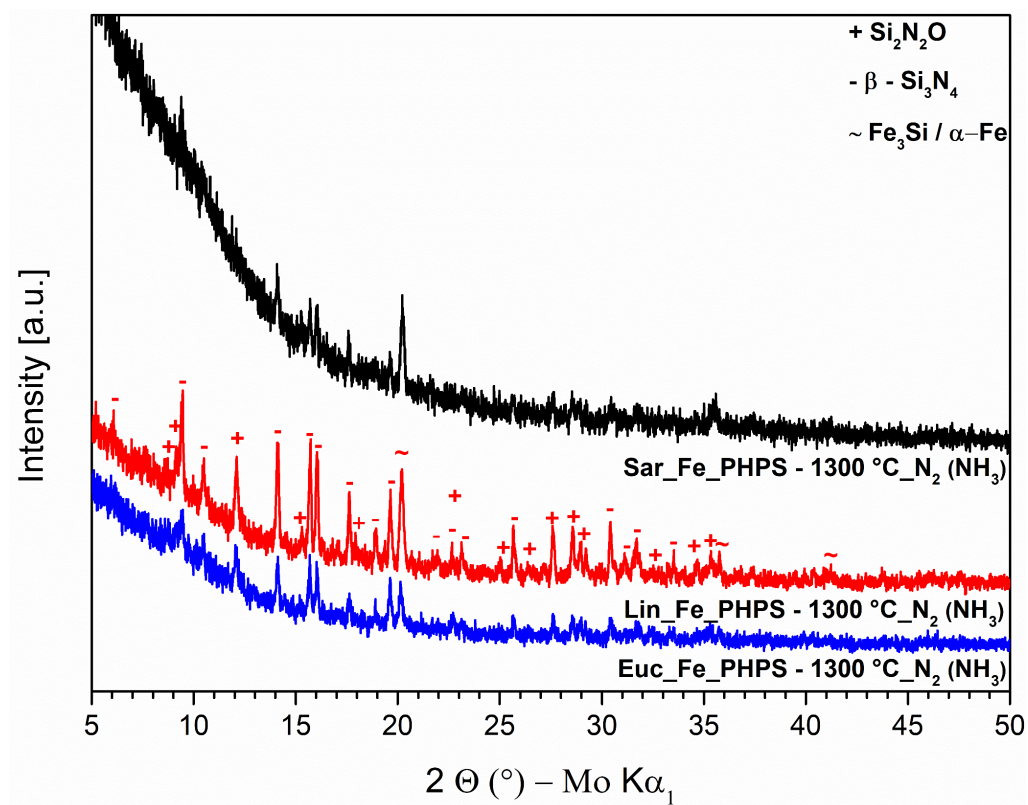
Figure 26. X-ray diffraction patterns of the iron-modified polysilazane (PHPS) precursor depicted in (a), the ceramic paper shown in (b), ammonolyzed at 500, 700, 900 and 1000 °C. The samples annealed at 1300 °C in nitrogen were ammonolyzed at 1000 °C before. (c) shows the influence of the different atmospheres and (d) of the paper template on the evolution of the phase composition

To further analyze the process of the conversion of the impregnated paper into ceramic paper, TG analysis of the Lin_Fe_PHPS sample was done (Figure 27). Table 11 summarizes the main evaporating species during measurement. The complete mass loss is around 85 % and the highest mass loss appears in region II, during which H_2O, carbonyl derivates, and NH_3 evaporate. It is assumed, that in region III, the ceramization process takes place, with an additional decomposition of the cellulose-based paper with the formation of CO and CO_2. The small mass loss of region IV. could indicate the VLS process, in which a part of the gaseous SiO is flushed away. The VLS process was also shown in previous studies but in Ar / N_2 atmosphere [96, 97].
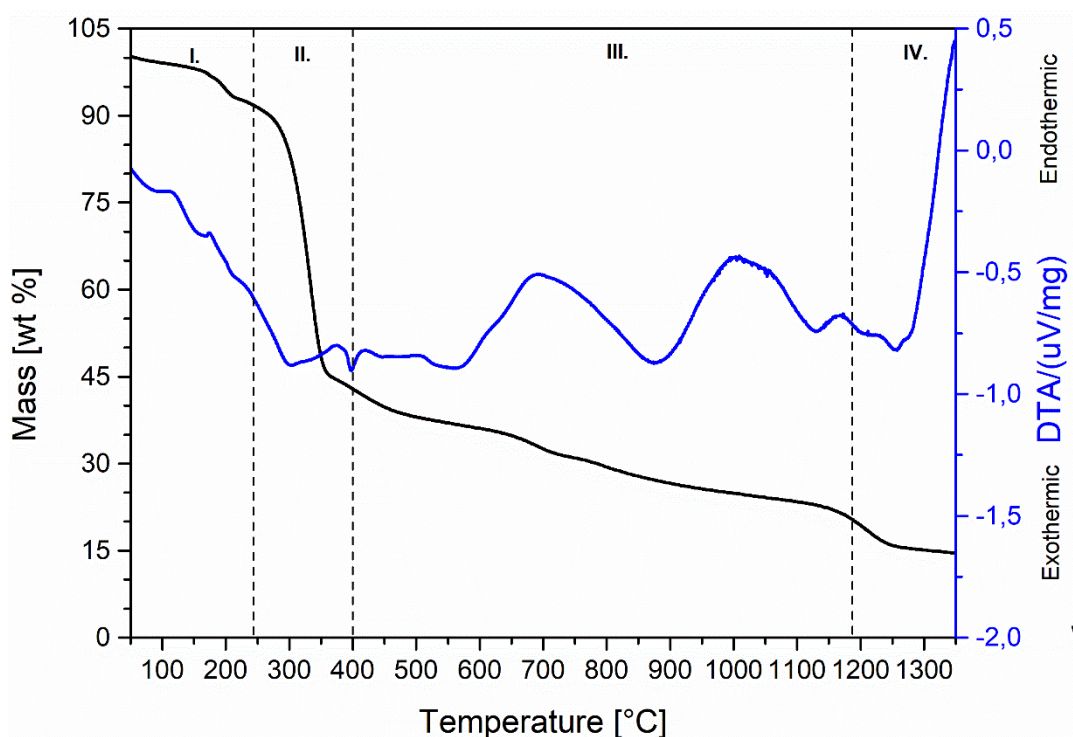
Figure 27. TGA analysis of the Lin-iron(III) acetylacetonate-modified polysilazane (PHPS) based paper in ammonia/argon (Ratio 90:10) atmosphere

Table 11. Summary of the evaporating species during pyrolysis in ammonia/argon atmosphere

Region	Temperature [°C]	Evaporating species
I.	50-240	H_2O;
II.	240-400	H_2O; Carbonyl derivate (CH_2O_2); NH_3
III.	400-1180	CO; CO_2;
IV.	1180-1350	SiO

Figure 28 (a) shows the evolution of the Sar_Fe_PHPS ammonolyzed sample at 500, 700, 900 °C and additionally at 1000 °C for all ceramic papers (Euc/Lin_Fe_PHPS). Comparable with the FTIR and XRD results, the template also does not have a significant influence on the shape of the µ-Raman spectra, as no additional bands appear, when comparing the samples ammonolyzed at 1000 °C. Furthermore, the spectra of the samples ammonolyzed at 500 °C - 1000 °C show the T band (1190 cm^{-1}), D band (1331 cm^{-1}), a-c band (1477 cm^{-1}), and G band (1570 cm^{-1}). The overtones (2D (2644 cm^{-1}) and D+G (2870 cm^{-1})) are hard to distinguish, as they are quite broad. The evolution of the characteristic Raman parameters is shown in Table 12. In the Sar_Fe_PHPS samples, the defect density rises, with higher temperature, while L_a is falling. This indicates that the carbon of the ceramic composite becomes amorphous and more defects are incorporated as more and more inorganic and organic compounds are evaporated. At low temperatures (500 °C) $L_a < L_{eq}$, due to the noisy spectra, which contributes to the fitting error. At 1000 °C, all three ceramic composites have similar values, although Linters and Eucalyptus have slightly higher values, compared to the Sartorius template, indicating a higher degree of graphitization.

(a)

(b)
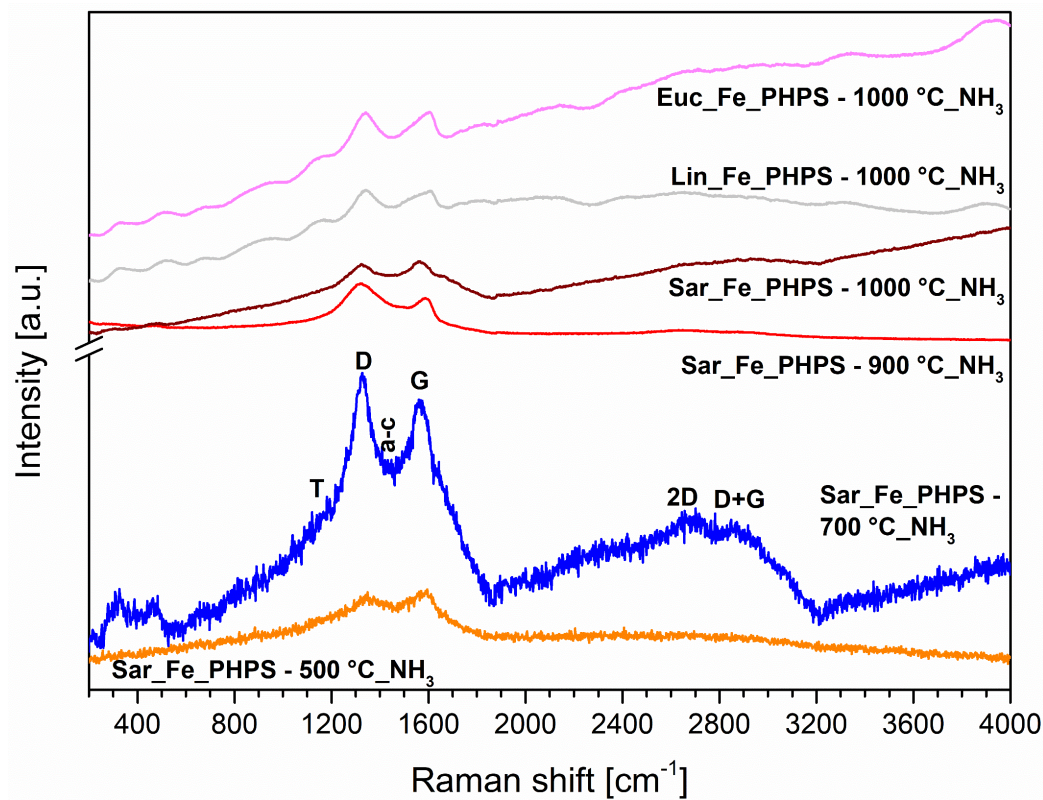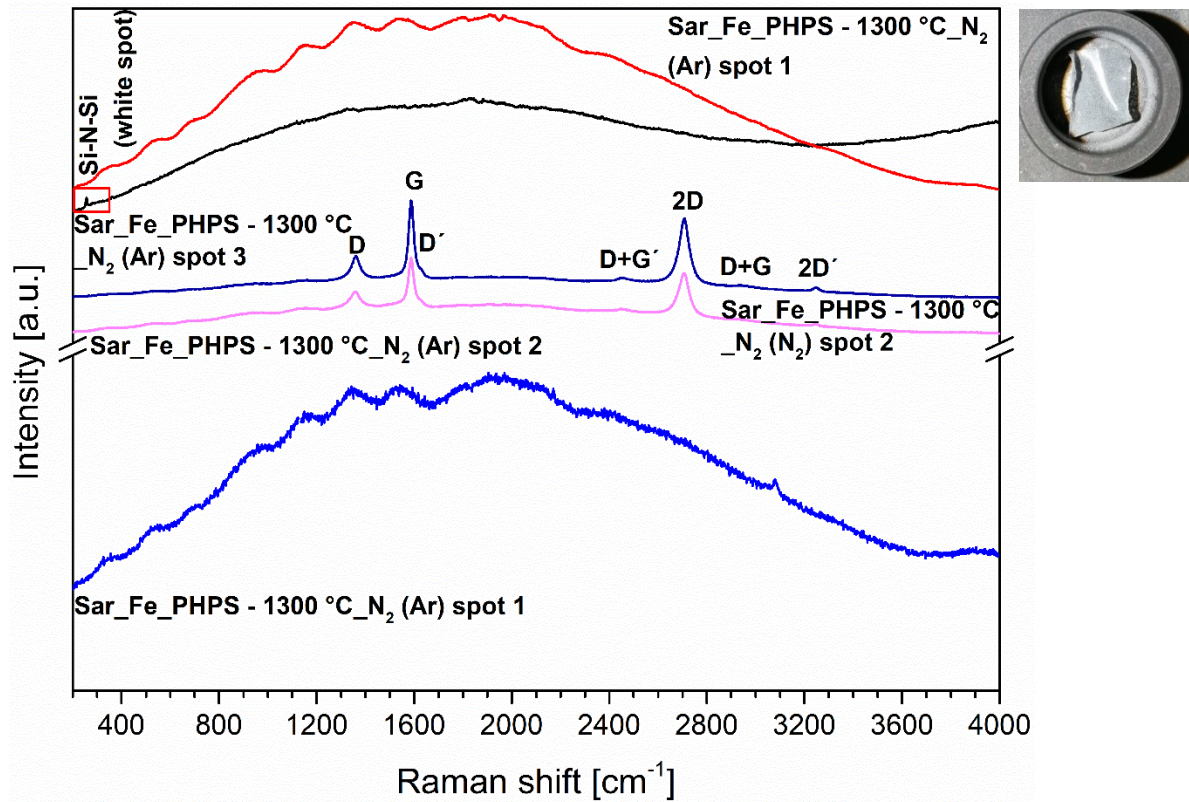
Figure 28. μ-Raman spectra of the Fe_PHPS modified ceramic Paper pyrolyzed in (a) NH₃ at 500, 700, 900, 1000 °C and (b) Sar_Paper annealed at 1300 °C in N₂ (multiple spots) with an inlay of a photograph showing the white coverage of the sample

Figure 28 (b) shows not only how the atmosphere during annealing at 1300 °C changes the Raman spectra, but also how much of an impact the pre-treatment at 1000 °C in Ar or N_2 has. First, there appear white spots on the ceramic paper annealed at 1300 °C in N_2 (see inset photograph), which exhibit a high fluorescence and only one small band at around 250 cm⁻¹. This band can be characterized as a Si-N-Si vibration [98] mainly coming from the Si_3N_4 whiskers. For those samples, no parameters could be calculated due to the high fluorescence.

Other spots on the samples show a low D (1363 cm⁻¹), a high G (1587 cm⁻¹), a D´ (1611 cm⁻¹) and a 2D (2707 cm⁻¹) band (among the other overtones), indicating a high degree of graphitization of the sample [45]. Comparing the A_{2D}/A_D ratio of the samples (Sar_Fe_PHPS-1300 °C_N_2 (Ar) Sar_Fe_PHPS-1300 °C_N_2 (N_2) – spots 2), results in values of 3.21 for Ar and 2.83 for N_2. Moreover, the graphitic domains are significantly larger with over 200 nm, compared to 28 nm at 1000 °C, while also having the lowest defect density. This points to a high degree of graphitization of the cellulose-based template [46]. Moreover, the inhomogeneous distribution of the whiskers on the cellulose-based template is visible, as the two shown spots (Figure 28 (b)) are significantly different.

Table 12. Calculated characteristic parameters from Raman spectroscopy (including mean values and standard deviation) of the iron(III)-PHPS modified templates pyrolyzed in different atmospheres and temperatures

Sample	A_D/A_G	A_{2D}/A_D	L_a (nm)	L_D (nm)	L_{eq} (nm)	n_D (x 10^{11}, cm^{-3})
Sar_Fe_PHPS-500 °C_NH$_3$	0.80±0.06	0.18±0.05	21.01±1.59	12.54±0.48	13.66±4.23	2.76±0.21
Sar_Fe_PHPS-700 °C_NH$_3$	1.09±0.20	0.16±0.04	15.93±2.93	10.88±1.01	12.51±2.88	3.74±0.69
Sar_Fe_PHPS-900 °C_NH$_3$	4.38±0.26	0.07±0.01	3.84±0.23	5.36±0.16	5.59±0.62	15.02±0.90
Sar_Fe_PHPS-1000 °C_NH$_3$	5.44±0.17	0.12±0.004	3.08±0.09	4.81±0.07	9.11±0.31	18.69±0.57
Lin_Fe_PHPS-1000 °C_NH$_3$	2.74±0.04	0.15±0.04	6.12±0.10	6.78±0.05	11.52±3.37	9.41±0.15
Euc_Fe_PHPS-1000 °C_NH$_3$	2.90±0.90	0.37±0.06	6.53±2.48	6.88±1.27	28.40±4.30	1.0±0.31
Sar_Fe_PHPS-1300 °C_N$_2$ (Ar)	0.53±0.07	3.21±0.69	32.12±3.98	15.49±0.96	247.48±53.08	1.82±0.23
Sar_Fe_PHPS-1300 °C_N$_2$ (N$_2$)	0.59±0.10	2.83±0.56	29.41±4.82	14.80±1.22	218.14±43.37	2.01±0.33

Figure 29 summarizes the evolution of the cellulose-based paper coated with Fe(acac)$_3$-modified PHPS. The paper template has an insignificant influence on the phase evolution at higher temperatures and the band vibrations. Slight differences in the crystallite sizes (L_a), especially between the Sartorius and the other two templates are present, but within the margin of error. Therefore, further evaluation of the characteristic changes will only contain Linters and occasionally Eucalyptus as the paper template – occurring differences between those will be included.
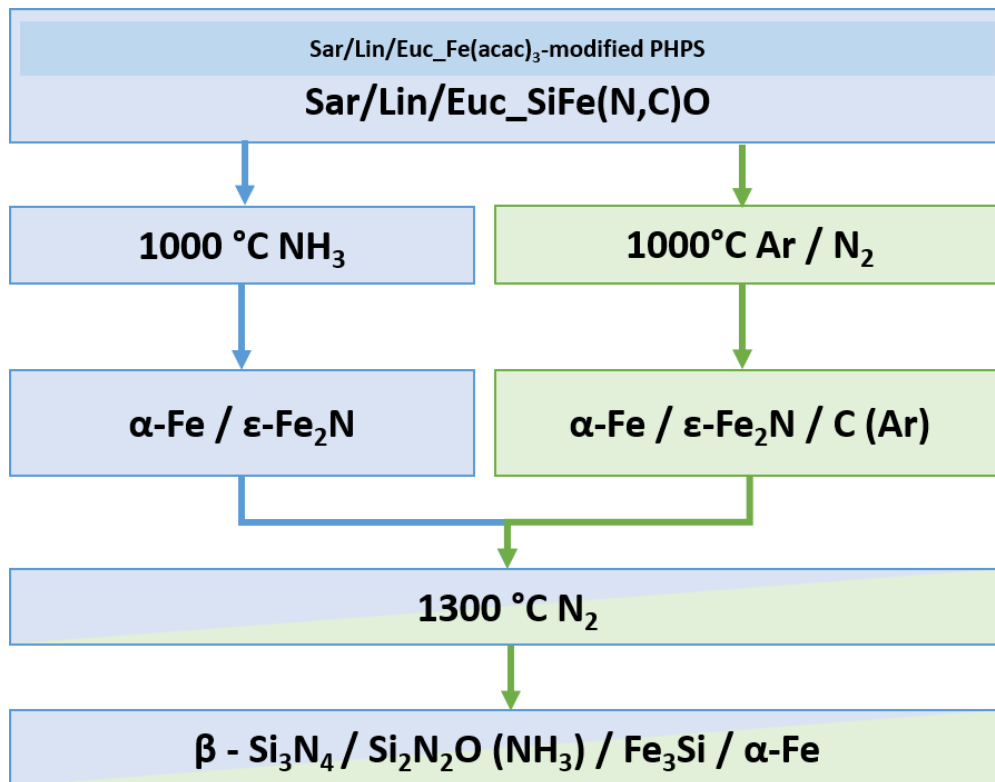
Figure 29. Summary of the phase evolution in the ceramic papers in different atmospheres

4.2.2 Si-Fe-O-(N) – Influence of Argon Atmosphere

In this chapter, the influence of the different atmospheres during the functionalization – in this case Ar – is investigated. In the case of N_2, neither the initial atmospheres (NH_3, N_2, Ar) nor the paper templates had a significant influence on the crystalline phases, which were present at 1300 °C.

Firstly, the TGA of Lin_Fe_PHPS is shown in Figure 30 (a). The mass loss curve is comparable to that of the TGA from the ammonolysis (Figure 27), with a slightly higher yield at 1350 °C (22 % vs 15 %). Here, the highest mass loss also occurs between 250 and 400 °C (II) and has a similar progression. Based on the MS results (Figure 30 (b)) this is due to the decomposition of the organic components in the modified ceramic paper including NH_3 and acetaldehyde (C_2H_4O) decomposed from the respective educts PHPS and Fe(acac)$_3$ [90, 99–101]. H_2O and CO originate from the paper template [84, 102]. At high temperatures (>1200 °C), only CO is produced with an additional mass loss of around 5 %. Table 13 summarizes the main evaporating species within the respective temperatures.

(a)
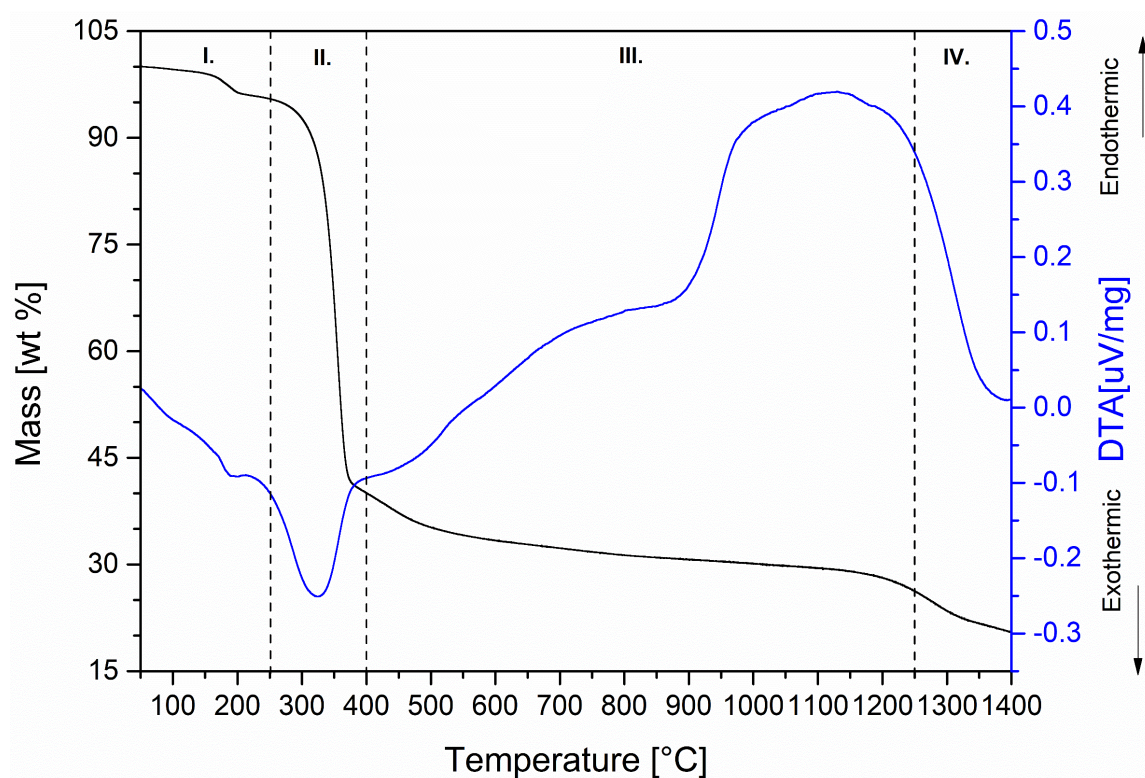
(b)
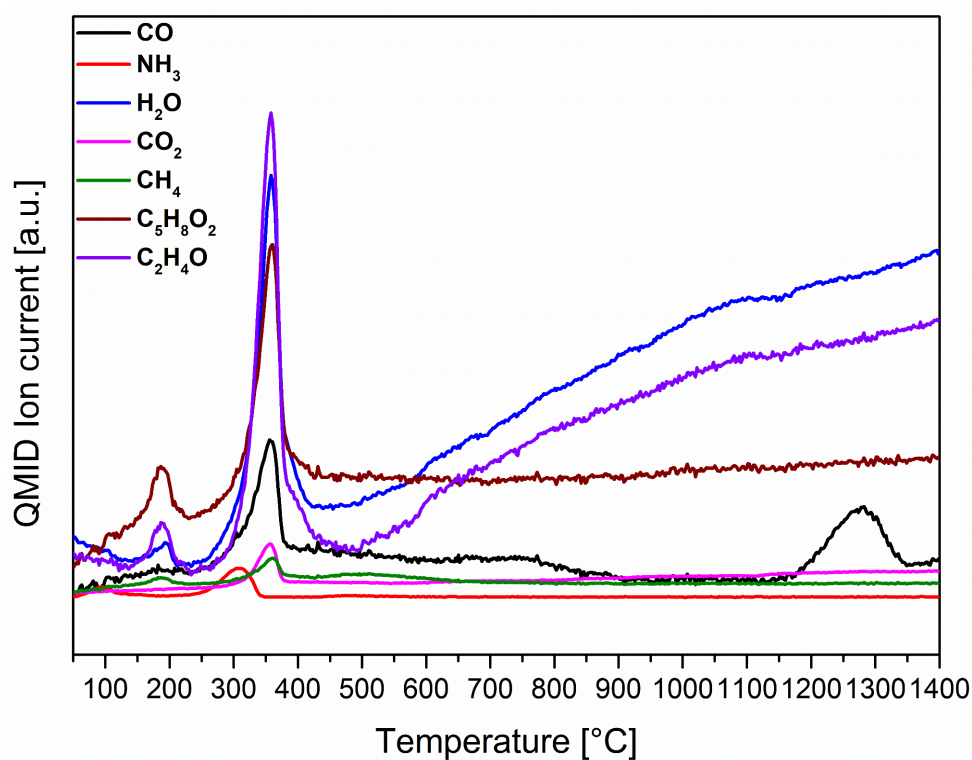
Figure 30. TGA analysis of the Lin-iron(III)-acetylacetonate-modified polysilazane (PHPS)-based paper in argon atmosphere

Table 13. Summary of the evaporating species in argon atmosphere

Region	Temperature [°C]	Evaporating species
I.	50-240	C_2H_4O; H_2O; $C_5H_8O_2$
II.	240-400	CO; NH_3; H_2O; CO_2; CH_4; Acetylacetone ($C_5H_8O_2$); C_2H_4O
III.	400-1180	CO
IV.	1180-1350	CO

The comparison between the FTIR spectra of the precursors and the ceramic papers is shown in Figure 31 below. The characteristic bands for the iron(III)-modified preceramic precursor are the same as before: the Si-O-Si band in the iron(III)-polysilazane (PHPS)-modified and pyrolyzed at 1000 °C in argon sample, shows a much broader Si-O-Si (620-1200 cm^{-1}) band, indicating a change in the Si-O-Si network structure [103]. Similar to the samples in ammonia, the absence of the organic bands C=O (1570 cm^{-1}), C-O (1270 cm^{-1}), and C=C (1520 cm^{-1}) show decomposition of the acetylacetonate groups. The Si-H band (2170 cm^{-1}) is being consumed during cross-linking reactions and conversions into Si-O-Si [104].

Annealing at higher temperatures in N_2 leads to a formation of Si-N-Si (490-1030 cm^{-1}) vibrations, whereas in Ar a Si-C (800 cm^{-1}) vibration appears with some additional Si-N-Si bands [92, 105, 106].

(a)
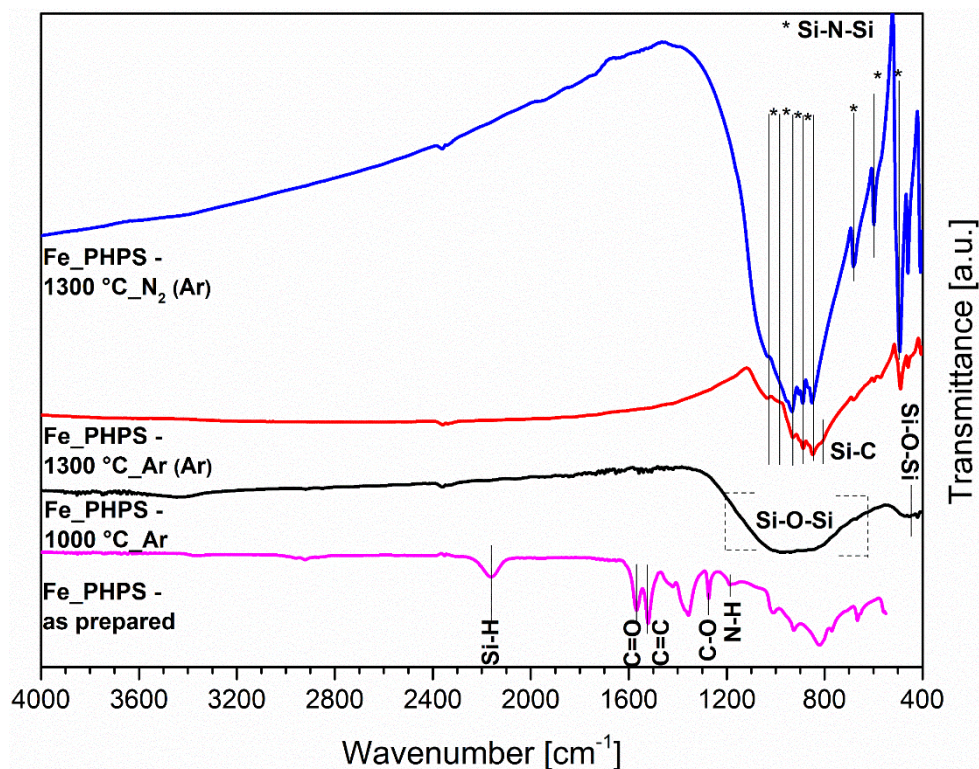
(b)
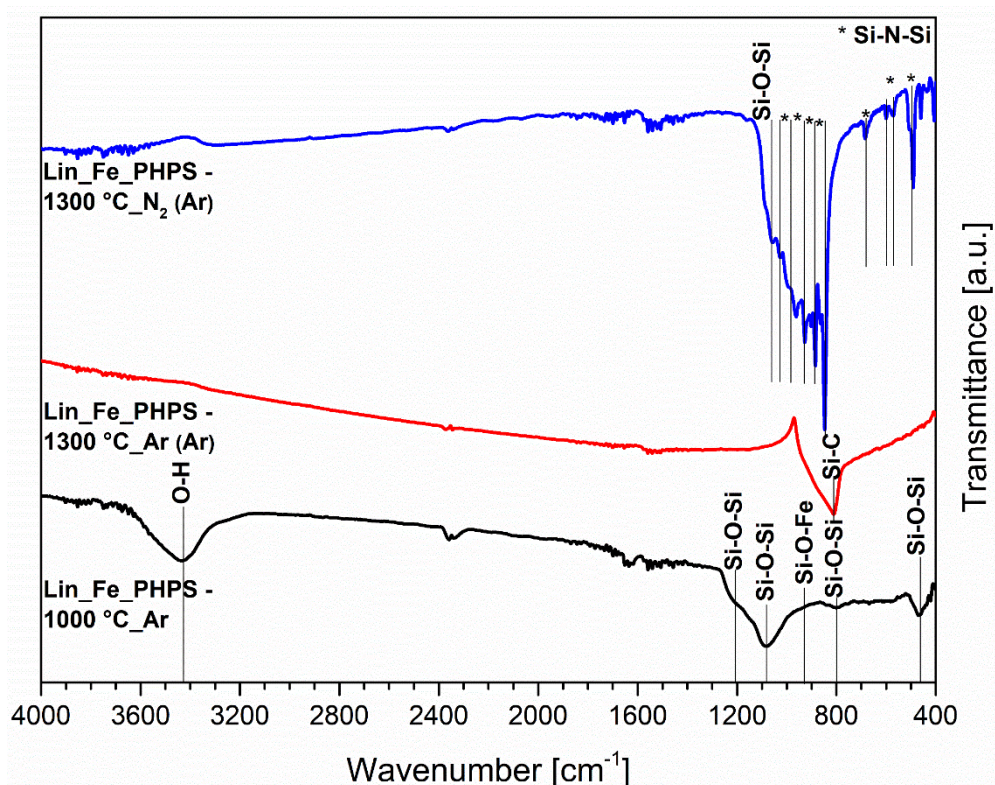
Figure 31. FTIR spectra of the iron(III) acetylacetonate-modified polysilazane powder shown in (a), the ceramic paper Lin given in (b), in the as-prepared state and after pyrolysis at different temperatures in Ar and N_2

As for the reactions at 1300 °C, in the case of Si-C, it is assumed that the additional carbon is generated from the decomposition of the organic remains of $Fe(acac)_3$, which then further reacts with SiO (equation Eq. 18) [94, 107]. Another possible reaction, in which SiC is produced is shown in equation Eq. 19:

$$2\ C\ (s) + SiO\ (g) \rightarrow SiC\ (s) + CO\ (g) \qquad \textbf{(Eq. 18)}$$

$$Si_3N_4\ (s) + 3\ C\ (s) \rightarrow 3\ SiC\ (s) + 2\ N_2\ (g) \qquad \textbf{(Eq. 19)}$$
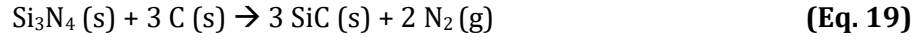
Replacing the atmosphere of Ar with N_2 and annealing the ceramic precursor at 1300 °C leads to mainly Si-N-Si vibrations, indicating the reactions shown in equations Eq. 20 and Eq. 21 [94]:

$$3\ SiO\ (g) + 2\ N_2\ (g) + 3\ C\ (s) \rightarrow Si_3N_4\ (s) + 3\ CO\ (g) \qquad \textbf{(Eq. 20)}$$

$$3\ SiO\ (g) + 3\ CO\ (g) + 2\ N_2\ (g) \rightarrow Si_3N_4\ (s) + 3\ CO_2\ (g) \qquad \textbf{(Eq. 21)}$$
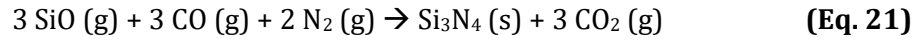
The ceramic paper differs mainly in the Si-O-Si and the Si-O-Fe bands, which are more comparable with the ammonolyzed samples at 1000 °C. Furthermore, annealing at 1300 °C in Ar results in one sharp band at 805 cm^{-1}, again resulting from Si-C vibrations [105, 106]. This is due to the excess carbon, which is present in the paper template, which promotes the reactions above (Eq. 18 and Eq. 19). In N_2 the structural features are very similar to the precursor, with only an additional band at 1040 cm^{-1} from Si-O-Si vibrations. This can be assigned to small remains of SiO_2, which are not completely converted into Si_3N_4.

To further confirm those assumptions, XRD analyses were performed for the precursor and the ceramic paper (Figure 32). The iron(III)-modified polysilazane precursor (PHPS) pyrolyzed at 1000 °C (Figure 32 (a)) shows the crystallization of a Fe_3Si (space group $Fm\overline{3}m$, (225)) or α-Fe phase (space group $Im\overline{3}1m$, (229)). Furthermore, annealing in Ar at 1300 °C lead to a crystalline ß-SiC (space group $F\overline{4}3m$, (216)) (comparable to FTIR results) phase. There appear additional a few reflexes pointing to a third phase, consisting of β-Si_3N_4 (space group P31c (159)), which was also visible in the FTIR spectra. In N_2, the XRD pattern is comparable to the ammonolyzed sample, but with no presence of the Si_2N_2O phase. The ceramic paper (Figure 32 (b)) shows a similar pattern, but only β-SiC in the samples pyrolyzed in Ar at 1300 °C can be identified. In the N_2 atmosphere, the crystalline phases are identical to the annealed precursor.

Comparing Linters and Eucalyptus templates further points out that no significant differences in the phase composition and therefore the influence of these is again negligible.

(a)
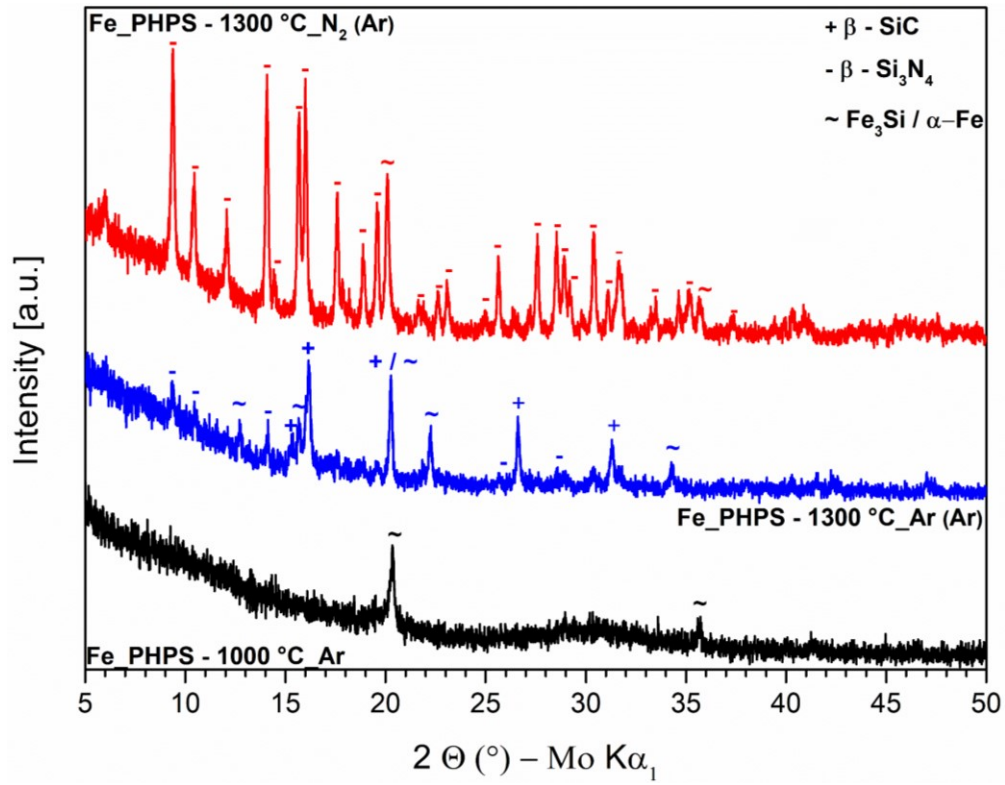
(b)
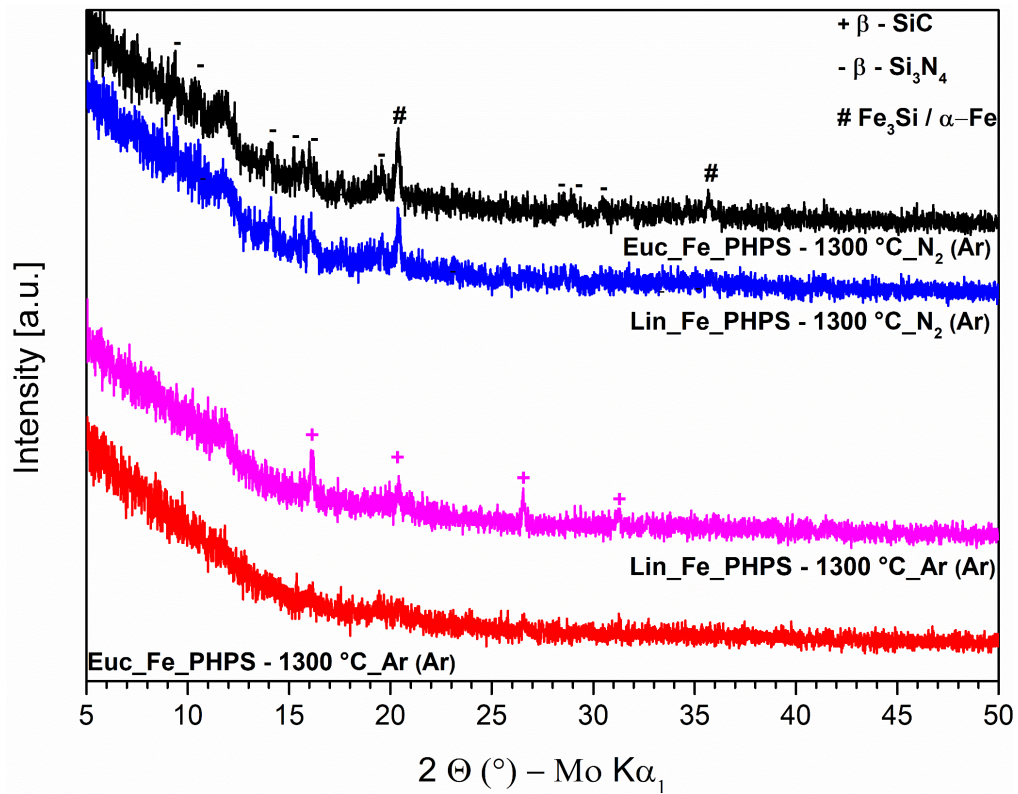
Figure 32. X-ray diffraction patterns of the iron-modified polysilazane (PHPS) precursor depicted in (a), the ceramic paper shown in (b), pyrolyzed at 1000 and 1300 °C in Ar and N_2, depending on the temperature

The phase stability diagram of Si-C-O-N systems based on O_2 pressure is shown in Figure 33. At 1300 °C the preferred phases, depending on the O_2 pressure, are β-Si_3N_4, C, Si_2N_2O, and SiO_2. The absence of Si_2N_2O in the XRD spectra indicates, that the pretreatment of the precursor in the argon atmosphere leaves less oxygen in the sample compared to the pretreatment with ammonia, which restricts the formation of Si_2N_2O. Additionally, iron catalyzes the reaction [90, 108] and therefore lowers the temperatures, that are needed for the reactions.
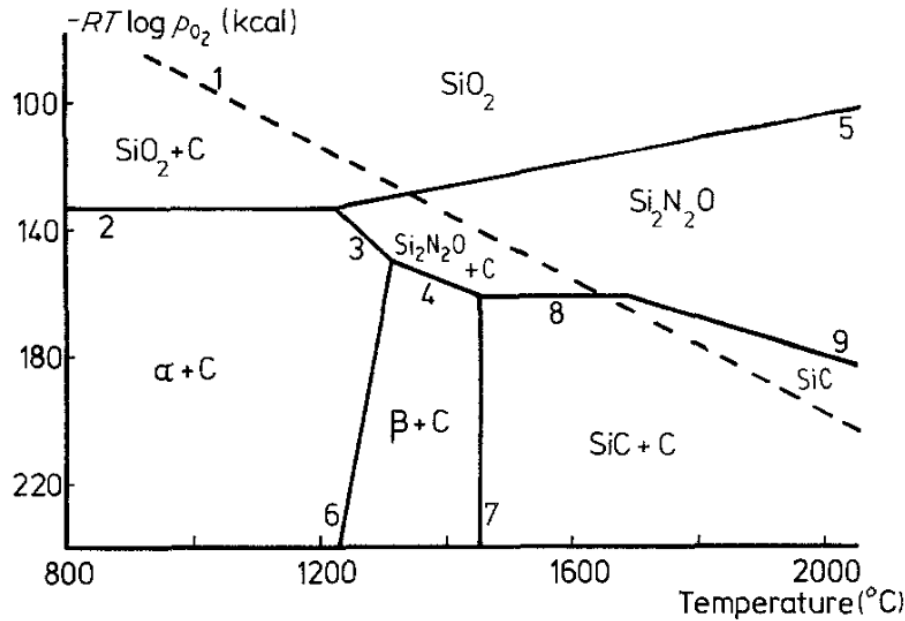
Figure 33. Phase stability diagram of Si-C-O-N systems based on O_2 pressure [109, 110]

The Raman spectra of the Lin_Fe_PHPS samples are shown in Figure 34. The biggest difference is, that already at 1000 °C in Ar (Figure 34 (a)), a sharper 2D band (2690 cm^{-1}) appears, which indicates a higher degree of graphitization of the carbon in the Fe-based ceramic paper [45], compared to the pyrolyzed paper at 1000 °C in Ar. This is also visible in the higher A_{2D}/A_D ratio (0.23 vs 0.12) in Table 14. Further annealing in Ar (Figure 34 (b)) increases the 2D (2701 cm^{-1}) and decreases in some spots – the D (1350 cm^{-1}) band hinting to an even higher degree of graphitization. The additional band at (790 cm^{-1}) originates from SiC vibrations [107], confirming previous results. The inhomogeneity of the sample can be also deduced from the Raman spectra, as not only do the intensities of the bands vary, but also SiC bands do not appear on all measured spots. Changing the atmosphere to N_2 (Figure 34 (c)) some spots have fluorescence and a small Si-N-Si band (260 cm^{-1}), pointing to Si_3N_4, while others appear with a (more) ordered carbon – further indicated by the decrease of the A_D/A_G and the increase of the A_{2D}/A_D ratio compared to the sample pyrolyzed at 1000 °C in Argon. Figure 34 (d) shows an exemplary fitted Raman plot based on Gaussian and Lorentz functions.

(a)

(b)

(c)

(d)
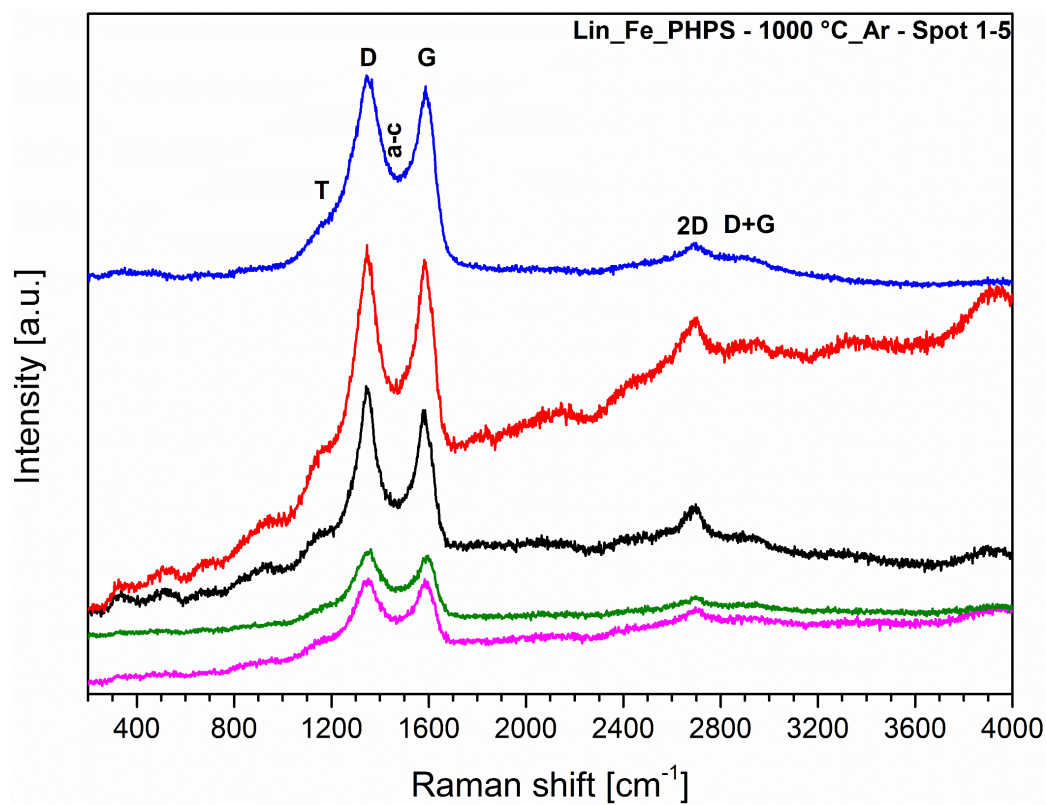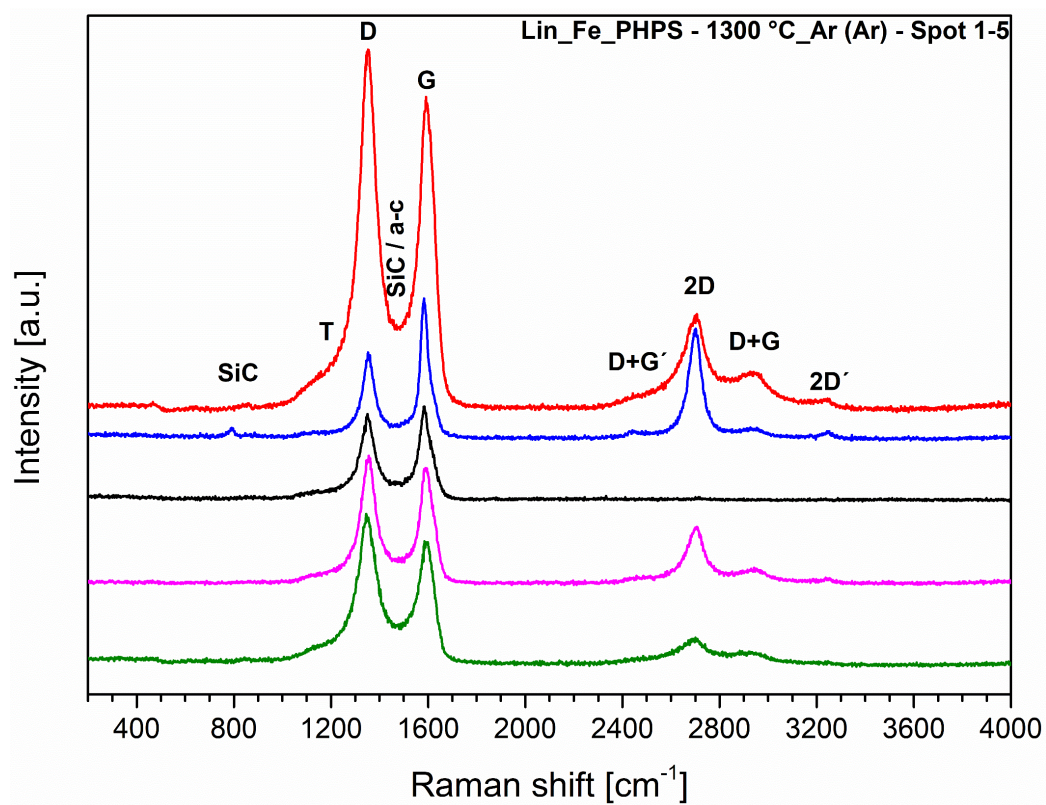
Figure 34. μ-Raman spectra of the Lin_Fe_PHPS ceramic papers annealed at (a) 1000 °C in Argon, (b) 1300 °C in Ar (previously at 1000 °C in Ar) and (c) 1300 °C in N_2 (previously at 1000 °C in Ar). (d) shows a fitted example

Table 14. Calculated characteristic parameters from Raman spectroscopy (including mean values and standard deviation) of the iron(III)-PHPS-modified Lin templates in different atmospheres and temperatures

Sample	A_D/A_G	A_{2D}/A_D	L_a (nm)	L_D (nm)	L_{eq} (nm)	n_D (x 10^{11}, cm^{-3})
Lin_Fe_PHPS-1000 °C_Ar	2.99±1.15	0.23±0.06	6.24±1.69	6.77±1.01	17.43±4.80	10.03±3.95
Lin_Fe_PHPS-1300 °C_Ar (Ar)	1.51±0.62	0.51±0.48	12.75±4.44	9.62±1.74	39.12±37.16	5.21±2.14
Lin_Fe_PHPS-1300 °C_N2 (Ar)	1.44±0.24	0.47±0.10	12.00±2.24	9.45±0.86	36.25±7.66	4.95±0.84

The most notable differences between the two used atmospheres (Ar and NH_3) at 1000 °C, include the partially different phases in the XRD spectra (i.e. ε-Fe_2N does not appear in Ar atmosphere). In FTIR the Si-O-Si bands of the ammonolyzed samples are more pronounced and the fitted Raman spectra showed insignificant deviations from the calculated parameters.

4.2.3   Si-Fe-C-(N) – Influence of Ammonia Atmosphere

In this chapter, Dur is used as the polymeric precursor, which unlike PHPS possesses methyl and vinyl groups. Figure 35 (a) shows the FTIR spectra of the iron(III)-modified Dur precursor after ammonolysis at 1000 °C with and without the paper template. The main differences are the broadening of the Si-O-Si band in the precursor, pointing to differences in the network structure. Furthermore, the Si-H bond is not present, indicating a possible hydrosilylation [111]. Annealing the cellulose-based sample further in N_2, leads to Si-N-Si vibrations, with some additional Si-O-Si vibrations (1090 cm^{-1} and 1190 cm^{-1}), which is comparable to the PHPS samples (Figure 24 (a) and (c)).

(a)
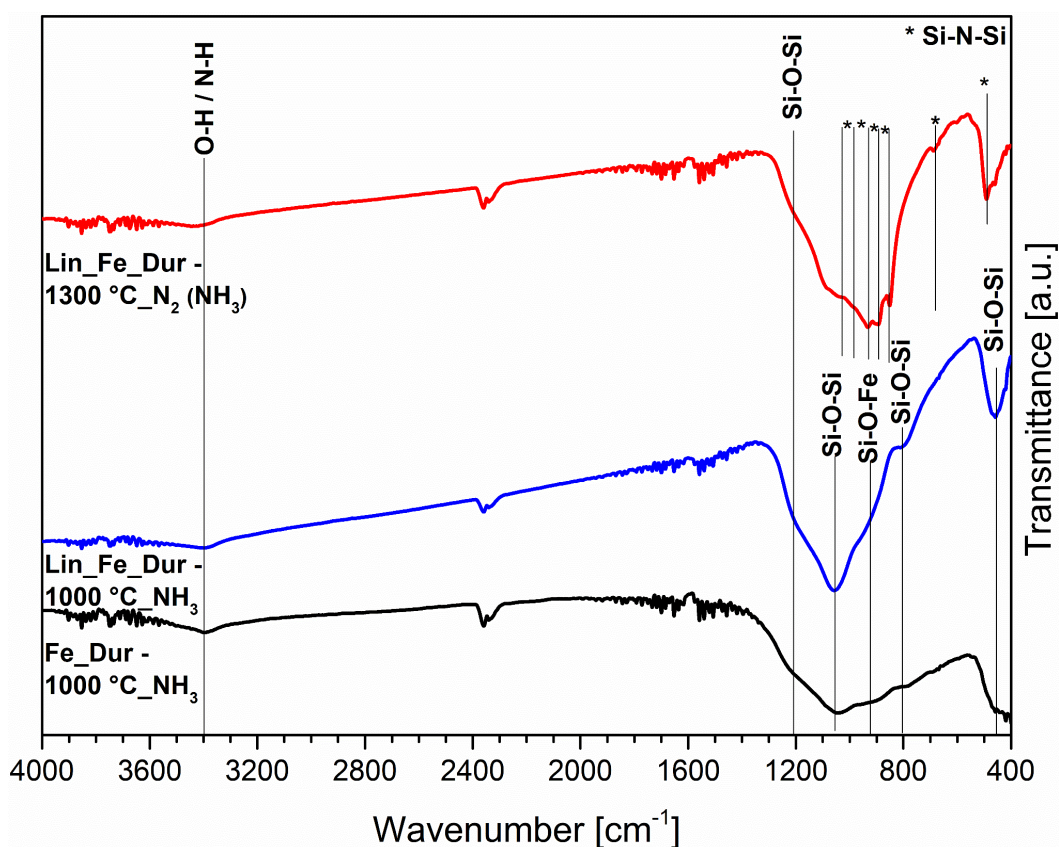
(b)
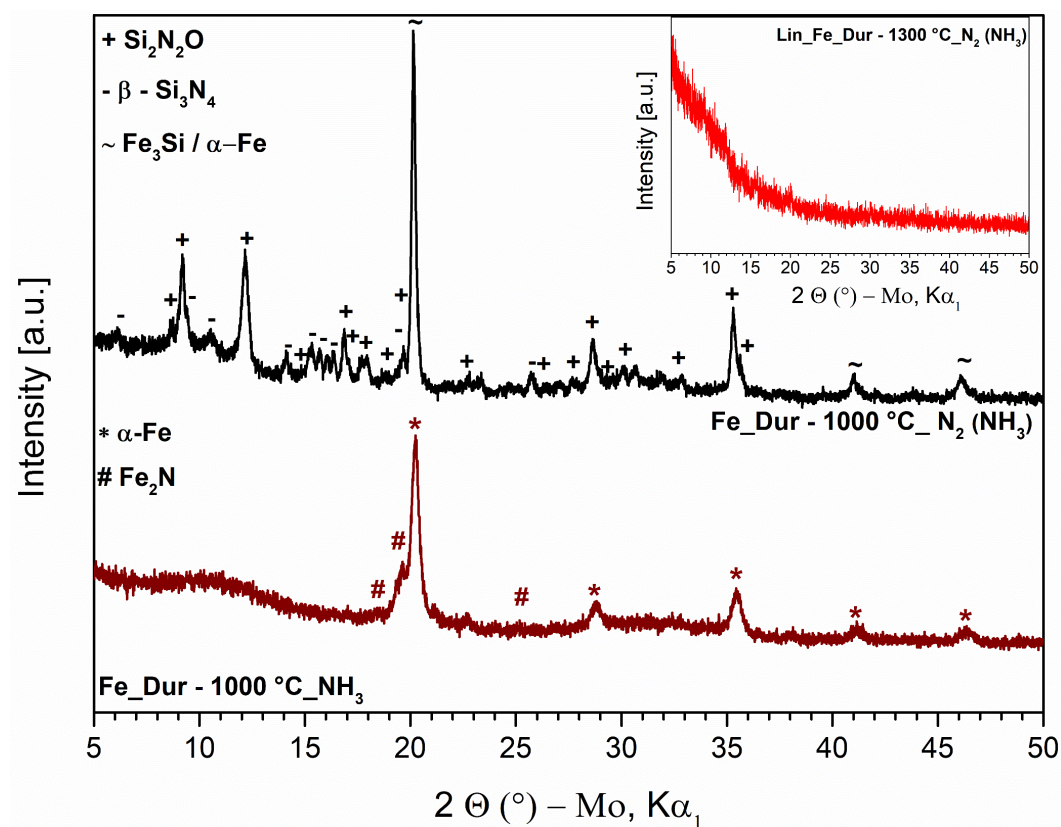
(c)
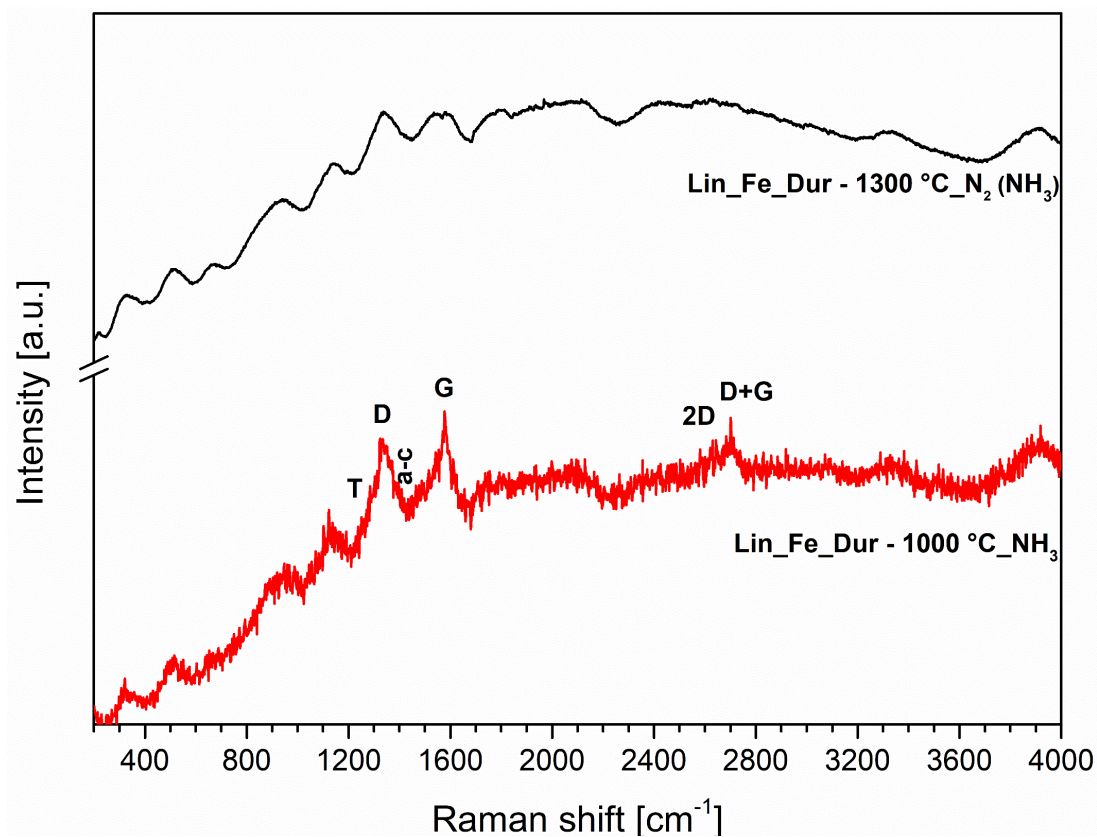
Figure 35. (a) FTIR spectra of the iron(III)-modified durazane precursor with and without a template. (b) XRD spectra and (c) μ-Raman spectra of the same samples

The iron(III)-modified Dur-based precursor pyrolyzed at 1000 °C in NH_3 (Figure 35 (b)), shows similarily to the PHPS system, an α-Fe phase (space group $Im\bar{3}1m$, (229) and an ε-Fe_2N (space group $P\bar{3}1m$, (162)) phase. Further annealing at 1300 °C in an N_2 atmosphere promotes the formation of a possible Fe_3Si (space group $Fm\bar{3}m$, (225)) phase. Additionally, a β-Si_3N_4 (space group P31c (159)) and Si_2N_2O (space group Cmc21, (36)) is formed. The only difference, compared to the iron(III)-modified PHPS-based system is, that by using a cellulose-based template, crystallinity becomes poor (see inset). Due to the fluorescence in the Raman spectra Figure 35 (c), it is not possible to calculate the characteristic values for those samples.

4.2.4 Si-Fe-C-(N) – Influence of Argon Atmosphere

The as-prepared iron(III)-modified Dur precursor has, compared to PHPS, similar, but slightly shifted characteristic bands in FTIR (Figure 36 (a)): Si-H (2115 cm^{-1}), N-H (3375 cm^{-1} and 1170 cm^{-1}), C-O (1250 cm^{-1}), C-H (2897 cm^{1} and 2950 cm^{-1}), C=O (1571 cm^{-1}) and C=C (1525 cm^{-1}). Otherwise, annealing at 1000 °C in Ar shows mainly Si-O-Si vibrations (445 cm^{-1}, 800 cm^{-1} and 1050 cm^{-1}) with a slight shift to lower wavenumbers. At 1300 °C in Ar, only one sharp band at around 805 cm^{-1} appears, which can be attributed to Si-C vibrations. In N$_2$, the bands of the Si-N-Si vibrations from Si$_3$N$_4$ are present. The addition of the paper template has an insignificant effect on the structural features in the FTIR spectra (Figure 36 (b)), as the spectra seem to be very similar to those of the ceramic polymer prepared without the template. Only the sharper Si-C (805 cm^{-1}) band appears assumably from a difference in the network structure.
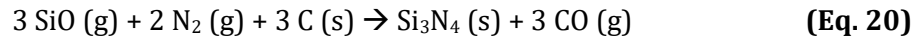
(a)
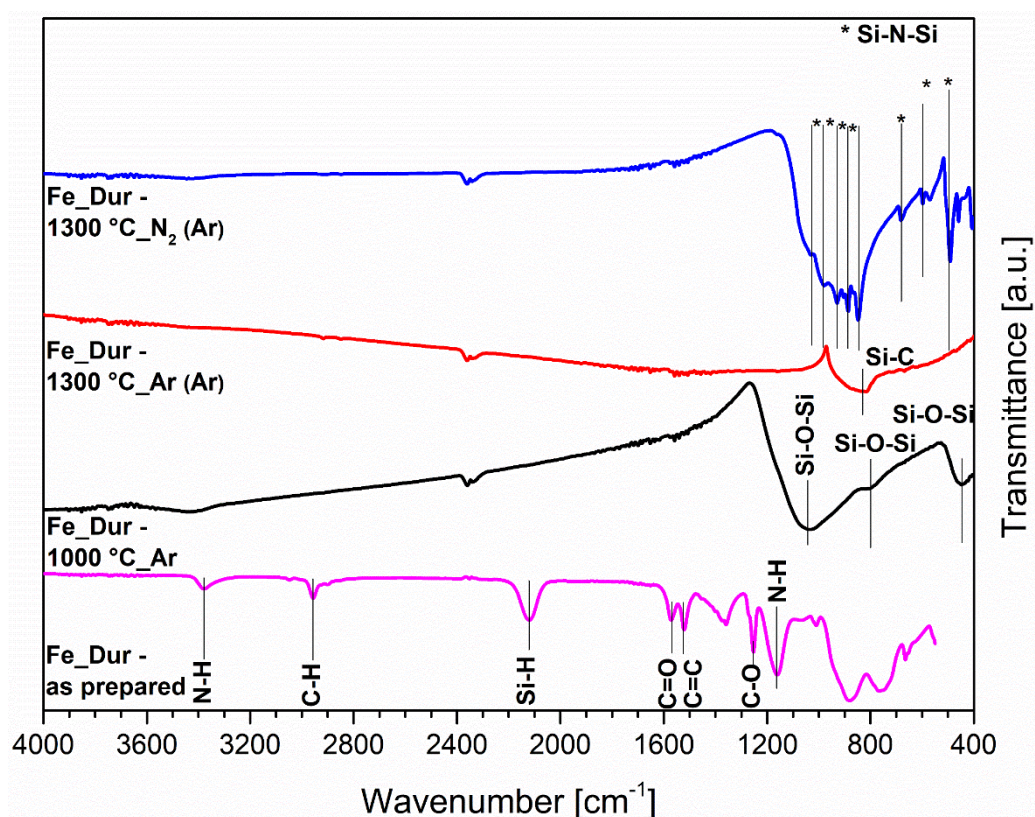
(b)
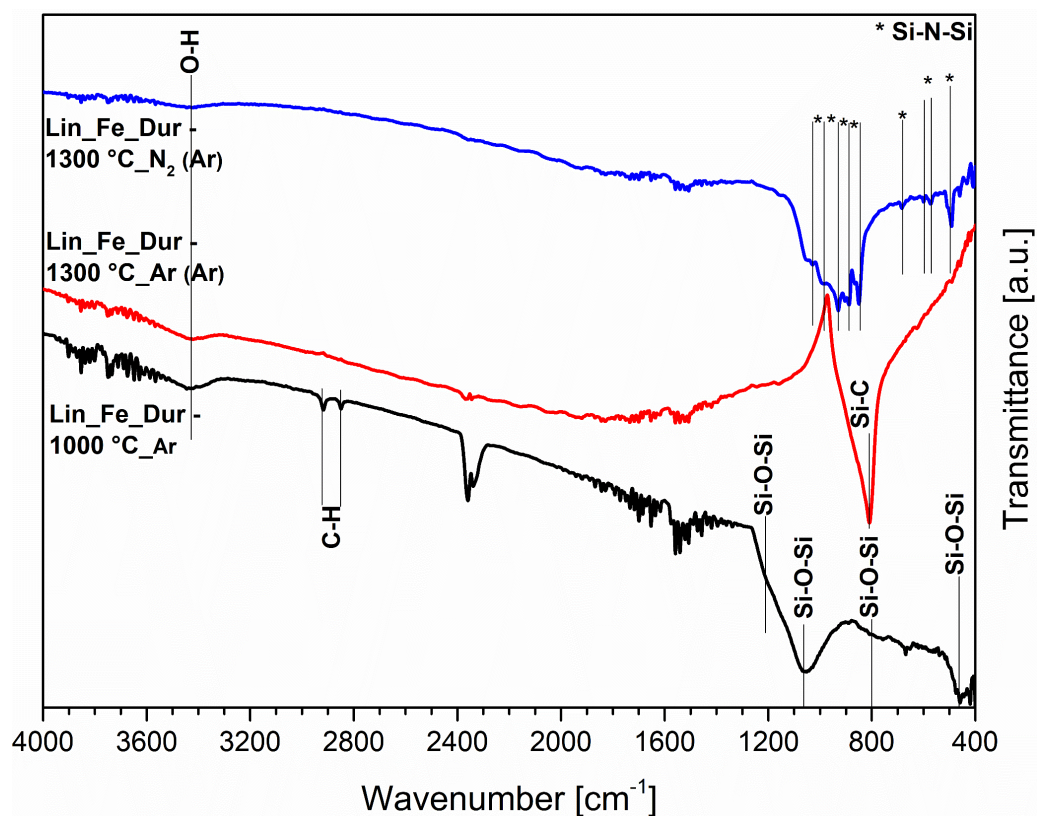
Figure 36. FTIR spectra of the iron(III)-modified durazane powder shown in (a), the ceramic paper Lin given in (b), in the as-prepared state and after pyrolysis in Ar and N_2

The phase composition from XRD with and without the template is shown in Figure 37. The evolution of the modified precursor indicates, that at 1000 °C Fe_3Si (space group $Fm\bar{3}m$, (225)) / α-Fe (space group $Im\bar{3}m$, (229)) is present, while further annealing at 1300 °C in Ar leads to a β-SiC phase (space group $F\bar{4}3m$, (216)). Annealing at 1300 °C in N_2 appears to have a significant effect on the β-Si_3N_4 (space group P31c (159), as it is less pronounced compared to the PHPS sample and Fe_3Si / α-Fe appears to be the dominant phase. Furthermore, the crystallization of the phases in the ceramic paper is even more retained, as only β-SiC can be identified in the sample annealed at 1300 °C in Ar (Lin_Fe_Dur – 1300 °C_Ar (Ar)), while in N_2 the sample (Lin_Fe_Dur – 1300 °C_N$_2$ (Ar)), is amorphous. This can be derived from the large amounts of carbon, which hinders the crystallization process [95].
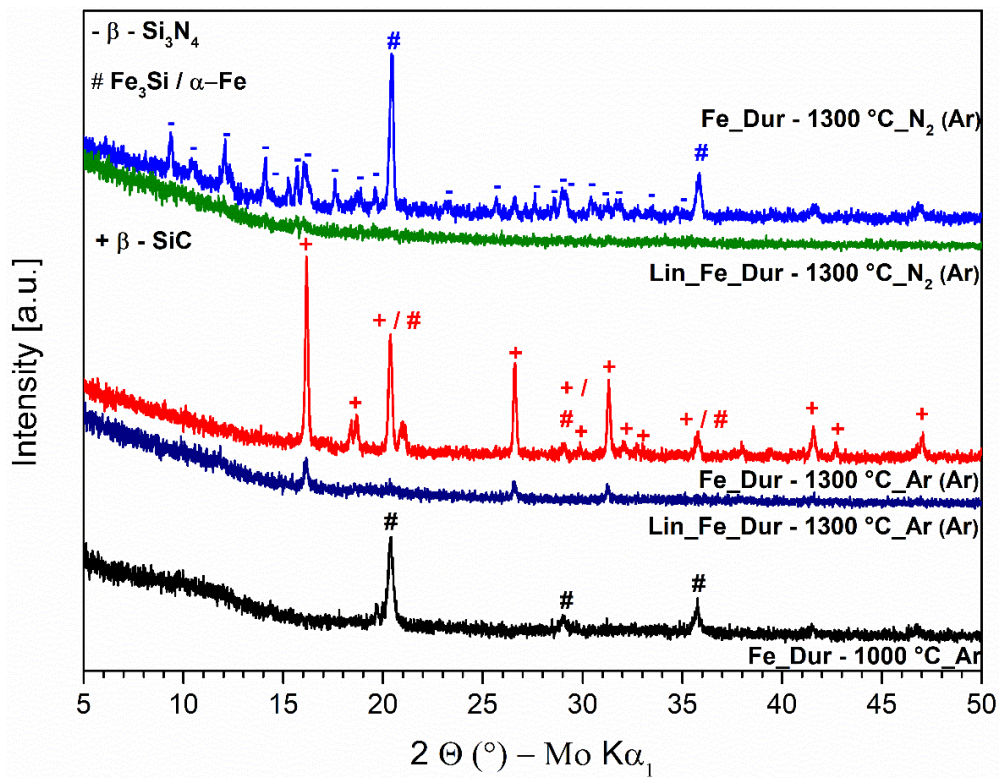
Figure 37. XRD pattern of the iron(III)-modified Dur precursor with and without the cellulose-based template annealed at different temperatures and atmospheres

Figure 38 shows exemplarily SEM images of the Lin_Fe_Dur-1300 °C Ar (Ar) and the Lin_Fe_Dur-1300 °C N$_2$ (Ar) samples with additional EDX spectra. It can be seen that the atmosphere at 1300 °C has a significant influence. In N_2 (Figure 38 (a)) Si_3N_4 wires – regarding to EDX (Figure 38 (b)) – with additional tips (assumably Fe_3Si) are formed. Zhou et al. [90], showed similar results, whereas samples were pre-treated in an ammonia atmosphere before.

In Ar (Figure 38 (c)) SiC whiskers – from EDX (Figure 38 (d)) - with round tips are on top of the fibers. Despite the atmosphere and the high temperature, the carbonized cellulose-based fiber is intact and has not decomposed.

(a)
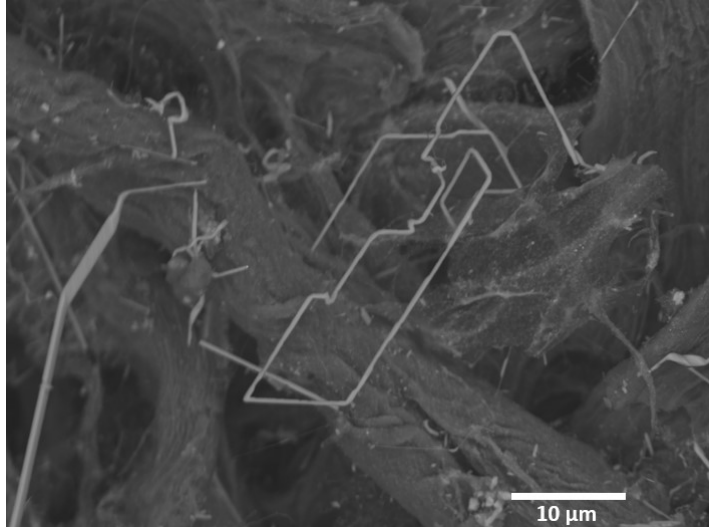
(b)
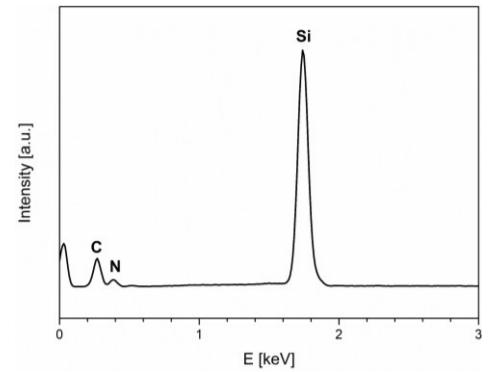
(c)
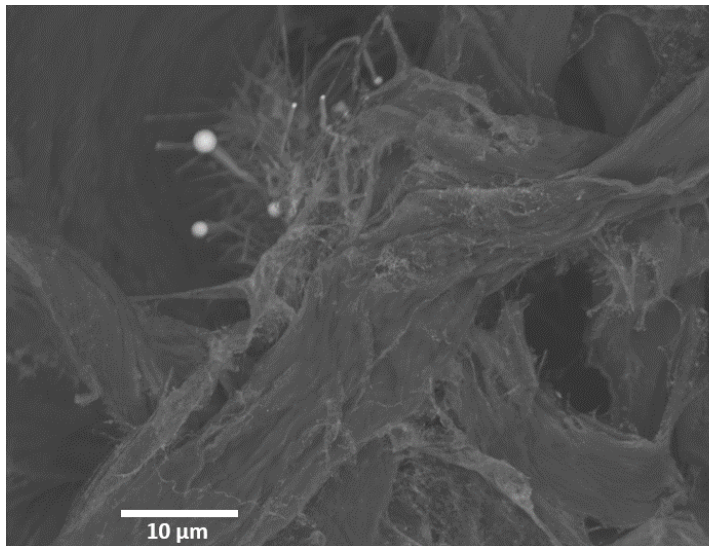
(d)
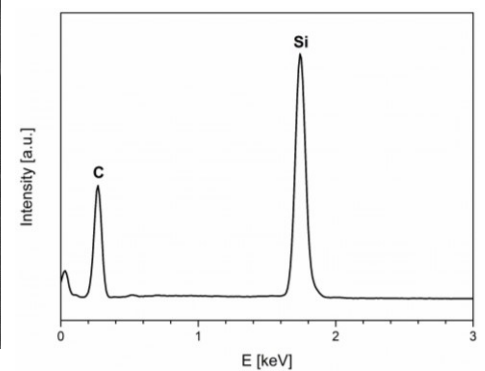
Figure 38. SEM image of the (a) Lin_Fe_Dur-1300 °C Ar (Ar) and the (c) Lin_Fe_Dur-1300 °C N_2 (Ar) samples with respective EDX spectra (b) and (d). Images and EDX spectra taken by Johannes Peter

Dur promotes higher ordering of the carbon at 1000 °C in Ar, as revealed by the presence of the distinct 2D band (2690 cm^{-1}) (Figure 39 (a)). Annealing at 1300 °C in argon ((Figure 39 (b)) increases the intensity of the 2D band and decreases the D band (1350 cm^{-1}), with an additional SiC band (802 cm^{-1}) appearing on some spots, indicating continuing graphitization. This is also visible from the characteristic values calculated from the Raman spectra (Table 15), as L_a in the 1000 °C is smaller than in the 1300 °C sample. Interestingly, by annealing at 1300 °C in N_2 (Figure 39 (c)) no Si-N-Si vibrations or fluorescence could be observed in the Raman spectra, pointing to less formation of Si_3N_4, which influences A_{2D}/A_D and L_{eq} as those values become higher compared to PHPS.

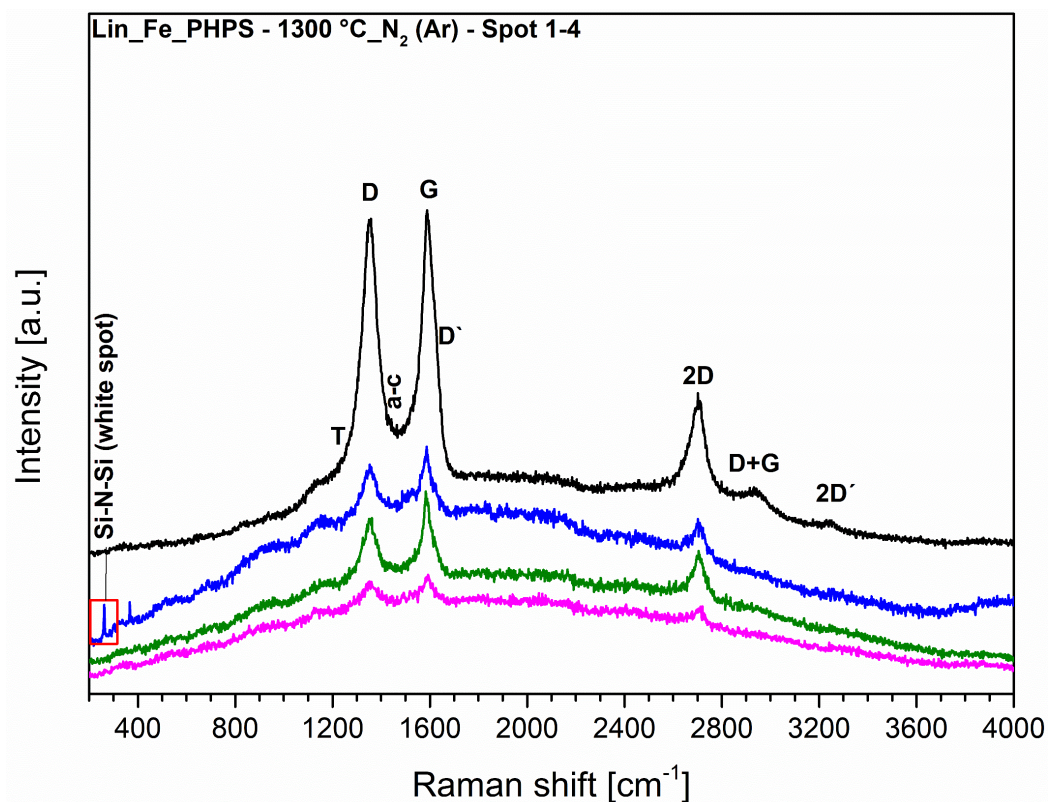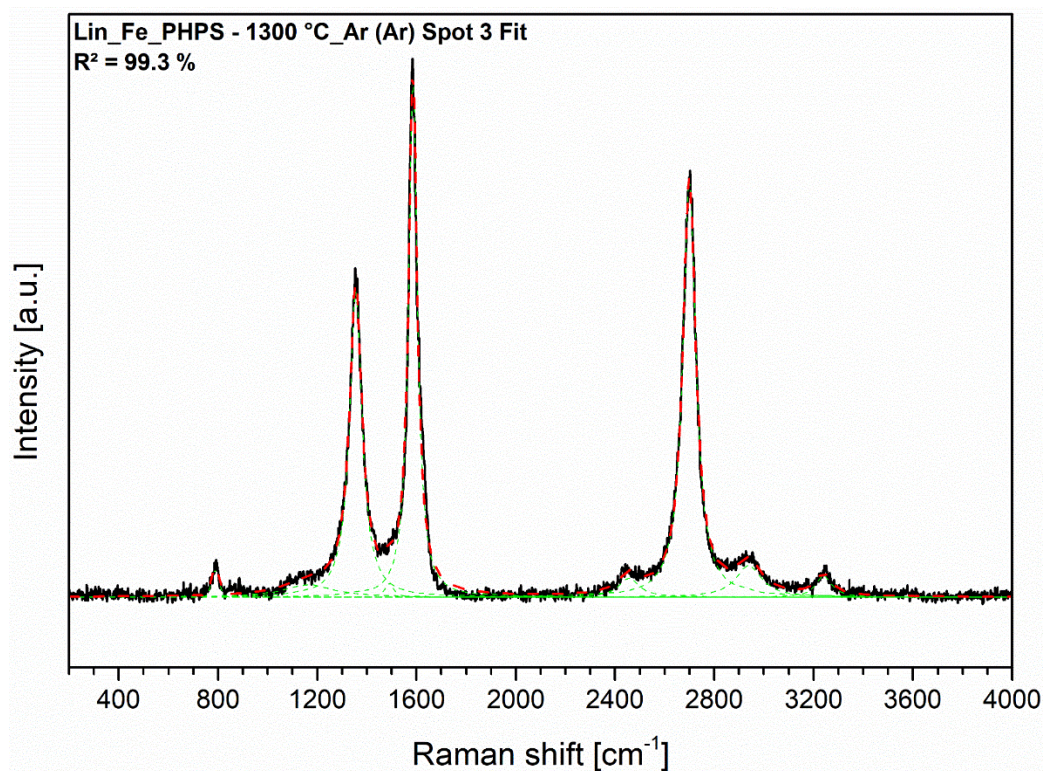**(a)**
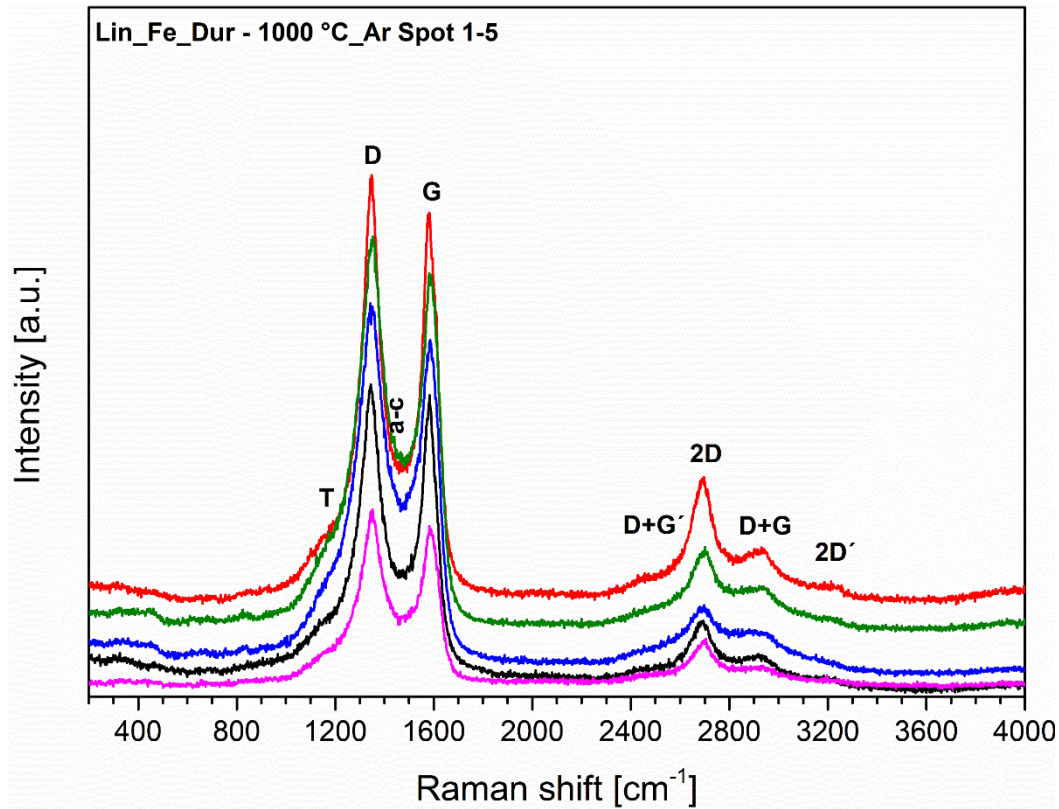
(b)
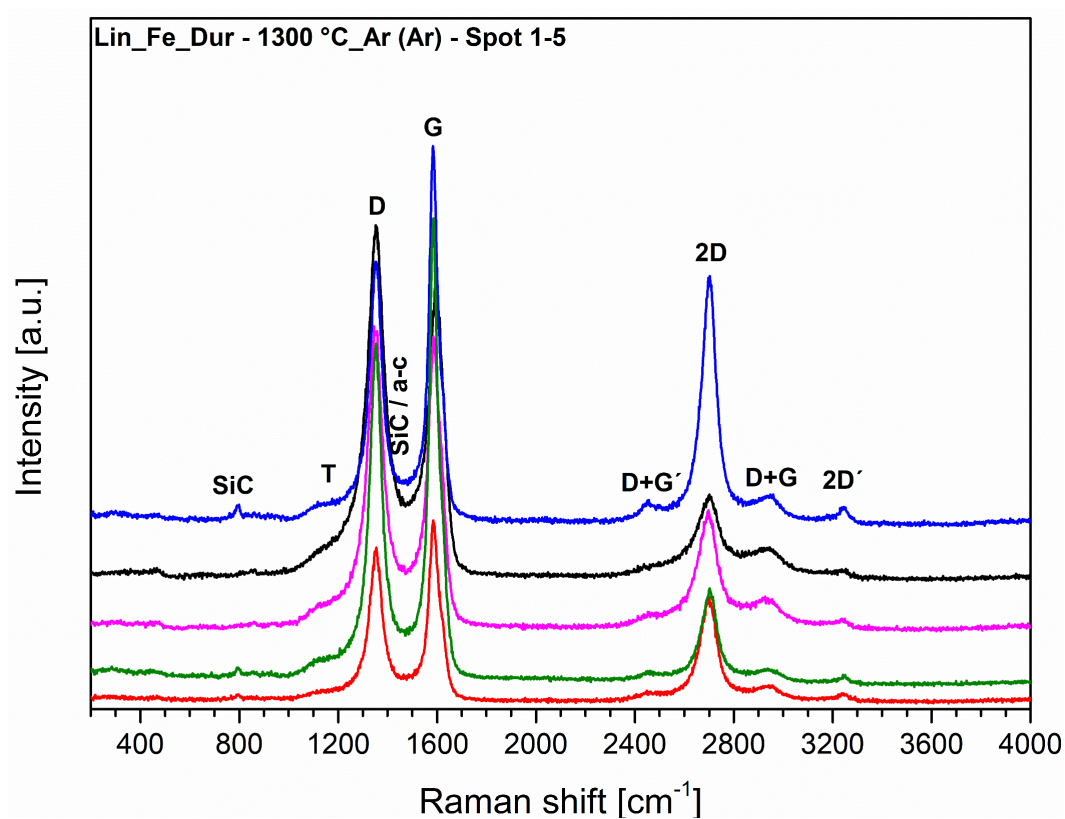
(c)

Figure 39. μ-Raman spectra of the Lin_Fe_Dur ceramic papers annealed at (a) 1000 °C in Argon, (b) 1300 °C in Ar (previously at 1000 °C in Ar) and (c) 1300 °C in N_2 (previous at 1000 °C in Ar)

Table 15. Calculated characteristic parameters from Raman spectroscopy (including mean values and standard deviation) of the iron(III)-Dur-modified Lin templates in different atmospheres and temperatures

Sample	A_D/A_G	A_{2D}/A_D	L_a (nm)	L_D (nm)	L_{eq} (nm)	n_D (x 10^{11}, cm^{-3})
Lin_Fe_Dur-1000 °C_Ar	2.49±0.35	0.22±0.08	6.87±0.92	7.16±0.49	17.33±6.21	8.55±1.20
Lin_Fe_Dur-1300 °C_Ar (Ar)	1.41±0.55	0.61±0.31	13.54±4.41	9.93±1.73	47.32±24.07	4.86±1.88
Lin_Fe_Dur-1300 °C_N_2 (Ar)	1.45±0.22	0.81±0.13	11.88±2.20	9.40±0.83	62.05±10.34	4.99±0.76

Eventually combining all results from XRD and Raman, it can be assumed, that with Dur in the iron system, similar crystalline phases and bands appear, when compared to the system, where PHPS was used.

4.2.5 Comparison Batch 1 and 2

As described in chapter 3.1 and shown in Table 5, two Batches with varying concentrations of the polysilazane (PHPS and Dur) and the iron(III)acetylacetonate were produced to study if additional bands appear in the characteristic measurements (FTIR and Raman). Previous studies by Kunkler [112] showed, that the dilution of polysiloxane in toluene, in which a cellulose-based template was dipped, affects the thickness of the coating on the template. Zhou [94] pointed out, that the amount of iron inside a cellulose-based sample "not only affected the yield of nanowires but also the growth mechanism of the 1D nanostructures" [94]. The other characteristic features, like band vibrations and degree of graphitization of the cellulose-based template, are similar between Batch 1 and 2 (comparison Figure 36 (b) with Figure A 4). Looking at the Raman spectra of the same sample, but only annealed at 1300 °C in Ar (Figure 38 (b) and Figure A 5), it appears, that some bands are more distinct in the less diluted sample, leading to more formation of β-SiC. Otherwise, similar bands appear in both Batches.

4.2.6 Summary Si-Fe-System

To sum this chapter up, the bonding characteristic at 1000 °C (based on FTIR) appears to be insignificant of the atmosphere (Ar or NH_3) and the preceramic precursor (PHPS or Dur) in the ceramic paper.

TGA analysis of the Lin-iron(III)acetylacetonate-modified polysilazane (PHPS) in Ar and NH_3 atmospheres showed, that the main exothermic mass loss in both atmospheres appears between 250 °C and 400 °C. Mainly H_2O, NH_3, and carbonyl derivates (like formic acid) are evaporated. Higher temperatures lead to the formation of CO, CO_2 and possibly SiO gas.

XRD analysis of the Fe-modified precursor revealed, that in the NH_3 atmosphere, independent of the polysilazane type, an additional ε-Fe_2N phase appears. In Ar, on the other hand, already at 1000 °C Fe_3Si / α-Fe (Dur and PHPS) phases are present. Further annealing leads to β-SiC. Changing the atmosphere at 1300 °C into N_2 a β-Si_3N_4 crystalline phase, instead of SiC, occurs in all samples. Additionally, a Si_2N_2O phase arises, when the sample is annealed at 1000 °C in NH_3 before. The paper template hinders the crystallization of the different phases, as they appear more amorphous and in some cases, no crystallization was seen in XRD analysis. SEM showed the formation of wires in Ar at 1300 °C consisting of SiC and in N_2 of Si_3N_4 with occasionally round tips on top of them. Thus, the formation thereof can be controlled by picking a suitable atmosphere.

Comparing the characteristic parameters calculated from the fitting of the Raman spectra, it can be seen that the graphitization of the carbon phase appears independent of the template or the polysilazane type. Generally, the graphitization of the cellulose-based paper is enhanced with the addition of Fe. With higher temperatures it is more progressed, whereas in Ar this progress appears to be further developed compared to N_2 (L_a (Ar) > L_a (N_2)). Therefore, for the next systems, at 1000 °C only argon atmosphere will be used, while further annealing will still be performed in N_2 and Ar atmosphere at 1300 °C.

4.3.0　Si-Pd-system

In comparison with Fe, Pd does not form crystalline phases with nitrogen but instead forms palladium silicides. Firstly, the influence of the Ar atmosphere on the Pd-modified PHPS will be discussed. Afterward, similar studies but with Dur as the used polysilazane will be carried out. The last chapter will shortly summarize the results.

4.3.1　Si-Pd-O-(N) – Influence of Argon Atmosphere

Firstly, the FTIR spectra of the palladium(II)acetylacetonate-modified PHPS with and without template during pyrolysis in Ar and N_2 are shown in Figure 40. The bands in the as-prepared PHPS precursor (Figure 40 (a)) are as follows: C-O (1270 cm^{-1}), C=C (1515 cm^{-1}), Si-H (2150 cm^{-1}) and N-H (1170 cm^{-1} and 3360 cm^{-1}). Pyrolysis at 1000 °C in argon leads to two Si-O-Si bands (450 cm^{-1} and 950 cm^{-1}), indicating the decomposition of the acetylacetonate groups in the preceramic polymers and further formation of Si-O-Si linkages. During further annealing at 1300 °C in Ar, a Si-C band (792 cm-1) appears, suggesting that SiC evolves from the Si-O-Si linkages. However, annealing in N_2 leads to Si-N-Si bands (490-1030 cm^{-1}), pointing to Si_3N_4. In the case of the ceramic paper (Figure 40 (b), similar bands appear, but pyrolysis at 1000 °C in Ar leads to sharper Si-O-Si bands, suggesting differences in the network structures.

(a)
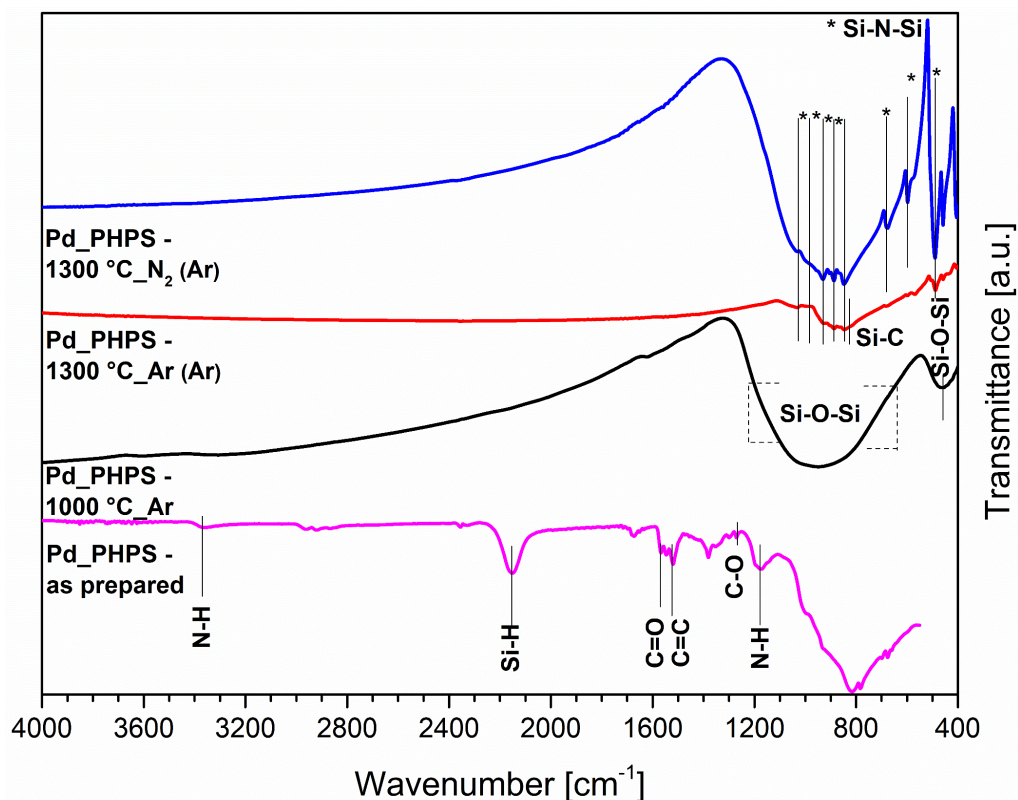
(b)
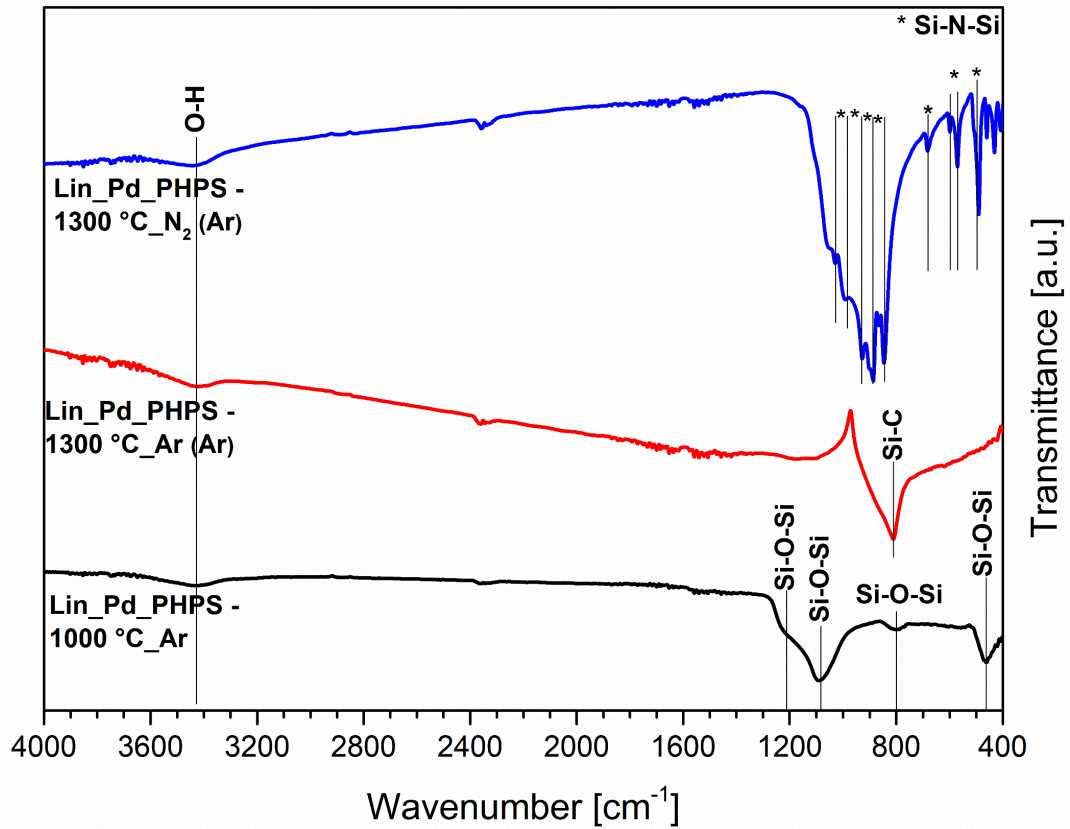
Figure 40. FTIR spectra of the palladium(II)-modified polysilazane (PHPS) powder shown in (a), the Lin ceramic paper given in (b), in the as-prepared state and after pyrolysis at different temperatures in Ar and N_2

XRD analyses of the template-free palladium(II)acetylacetonate-modified polysilazane (PHPS) annealed at 1000 °C in Ar show (Figure 41 (a)), that only a single crystalline phase of Pd_2Si (space group $P\bar{6}2m$, (189)) is formed. Further annealing in Ar (1300 °C) results in an additional crystalline β-SiC phase (space group $F\bar{4}3m$, (216)) and a PdSi phase (space group Pbmn, (62)). Annealing in N_2 a crystalline β-Si_3N_4 (space group P3$1c$, (159)) phase occurs. The crystalline phases are similar in the template, but with inferior crystallinity (Figure 41 (b)). Papakollu et al. [113] showed similar phases in the case of polysiloxanes, following the reactions (equations Eq. 22 and Eq. 23) below:

$$\text{PdO (s)}+ \text{C (Graphite)} \rightarrow \text{Pd (s)} + \text{CO (g)} \qquad \textbf{(Eq. 22)}$$

$$2\,\text{Pd (s)} + \text{SiO}_2\,\text{(amorphous)}+ 3\,\text{C (s)} \rightarrow \text{Pd}_2\text{Si} + \text{C (s)} + 2\,\text{CO (g)} \qquad \textbf{(Eq. 23)}$$

$$\text{Pd (s)} + \text{SiO (g)} + \text{C} \rightarrow \text{PdSi (s)} + \text{CO (g)} \qquad \textbf{(Eq. 24)}$$
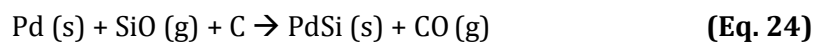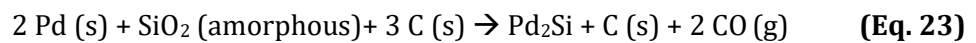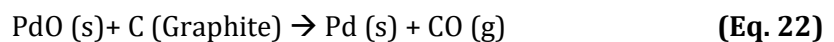
These reactions are also possible with PHPS, as the palladium(II)acetylacetonate contains oxygen, creating at 1000 °C Si-O-Si (SiO_2) bands, as shown in the FTIR spectra Figure 40 (a), which then react with Pd to form Pd_2Si. Equation Eq. 24 is assumed due to the formation of the PdSi phase with the help of gaseous SiO. Previous studies reported the formation of Pd below 1000 °C [114, 115]. The formation of β-SiC and β-Si_3N_4 could have a similar reaction as described in equations Eq. 18 till Eq. 21 before.

(a)
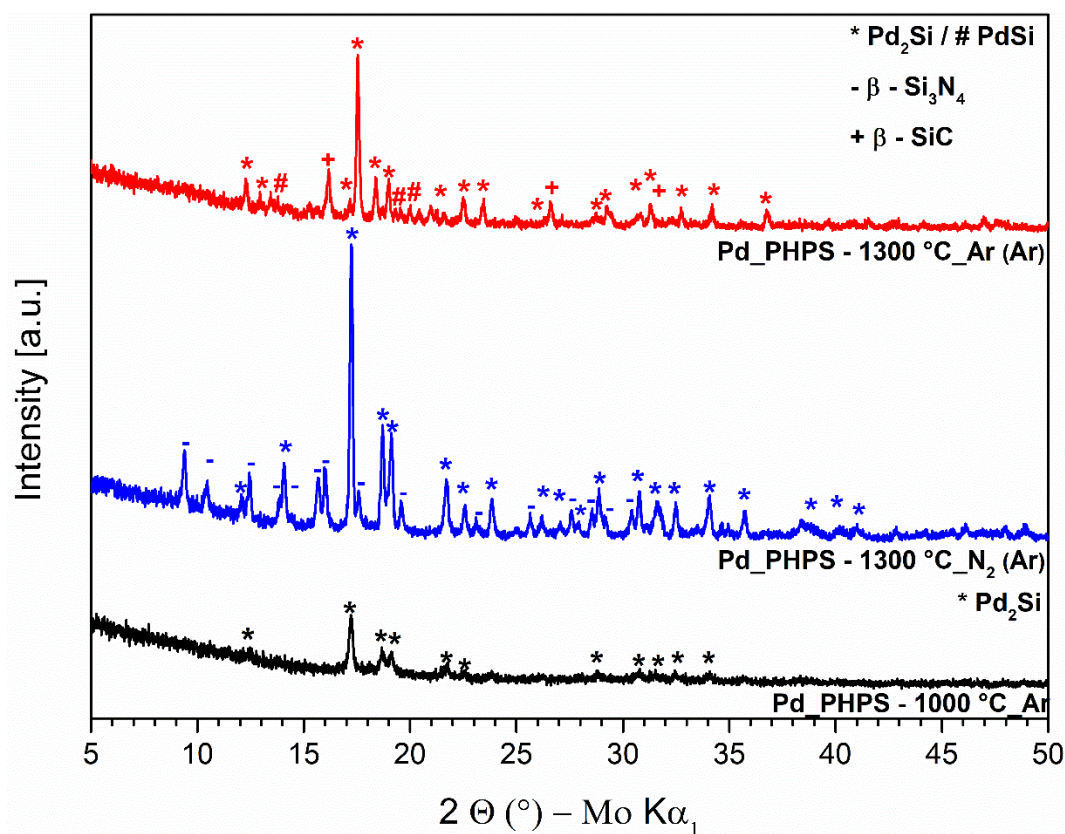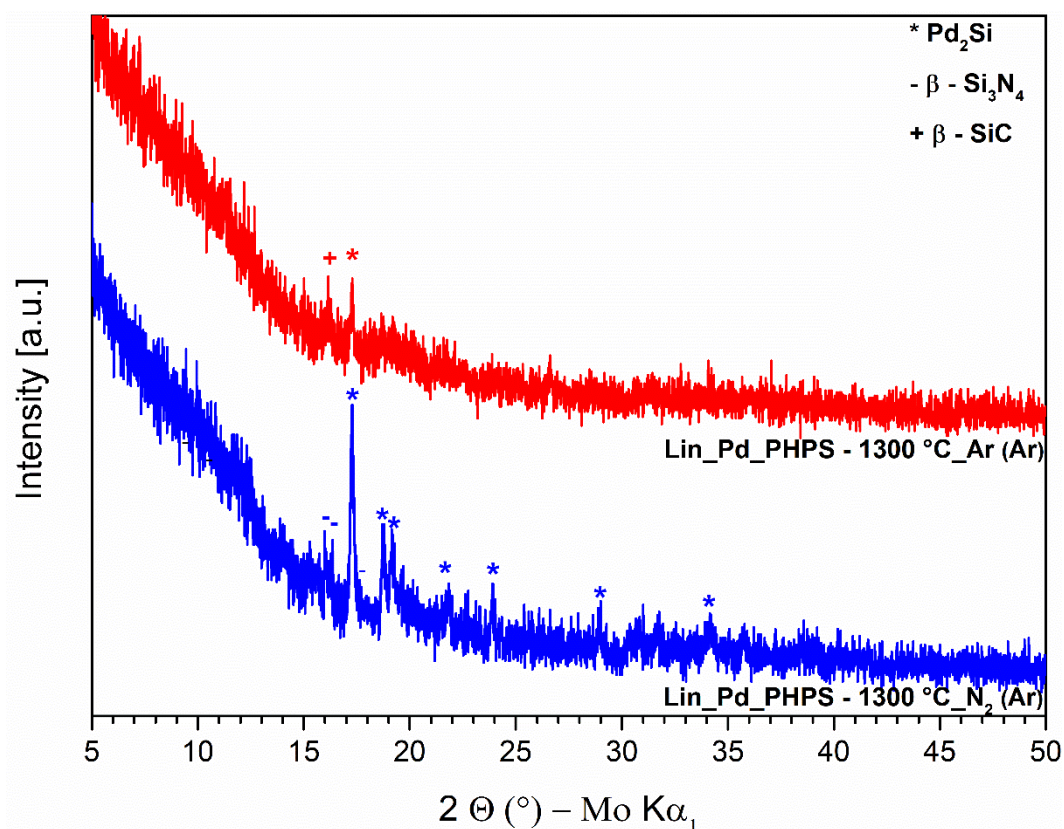
Figure 41. X-ray diffraction patterns of the palladium(II)-modified polysilazane (PHPS) precursor depicted in (a), the ceramic paper shown in (b), pyrolyzed at 1000 and 1300 °C in Ar and N_2, depending on the temperature

Figure 42 depicts the Raman spectra of the Euc_Pd-modified PHPS ceramic papers, annealed at different temperatures and atmospheres. Annealing the ceramic paper at 1000 °C in Ar (Figure 42 (a)) leads to a partially amorphous carbon structure. Increasing the temperature (1300 °C) not only forms SiC bands (790 cm^{-1}), but also the 2 D band (2704 cm^{-1}) becomes more distinct, indicating more graphitized carbon (Figure 42 (b)). Changing the atmosphere to N_2 (Figure 42 (c)), leads partially to fluorescence, due to the Si_3N_4 wires, whereas the degree of graphitization of the carbon appears to be less pronounced, compared to the sample annealed at 1300 °C in Ar (less sharp 2 D band).

The calculated characteristic parameters (Table 16) show a similar trend – with higher annealing temperature the graphitization of the carbon becomes more distinct – due to higher values of A_{2D}/A_D, L_a and L_{eq}. Furthermore, the decrease of the defect density and the increase of the defect distance support this assumption.

(a)

Euc_Pd_PHPS - 1000 °C_Ar - Spot 1-5

(b)

Euc_Pd_PHPS - 1300 °C_Ar (Ar) - Spot 1-5

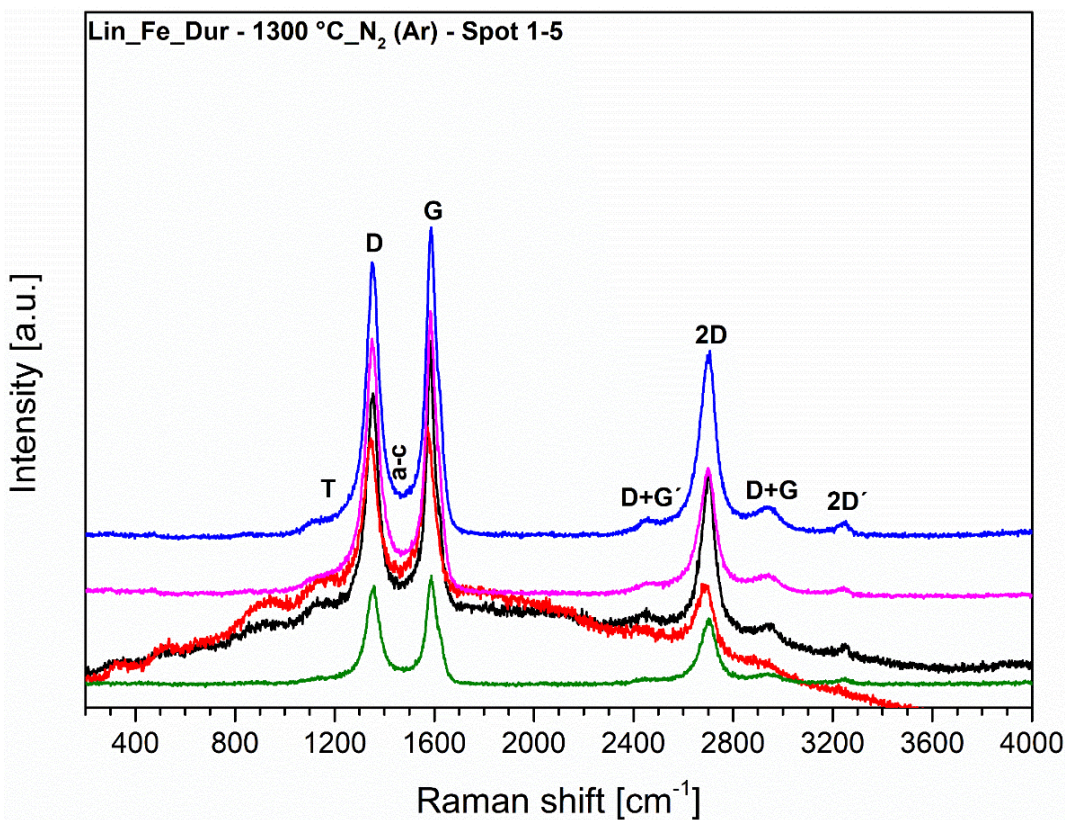**(c)**
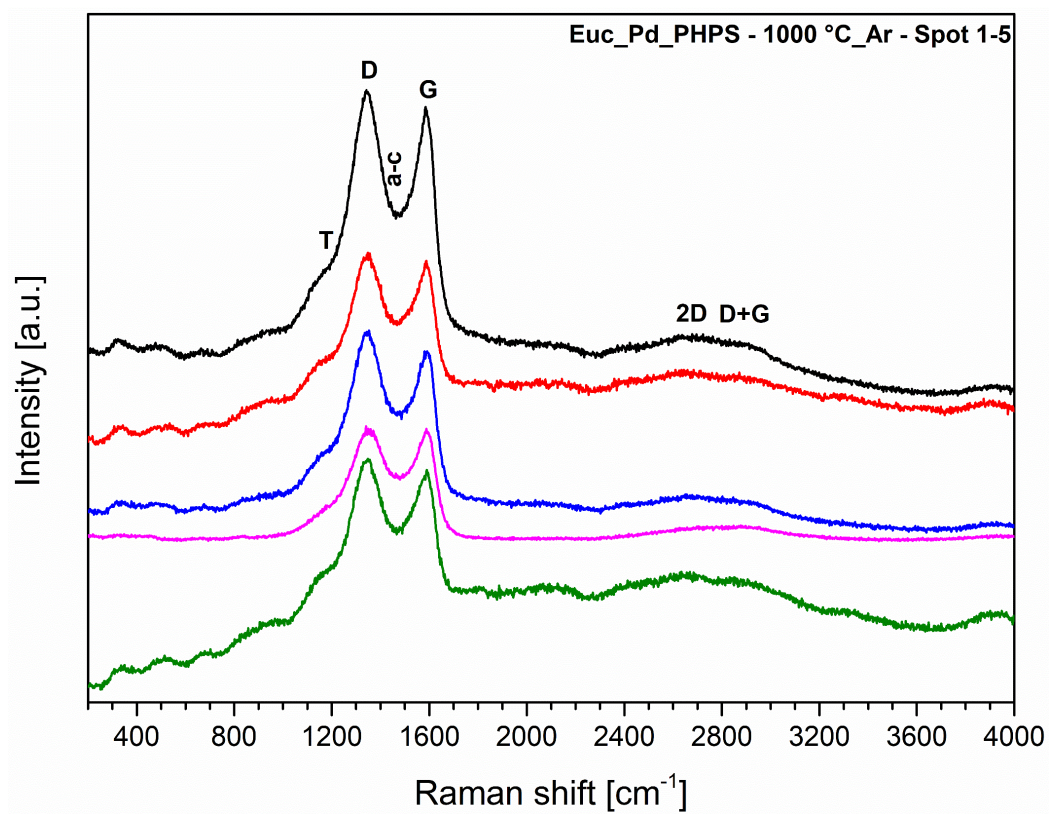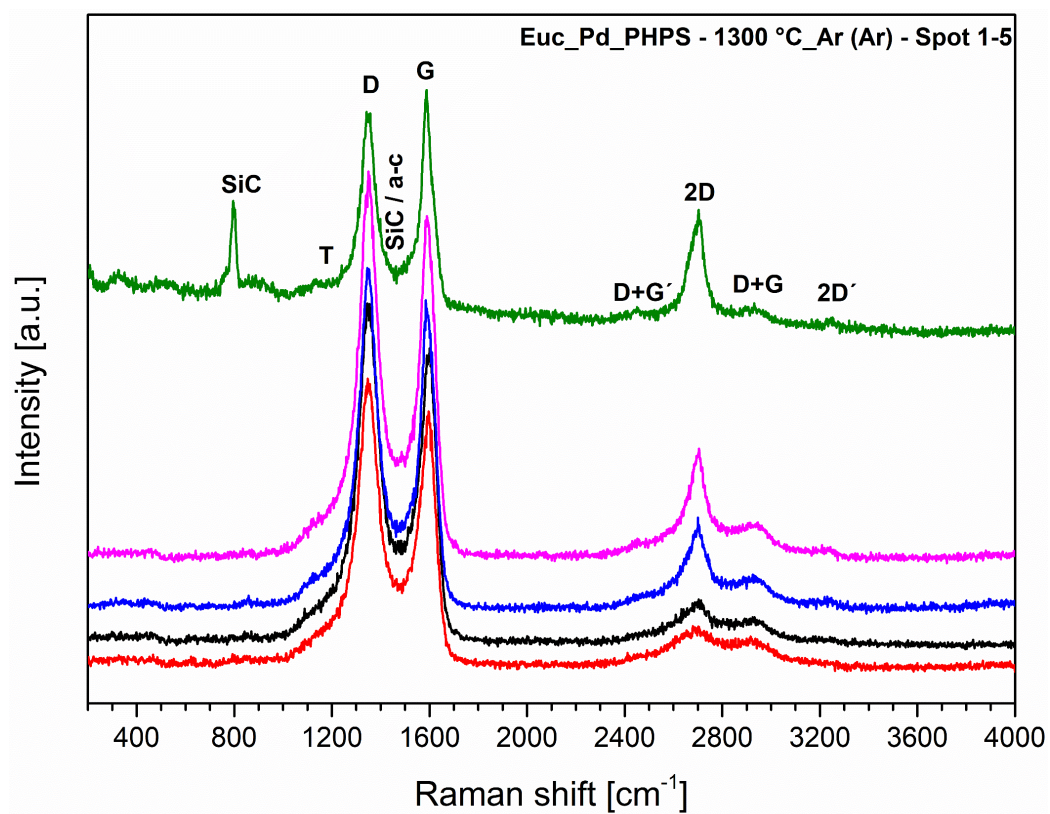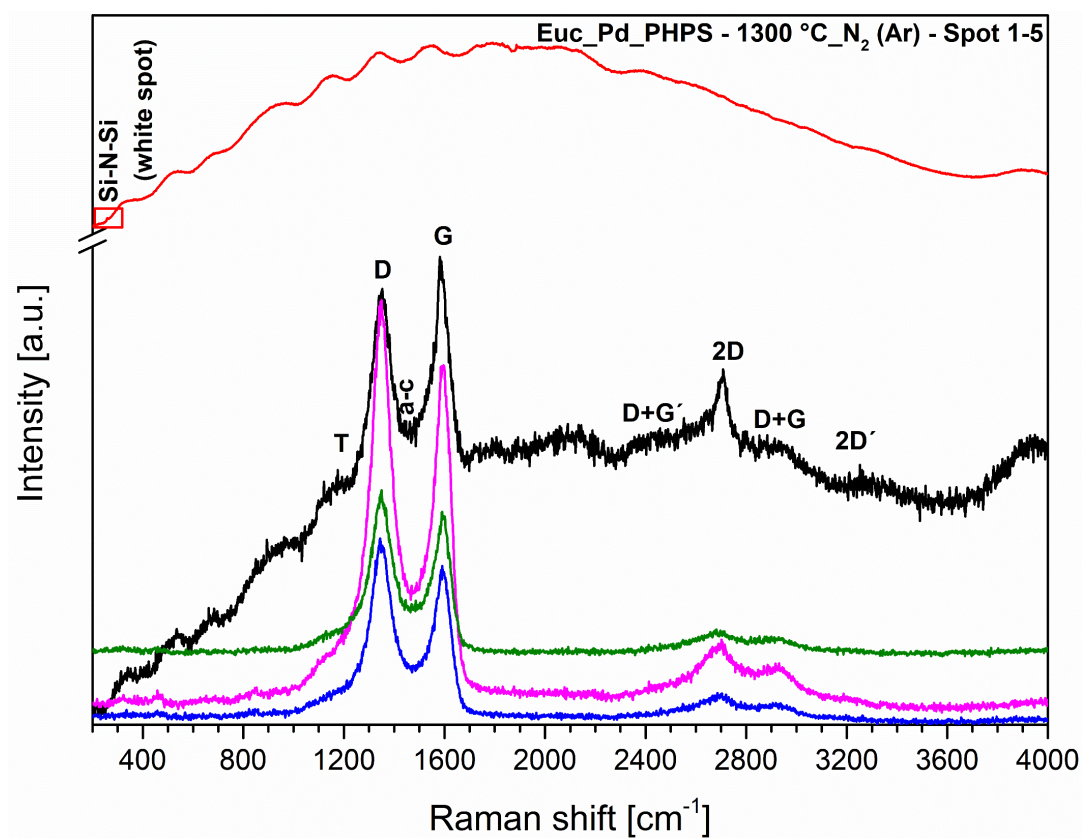
Figure 42. μ-Raman spectra of the Euc_Pd_PHPS ceramic papers annealed at (a) 1000 °C in Argon, (b) 1300 °C in Ar (previous at 1000 °C in Ar) and (c) 1300 °C in N_2 (previous at 1000 °C in Ar)

Table 16. Calculated characteristic parameters from Raman spectroscopy (including mean values and standard deviation) of palladium(II)-PHPS-modified Euc templates in different atmospheres and temperatures

Sample	A_D/A_G	A_{2D}/A_D	L_a (nm)	L_D (nm)	L_{eq} (nm)	n_D (x 10^{11}, cm^{-3})
Euc_Pd_PHPS-1000 °C Ar	4.02±0.22	0.15±0.05	4.18±0.23	5.60±0.15	11.63±3.63	13.8±0.76
Euc_Pd_PHPS-1300 °C Ar (Ar)	2.30±0.52	0.32±0.22	7.79±2.33	7.57±1.06	24.62±17.10	7.92±1.80
Euc_Pd_PHPS-1300 °C N_2 (Ar)	2.59±0.32	0.25±0.07	6.58±0.96	7.01±0.49	19.27±5.39	8.92±1.12

4.3.2   Si-Pd-C-(N) – Influence of Argon Atmosphere

The preceramic polymer precursor based on palladium(II)-modified Dur (Figure 43 (a)) shows the following bands: C-O (1255 cm^{-1}), C=C (1521 cm^{-1}), C=O (1570), C-H (2950 cm^{-1}) and N-H (1170 cm^{-1} and 3370 cm^{-1}). Interestingly, no Si-H band is visible, indicating that a reaction took place at the Si-H bond. Figure 43 (c) depicts the possible resulting products of this reaction. Otherwise annealing the preceramic precursor at 1000 °C in Ar leads to two broad Si-O-Si vibrations (450 and 930 cm^{-1}). Higher Temperatures lead to one Si-C band (800 cm^{-1}). Changing the atmosphere at 1300 °C to N$_2$ forms Si-N-Si bonds (from 480 cm^{-1} to 1030 cm^{-1}), indicated by the resulting vibrations. The palladium-modified ceramic paper (Figure 43 (b)) pyrolyzed at 1000 °C in Ar has an OH band (3430 cm^{-1}) and more sharp Si-O-Si bands (450 cm^{-1}, 815 cm^{-1}, 1050 cm^{-1} and 1200 cm^{-1}), resulting from the differences in the Si-O-Si network structure. Further annealing at 1300 °C forms one sharp Si-C band (810 cm^{-1}), while in N$_2$ similar bands point to Si-N-Si (from 480 cm^{-1} to 1030 cm^{-1}) vibrations, like in the PHPS modified polymer precursor.

(a)
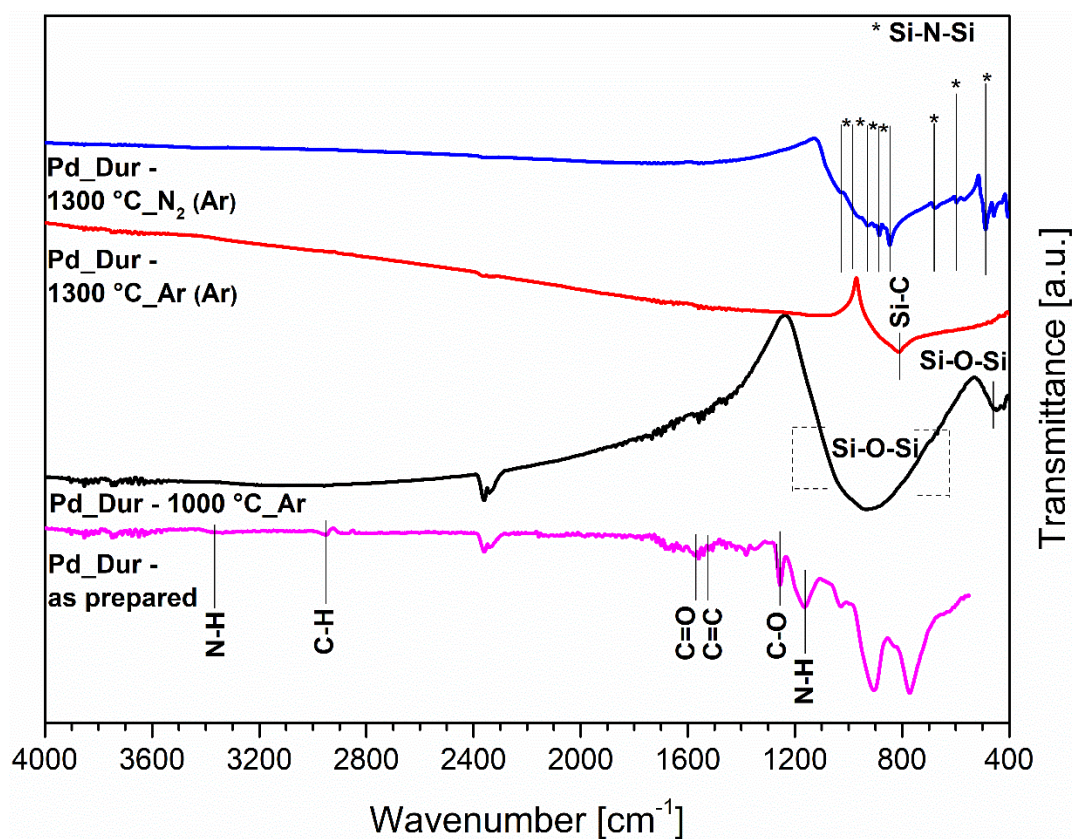
(b)
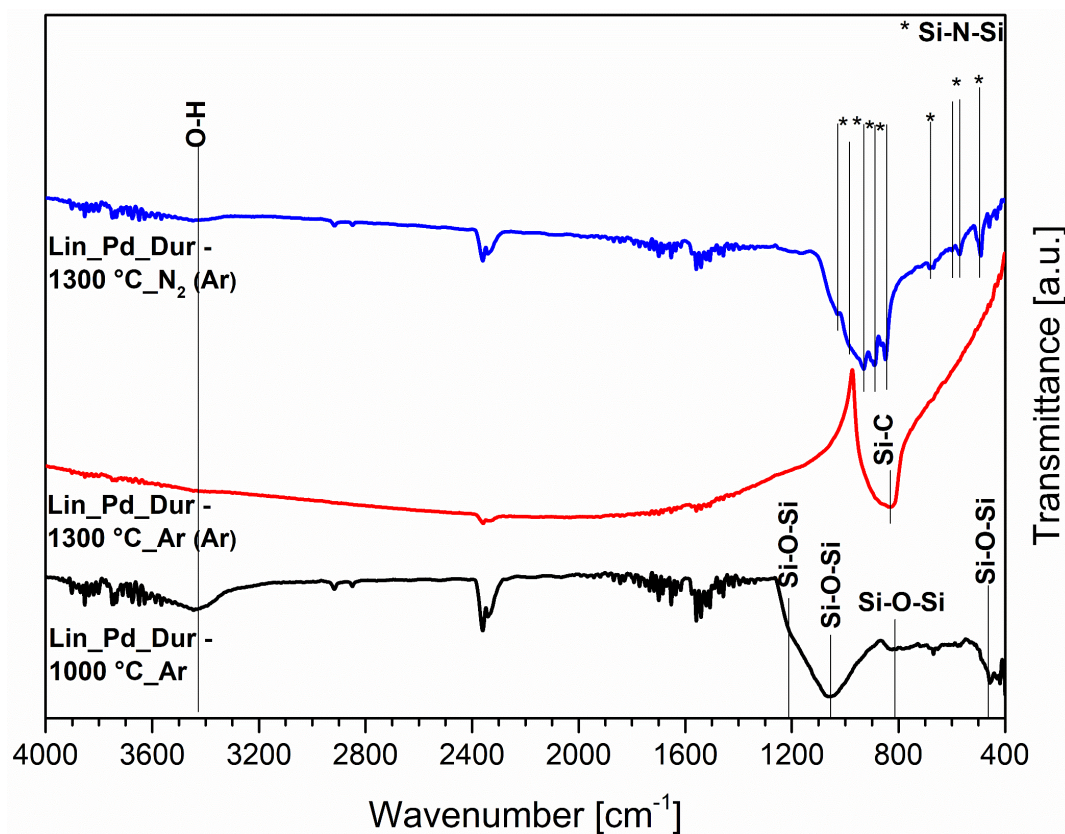
(c)

Figure 43. FTIR spectra of palladium(II)-modified Dur in the (a) precursor state and (b) with the template at different temperatures. (c) shows two possible reaction paths in the precursor state based on (a). While in (i) a substitution reaction at the Si-H groups is represented, (ii) depicts the hydrosilylation of the C=O groups of acetylacetonate

Figure 44 shows the characterization of the different crystalline phases of the palladium-modified Dur with and without (here Eucalyptus) template utilizing XRD analysis. The temperature evolution of the precursor can be described as follows: at 1000 °C in Ar, only a Pd_2Si phase exists (space group $P\bar{6}2m$, (189)), while further annealing at 1300 °C, enables the formation of an additional β-SiC phase (space group $F\bar{4}3m$, (216)). Interestingly, no PdSi phase could be observed, indicating that the reaction shown in equation Eq. 24 did not occur. Changing the atmosphere at this temperature to N_2 instead of Ar promotes the crystallization of β-Si_3N_4. The influence of the template on the hindrance of the crystallization appears to be higher in N_2 compared to Ar, as fewer phases are visible (Figure 44 (b)). This could be because in Durazane more carbon is present, leading to less formation of β-Si_3N_4.

(a)
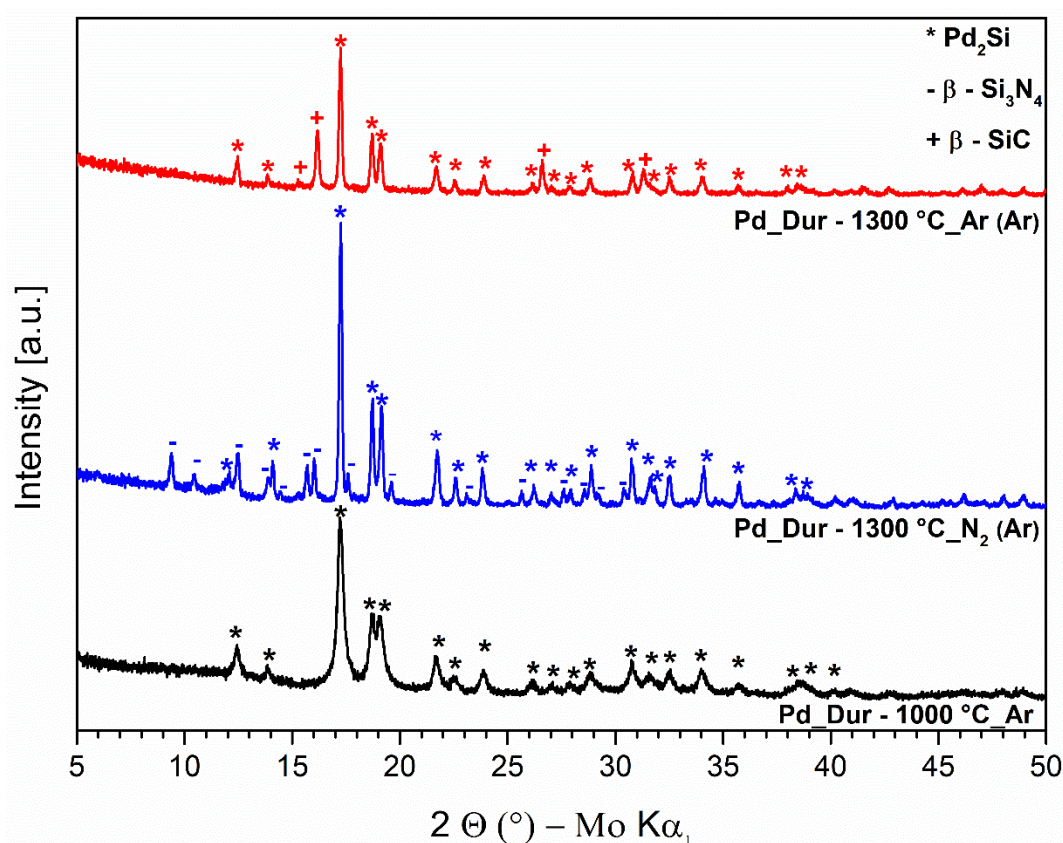
(b)
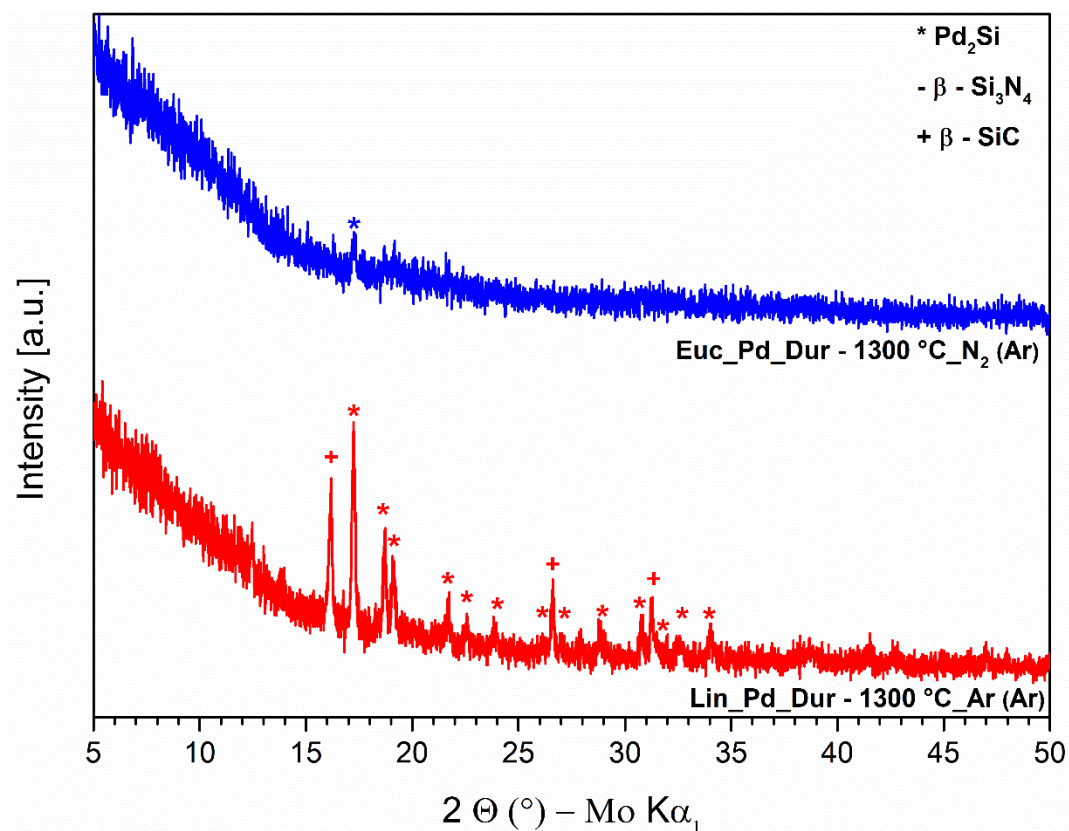
Figure 44. X-ray diffraction patterns of the palladium(II)-modified polysilazane (Dur) precursor depicted in (a), the ceramic paper shown in (b), pyrolyzed at 1000 and 1300 °C in Ar and N_2, depending on the temperature

Raman spectroscopy of the palladium(II)-durazane modified ceramic papers pyrolyzed at 1000 °C in Ar (Figure 45 (a)) indicates a partially amorphous state of the carbon phase. Pyrolyzing at 1300 °C promotes the SiC band (794 cm^{-1}) and the 2 D band (2701 cm^{-1}) becomes sharper, resulting in a more graphitized carbon template (Figure 45 (b)). The SiC band does not appear on each measured spot. This indicates an inhomogeneous distribution thereof. Annealing at 1300 °C in N_2, results not only in sharper 2 D bands but also in spots with fluorescence and one small band at (260 cm^{-1}) pointing to Si-N-Si vibrations (Figure 44 (c)).

Comparing the characteristic parameters in Table 17 shows, that even though the A_D/A_G ratio is larger in the sample pyrolyzed at 1000 °C in Ar, turbostratic carbon is present, as $L_{eq} > L_a$. Increasing the temperature to 1300 °C lowers the defect density, which indicates a more graphitized carbon phase. This appears independent of the atmosphere, but in Ar, it is more pronounced, as L_a, L_{eq}, and L_D are higher than in N_2.

(a)

(b)

(c)
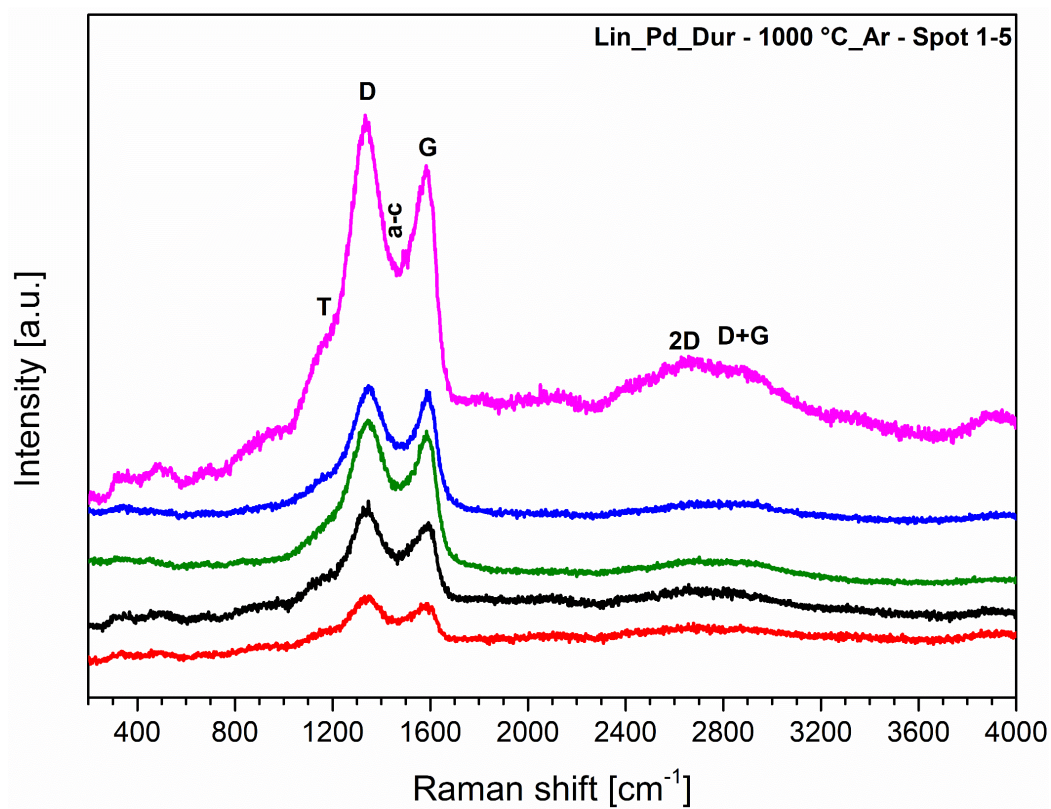
Figure 45. µ-Raman spectra of the Lin_Pd_Dur ceramic papers annealed at (a) 1000 °C in Argon, (b) 1300 °C in Ar (previous at 1000 °C in Ar) and (c) 1300 °C in N_2 (previous at 1000 °C in Ar)

Table 17. Calculated characteristic parameters from Raman spectroscopy (including mean values and standard deviation) of palladium(II)-Dur-modified Lin templates in different atmospheres and temperatures

Sample	A_D/A_G	A_{2D}/A_D	L_a (nm)	L_D (nm)	L_{eq} (nm)	n_D (x 10^{11}, cm^{-3})
Lin_Pd_Dur-1000 °C Ar	4.36±0.25	0.25±0.12	3.86±0.22	5.38±0.16	18.89±9.49	15.0±0.87
Lin_Pd_Dur - 1300 °C Ar (Ar)	1.38±0.36	0.88±0.13	12.80±2.47	9.74±1.02	67.71±10.21	4.74±1.25
Lin_Pd_Dur - 1300 °C N_2 (Ar)	2.44±0.67	0.27±0.08	7.71±3.02	7.48±1.38	20.50±6.23	8.38±2.32

4.3.3   Summary Si-Pd-system

This chapter summarizes the main differences between the usage of PHPS and Dur precursor on the ceramic paper, based on FTIR, XRD and Raman results. In Dur in the precursor state, it appears, that the palladium(II)acetylacetonate bonds to the Si-H group (Figure 43 (c)), as this disappears in the FTIR spectrum. Additionally, a metal-catalyzed hydrosilylation reaction could occur. Similar bonding appears in PHPS, but due to the fact, that Si has two hydrogen bonds, the Si-H bond is still visible (Figure 40 (a)). Otherwise, similar bands are present independent of the precursor taken: Si-O-Si at 1000 °C in Ar, Si-C at 1300 °C in Ar and Si-N-Si at 1300 °C in N_2.

In Ar at 1300 °C in the Pd_PHPS-based sample, PdSi is formed in addition to Pd_2Si and β-SiC. Contrary to the Dur-based sample, where only Pd_2Si and β-SiC are present. The additional PdSi crystalline phase could be due to the gaseous reaction of SiO and Pd, as was shown by Papakollu et al. [113] during the reaction of polymethylsilsesquioxane modified palladium acetate. In N_2 only β-Si_3N_4 and Pd_2Si crystallizes, independent of the precursor type. This is also the case for the samples annealed at 1000 °C, where only a Pd_2Si is formed. Comparing the two precursors in the ceramic template (Figure 41 (b) and Figure 44 (b)) shows that by using PHPS the formation of β-Si_3N_4 in N_2 is more pronounced when compared with Dur. Vice versa the formation of β-SiC is more pronounced in the Dur precursor in Ar than in the usage of PHPS.

Even though the Raman spectra appear to be similar, the biggest difference occurs between the Lin_Pd_Dur 1300 °C Ar (Ar) and the Euc_Pd_Dur 1300 °C Ar (Ar) samples due to the L_{eq} value (67 vs. 25). One reason for the big difference could be the additional SiC phase, which also forms from the carbon of the cellulose-based template and therefore reduce its degree of graphitization (Figure 42 (b)) and leads to lower L_{eq} values. On the contrary, in Figure 45 (b) the SiC is not visible, while the distinct 2 D band indicates a highly ordered phase. Otherwise, in both systems, the degree of graphitization of the carbon template progresses with higher annealing temperature and the Ar atmosphere promotes it better than the N_2 atmosphere.

Comparable to the discussion in chapter 4.2.5, there are no large differences between Batch 1 and 2 based on FTIR and Raman spectroscopy for the Si-Pd-system, but the poor solubility of Pd(II)-acetylacetonate in toluene favors Batch 2. This can also be seen, when using Ni as the transition metal, which will be discussed in Chapter 4.4.3.

4.4.0   Si-Ni-system

As nickel is in the same group as palladium, it is expected, that it has similar chemical behavior. Firstly, the influence of the Ar atmosphere on the Ni-modified PHPS will be discussed. Afterward, similar studies but with Dur as the used polysilazane will be investigated. The last chapter will shortly summarize the results.

4.4.1   Si-Ni-O-(N) – Influence of Argon Atmosphere

The FTIR spectra of the nickel(II)acetylacetonate modified PHPS are shown in Figure 46 (a) at different temperatures and atmospheres. In the preceramic state, C-O (1290 cm^{-1}), C=C (1530 cm^{-1}), C=O (1570 cm^{-1}), Si-H (2155 cm^{-1}) and small N-H (1168 cm^{-1} and 3366 cm^{-1}) bands are visible. With annealing at 1000 °C, only two Si-O-Si bands (450 cm^{-1} and 1040 cm^{-1}) remain, indicating the decomposition of the organic groups and formation of a Si-O-Si network. Further annealing at 1300 °C in Ar leads to Si-C (805 cm^{-1}) vibrations, resulting from the formation thereof. Annealing in N$_2$ shows Si-N-Si vibrations (490 cm^{-1} and 1040 cm^{-1}) from presumably Si$_3$N$_4$ whiskers. The nickel-modified ceramic paper (Figure 46 (b)) consists of a similar bonding situation, albeit the Si-O-Si (455 cm^{-1}, 800 cm^{-1}, 1090 cm^{-1} and 1208 cm^{-1}) and the Si-C (800 cm^{-1}) vibrations in the 1000 °C and 1300 °C samples are sharper, indicating differences in the network structure.
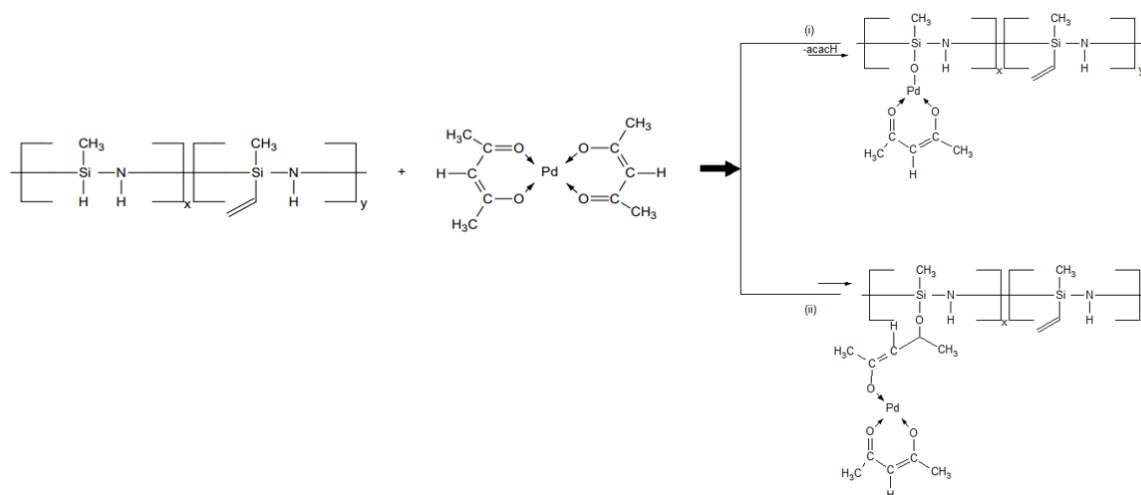
(a)
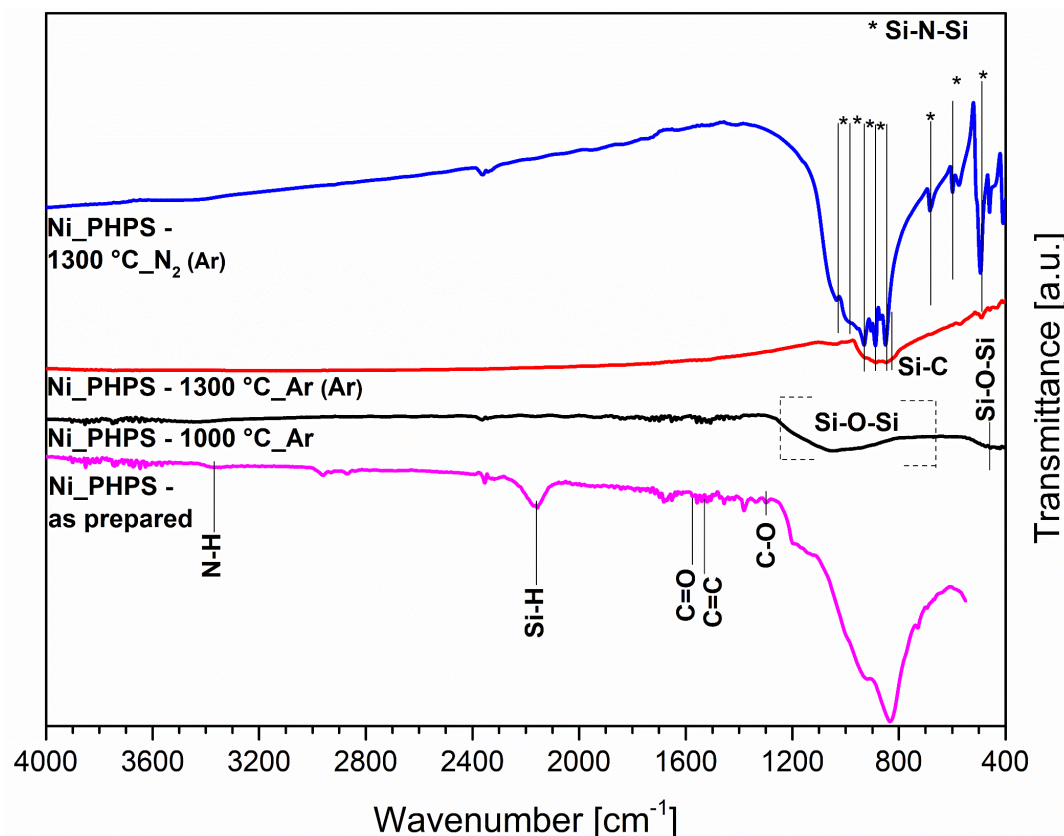
(b)
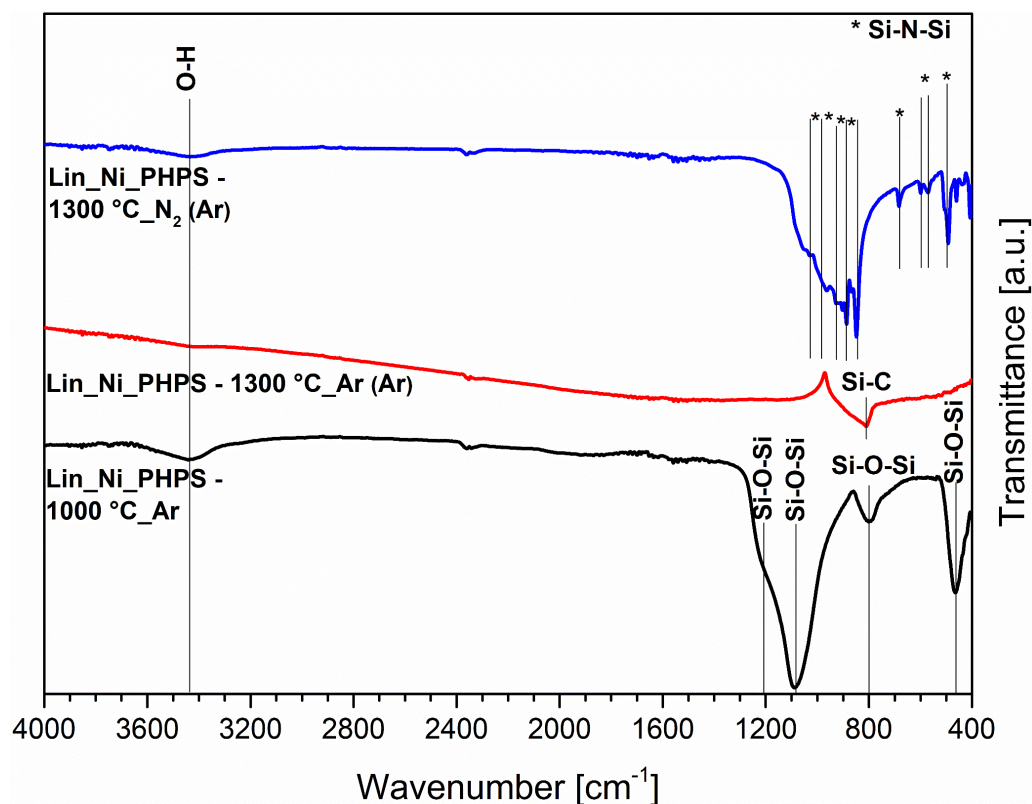
Figure 46. FTIR spectra of nickel(II)-modified PHPS in the (a) precursor state and (b) with the template at different temperatures

The XRD analysis of the nickel(II)modified PHPS precursor is shown in Figure 47 (a). At 1000 °C, a Ni (space group P63/mmc, (194)) and Ni_2Si (space group Pbnm, (62)) crystalline phase is present, indicating that not all of the Ni has reacted yet into Ni_2Si. Further annealing till 1300 °C in Ar, a β-SiC phase (space group $F\bar{4}3m$, (216)) arise and no Ni phase was identified. Changing the atmosphere to N_2 promotes β-Si_3N_4 with two different space groups (space group P31c, (159) / (space group P63/m, (176))) and an additional NiSi phase (space group Pnma, (62)), besides the Ni_2Si phase, occurs. By using the template (Figure 47 (b)), interestingly, a C-phase (space group P63mmc, (194)) appears at 1300 °C in Ar, with an additional β-SiC phase (space group $F\bar{4}3m$, (216)). No NiSi phases could be identified.

Contrary to Ar, in N_2, a β-Si_3N_4 (space group P31c, (159)) and an additional Ni_2Si (space group Pbnm, (62)) crystalline phase is visible. Either in the Ar atmosphere, the Ni_2Si phase is still amorphous or the crystallites are too small and therefore not visible in the XRD data. A previous study [116] showed that the reaction of PHPS and nickel(II)acetate-tetrahydrate form similar phases.

For the evolution of the phases the following reactions (equations Eq. 25 till Eq. 27) are suggested, which are comparable to the Pd system:

$$NiO\ (s) + C\ (Graphite) \rightarrow Ni\ (s) + CO\ (g)$$ **(Eq. 25)**

$$2\ Ni\ (s) + SiO_2\ (amorphous) + 3\ C\ (s) \rightarrow Ni_2Si\ (s) + C\ (s) + 2\ CO\ (g)$$ **(Eq. 26)**

$$Ni\ (s) + SiO\ (g) + C\ (s) \rightarrow NiSi\ (s) + CO\ (g)$$ **(Eq. 27)**
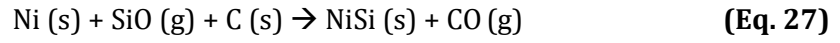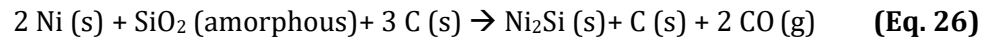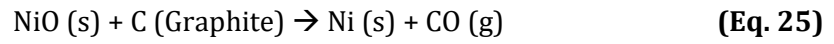
(a)
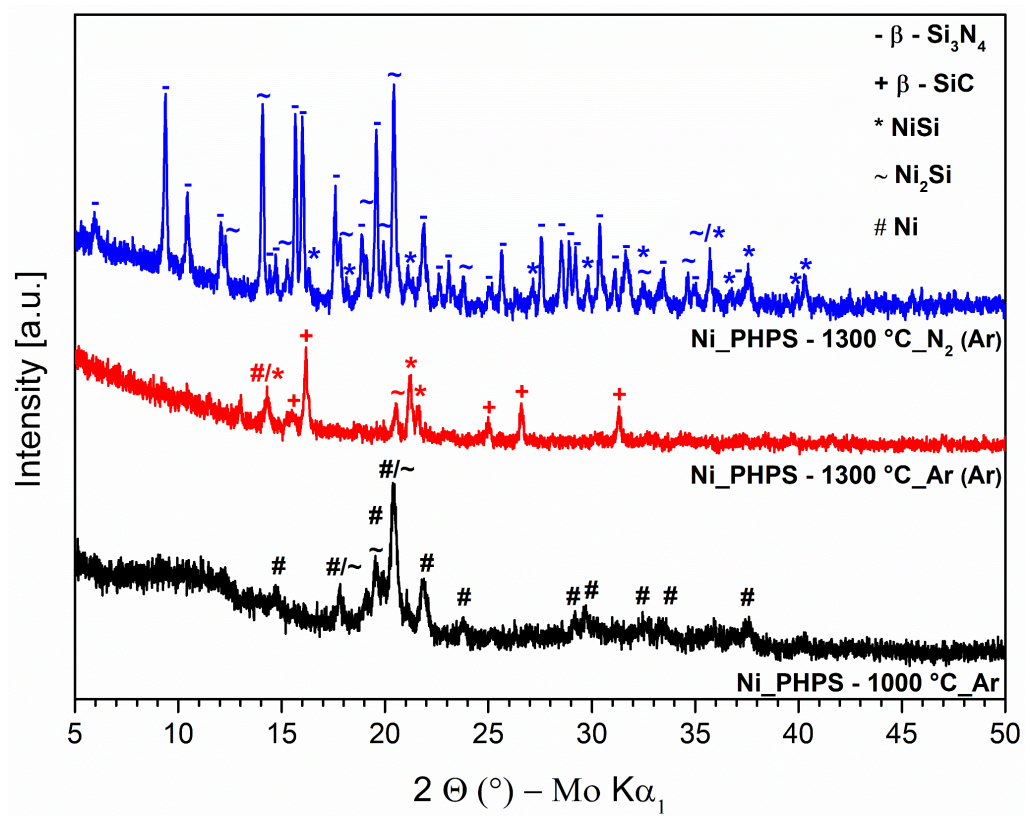
(b)
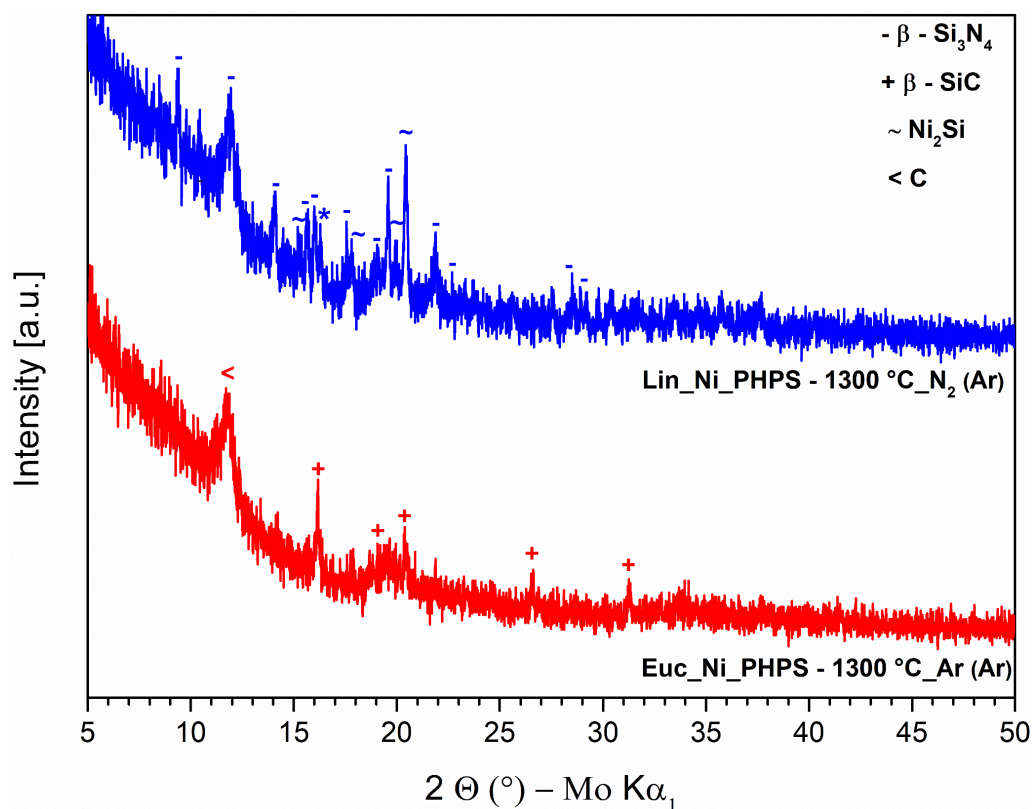
Figure 47. X-ray diffraction patterns of the nickel(II)-modified polysilazane (PHPS) precursor depicted in (a), the ceramic paper shown in (b), pyrolyzed at 1000 and 1300 °C in Ar and N_2, depending on the temperature
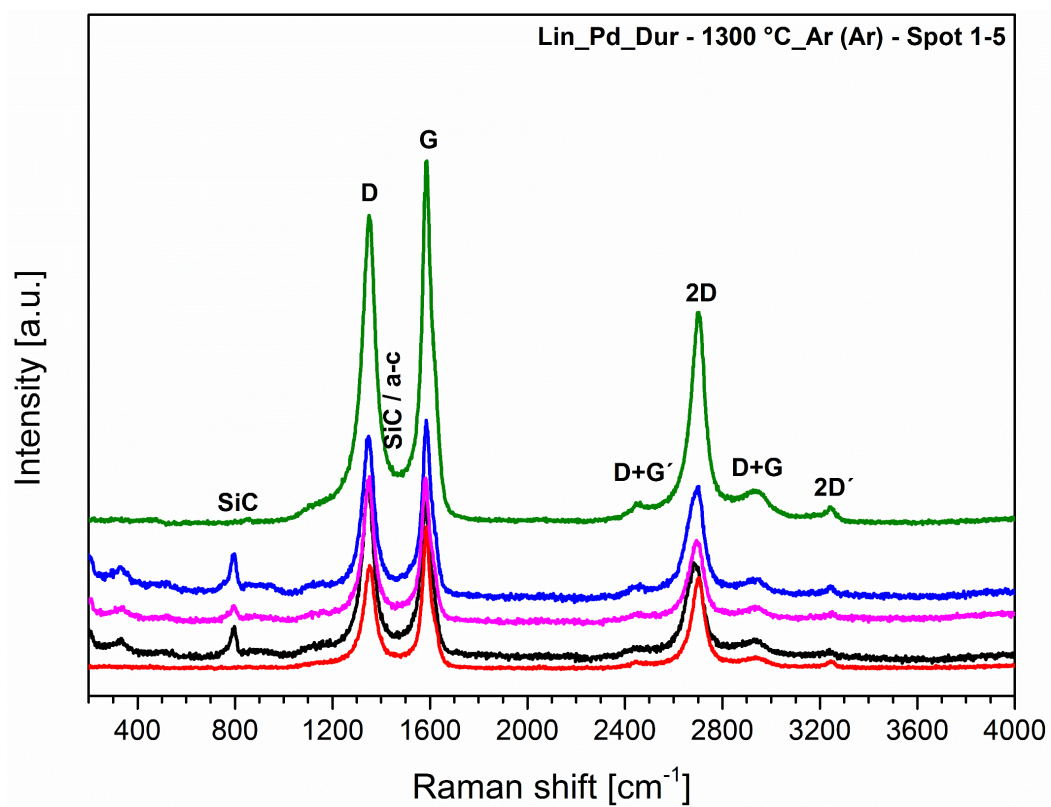
In Raman spectroscopy (Figure 48 (a)) of the Lin_Ni-PHPS sample annealed at 1000 °C in Ar, some spots already show partially graphitized carbon, resulting from the pronounced 2D band (2685 cm^{-1}). At higher temperatures (Figure 48 (b)) the SiC band becomes visible in nearly all spots, indicating a more homogeneous distribution. Furthermore, the 2D band (2700 cm^{-1}) gets even more distinct, resulting from the ongoing graphitization of the carbon phase from the cellulose template. In N_2, only the fluorescence of the Si_3N_4 whiskers is additionally visible, otherwise, the 2D band (2698 cm^{-1}) is also more distinct (Figure 48 (c)). Interestingly, no other overtones (D+G, D+G and 2D´) are visible.

The characteristic parameters based on Raman fitting are shown in Table 18. They also show a similar trend: annealing over 1000 °C promotes the graphitization of the carbon phase (A_{2D}/A_D ratio is getting higher and A_D/A_G ratio is lower compared to the 1000 °C sample). This can also be seen in the lower defect density. The significantly bigger L_a indicates larger crystallite sizes, within larger graphitic curved domains ($L_{eq} >> L_a$). In N_2, these values are lower but show similar sizes.

(a) Lin_Ni_PHPS - 1000 °C_Ar - Spot 1-5
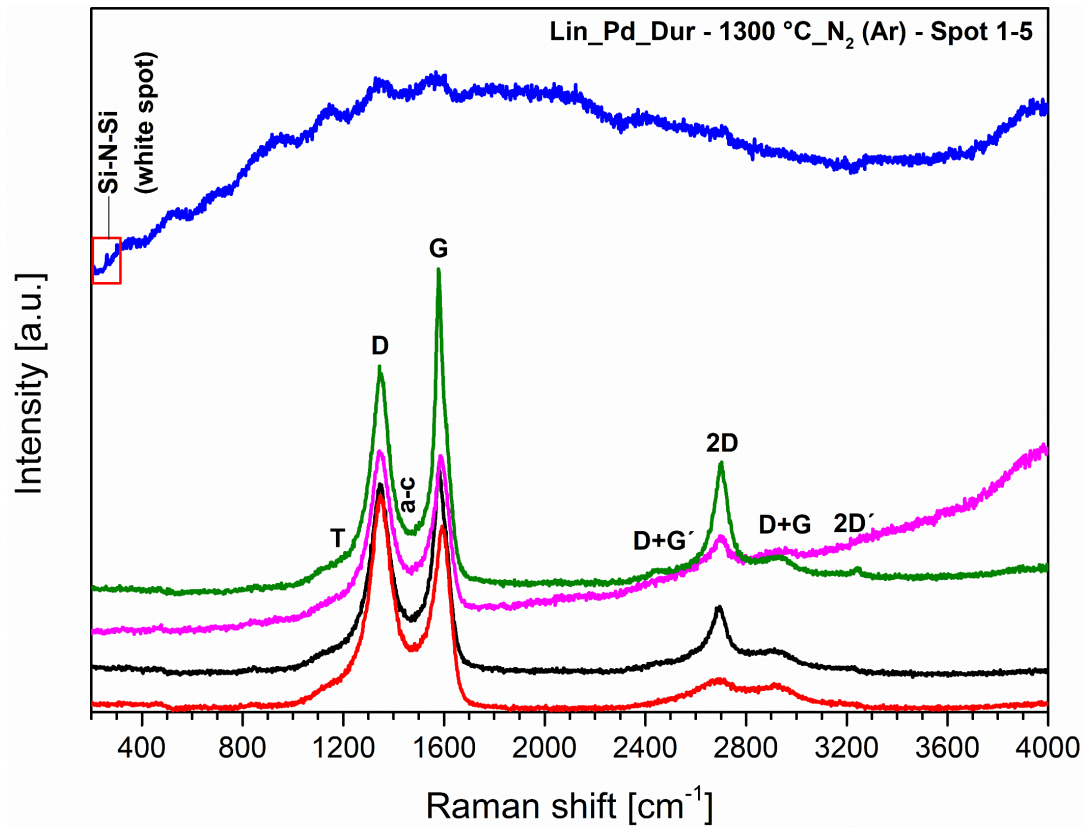
(b) Lin_Ni_PHPS - 1300 °C_Ar (Ar) - Spot 1-5

(c)
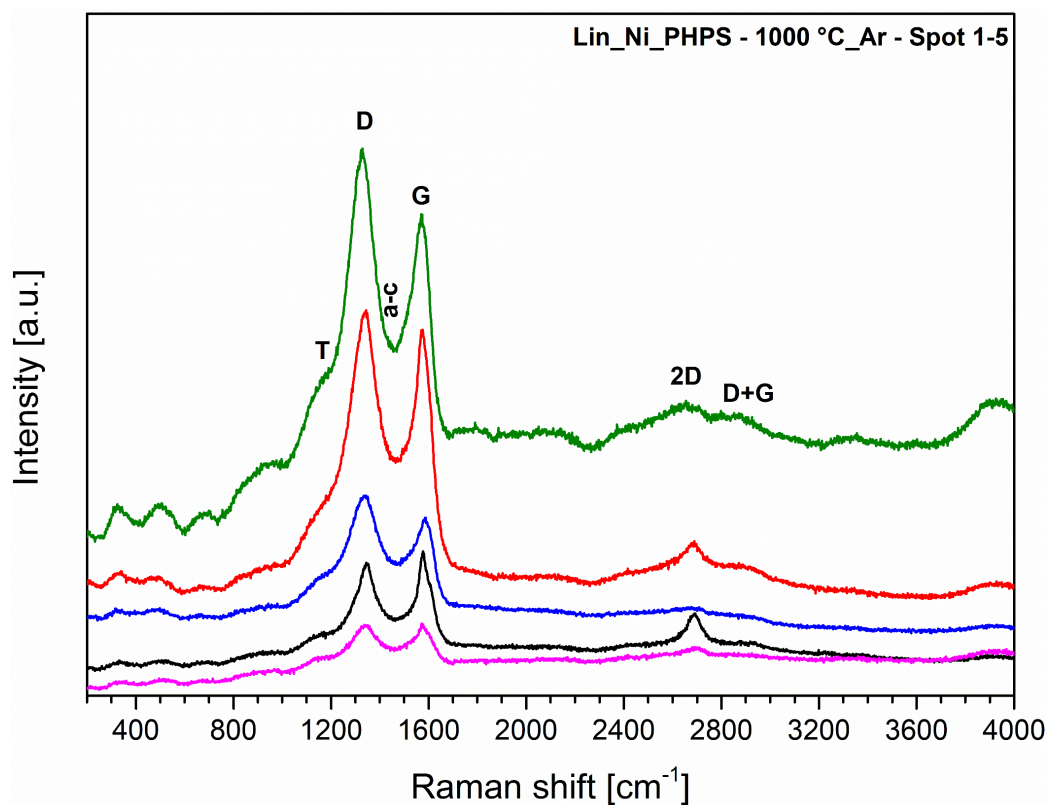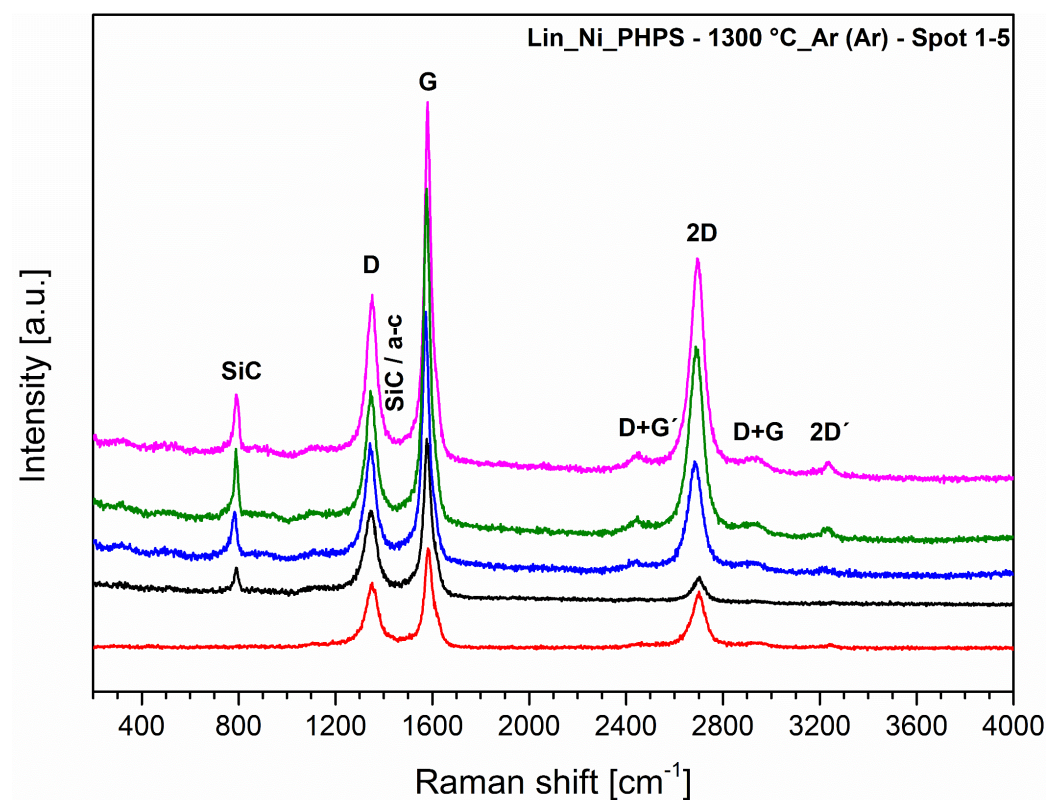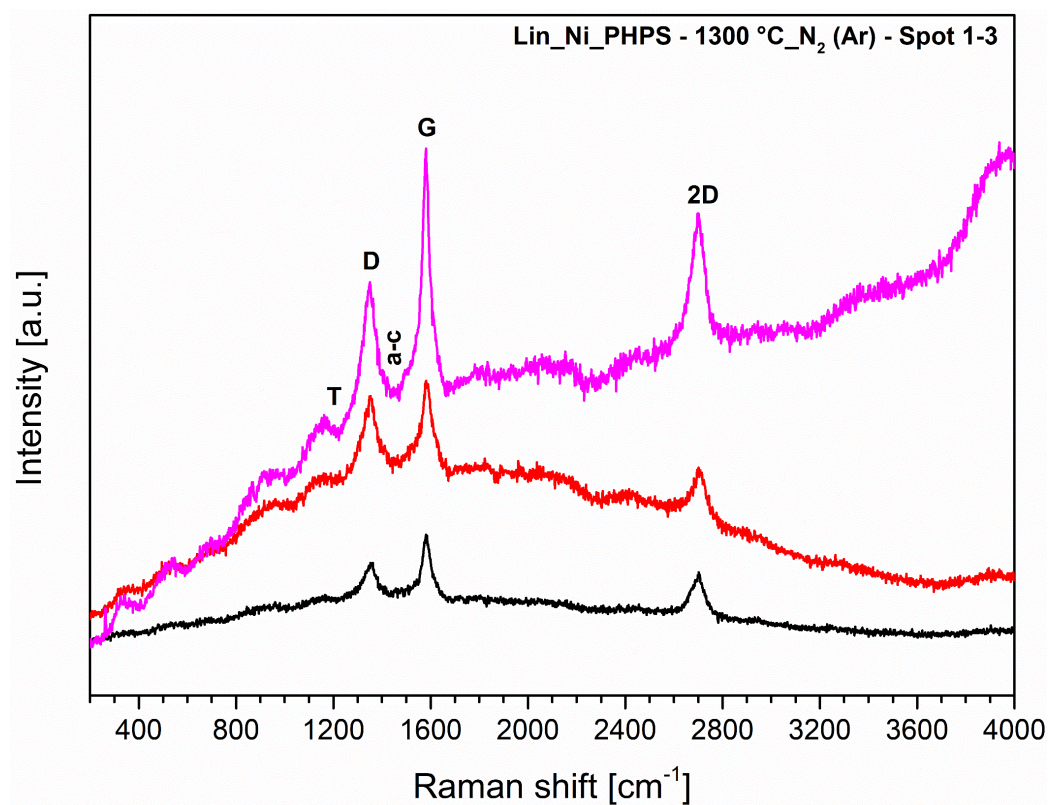
Figure 48. μ-Raman spectra of the Lin_Ni_PHPS ceramic papers annealed at (a) 1000 °C in Argon, (b) 1300 °C in Ar (previously at 1000 °C in Ar) and (c) 1300 °C in N_2 (previously at 1000 °C in Ar)

Table 18. Calculated characteristic parameters from Raman spectroscopy (including mean values and standard deviation) of nickel(II)-PHPS-modified Lin templates in different atmospheres and temperatures

Sample	A_D/A_G	A_{2D}/A_D	L_a (nm)	L_D (nm)	L_{eq} (nm)	n_D (x 10^{11}, cm^{-3})
Lin_Ni_PHPS-1000 °C Ar	3.66±0.76	0.25±0.08	4.82±1.17	5.97±0.70	19.58±6.42	12.6±2.62
Lin_Ni_PHPS - 1300 °C Ar (Ar)	0.75±0.12	1.20±0.57	22.95±3.52	13.08±1.01	92.50±43.78	2.57±0.40
Lin_Ni_PHPS - 1300 °C N_2 (Ar)	0.97±0.10	1.33±0.11	17.38±1.93	11.40±0.62	102.72±8.19	3.35±0.35

4.4.2 Si-Ni-C-(N) – Influence of Argon Atmosphere

Interestingly, the FTIR spectrum of the as-prepared Ni(II)-modified Dur sample (Figure 49 (a)) shows also no Si-H band (similarly to Pd(II)-modified Dur (Figure 43 (a)), indicating that the reaction took place at this bond. Figure A 6 in the Appendix shows a possible reaction. Otherwise, the following bands are present: C-O (1253 cm^{-1}), C=C (1514 cm^{-1}), C=O (1565 cm^{-1}) and C-H (2844 cm^{-1} and 2920 cm^{-1}). Pyrolysis at 1000 °C in Ar leads to the formation of one broad and a smaller Si-O-Si band (452 cm^{-1} and 970 cm^{-1}). At 1300 °C, one sharp Si-C band (805 cm^{-1}) is visible, showing that Si-C has formed. Contrary to Ar, in N$_2$ Si-N-Si vibrations occur (from 490 cm^{-1} to 1035 cm^{-1}), pointing to the formation of Si$_3$N$_4$. Comparing the FTIR structure of the nickel-modified ceramic paper (Figure 49 (b)), shows a similar bonding situation, although the Si-O-Si (460 cm^{-1}, 800 cm^{-1}, 1080 cm^{-1} and 1204 cm^{-1}) and the Si-C (800 cm^{-1}) vibrations in the 1000 °C and 1300 °C samples are more distinct, indicating a more ordered structure. Additionally, an O-H band (3430 cm^{-1}) in the 1000 and 1300 °C samples, annealed in Ar and N$_2$ respectively is present.

(a)
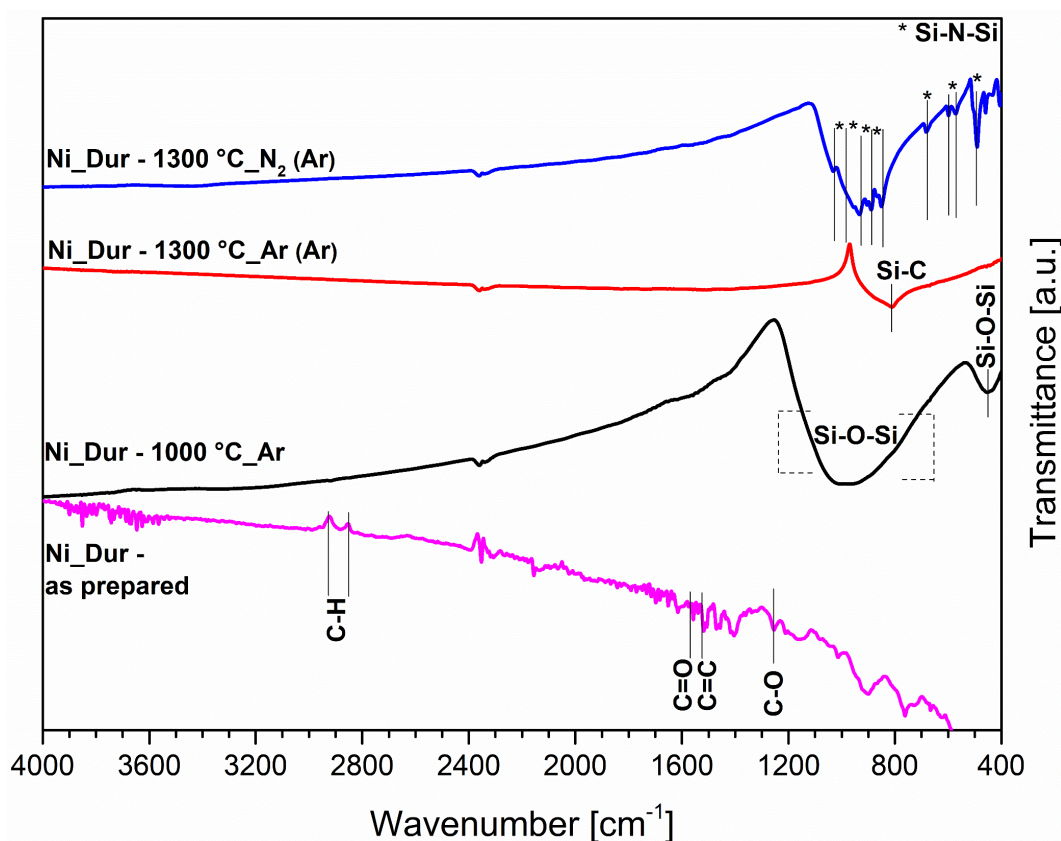
(b)
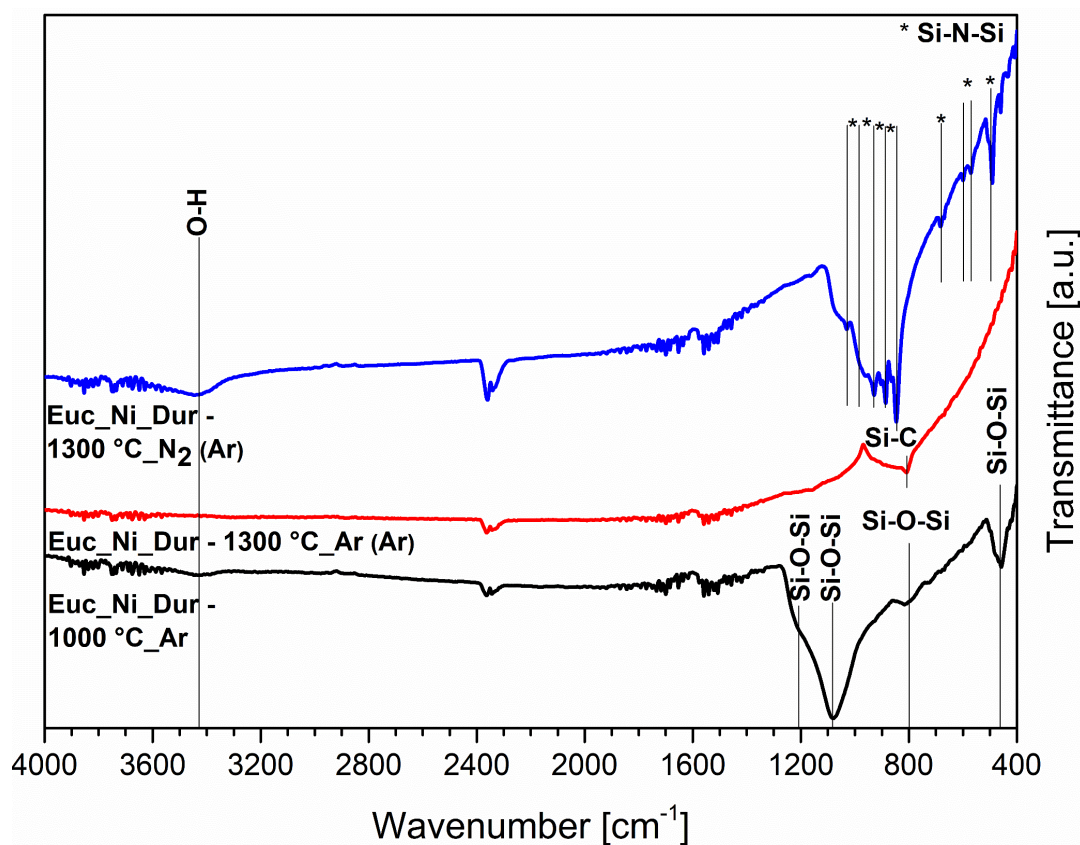
Figure 49. FTIR spectra of nickel(II)-modified Dur in the (a) precursor state and (b) with the template at different temperatures

Looking into the XRD spectra of the nickel(II)modified Dur precursor (Figure 50 (a)) at 1000 °C in Ar, Ni (space group P63/mmc, (194)) and Ni_2Si (space group Pbnm, (62)) crystalline phases appear. At 1300 °C, an additional β-SiC phase (space group $F\bar{4}3m$, (216)) is formed. In N_2 on the other hand, crystalline β-Si_3N_4 (space group P31c, (159) and (space group P63/m, (176))) appears instead of β-SiC. By using the Eucalyptus template (Figure 50 (b)), the XRD pattern is quite featureless, indicating the amorphous nature of the material, but the beginning of crystallization at 1300 °C in Ar and N_2 is visible with β-SiC and β-Si_3N_4 / Ni_2Si phases respectively. It is assumed that similar reactions, as described in chapter 4.4.1 (equations Eq. 25 – Eq. 27), take place in the case of the Dur precursor.

(a)
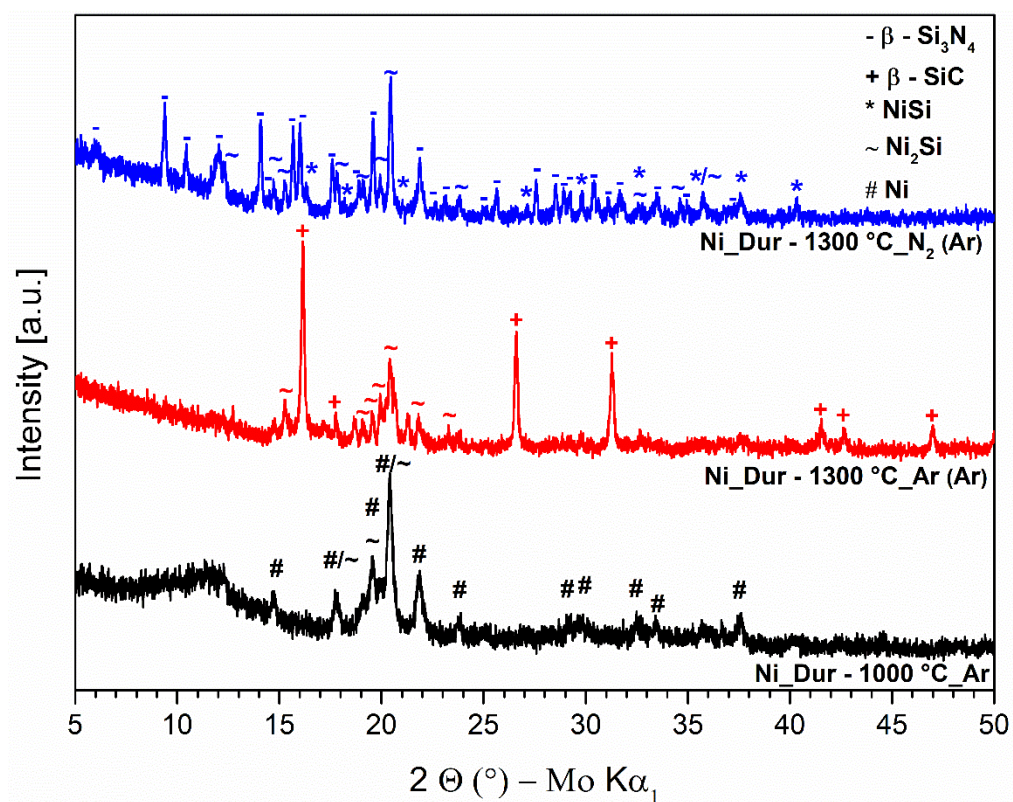
(b)
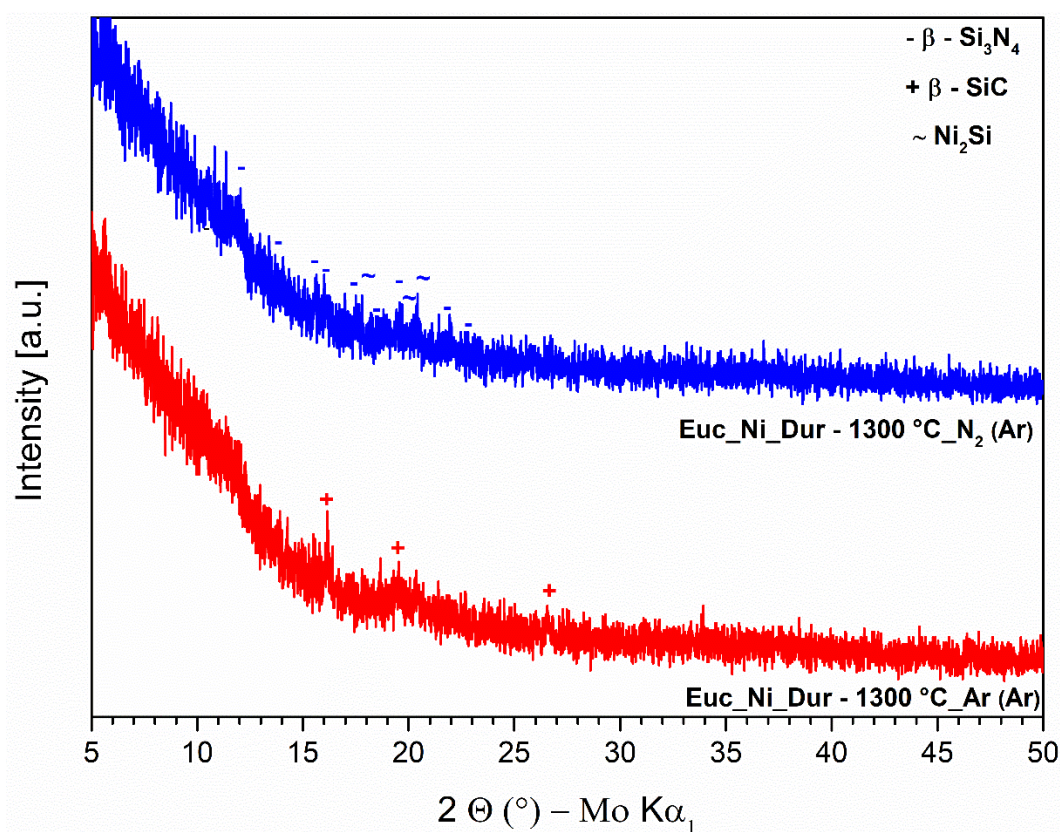
Figure 50. X-ray diffraction patterns of the nickel(II)-modified polysilazane (Dur) precursor depicted in (a), the ceramic paper shown in (b), pyrolyzed at 1000 and 1300 °C in Ar and N_2, depending on the temperature

The characteristic parameters calculated from the fitted Raman spectra are shown in Table 19. With higher annealing temperatures, the A_D/A_G, L_a and L_{eq} rise due to the graphitization of the (turbostratic) carbon. This can be also seen, when comparing the 2D band (2688 cm^{-1}) of the sample pyrolyzed at 1000 °C and 1300 °C in Ar, as it becomes more distinct and sharper (Figure 51 (a) and (b)). The SiC band in the latter sample is almost not visible, indicating less SiC formation. This is in congruence with the XRD Data. Here, the sample annealed at 1300 °C in N_2 (Figure 51 (c)) has a higher graphitization, compared to the sample annealed in Ar, which is not only visible from the more distinct 2D band, but also the much higher L_a and A_{2D}/A_D values.

(a)

(b)

(c)
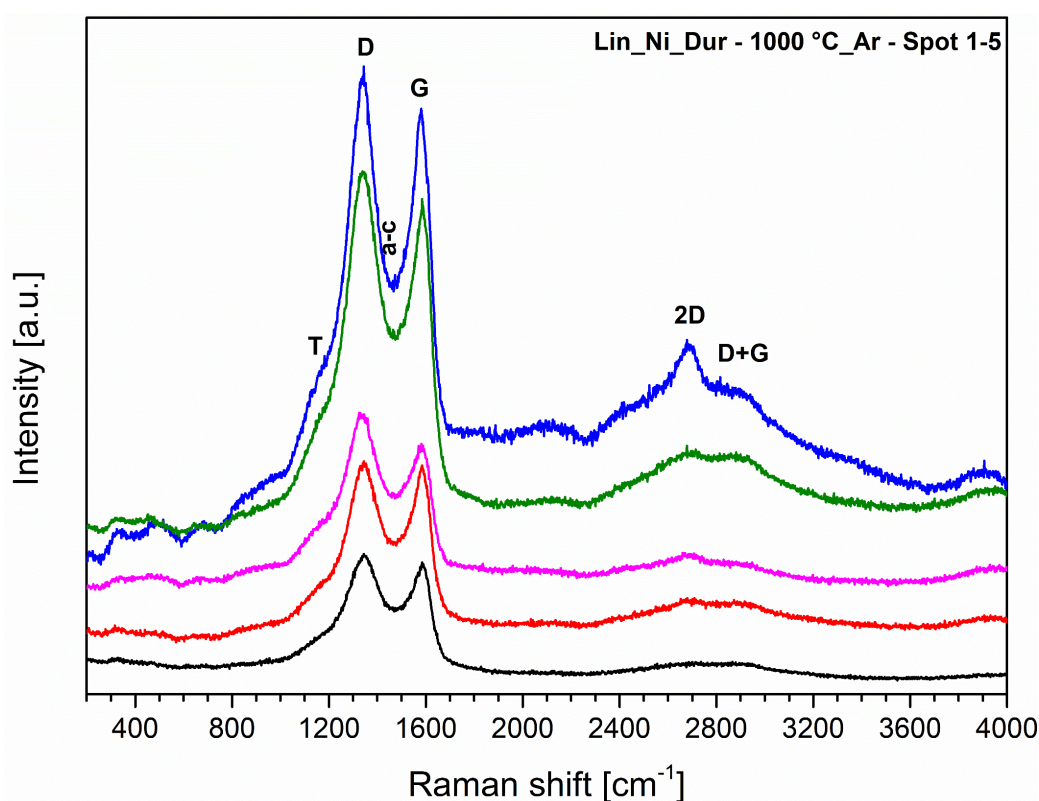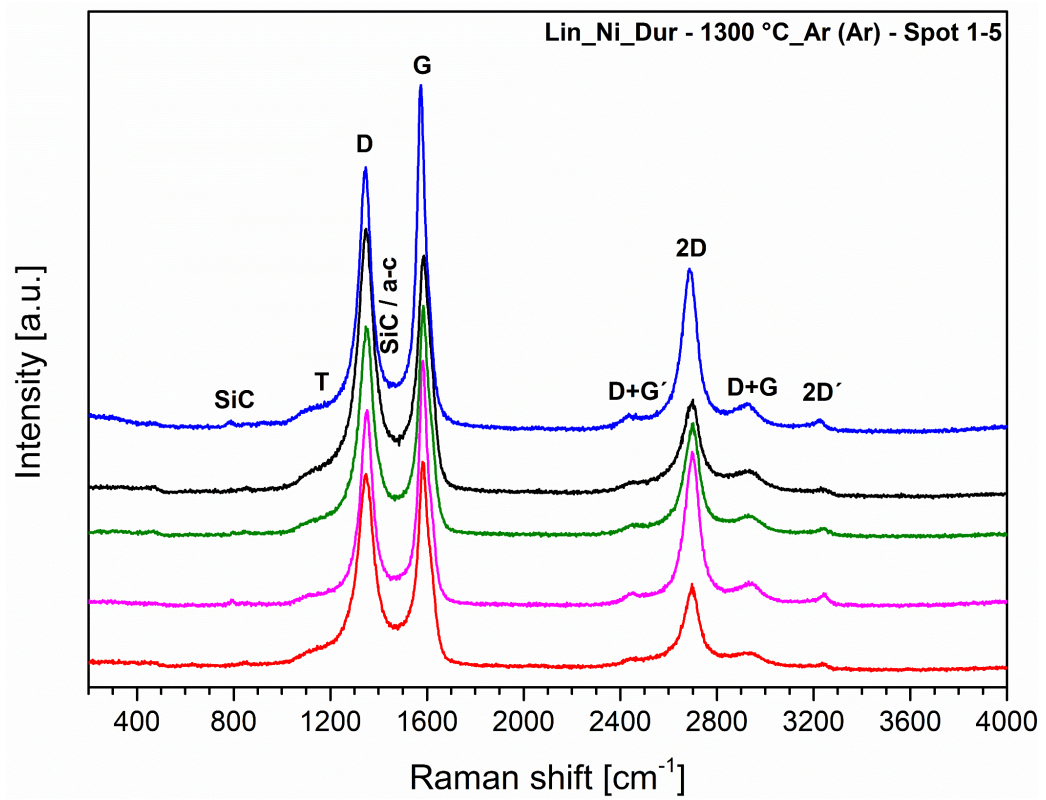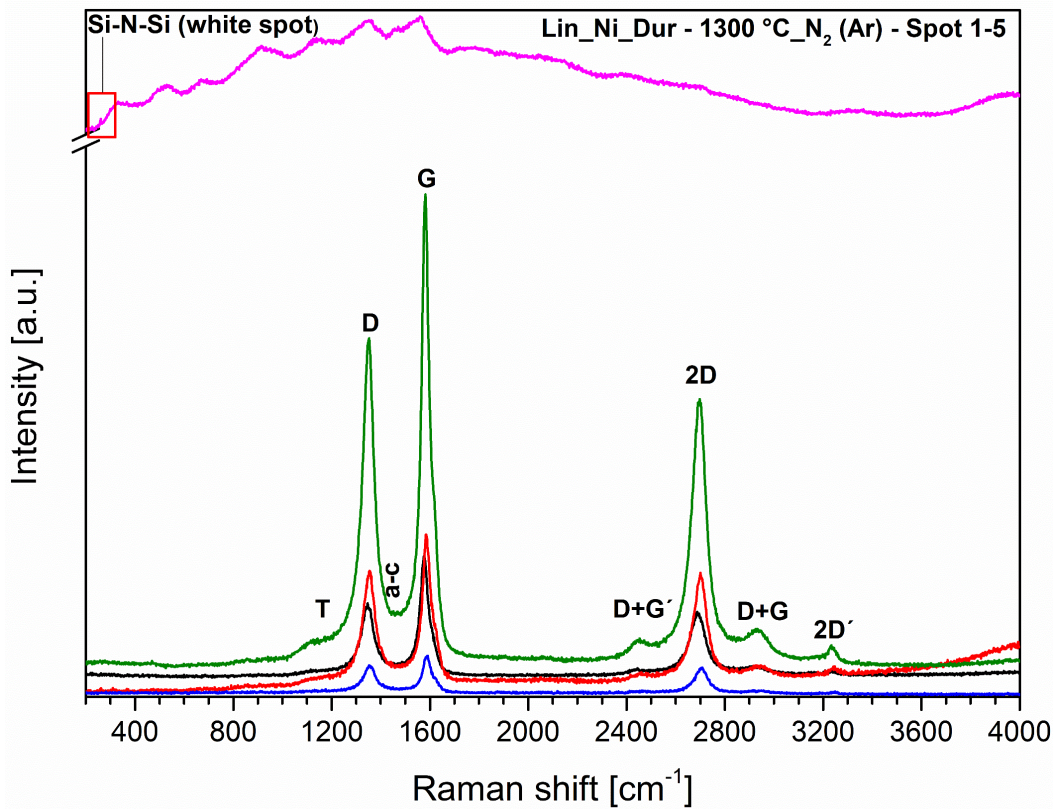
Figure 51. μ-Raman spectra of the Lin_Ni_Dur ceramic papers annealed at (a) 1000 °C in Argon, (b) 1300 °C in Ar (previously at 1000 °C in Ar) and (c) 1300 °C in N₂ (previously at 1000 °C in Ar)

Table 19. Calculated characteristic parameters from Raman spectroscopy (including mean values and standard deviation) of the nickel(II)-Dur-modified Lin templates in different atmospheres and temperatures

Sample	A_D/A_G	A_{2D}/A_D	L_a (nm)	L_D (nm)	L_{eq} (nm)	n_D (x 10^{11}, cm^{-3})
Lin_Ni_Dur-1000 °C Ar	3.95±0.26	0.18±0.06	4.26±0.28	5.65±0.18	13.95±4.37	13.60±0.88
Lin_Ni_Dur - 1300 °C Ar (Ar)	1.49±0.50	0.61±0.23	12.48±3.70	9.56±1.49	46.65±17.35	5.12±1.71
Lin_Ni_Dur - 1300 °C N_2 (Ar)	0.95±0.06	1.04±0.03	17.80±1.21	11.55±0.39	79.99±2.09	3.25±0.22

4.4.3 Comparison Batch 1 and 2

The influence of the dilution of the Ni(II)-acetylacetonate modified PHPS solution in toluene and therefore the differences between Batch 1 and 2 are shown in the photographs of the dip-coated Ni(II)-acetylacetonate modified PHPS-based templates (Figure 52) below.

It can be seen, that the coating of the cellulose-based template in Batch 1 is not homogeneous and has bigger agglomerations on top. This leads to the localized formation of the above-mentioned phases.

(a)   **(b)**
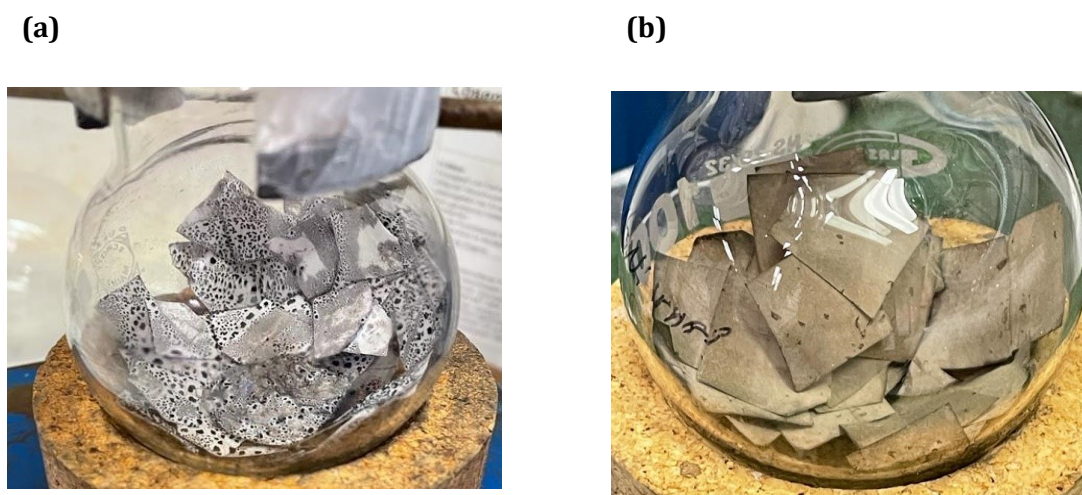
Figure 52. Photographs of the dip-coated and vacuum dried Ni(II)acetylacetonate modified PHPS-based templates of (a) Batch 1 and (b) Batch 2 before pyrolysis

4.4.4 Summary Si-Ni-system

The main differences between the usage of PHPS and Dur precursor, based on FTIR results can be summarized as follow: in PHPS in the precursor state, the nickel(II)acetylacetonate appears to bond to the Si-H group (Figure 46 (a)). In Durazane this is more apparent, as the latter disappears in the FTIR spectrum (Figure 49 (a)). Furthermore, a hydrosilylation reaction can also occur, as shown in the appendix in Figure A 6. Otherwise, similar bands appear independent of the precursor taken: Si-O-Si at 1000 °C in Ar, Si-C at 1300 °C in Ar and Si-N-Si at 1300 °C in N_2. The influence of the cellulose template is insignificant and does not affect the above-mentioned bonds, even though they are more pronounced.

In XRD, the precursor (PHPS or Dur) has a small influence on the presence of the crystalline phase composition: In Ar at 1000 °C in PHPS, Ni and Ni_2Si are present. Further annealing produces β-SiC and additionally, NiSi was identified. Changing the atmosphere to N_2 promotes the crystallization of β-Si_3N_4, Ni_2Si and NiSi. While Dur appears to have similar phases in Ar at 1000 °C, at a higher temperature only Ni_2Si and β-SiC could be identified. However, in N_2 the phases were comparable with the PHPS sample. When using the two precursors in the ceramic template (Figure 47 (b) and Figure 50 (b)), it appears that using PHPS, independently of the atmosphere, promotes the crystallization of the different phases more than Dur. An additional carbon phase could be identified only in the Euc_Ni_PHPS – 1300 °C_ Ar (Ar) sample, hinting toward the graphitization of the cellulose-based template.

Raman spectroscopy showed in the Lin_Ni_PHPS – 1300 °C Ar (Ar) sample the highest graphitization of carbon, based on the L_a, L_{eq} and A_{2D}/A_D values. This could be due to the still available Ni-phase at 1000 °C, which promotes the transformation of amorphous into graphitic carbon. Otherwise, a similar trend occurs independently of the polymeric precursor: higher annealing temperature proceeds the graphitization of the cellulose-based template. Chen et al. showed, that Ni can be used as a catalyst to produce graphitic cellulose [117], which is in agreement with the presented results.

4.5 Summary Transition Metals and Atmosphere

In this chapter, the influences of the transition metals (Fe, Pd, Ni) and the atmospheres on the phase composition will be discussed. Figure 53 shows a summary of the previous results. Note that for the ammonolyzed samples only the results from 1000 °C and upwards are shown.

The FTIR analysis showed, that independently of the transition metal, Si-O-Si (1000 °C, NH_3 and Ar), SiC (1300 °C Ar) and Si-N-Si (1300 °C, N_2) bands have been identified, which were quite similar with respect to band structure. Raman spectroscopy showed that the transition metal (Fe, Pd, Ni) promotes the graphitization of the cellulose-based paper at low temperatures (at 1000 °C already), which has also been shown in many previous studies [117–119]. When comparing the characteristic parameters from the fitted Raman spectroscopy, the highest graphitization of the carbon phase at 1000 °C in Ar was reached with the combination of Fe and Dur precursor in the Lin-cellulose-based paper. At 1300 °C in Ar the Ni-PHPS system had the highest in-plane crystallite size (L_a) pointing to the highest graphitization of the carbon. While L_a in N_2 at 1300 °C Ni-Dur and Ni-PHPS were similar. Fe and Ni showed a higher degree of graphitization of the carbonized fiber compared to Pd. Furthermore, the transition metals not only promote the graphitization of the cellulose but also catalyze at higher temperatures (1300 °C) - besides the formation of silicides - additional β-Si_3N_4 and SiC phases in N_2 and Ar atmospheres, which have also been shown in various studies [90, 108, 120–122]. The polysilazane (PHPS and Dur) appears to have a limited influence on the crystalline phases, as in some cases, for instance in the Ni_PHPS_1300 °C Ar (Ar) sample, only additional phases appear with PHPS. On the other hand, the ammonia atmosphere promotes the formation of ε-Fe_2N, which is not present when Ar atmosphere is used. Additionally, the usage of polysilazane protects the cellulose-based template from decomposition, as it forms a thin coating on top of it. This is especially visible in the TGA analysis in the ammonia atmosphere, where the mass loss without coating is 100 %. The type of template (Sar, Lin, Euc) appears to have an insignificant influence on the crystalline phases and the graphitization process, as it occurs independently of it. SEM images of the Lin_Fe_Dur-1300 °C Ar (Ar) and the Lin_Fe_Dur-1300 °C N_2 (Ar) sample showed, that depending on the atmosphere different Si-based phases are formed and despite high temperatures, the cellulose-based template does not decompose.

The functionalized ceramic papers with their different crystalline phases and graphitized templates are candidates for various possible applications, which will be discussed in chapter 5.

Raman [nm]:

XRD:

FTIR:

Fe

PHPS — NH$_3$ — 1000 °C
- Ar — 1300 °C — Si-O-Si; Si-O-Fe; N-H — α-Fe; ϵ-Fe$_2$N — L$_a$: 3.08 / L$_{eq}$: 9.11
- N$_2$ — 1300 °C — Si-N-Si; O-H — α-Fe; β-Si$_3$N$_4$; Si$_2$N$_2$O — -

Dur — NH$_3$ — 1000 °C
- Ar — 1300 °C — Si-O-Si; Si-O-Fe; O-H — α-Fe; ϵ-Fe$_2$N — -
- N$_2$ — 1300 °C — Si-N-Si; Si-O-Si — α-Fe; Fe$_3$Si; β-Si$_3$N$_4$; Si$_2$N$_2$O — -

PHPS — Ar — 1000 °C
- Ar — 1300 °C — Si-C; Si-N-Si — FeSi; β-SiC — L$_a$: 12.75 / L$_{eq}$: 39.12
- — Si-O-Si — α-Fe; Fe$_3$Si — L$_a$: 6.24 / L$_{eq}$: 17.43
- N$_2$ — 1300 °C — Si-N-Si — β-Si$_3$N$_4$; Fe$_3$Si; α-Fe — L$_a$: 12.00 / L$_{eq}$: 36.25

Dur — Ar — 1000 °C
- Ar — 1300 °C — Si-C — β-SiC; α-Fe; Fe$_3$Si — L$_a$: 13.54 / L$_{eq}$: 47.32
- — Si-O-Si — α-Fe; Fe$_3$Si — L$_a$: 6.87 / L$_{eq}$: 17.33
- N$_2$ — 1300 °C — Si-N-Si — β-Si$_3$N$_4$; Fe$_3$Si; α-Fe — L$_a$: 11.88 / L$_{eq}$: 62.05

Pd

PHPS — Ar — 1000 °C
- Ar — 1300 °C — Si-C; Si-N-Si — Pd$_2$Si; PdSi; β-SiC — L$_a$: 4.18 / L$_{eq}$: 24.64
- — Si-O-Si — Pd$_2$Si — L$_a$: 4.18 / L$_{eq}$: 11.63
- N$_2$ — 1300 °C — Si-N-Si — Pd$_2$Si; β-Si$_3$N$_4$ — L$_a$: 6.58 / L$_{eq}$: 19.27

Dur — Ar — 1000 °C
- Ar — 1300 °C — Si-C — Pd$_2$Si; β-SiC — L$_a$: 12.80 / L$_{eq}$: 67.71
- — Si-O-Si — Pd$_2$Si — L$_a$: 3.86 / L$_{eq}$: 18.89
- N$_2$ — 1300 °C — Si-N-Si — Pd$_2$Si; β-Si$_3$N$_4$ — L$_a$: 7.71 / L$_{eq}$: 20.50

Ni

PHPS — Ar — 1000 °C
- Ar — 1300 °C — Si-C — Ni; NiSi; Ni$_2$Si; β-SiC; (C) — L$_a$: 22.95 / L$_{eq}$: 92.50
- — Si-O-Si — Ni; Ni$_2$Si — L$_a$: 4.82 / L$_{eq}$: 19.58
- N$_2$ — 1300 °C — Si-N-Si — NiSi; Ni$_2$Si; β-Si$_3$N$_4$ — L$_a$: 17.38 / L$_{eq}$: 102.72

Dur — Ar — 1000 °C
- Ar — 1300 °C — Si-C — Ni; NiSi; Ni$_2$Si; β-SiC — L$_a$: 12.48 / L$_{eq}$: 46.65
- — Si-O-Si — Ni; Ni$_2$Si — L$_a$: 4.26 / L$_{eq}$: 13.95
- N$_2$ — 1300 °C — Si-N-Si — NiSi; Ni$_2$Si; β-Si$_3$N$_4$ — L$_a$: 17.80 / L$_{eq}$: 79.99

Figure 53. Overview of the influence of the transition metals, polysilazanes, atmospheres and temperatures on the FTIR, XRD and µ-Raman spectrum (characteristic values, L$_a$ and L$_{eq}$ are shown excluding standard deviation values)

5. Applications

This chapter focuses on possible applications of the different ceramic papers. As the samples are larger in dimension for the measurements, the synthesis method was adapted, as described in chapter 3.1.2. First, the results of HER and OER measurements will be shown, followed by the electromagnetic shielding measurements.

5.1 Hydrogen Evolution (HER) and Oxygen Evolution Reaction (OER)

For the electro-catalytical tests the following samples were used:

I. Linters pristine template pyrolyzed at 1000 °C in Ar (Lin_1000 °C-Ar)

II. Linters pristine template pyrolyzed at 1000 °C and annealed at 1300 °C in Ar (Lin_1300 °C Ar (Ar))

III. Linters template impregnated with Ni and pyrolyzed at 1000 °C in Ar (Lin_Ni-1000 °C Ar)

IV. Linters template impregnated with Ni pyrolyzed at 1000 °C and annealed at 1300 °C in Ar (Lin_Ni-1300 °C Ar (Ar))

V. Linters template impregnated with Ni and Dur and pyrolyzed at 1000 °C in Ar (Lin_Ni_Dur-1000°C Ar)

VI. Linters template impregnated with Ni and Dur pyrolyzed at 1000 °C and annealed at 1300 °C in Ar (Lin_Ni_Dur-1300°C Ar (Ar))

Before and after the electro-catalytical tests, the samples were analyzed with the help of FTIR and Raman spectroscopy. The results are shown in the Appendix in Figure A 7 to Figure A 9 and Table A 2 as well as Table A 3 summarizes the characteristic parameters from Raman spectroscopy. The FTIR spectra (Figure A 7) shows, that the cyclic voltammetry does not influence the bonding situation of the tested samples, as no new bands appear. Also, the Raman spectroscopy shows similar bands compared to the previous results. The addition of Ni into the cellulose-based sample promotes graphitization, which has already been discussed in chapter 4.5 before. Evaluation of the characteristic parameters shows a similar trend, as A_{2D}/A_D and L_a is much higher in the Lin_Ni samples as compared to the pure Lin samples (0.37 vs. 0.12 for A_{2D}/A_D and 4.70 vs 8.44 for L_a at 1000 °C; Table A 2). Interestingly, the characteristic parameters of the Lin_Ni sample (Table A 2 and A 3) show that the electro-catalytic tests influenced the graphitization, as after the tests the calculated values of L_a and L_D were higher for both temperatures.

Figure 54 shows the electro catalytic measurements of the samples pyrolyzed at 1000 °C (a) and 1300 °C (b) after conditioning (CV 2). The measurements at 1000 °C (Figure 54 (a)) show a broad CV curve, which becomes narrower in the impregnated samples pyrolyzed at 1300 °C in Ar. Independent of the temperature, the cellulose-based paper had the lowest performance in the OER region, as it reached current densities of around 2 mA/cm². The best performance at 1000 °C

was reached by the paper, which was only impregnated with nickel (9.19 mA/cm^2), while at 1300 °C the Lin_Ni_Dur composite reaches the highest values (8.71 mA/cm^2). Furthermore, with each cycle, the performance increases slightly (indicated by the arrows).

The Tafel slope (Figure 54 (c) and (d)) indicate a similar trend, as Lin_Ni and the Lin_Ni_Dur show higher slopes compared to the carbonized Lin paper. Lü et al. [123] impregnated carbon paper with Strontium-doped lanthanum manganite and performed electrocatalytic tests and achieved similar results regarding the current densities.

(a)
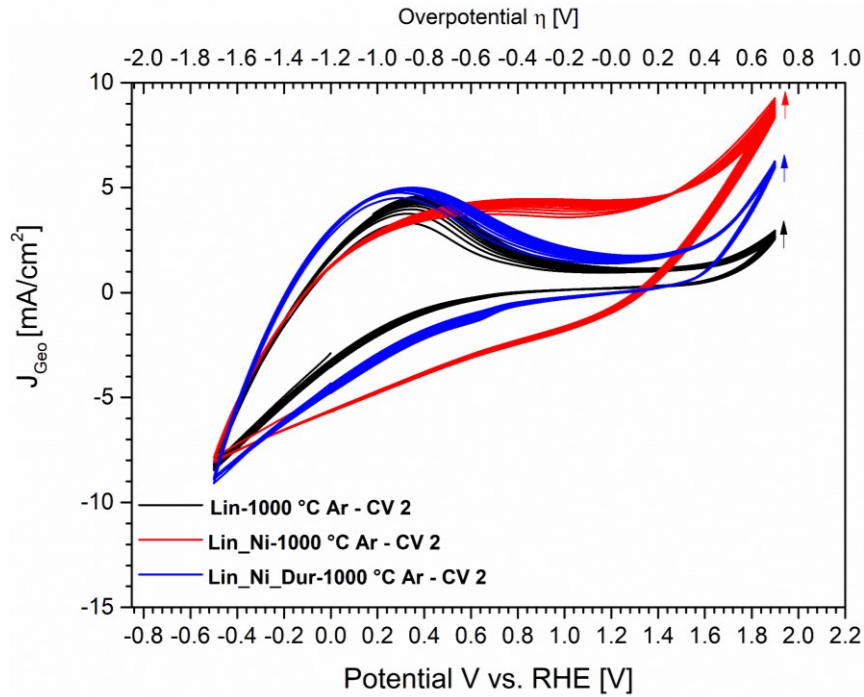
(b)
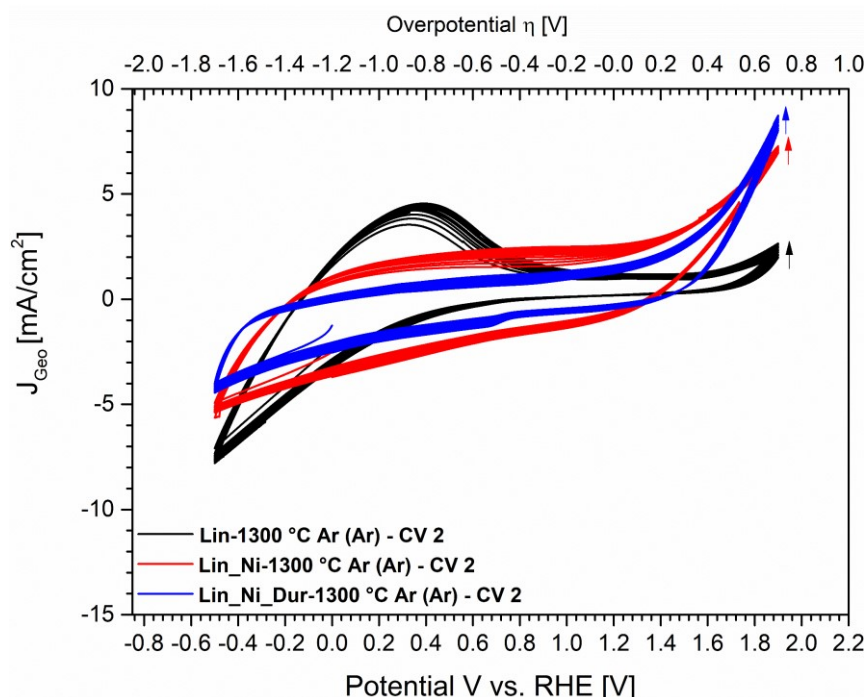
(c)
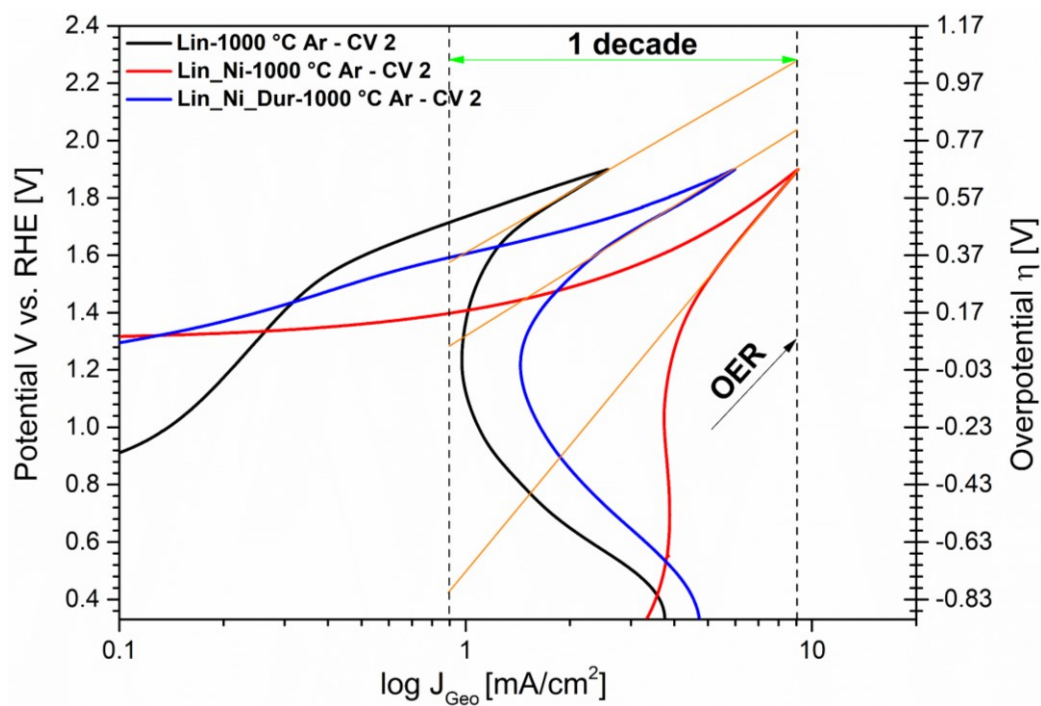
(d)
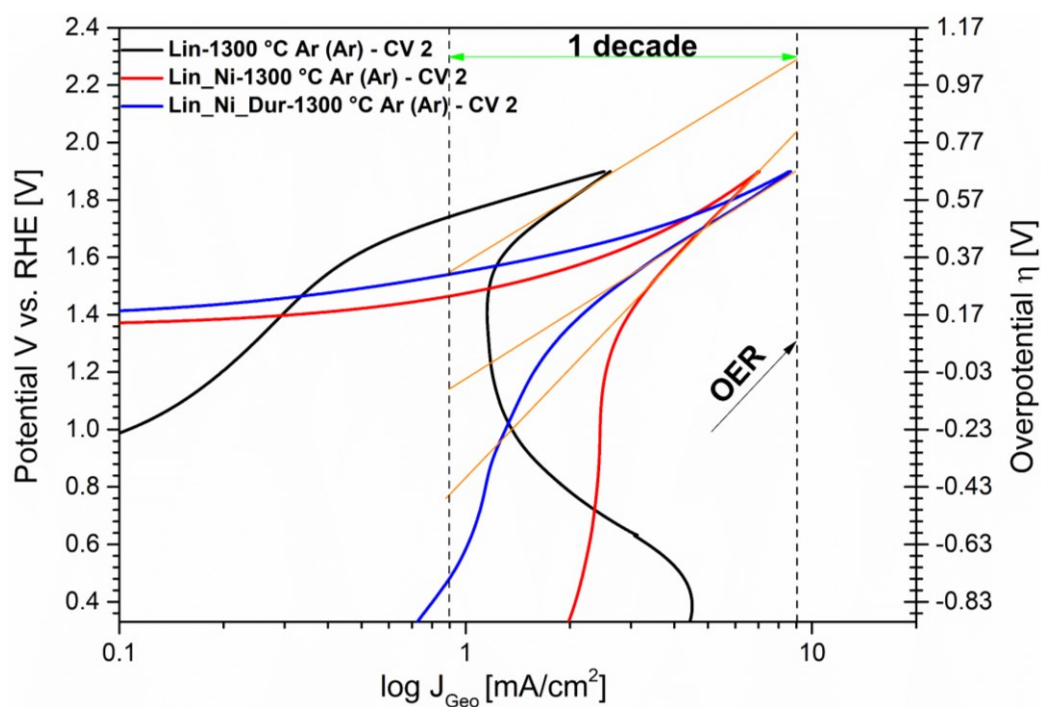
Figure 54. Cyclic voltammetry measurements of the different (ceramic) paper compositions pyrolyzed at (a) 1000 °C and (b) 1300 °C in Argon. (c) and (d) shows the respective Tafel slopes in the J value range from 0.9 mA/cm² to 9 mA/cm² (1 decade)

Ren and Antonietti et al. [124] used a cellulose filter paper and first infiltrated it with nickel acetate (nickel source) and phenanthroline (ligand and nitrogen source) before carbonization at 800 °C. The as-produced catalyst showed a low onset potential (330 mV vs reversible hydrogen electrode) and high current densities (e.g., $J > 25$ mA/cm^2 at $\eta = 430$ mV). Those results are much higher than the results from this study, but it has to be taken into account, that here the weight percentage of Ni is only about 2 wt % compared to 10 wt % used in that study.

From the electrocatalytic measurements, it becomes clear, that the catalytic active material is Ni, which is also present in the ceramic composite (Lin_Ni_Dur, see Figure 53). Therefore, the possible reactions of Ni from the cyclic voltammetry can be deduced from the Pourbaix diagram, which is shown in Figure 55 (a). At pH 14, the possible phases are – depending on the electrode potential – Ni, nickel(II)oxide (NiO), nickel(III)oxyhydroxide (NiOOH) and nickel(IV)oxide (NiO$_2$). The water oxidation refers to equation Eq. 9 from Chapter 2.4.1.

(a)

(b)
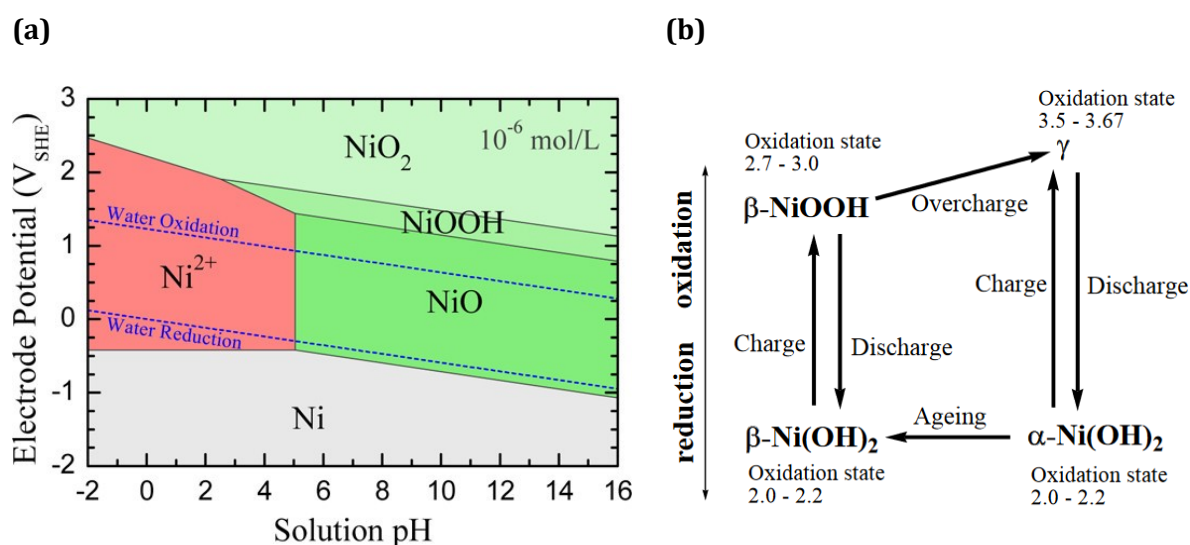
Figure 55. Pourbaix diagram of Nickel in water [125] (a) and Bode scheme for the redox reaction of Ni(OH)$_2$ and NiOOH [126, 127] in (b)

By immersing the ceramic paper in the KOH, it is assumed that NiOOH phases are generated. Various studies suggested [127–130], that mainly β-Ni(OH), β-NiOOH, γ-NiOOH and α-Ni(OH)$_2$ participate in the redox reaction. Bode and Dehmelt et. al. suggested a scheme (Figure 55 (b)) for possible reactions at different potentials.

In conclusion, it was possible to perform catalytic HER/OER measurements with a custom-made setup and without the usage of additional membranes like Nafion™ or support templates like glass-like carbon. Instead, a partially graphitized cellulose-based template was used, which performance lies at around 2 mA/cm² independent of the pyrolysis temperature. This is comparable with the performance of glass-like carbon, which is between 2 to 4 mA/cm², depending on the used electrolyte [131]. The study showed, that Ni enhanced the performance to around 9 mA/cm² at 1000 °C and that the addition of Dur lowers it. At 1300 °C both Lin-paper-based samples (with only Ni and with Ni-Dur) had similar performances with around 6 to 7 mA/cm². It could be concluded, that mainly Ni/its derivates act as the active material, and based on the Tafel slopes the performance worsens if Dur is added. A possible reason for this is the formation of the SiC phase (chapter 4.4.2), which hinders the catalytic activity of the Ni.

5.2 Electromagnetic Shielding (EMS)

The equation for the total shielding was already shown in equation Eq. 15. Considering that the thickness of the ceramic paper is higher than the penetration depth, it can be rewritten as equation Eq. 28 below [69]:

$$SE_T \text{ (dB)} = SE_A + SE_R \qquad \textbf{(Eq. 28)}$$

As for this work, the scattering parameters were measured by a vector analyzer in the waveguide method. The total shielding can be calculated from those parameters (T = transmission and R = reflection), according to equations Eq. 29, Eq. 30 and Eq. 31 [69, 132]:

$$SE_R \text{ (dB)} = -10 \times \log_{10}(1-R) \qquad \textbf{(Eq. 29)}$$

$$SE_A \text{ (dB)} = -10 \times \log_{10}(T/(1-R)) \qquad \textbf{(Eq. 30)}$$

$$R = |S_{11}|^2 = |S_{22}|^2, \ T = |S_{21}|^2 = |S_{12}|^2 \qquad \textbf{(Eq. 31)}$$

Generally, the different parameters (R, A, and T) describe the ability of a material to reflect, absorb or transmit an electromagnetic wave. The total shielding of a sample depends on these three parameters (see chapter 2.4.2) and describes the performance of a material over a defined frequency. The higher the value over a large range, the better its performance. The results of the electromagnetic shielding experiments for Pd and Ni samples are shown in Figure 56. For the measurement one to four pieces of synthesized ceramic papers, with a total thickness between 0.2 mm and 1.2 mm, were stacked, to amplify the EMS effect. Figure 56 (a) shows the total electromagnetic shielding value of the Lin_Ni_Dur-1000 °C_Ar sample. Over the whole studied frequency range (from 8.2 to 12.5 GHz, the so-called X band) the EMS is constant, meaning, that the sample exhibit no frequency, which has characteristically high shielding values. Other composites, like ultrathin Mo_2C films on graphene layers, which were synthesized by Liu et al. [64], exhibited higher total shielding values in the range of 9.5 to 10 GHz (up to 48 dB). Stacking two samples, increase the thickness and therefore the ability to shield against the electromagnetic waves, due to the longer pathway (Figure 5) and therefore rises the effectiveness by about 37 %, compared to only one sample. Changing the transition metal from Ni to Pd (Figure 56 (b)) has an insignificant effect on the total SE, as both are comparable with each other. This is due to the similar phase composition of both ceramic papers: Pd_2Si, Ni / Ni_2Si, and

amorphous SiO_2 are present in both samples at 1000 °C. Further annealing of the Lin_Pd_Dur ceramic paper at 1300 °C leads to an increase of the SE_T to around 30 dB. This is due to the formation of additional crystalline phases, like SiC, which increases the total shielding. Furthermore, the graphitization of the cellulose template increases the conductivity of the system.

(a)

(b)
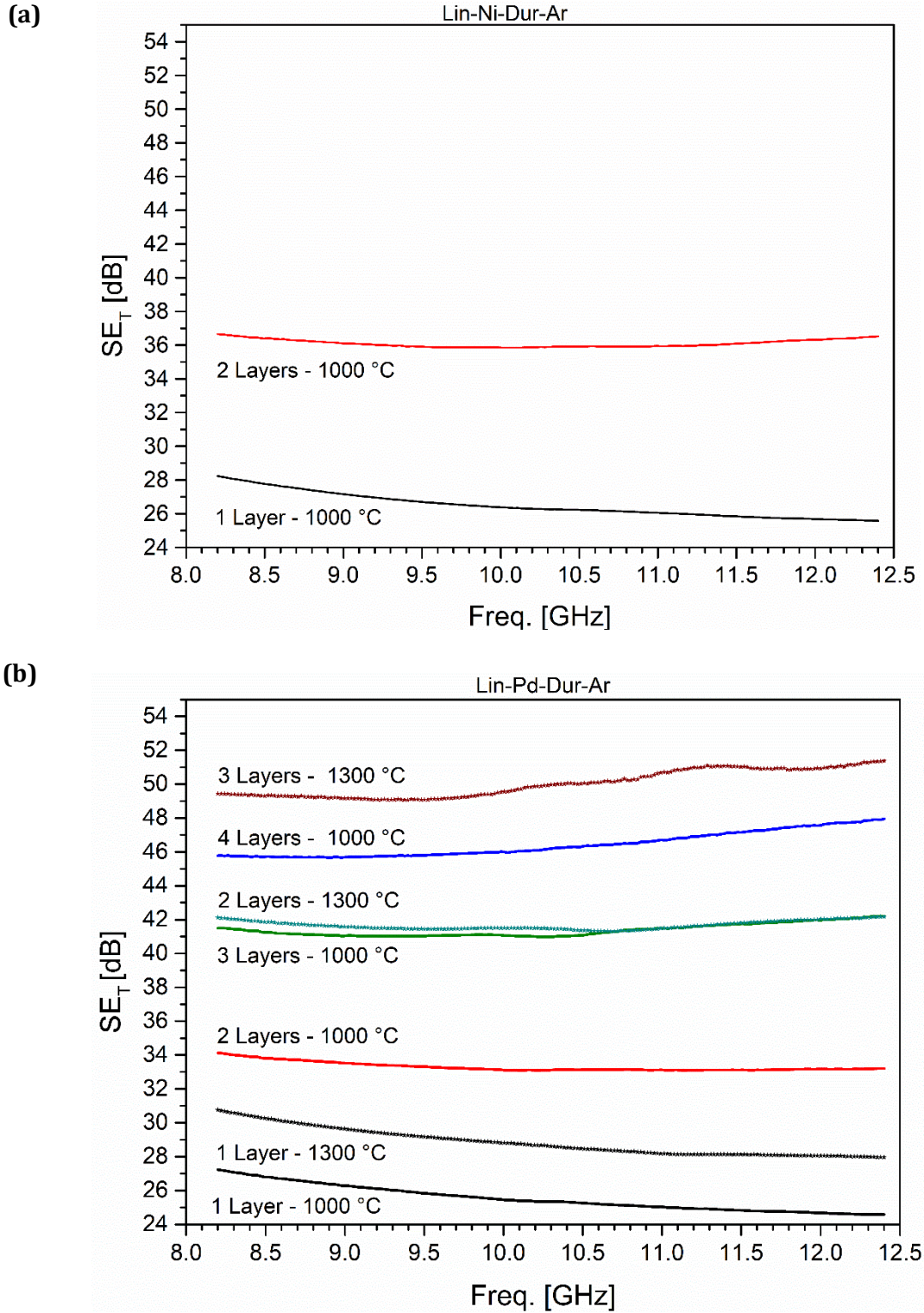
Figure 56. Electromagnetic shielding results from (a) Lin_Ni_Dur-Ar and (b) Lin_Pd_Dur-Ar pyrolyzed at different temperatures and with multiple layers

For the EMS, the best performance was reached by stacking three Lin_Pd_Dur samples, which were previously annealed at 1300 °C in Ar (50 dB). Comparing both results with Literature from Table 2 it can be said, that the synthesized ceramic papers have a good performance (26 dB vs 24.6 dB for pure carbon nanofiber/cellulose). It has also to be taken into account, that the thickness of one ceramic paper is around 0.2 - 0.3 mm (compared to 1 mm for carbon nanofiber/cellulose).

SEM in Figure 57 shows the microstructure of the Lin_Ni_Dur-1000 °C Dur and the Lin_Pd_Dur – 1000 and 1300 °C samples. In both 1000 °C samples (Figure 57 (a) and (c)), the precipitations are visible. As described in chapter 2.4.2, the material needs to be conductive, as this weakens the incoming electromagnetic wave, due to redistribution of charge carriers inside the shielding material, which indicate an opposing electromagnetic field [63]. Conductivity measurements of the pyrolyzed pristine Lin template pyrolyzed at 1000 °C in Ar, as described in the paper by Ricohermoso et al. [133], showed values of $1.81 \cdot 10^2 \frac{S}{m}$. These are comparable with the values from Literature (from $3.3 \cdot 10^2 \frac{S}{m}$ to $3 \cdot 10^5 \frac{S}{m}$ depending on the direction of the basal plane and type of carbon [134]). As graphite is more conductive compared to amorphous carbon, the graphitization of the cellulose-based template should increase the conductivity thereof. Additionally, the precipitations act as interfaces and contribute to the reflections of the electromagnetic wave and thicker samples raise the absorption potential of a sample. At 1300 °C in the Pd sample (Figure 57 (b)), the coating appears to be thicker, which results in an even better electromagnetic shielding, which has been also shown in Figure 57 (b).

(a)
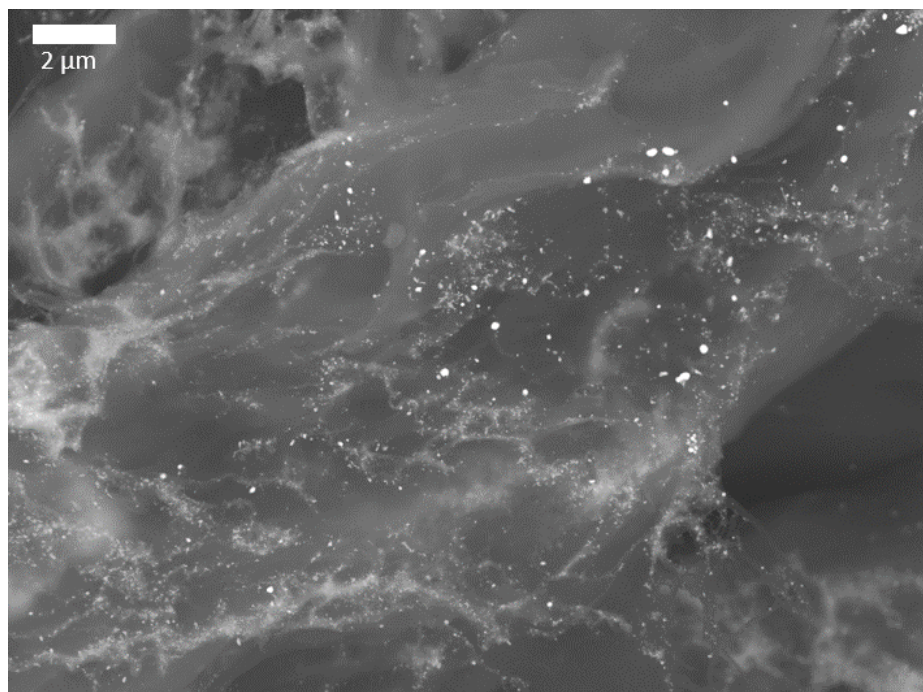
(b)
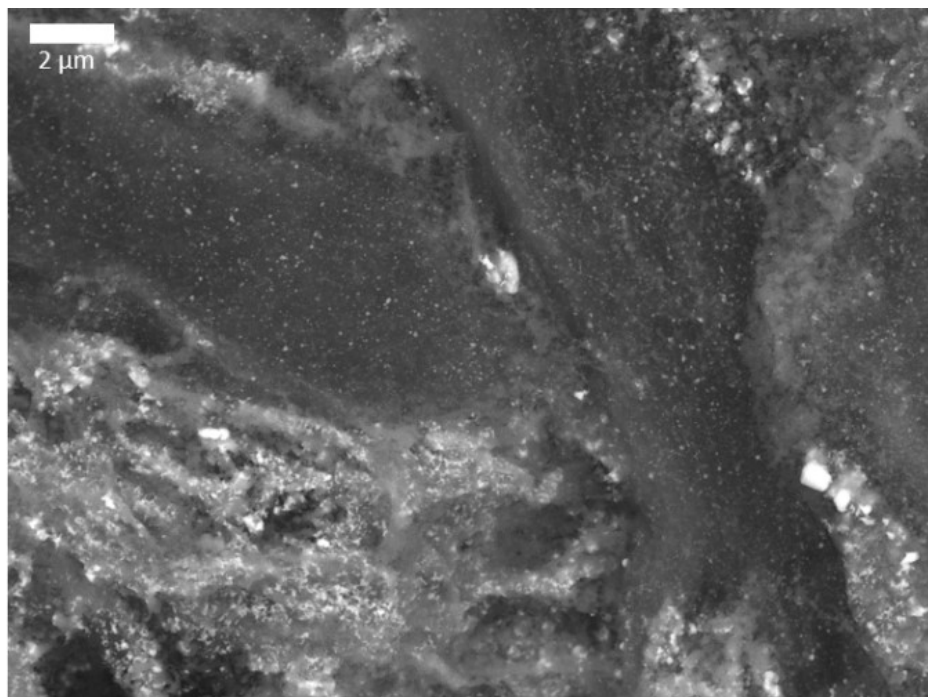
(c)
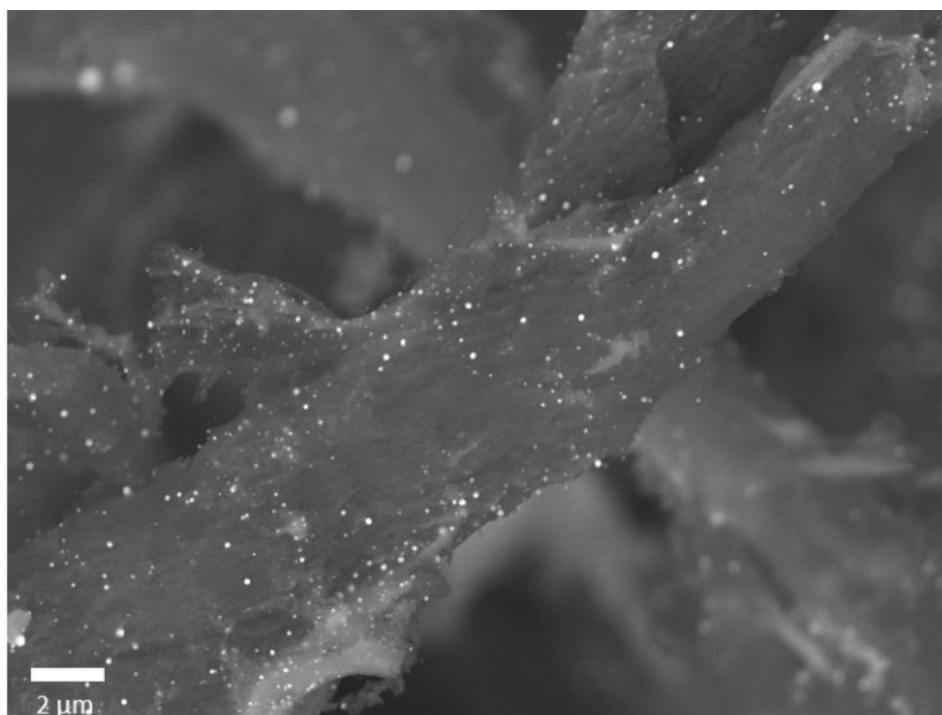
Figure 57. SEM images of Lin_Pd_Dur-1000 °C Ar (a), Lin_Pd_Dur-1300 °C Ar (Ar) (b) and Lin_Ni_Dur-1000 °C Ar (c), show the microstructure of the synthesized ceramic papers

This chapter showed that the synthesized Pd or Ni-Dur-based ceramic papers exhibited high and constant electromagnetic shielding values over a broad frequency range and were comparable with state-of-the-art compounds. Furthermore, it did not matter if Ni or Pd was used, as both showed similar results. Higher pyrolysis temperatures and thicker samples (multiple layers) increased significantly the performance of the EMS, due to additional crystalline phases and larger pathways for the electromagnetic wave.

6. Conclusion and Outlook

One part of this study focused to get a better understanding of the conversion of different cellulose-based papers into metal-polysilazane-modified (functionalized) ceramic papers.

Firstly, the influence of different atmospheres (Ar or NH_3) on different cellulose-based templates was studied and showed, that their behavior during pyrolysis in Ar and NH_3 differs slightly. Raman spectroscopy suggested, that in NH_3 incorporation of nitrogen into the cellulose template occurs and indicated the formation of turbostratic carbon at 1000 °C in both atmospheres. TG analysis depicted, that between 250 °C and 400 °C the highest mass loss of the cellulose-based templates occurs, due to the decomposition thereof, which was also shown in various studies before [79, 80].

The second part introduced different transition metals (Fe, Ni, or Pd) and polysilazanes (PHPS or Dur) into the system, which protected the cellulose-based templates from complete decomposition. The additional transition metals showed a catalytic effect on the graphitization of the cellulose-derived amorphous carbon fibers, as was also shown in previous research [117, 118, 135]. Furthermore, depending on the atmosphere, different phases could be identified: only in NH_3, an ε-Fe_2N phase was produced, as the other two transition metals do not form a crystalline phase with nitrogen. All systems showed similar behavior when annealing at higher temperatures: in N_2 β-Si_3N_4 was formed, while the Ar atmosphere produced SiC phases. Therefore, at higher temperatures, the used atmosphere has a significantly larger influence on the formation of the desired Si-based phases (SiC or Si_3N_4) than the used transition metal or polysilazane.

FTIR results showed, that in the Ni / Pd and Dur systems, the reaction between the precursor and the transition metal occurred after the refluxing process, as the Si-H band was not present anymore in those samples, due to hydrosilylation processes [111]. Otherwise, the FTIR results indicated similar bonding situations in all systems and atmospheres, independent of the precursor/template or transition metal: At 1000 °C mainly Si-O-Si vibrations were present, while annealing in Ar at 1300 °C showed Si-C bonds. Changing the atmosphere to N_2 pronounced Si-N-Si vibrations.

Lastly, two possible applications for the ceramic papers were studied. The electrocatalytic results depicted, that mainly Ni was responsible for the catalytic activity in HER/OER and that the addition of a SiC phase, lowers the performance. It was still higher compared to the pure pyrolyzed paper, but worse, than state-of-the-art materials. However, facile synthesis without using additional binders or electrolytes makes it a good candidate for possible future applications. EMS measurements showed that the thickness of the sample and the availability of additional crystalline phases increased the amount of the total electromagnetic shielding. The results were comparable to similar systems and showed good performances.

Based on the FTIR results of the pyrolyzed samples, which showed Si-O-Si bands, it was not possible to produce oxygen-free ceramic papers/precursors, due to the high amount of oxygen, which is present in the cellulose-based templates and the acetylacetonate. Thus, in future studies oxygen-free compounds and for example, an already graphitic template are more suitable for the synthesis of ceramic papers.

Furthermore, the catalytic performance of the Ni-Dur-ceramic papers was tested only for HER/OER, but there exist other applications in which the functionalized ceramic papers could be of interest. Wang et al. [136] produced a nickel-containing silicon oxycarbonitride ceramic, which was tested as a catalytic material in the so-called "dry reforming of methane process". Another interesting catalytic-driven application is the so-called Sabatier reaction, in which a Ni-catalyzed CO_2 methanation reaction occurs [137].

The EMS appears to be the most suitable application yet and the synthesis of the metal-modified-ceramic papers is facile and produces light ($\sim$ 15-20 mg per sheet) and thin samples. Future studies can focus on thicker samples with a higher amount of ceramic compounds to increase the total electromagnetic shielding.

(a)
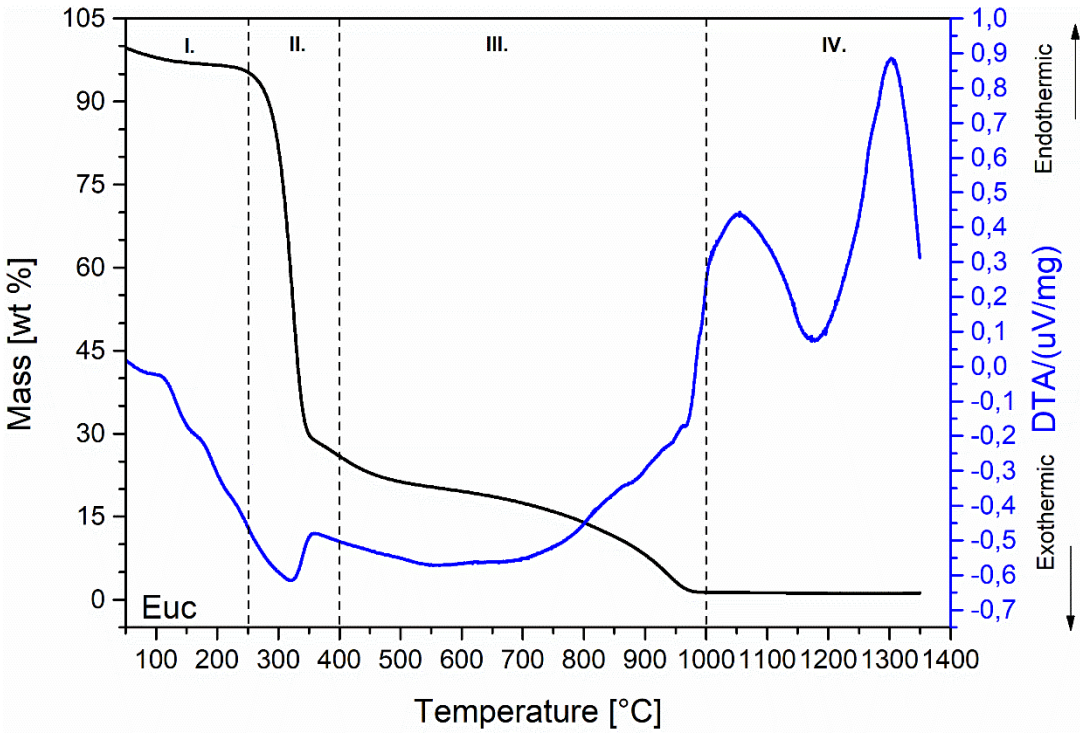
(b)
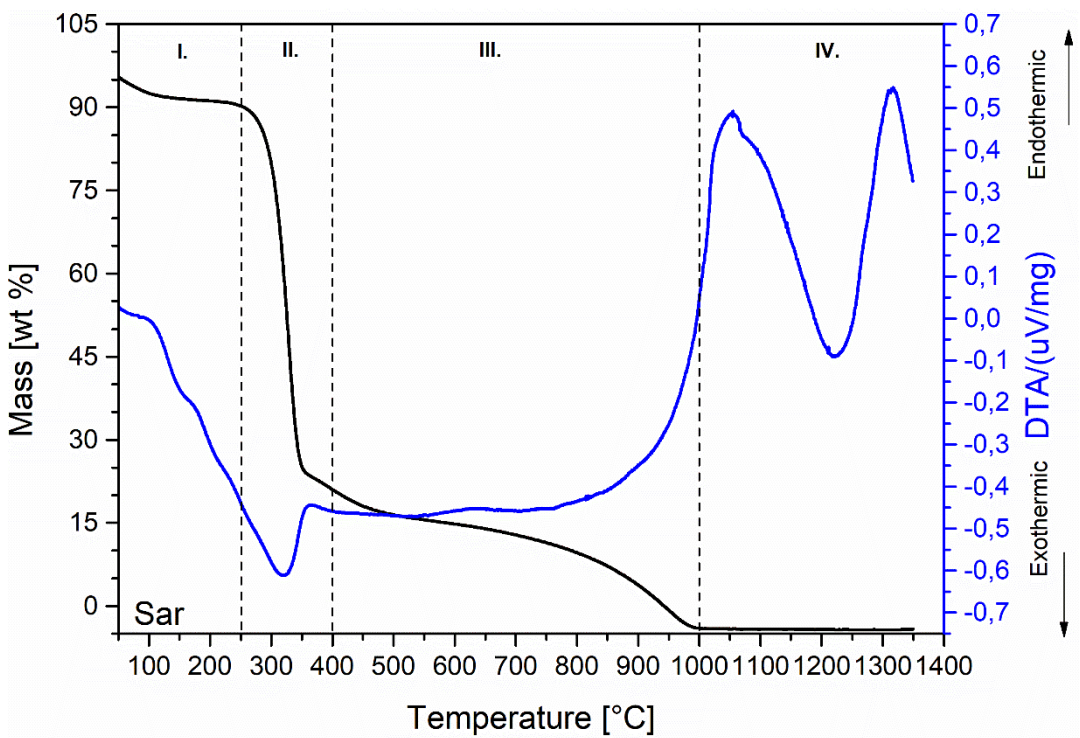
Figure A 1. TG analysis of (a) Linters and (b) Sartorius paper template in ammonia/argon (Ratio 90:10) atmosphere
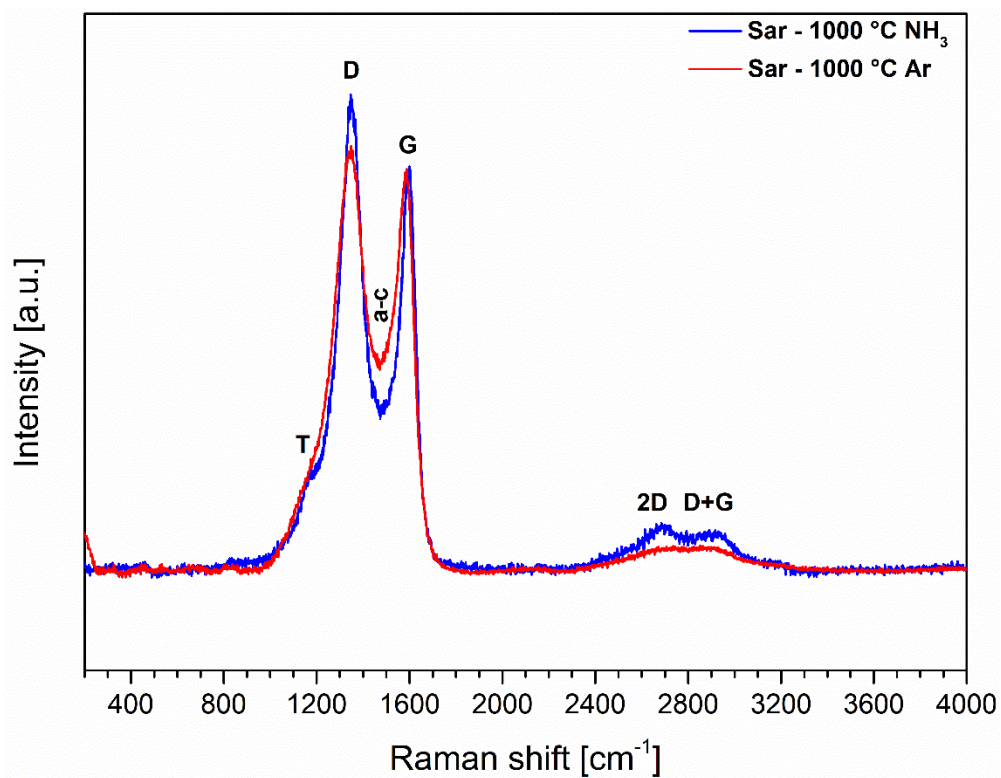
Figure A 2. Normalized μ-Raman spectra of Sar template pyrolyzed in NH_3 and Ar atmosphere at 1000 °C
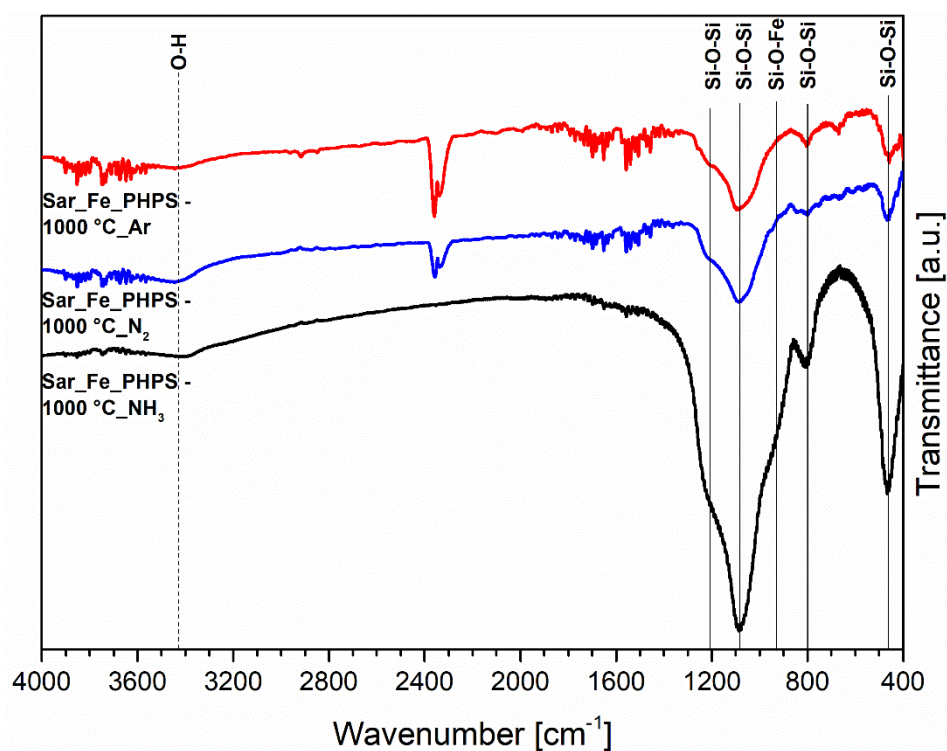
Figure A 3. FTIR spectra of the iron(III) acetylacetonate-modified polysilazane (PHPS) Sartorius based-ceramic paper annealed in different atmospheres

Table A 1. Characteristic parameters as determined from Raman spectroscopy (including mean values and standard deviation) for the Lin_Pd_PHPS samples

Sample	AD/AG	A_{2D}/AD	L_a (nm)	L_D (nm)	L_{eq} (nm)	n_D (x 10^{11}, cm^{-3})
Lin_Pd_PHPS-1000 °C Ar*	3.59±0.85	1.20±0.90	4.67±2.12	5.92±1.13	92.11±22.37	12.34±2.93
Lin_Pd_PHPS-1300 °C Ar (Ar)	2.08±0.65	0.39±0.28	9.12±3.65	8.12±1.54	30.06±21.38	7.17±2.24
Lin_Pd_PHPS-1300 °C N_2 (Ar)	2.26±0.11	0.22±0.10	7.41±0.35	7.45±0.18	17.19±7.52	7.79±0.37

* Based on two fits
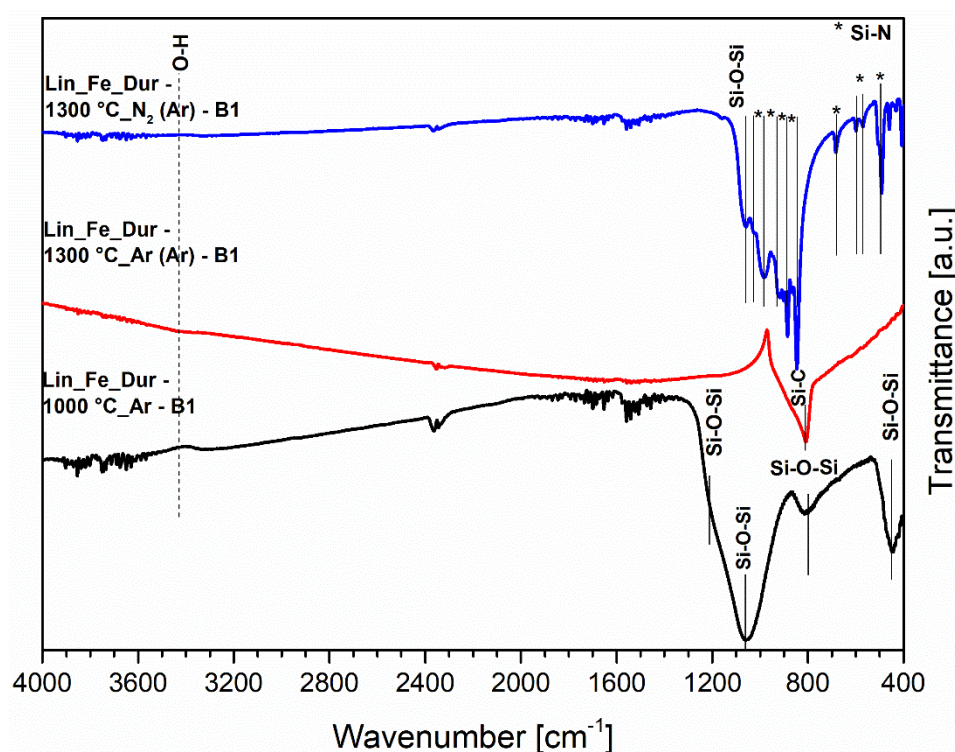
Figure A 4. FTIR spectra of the Lin iron(III) acetylacetonate-modified durazane ceramic paper in the as-prepared state and after pyrolysis in Ar and N_2 (Batch 1)
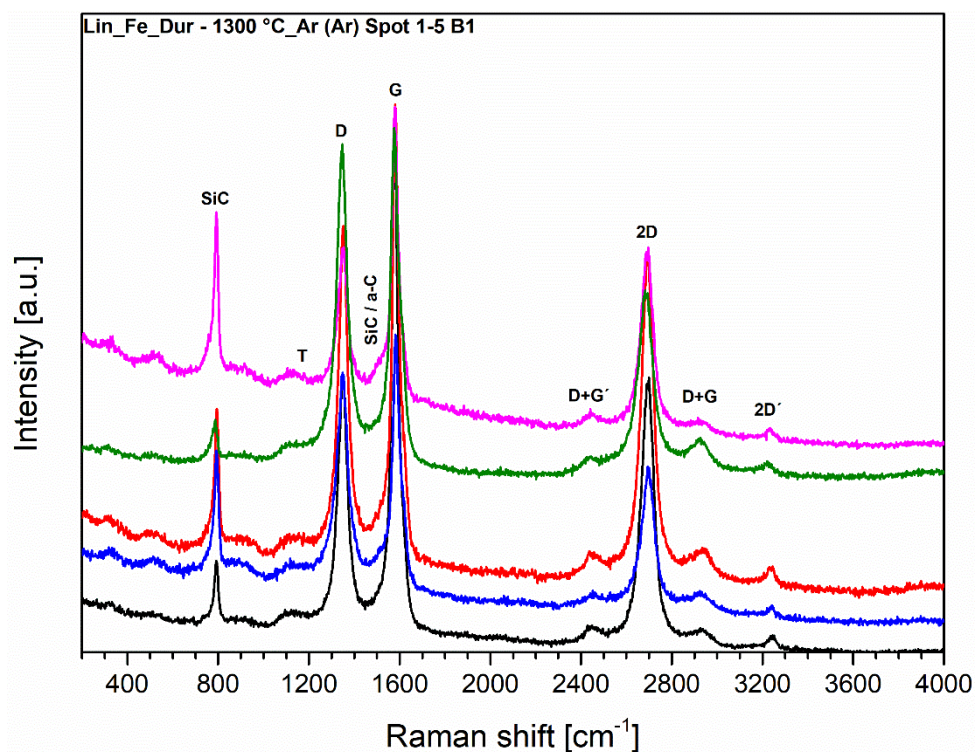
Figure A 5. Raman spectra of the Lin_Fe_Dur ceramic papers annealed at 1300 °C in Ar (previous at 1000 °C in Ar) (Batch 1)
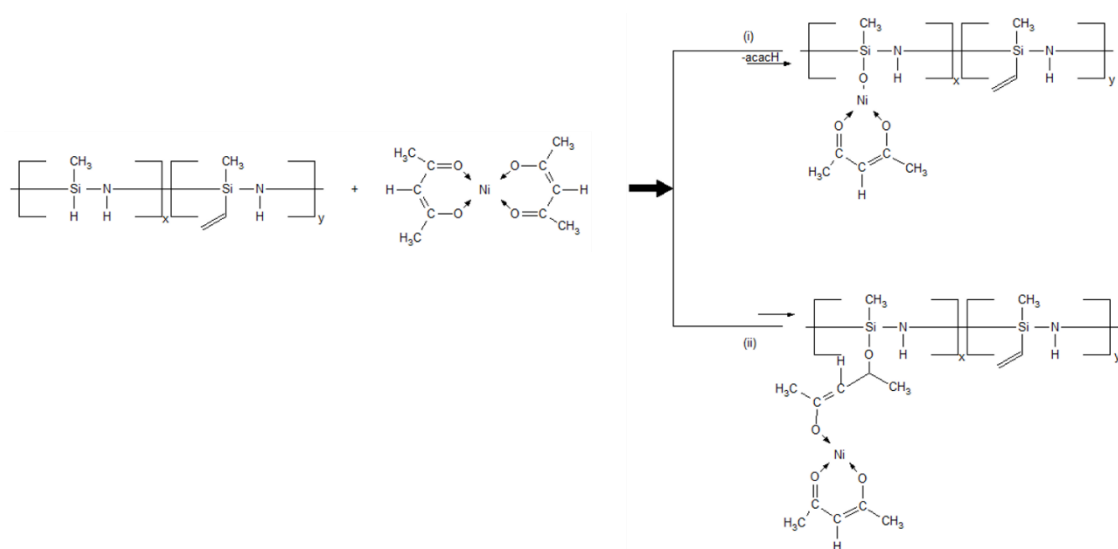
Figure A 6. Two possible reaction paths in the precursor state of the Ni(II)acetylacetonate/Dur system based on FTIR spectra. While in (i) the hydrosilylation of the C=O groups of acetylacetonate is shown, (ii) depicts the reaction at the Si-H groups

(a)

(b)
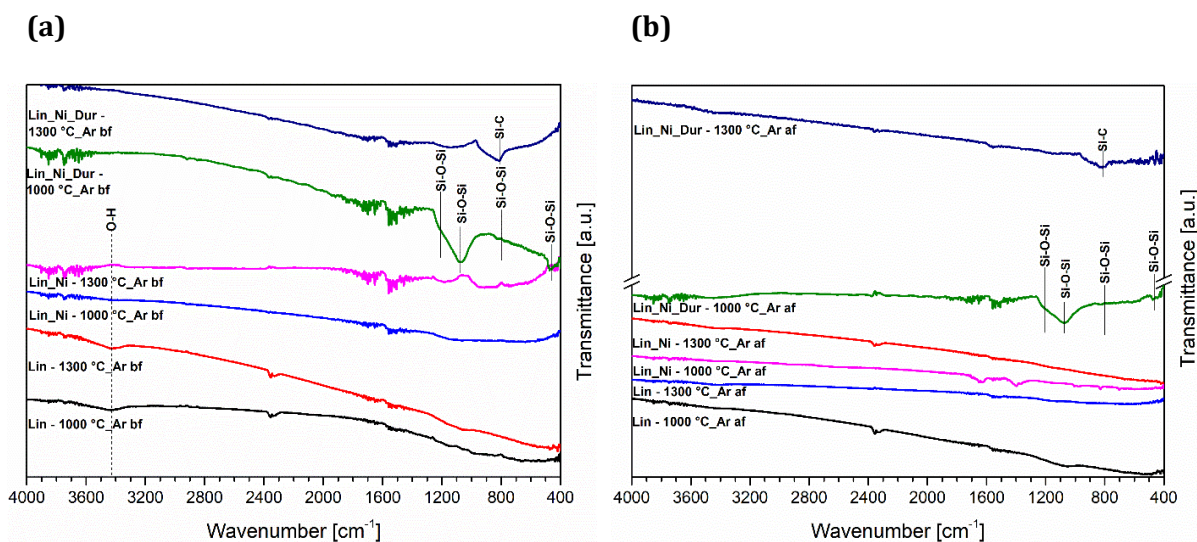
Figure A 7. FTIR spectra of all the samples used before (a) and after (b) electrocatalytic measurements

(a)

(b)

(c)

(d)

(e)

(f)
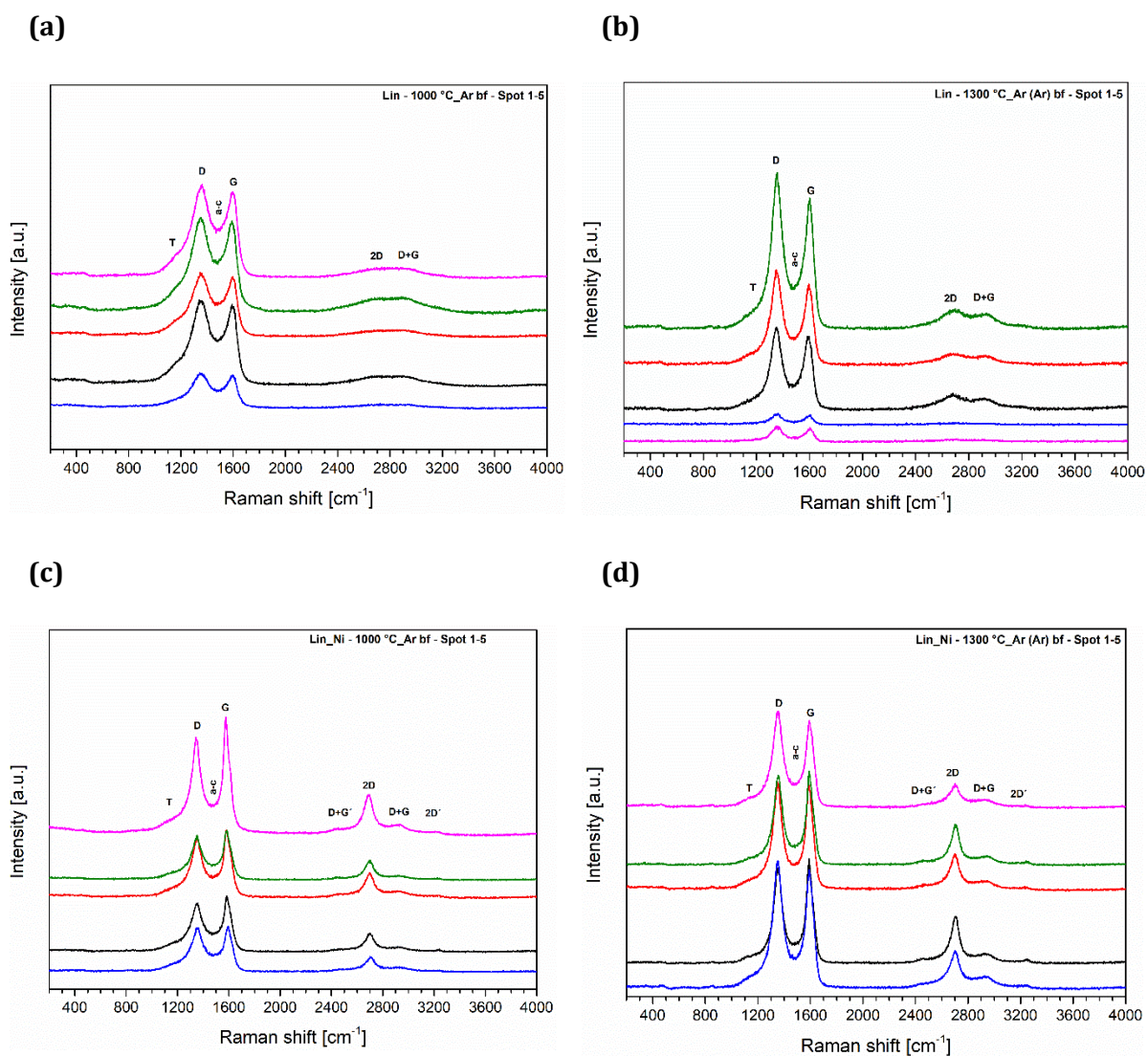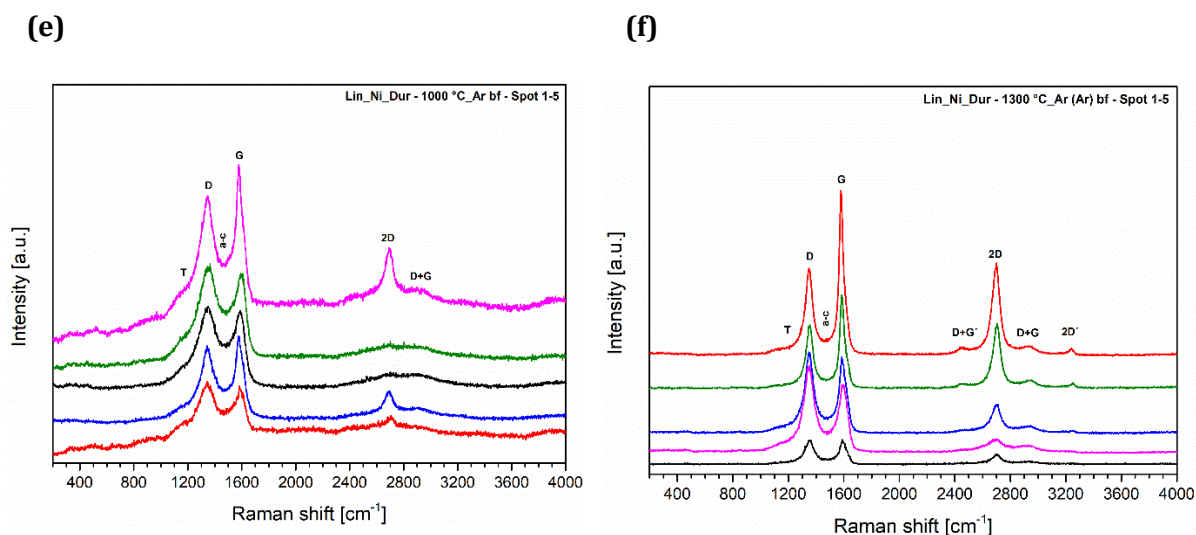
Figure A 8. Raman spectroscopy measurements before electrocatalytic tests of (a) Lin_1000 °C Ar, (b) Lin_1300 °C Ar (Ar), (c) Lin_Ni_1000 °C Ar, (d) Lin_Ni_1300 °C Ar (Ar), (e) Lin_Ni_Dur_1000 °C Ar and (d) Lin_Ni_Dur-1300 °C Ar (Ar)

Table A 2. Characteristic parameters, determined from the fitting of the Raman spectroscopy Data shown in Figure A 8

Sample	A_D/A_G	A_{2D}/A_D	L_a (nm)	L_D (nm)	L_{eq} (nm)	n_D (x 10^{11}, cm^{-3})
Lin-1000 °C Ar bf	3.79±0.13	0.12±0.03	4.43±0.16	5.76±0.10	8.91±2.16	13.0±0.46
Lin-1300 °C Ar bf	3.17±0.18	0.25±0.03	5.30±0.29	6.30±0.18	19.48±2.31	10.9±0.61
Lin_Ni- 1000 °C Ar bf	2.01±0.24	0.37±0.09	8.44±0.09	7.94±0.45	28.73±6.94	6.91±0.81
Lin_Ni- 1300 °C Ar bf	2:08±0.21	0.31±0.08	8.12±0.79	87.79±0.38	23.72±6.05	7.16±0.71
Lin_Ni_Dur - 1000 °C Ar (Ar) bf	3.17±0.79	0.21±0.05	5.60±1.28	6.44±0.76	16.40±4.13	10.90±2.71
Lin_Ni_Dur - 1300 °C Ar (Ar) bf	1.46±0.52	0.63±0.40	13.20±4.85	9.78±1.83	48.88±31.18	5.00±1.78
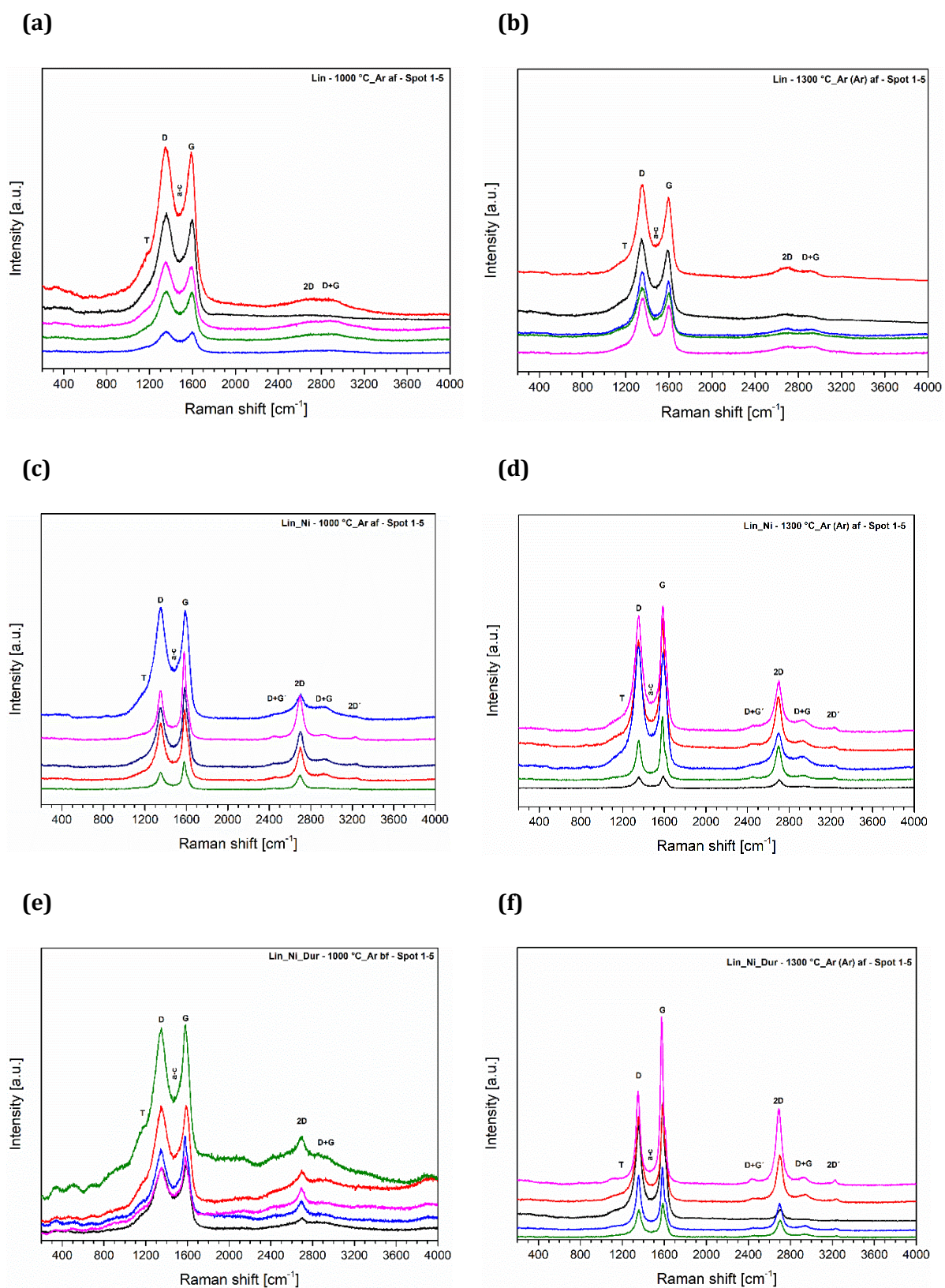
Figure A 9. Raman spectroscopy measurements after electrocatalytic tests of (a) Lin_1000 °C Ar, (b) Lin_1300 °C Ar (Ar), (c) Lin_Ni_1000 °C Ar, (d) Lin_Ni_1300 °C Ar (Ar), (e) Lin_Ni_Dur_1000 °C Ar and (d) Lin_Ni_Dur-1300 °C Ar (Ar)

Table A 3. Characteristic parameters, determined from the fitting of the Raman spectroscopy Data shown in Figure A 9

Sample	A_D/A_G	A_{2D}/A_D	L_a (nm)	L_D (nm)	L_{eq} (nm)	n_D (x 10^{11}, cm^{-3})
Lin-1000 °C Ar af	3.58±0.19	0.12±0.05	4.70±0.26	5.93±0.16	9.22±3.76	12.3±0.67
Lin-1300 °C Ar af	3.15±0.18	0.19±0.01	5.33±0.29	6.32±0.17	14.32±0.91	10.8±0.61
Lin_Ni-1000 °C Ar af	1.58±0.85	0.66±0.35	13.94±6.84	9.90±2.56	50.87±26.62	5.44±2.91
Lin_Ni-1300 °C Ar af	1.55±0.56	0.66±0.34	12.40±4.62	9.48±1.78	50.52±26.22	5.33±1.93
Lin_Ni_Dur - 1000 °C Ar (Ar) af	3.18±0.31	0.13±0.06	5.32±0.52	6.31±0.31	9.89±4.32	10.90±1.06
Lin_Ni_Dur - 1300 °C Ar (Ar) af	0.95±0.12	0.67±0.33	17.99±2.66	11.58±0.83	51.78±25.59	3.26±0.41

Literature

[1] Zhang, W., Huang, Z.-H., Cao, G., Kang, F., and Yang, Y. **2012**. A novel mesoporous carbon with straight tunnel-like pore structure for high rate electrochemical capacitors. *Journal of Power Sources* 204, 230–235.

[2] Konno, H., Onishi, H., Yoshizawa, N., and Azumi, K. **2010**. MgO-templated nitrogen-containing carbons derived from different organic compounds for capacitor electrodes. *Journal of Power Sources* 195, 2, 667–673.

[3] Xu, S. and Lei, Y. **2018**. Template-Assisted Fabrication of Nanostructured Arrays for Sensing Applications. *ChemPlusChem* 83, 8, 741–755.

[4] Travitzky, N., Windsheimer, H., Fey, T., and Greil, P. **2008**. Preceramic Paper-Derived Ceramics. *Journal of the American Ceramic Society* 91, 11, 3477–3492.

[5] Yang, L., Cheng, S., Ding, Y., Zhu, X., Wang, Z. L., and Liu, M. **2012**. Hierarchical network architectures of carbon fiber paper supported cobalt oxide nanonet for high-capacity pseudocapacitors. *Nano Lett.* 12, 1, 321–325.

[6] Li, G., Ma, J., Peng, G., Chen, W., Chu, Z., Li, Y., Hu, T., and Li, X. **2014**. Room-temperature humidity-sensing performance of SiC nanopaper. *ACS Appl. Mater. Interfaces* 6, 24, 22673–22679.

[7] Li, Y., Nagao, M., Kobayashi, K., Jin, Y., and Hibino, T. **2020**. A Cellulose Electrolysis Cell with Metal-Free Carbon Electrodes. *Catalysts* 10, 1, 106.

[8] Parit, M., Du, H., Zhang, X., Prather, C., Adams, M., and Jiang, Z. **2020**. Polypyrrole and cellulose nanofiber based composite films with improved physical and electrical properties for electromagnetic shielding applications. *Carbohydrate polymers* 240, 116304.

[9] Song, S., Li, H., Liu, P., and Peng, X. **2022**. Applications of cellulose-based composites and their derivatives for microwave absorption and electromagnetic shielding. *Carbohydrate polymers* 287, 119347.

[10] Chantrell, P. and P. Popper. **1965**. Inorganic polymers and ceramics. *Special Ceramics*, 67.

[11] Ainger, F. and J. Herbert,. **1960**. The preparation of phosphorus-nitrogen compounds as non-porous solids. *Special Ceramics*, 168–182.

[12] Verbeek W. and Winter G. **1974,** Ger. Pat. No. 2236078.

[13] Yajima, S., Okamura, K., and Hayashi, J. **1975**. STRUCTURAL ANALYSIS IN CONTINUOUS SILICON CARBIDE FIBER OF HIGH TENSILE STRENGTH. *Chem. Lett.* 4, 12, 1209–1212.

[14] Yajima, S., Hayashi, J., and Omori, M. **1975**. CONTINUOUS SILICON CARBIDE FIBER OF HIGH TENSILE STRENGTH. *Chem. Lett.* 4, 9, 931–934.

[15] Riedel, R., Seher, M., Mayer, J., and Szabó, D. **1995**. Polymer-derived Si-based bulk ceramics, part I: Preparation, processing and properties. *Journal of the European Ceramic Society* 15, 8, 703–715.

[16] Mera, G. and Ionescu, E. **2011**. Silicon-Containing Preceramic Polymers. In *Encyclopedia of polymer science and technology*, H. F. Mark, Ed. Wiley-Interscience, Hoboken, N.J. DOI=10.1002/0471440264.pst591.

[17] Ishikawa, Kajii, Matsunaga, Hogami, Kohtoku, and Nagasawa. **1998**. A tough, thermally conductive silicon carbide composite with high strength up to 1600 °C in Air. *Science (New York, N.Y.)* 282, 5392, 1295–1297.

[18] Studart, A. R., Gonzenbach, U. T., Tervoort, E., and Gauckler, L. J. **2006**. Processing Routes to Macroporous Ceramics: A Review. *Journal of the American Ceramic Society* 89, 6, 1771–1789.

[19] Colombo, P. and Hellmann, J. R. **2002**. Ceramic foams from preceramic polymers. *Materials Research Innovations* 6, 5-6, 260–272.

[20] Du, Z., Yao, D., Xia, Y., Zuo, K., Yin, J., Liang, H., and Zeng, Y.-P. **2019**. Tailoring the microstructure of high porosity Si_3N_4 foams by direct foaming with mixed surfactants. *Journal of the American Ceramic Society* 102, 11, 6827–6836.

[21] Jana, D. C., Sundararajan, G., and Chattopadhyay, K. **2017**. Effect of Porosity on Structure, Young's Modulus, and Thermal Conductivity of SiC Foams by Direct Foaming and Gelcasting. *Journal of the American Ceramic Society* 100, 1, 312–322.

[22] BHASKAR, S., CHO, G. H., PARK, J. G., KIM, S. W., KIM, H. T., and KIM, I. J. **2015**. Micro porous SiO_2–SiC ceramics from particle stabilized foams by direct foaming. *J. Ceram. Soc. Japan* 123, 1437, 378–382.

[23] Bauer, C., Scheffler, F., and Schwidder, M. **2015**. Direct Crystallization of Silicoaluminophosphates onto the Surface of Open-Celled SiC Foam. *Adv. Eng. Mater.* 17, 5, 656–662.

[24] Fukasawa, T., Ando, M., Ohji, T., and Kanzaki, S. **2001**. Synthesis of Porous Ceramics with Complex Pore Structure by Freeze-Dry Processing. *Journal of the American Ceramic Society* 84, 1, 230–232.

[25] Ren, L., Zeng, Y.-P., and Jiang, D. **2007**. Fabrication of Gradient Pore TiO_2 Sheets by a Novel Freeze-Tape-Casting Process. *Journal of the American Ceramic Society* 90, 9, 3001–3004.

[26] Xia, Y., Zeng, Y.-P., and Jiang, D. **2012**. Microstructure and mechanical properties of porous Si_3N_4 ceramics prepared by freeze-casting. *Materials & Design* 33, 98–103.

[27] Yoon, B.-H., Lee, E.-J., Kim, H.-E., and Koh, Y.-H. **2007**. Highly Aligned Porous Silicon Carbide Ceramics by Freezing Polycarbosilane/Camphene Solution. *Journal of the American Ceramic Society* 90, 6, 1753–1759.

[28] Verma, J., Vijayakumar, M., and Mitra, R. **2015**. Processing and microstructure of freeze-cast silica foams. *Materials Letters* 153, 168–170.

[29] K. Schwartzwalder and A. V. Somers. *Method of Making Porous Ceramic Articles,* US Pat. No. 3090094.

[30] Luyten, J., Thijs, I., Vandermeulen, W., Mullens, S., Wallaeys, B., and Mortelmans, R. **2005**. Strong ceramic foams from polyurethane templates. *Advances in Applied Ceramics* 104, 1, 4–8.

[31] Richardson, J., Peng, Y., and Remue, D. **2000**. Properties of ceramic foam catalyst supports: pressure drop. *Applied Catalysis A: General* 204, 1, 19–32.

[32] Pu, X., Liu, X., Qiu, F., and Huang, L. **2004**. Novel Method To Optimize the Structure of Reticulated Porous Ceramics. *Journal of the American Ceramic Society* 87, 7, 1392–1394.

[33] Saggio-Woyansky, J., Scott, C. E., and Minnear, W. P. **1992**. Processing of porous ceramics. *American Ceramic Society Bulletin* 71, 1674–1682.

[34] Nangrejo, M. R., Bao, X., and Edirisinghe, M. J. **2001**. Processing of Ceramic Foams from Polymeric Precursor-Alumina Suspensions. *Cellular Polymers* 20, 1, 17–36.

[35] Nangrejo, M., Bao, X., and Edirisinghe, M. J. **2000**. Preparation of silicon carbide–silicon nitride composite foams from pre-ceramic polymers. *Journal of the European Ceramic Society* 20, 11, 1777–1785.

[36] Nangrejo, M. R. and Edirisinghe, M. J. **2002**. Porosity and Strength of Silicon Carbide Foams Prepared Using Preceramic Polymers. *Journal of Porous Materials* 9, 2, 131–140.

[37] Nurfatihah, Y. S., Alwi, A., Azura, A. R., and Ahmad, Z. **2012**. Synthesis of Porous Silica via Styrene Natural Rubber Sacrificial Template. *AMR* 626, 823–827.

[38] Naga, S., El-Maghraby, A., EL-Rafei, A., and Greil, P. **2006**. Porous Fibrous Mullite Bodies. *American Ceramic Society Bulletin* 85.

[39] Zhang, G.-J., Yang, J.-F., and Ohji, T. **2001**. Fabrication of Porous Ceramics with Unidirectionally Aligned Continuous Pores. *Journal of the American Ceramic Society* 84, 6, 1395–1397.

[40] Mizutani, M., Takase, H., Adachi, N., Ota, T., Daimon, K., and Hikichi, Y. **2005**. Porous ceramics prepared by mimicking silicified wood. *Science and Technology of Advanced Materials* 6, 1, 76–83.

[41] Ota, T., Takahashi, M., Hibi, T., Ozawa, M., Suzuki, S., Hikichi, Y., and Suzuki, H. **1995**. Biomimetic Process for Producing SiC "Wood". *Journal of the American Ceramic Society* 78, 12, 3409–3411.

[42] Yi, G. and Schwarzacher, W. **1999**. Single crystal superconductor nanowires by electrodeposition. *Appl. Phys. Lett.* 74, 12, 1746–1748.

[43] Tishkevich, D. I., Vorobjova, A. I., and Vinnik, D. A. **2019**. Template Assisted Ni Nanowires Fabrication. *MSF* 946, 235–241.

[44] Yang, M. and Wang, G. **2009**. Synthesis of hierarchical porous carbon particles by hollow polymer microsphere template. *Colloids and Surfaces A: Physicochemical and Engineering Aspects* 345, 1-3, 121–126.

[45] Merlen, A., Buijnsters, J., and Pardanaud, C. **2017**. A Guide to and Review of the Use of Multiwavelength Raman Spectroscopy for Characterizing Defective Aromatic Carbon Solids: from Graphene to Amorphous Carbons. *Coatings* 7, 10, 153.

[46] Rosenburg, F. **2018**. *The state of carbon and the piezoresistive effect in silicon oxycarbide ceramics*. Dissertation, Universitäts- und Landesbibliothek Darmstadt.

[47] Reich, S. and Thomsen, C. **2004**. Raman spectroscopy of graphite. *Philosophical transactions. Series A, Mathematical, physical, and engineering sciences* 362, 1824, 2271–2288.

[48] Kawashima and Katagiri. **1995**. Fundamentals, overtones, and combinations in the Raman spectrum of graphite. *Physical review. B, Condensed matter* 52, 14, 10053–10059.

[49] Ferrari, A. C. and Basko, D. M. **2013**. Raman spectroscopy as a versatile tool for studying the properties of graphene. *Nature nanotechnology* 8, 4, 235–246.

[50] Couzi, M., Bruneel, J.-L., Talaga, D., and Bokobza, L. **2016**. A multi wavelength Raman scattering study of defective graphitic carbon materials: The first order Raman spectra revisited. *Carbon* 107, 388–394.

[51] Tuinstra, F. and Koenig, J. L. **1970**. Raman Spectrum of Graphite. *The Journal of Chemical Physics* 53, 3, 1126–1130.

[52] Tuinstra, F. and Koenig, J. L. **1970**. Characterization of Graphite Fiber Surfaces with Raman Spectroscopy. *Journal of Composite Materials* 4, 4, 492–499.

[53] Knight, D. S. and White, W. B. **1989**. Characterization of diamond films by Raman spectroscopy. *J. Mater. Res.* 4, 2, 385–393.

[54] Jawhari, T., Roid, A., and Casado, J. **1995**. Raman spectroscopic characterization of some commercially available carbon black materials. *Carbon* 33, 11, 1561–1565.

[55] Nikiel, L. and Jagodzinski, P. W. **1993**. Raman spectroscopic characterization of graphites: A re-evaluation of spectra/ structure correlation. *Carbon* 31, 8, 1313–1317.

[56] Cançado, L. G., Takai, K., Enoki, T., Endo, M., Kim, Y. A., Mizusaki, H., Jorio, A., Coelho, L. N., Magalhães-Paniago, R., and Pimenta, M. A. **2006**. General equation for the determination of the crystallite size L_a of nanographite by Raman spectroscopy. *Appl. Phys. Lett.* 88, 16, 163106.

[57] Cançado, L. G., Jorio, A., Ferreira, E. H. M., Stavale, F., Achete, C. A., Capaz, R. B., Moutinho, M. V. O., Lombardo, A., Kulmala, T. S., and Ferrari, A. C. **2011**. Quantifying defects in graphene via Raman spectroscopy at different excitation energies. *Nano Lett.* 11, 8, 3190–3196.

[58] Larouche, N. and Stansfield, B. L. **2010**. Classifying nanostructured carbons using graphitic indices derived from Raman spectra. *Carbon* 48, 3, 620–629.

[59] Wang, S., Lu, A., and Zhong, C.-J. **2021**. Hydrogen production from water electrolysis: role of catalysts. *Nano convergence* 8, 1, 4.

[60] Vij, V., Sultan, S., Harzandi, A. M., Meena, A., Tiwari, J. N., Lee, W.-G., Yoon, T., and Kim, K. S. **2017**. Nickel-Based Electrocatalysts for Energy-Related Applications: Oxygen Reduction, Oxygen Evolution, and Hydrogen Evolution Reactions. *ACS Catal.* 7, 10, 7196–7225.

[61] Kuriki, R., Ishitani, O., and Maeda, K. **2016**. Unique Solvent Effects on Visible-Light CO_2 Reduction over Ruthenium(II)-Complex/Carbon Nitride Hybrid Photocatalysts. *ACS Appl. Mater. Interfaces* 8, 9, 6011–6018.

[62] Pfeifer, V., Jones, T. E., Velasco Vélez, J. J., Arrigo, R., Piccinin, S., Hävecker, M., Knop-Gericke, A., and Schlögl, R. **2017**. In situ observation of reactive oxygen species forming on oxygen-evolving iridium surfaces. *Chemical science* 8, 3, 2143–2149.

[63] Zachariah, S. M., Grohens, Y., Kalarikkal, N., and Thomas, S. **2022**. Hybrid materials for electromagnetic shielding: A review. *Polymer Composites* 43, 5, 2507–2544.

[64] Liu, X., Xu, H., Xie, F., Fasel, C., Yin, X., and Riedel, R. **2020**. Highly flexible and ultrathin Mo_2C film via in-situ growth on graphene oxide for electromagnetic shielding application. *Carbon* 163, 254–264.

[65] Liu, X., Yin, X., Kong, L., Li, Q., Liu, Y., Duan, W., Zhang, L., and Cheng, L. **2014**. Fabrication and electromagnetic interference shielding effectiveness of carbon nanotube reinforced carbon fiber/pyrolytic carbon composites. *Carbon* 68, 501–510.

[66] Liu, X., Xu, H., Xie, F., Yin, X., and Riedel, R. **2020**. Light-weight and highly flexible TaC modified PyC fiber fabrics derived from cotton fiber textile with excellent electromagnetic shielding effectiveness. *Chemical Engineering Journal* 387, 124085.

[67] Liu, X., Yu, Z., Ishikawa, R., Chen, L., Liu, X., Yin, X., Ikuhara, Y., and Riedel, R. **2017**. Single-source-precursor derived RGO/CNTs-SiCN ceramic nanocomposite with ultra-high electromagnetic shielding effectiveness. *Acta Materialia* 130, 83–93.

[68] Zeng, Z., Jin, H., Chen, M., Li, W., Zhou, L., and Zhang, Z. **2016**. Lightweight and Anisotropic Porous MWCNT/WPU Composites for Ultrahig Performance Electromagnetic Interference Shielding. *Adv. Funct. Mater.* 26, 2, 303–310.

[69] Anju, V. P. Chapter 6 - Nanocellulose-based composites for EMI shielding applications. In *Thomas, Pottathara (Hg.) – Nanocellulose Based Composites for Electronics*, 125–161. DOI=10.1016/B978-0-12-822350-5.00006-0.

[70] Cichosz, S. and Masek, A. **2020**. IR Study on Cellulose with the Varied Moisture Contents: Insight into the Supramolecular Structure. *Materials (Basel, Switzerland)* 13, 20.

[71] Doncea, S. M., Ion, R. M., Fierascui, R. C., Bacalum, E., Bunaciu, A. A., and Aboul-Enein, H. Y. **2009**. SPECTRAL METHODS FOR HISTORICAL PAPER ANALYSIS: COMPOSITION AND AGE APPROXIMATION. *Instrumentation Science & Technology* 38, 1, 96–106.

[72] Wulandari, W. T., Rochliadi, A., and Arcana, I. M. **2016**. Nanocellulose prepared by acid hydrolysis of isolated cellulose from sugarcane bagasse. *IOP Conf. Ser.: Mater. Sci. Eng.* 107, 12045.

[73] Nikonenko, N. A., Buslov, D. K., Sushko, N. I., and Zhbankov, R. G. **2000**. Investigation of stretching vibrations of glycosidic linkages in disaccharides and polysaccharides with use of IR spectra deconvolution. *Biopolymers* 57, 4, 257–262.

[74] Cabrales, L., Abidi, N., and Manciu, F. **2014**. Characterization of Developing Cotton Fibers by Confocal Raman Microscopy. *Fibers* 2, 4, 285–294.

[75] Kavkler, K. and Demšar, A. **2011**. Examination of cellulose textile fibres in historical objects by micro-Raman spectroscopy. *Spectrochimica acta. Part A, Molecular and biomolecular spectroscopy* 78, 2, 740–746.

[76] Lára. *Cellulose: Structure & Function*. https://www.savemyexams.co.uk/a-level/biology/cie/22/revision-notes/2-biological-molecules/2-2-carbohydrates--lipids/2-2-6-cellulose/ . Accessed 18 May 2022.

[77] Sunasee, R. and Hemraz, U. **2018**. Synthetic Strategies for the Fabrication of Cationic Surface-Modified Cellulose Nanocrystals. *Fibers* 6, 1, 15.

[78] Luo, W., Wang, B., Heron, C. G., Allen, M. J., Morre, J., Maier, C. S., Stickle, W. F., and Ji, X. **2014**. Pyrolysis of Cellulose under Ammonia Leads to Nitrogen-Doped Nanoporous Carbon Generated through Methane Formation. *Nano Lett.* 14, 4, 2225–2229.

[79] Jakab, E., Liu, K., and Meuzelaar, H. L. C. **1997**. Thermal Decomposition of Wood and Cellulose in the Presence of Solvent Vapors. *Ind. Eng. Chem. Res.* 36, 6, 2087–2095.

[80] Cagniant, D., Magri, P., Gruber, R., Berlozecki, S., Salbut, P., Bimer, J., and Nansé, G. **2002**. Ammoxidation of cellulose—a structural study. *Journal of Analytical and Applied Pyrolysis* 65, 1, 1–23.

[81] Chaiwat, W., Hasegawa, I., Tani, T., Sunagawa, K., and Mae, K. **2009**. Analysis of Cross-Linking Behavior during Pyrolysis of Cellulose for Elucidating Reaction Pathway. *Energy Fuels* 23, 12, 5765–5772.

[82] Singh, V. K., Ali, M. M., and Mandal, U. K. **1990**. Formation Kinetics of Calcium Aluminates. *Journal of the American Ceramic Society* 73, 4, 872–876.

[83] Nemanich, R. J. and Solin, S. A. **1979**. First- and second-order Raman scattering from finite-size crystals of graphite. *Phys. Rev. B* 20, 2, 392–401.

[84] Gao, Z., Li, N., Chen, M., and Yi, W. **2019**. Comparative study on the pyrolysis of cellulose and its model compounds. *Fuel Processing Technology* 193, 131–140.

[85] Banyasz, J., Li, S., Lyons-Hart, J., and Shafer, K. **2001**. Gas evolution and the mechanism of cellulose pyrolysis. *Fuel* 80, 12, 1757–1763.

[86] Li, S., Lyons-Hart, J., Banyasz, J., and Shafer, K. **2001**. Real-time evolved gas analysis by FTIR method: an experimental study of cellulose pyrolysis. *Fuel* 80, 12, 1809–1817.

[87] Ayiania, M., Weiss-Hortala, E., Smith, M., McEwen, J.-S., and Garcia-Perez, M. **2020**. Microstructural analysis of nitrogen-doped char by Raman spectroscopy: Raman shift analysis from first principles. *Carbon* 167, 559–574.

[88] Hojamberdiev, M., Prasad, R. M., Fasel, C., Riedel, R., and Ionescu, E. **2013**. Single-source-precursor synthesis of soft magnetic Fe_3Si- and Fe_5Si_3-containing SiOC ceramic nanocomposites. *Journal of the European Ceramic Society* 33, 13-14, 2465–2472.

[89] Yu, Z., Zhang, P., Feng, Y., Li, S., and Pei, Y. **2016**. Template-Free Synthesis of Porous Fe_3O_4 /SiOC(H) Nanocomposites with Enhanced Catalytic Activity. *J American Ceramic Society* 99, 8, 2615–2624.

[90] Zhou, C., Fasel, C., Ishikawa, R., Gallei, M., Ikuhara, Y., Lauterbach, S., Kleebe, H.-J., Riedel, R., and Ionescu, E. **2017**. One-pot synthesis of a C/SiFeN(O)-based ceramic paper with in-situ generated hierarchical micro/nano-morphology. *Journal of the European Ceramic Society* 37, 16, 5193–5203.

[91] Ott, A., Peter, J., Wiehl, L., Potapkin, V., Kramm, U. I., Kleebe, H.-J., Riedel, R., and Ionescu, E. **2022**. Conversion of a polysilazane-modified cellulose-based paper into a C/SiFe(N,C)O ceramic paper via thermal ammonolysis. *International Journal of Applied Ceramic Technology* 19, 2, 838–846.

[92] Warner, T. E. and Fray, D. J. **2000**. Synthesis of silicon nitride fibers from ferrosilicon. *Journal of Materials Science Letters* 19, 9, 733–734.

[93] Ionescu, E., Kleebe, H.-J., and Riedel, R. **2012**. Silicon-containing polymer-derived ceramic nanocomposites (PDC-NCs): preparative approaches and properties. *Chemical Society reviews* 41, 15, 5032–5052.

[94] Zhou, C. **2017**. *Ternary Si-Metal-N Ceramics: Single-Source-Precursor Synthesis, Nanostructure and Properties Characterization*. Dissertation, Universitäts- und Landesbibliothek Darmstadt.

[95] Wen, Q., Yu, Z., and Riedel, R. **2020**. The fate and role of in situ formed carbon in polymer-derived ceramics. *Progress in Materials Science* 109, 100623.

[96] Segatelli, M. G., Pires, A. T. N., and Yoshida, I. V. P. **2008**. Synthesis and structural characterization of carbon-rich SiC_xO_y derived from a Ni-containing hybrid polymer. *Journal of the European Ceramic Society* 28, 11, 2247–2257.

[97] Vakifahmetoglu, C., Pippel, E., Woltersdorf, J., and Colombo, P. **2010**. Growth of One-Dimensional Nanostructures in Porous Polymer-Derived Ceramics by Catalyst-Assisted Pyrolysis. Part I: Iron Catalyst. *Journal of the American Ceramic Society* 93, 4, 959–968.

[98] Oura, M., Kambara, T., Kanai, Y., Kravis, S. D., Zou, Y., Awaya, Y., and Pálinkás, J. **1993**. Measurement of RER x-rays from 0.8 MeV/u Ar ions excited by a foil. In *AIP Conference Proceedings*. AIP, 642–645. DOI=10.1063/1.43636.

[99] Biesuz, M., Bettotti, P., Signorini, S., Bortolotti, M., Campostrini, R., Bahri, M., Ersen, O., Speranza, G., Lale, A., Bernard, S., and Sorarù, G. D. **2019**. First synthesis of silicon nanocrystals in amorphous silicon nitride from a preceramic polymer. *Nanotechnology* 30, 25, 255601.

[100] Yan, Q., Li, J., Zhang, J., and Cai, Z. **2018**. Thermal Decomposition of Kraft Lignin under Gas Atmospheres of Argon, Hydrogen, and Carbon Dioxide. *Polymers* 10, 7.

[101] Lalancette, R. A., Syzdek, D., Grebowicz, J., Arslan, E., and Bernal, I. **2019**. The thermal decomposition and analyses of metal tris-acetylacetonates. *J Therm Anal Calorim* 135, 6, 3463–3470.

[102] Shen, D., Ye, J., Xiao, R., and Zhang, H. **2013**. TG-MS analysis for thermal decomposition of cellulose under different atmospheres. *Carbohydrate polymers* 98, 1, 514–521.

[103] Wen, J. B., Huang, S., and Wang, H. J. **2014**. Oxidation Behavior of Amorphous Nano-Si_3N_4 Powders. *KEM* 602-603, 367–370.

[104] Günthner, M., Wang, K., Bordia, R. K., and Motz, G. **2012**. Conversion behaviour and resulting mechanical properties of polysilazane-based coatings. *Journal of the European Ceramic Society* 32, 9, 1883–1892.

[105] Kim, R., Qin, W., Wei, G., Wang, G., Wang, L., Zhang, D., Zheng, K., and Liu, N. **2010**. Growth of SiO_2 hierarchical nanostructure on SiC nanowires using thermal decomposition of ethanol and titanium tetrachloride and its FTIR and PL property. *Materials Chemistry and Physics* 119, 1-2, 309–314.

[106] Li, Y., Chen, C., Li, J.-T., Yang, Y., and Lin, Z.-M. **2011**. Surface charges and optical characteristic of colloidal cubic SiC nanocrystals. *Nanoscale research letters* 6, 1, 454.

[107] Colomban, P., Gouadec, G., and Mazerolles, L. **2002**. Raman analysis of materials corrosion: the example of SiC fibers. *Materials and Corrosion* 53, 5, 306–315.

[108] Huang, J., Huang, Z., Yi, S., Liu, Y., Fang, M., and Zhang, S. **2013**. Fe-catalyzed growth of one-dimensional α-Si_3N_4 nanostructures and their cathodoluminescence properties. *Scientific reports* 3, 3504.

[109] Okamoto, H. **2007**. Pd-Si (Palladium-Silicon). *J Phs Eqil and Diff* 28, 2, 231–232.

[110] Siddiqi, S. A. and Hendry, A. **1985**. The influence of iron on the preparation of silicon nitride from silica. *J Mater Sci* 20, 9, 3230–3238.

[111] Seyferth, D., Lang, H., Sobon, C. A., Borm, J., Tracy, H. J., and Bryson, N. **1992**. Chemical modification of preceramic polymers: Their reactions with transition metal complexes and transition metal powders. *J Inorg Organomet Polym* 2, 1, 59–77.

[112] Jean-Philipp Kunkler**. 2022**. *Einfluss der Präkursor-verdünnung auf die pseudomorphe Umwandlung Polymer-abgeleiteter SiOC Papiere*. Bachelor-Thesis, Technische Universität Darmstadt.

[113] Papakollu, K., Moharana, N., Hari Kumar, K. C., Lauterbach, S., Kleebe, H.-J., Ionescu, E., and Kumar, R. **2022**. Synthesis and Temperature-Dependent Evolution of the Phase Composition in Palladium-Containing Silicon Oxycarbide Ceramics. *Journal of the European Ceramic Society*.

[114] Cominos, V. and Gavriilidis, A. **2001**. Sublimation and deposition behaviour of palladium (II) acetylacetonate. *Eur. Phys. J. AP* 15, 1, 23–33.

[115] Poston, S. and Reisman, A. **1989**. The relative stabilities of tungsten hexacarbonyl, silver neodecanoate some metal acetyl- and hexafluoroacetylacetonates and the thermal properties of the palladium(II) acetonates. *J. Electron. Mater.* 18, 4, 553–560.

[116] Wang, J., Gili, A., Grünbacher, M., Praetz, S., Epping, J. D., Görke, O., Schuck, G., Penner, S., Schlesiger, C., Schomäcker, R., Gurlo, A., and Bekheet, M. F. **2021**. Silicon oxycarbonitride ceramic containing nickel nanoparticles: from design to catalytic application. *Mater. Adv.* 2, 5, 1715–1730.

[117] Chen, C., Sun, K., Wang, A., Wang, S., and Jiang, J. **2018**. Catalytic Graphitization of Cellulose Using Nickel as Catalyst. *BioResources* 13, 2.

[118] Hunter, R. D., Ramírez-Rico, J., and Schnepp, Z. **2022**. Iron-catalyzed graphitization for the synthesis of nanostructured graphitic carbons. *J. Mater. Chem. A* 10, 9, 4489–4516.

[119] Wu, F., Huang, R., Mu, D., Wu, B., and Chen, Y. **2016**. *Controlled synthesis of graphitic carbon-encapsulated α-Fe$_2$O$_3$ nanocomposite via low-temperature catalytic graphitization of biomass and its lithium storage property* 187.

[120] Li, J., Wang, J., Gao, D., Li, X., Miao, S., Wang, G., and Bao, X. **2016**. Silicon carbide-supported iron nanoparticles encapsulated in nitrogen-doped carbon for oxygen reduction reaction. *Catal. Sci. Technol.* 6, 9, 2949–2954.

[121] Xu, H., Jin, X., Zhou, X., Du, X., Xing, P., and Zhuang, Y. **2021**. Recycling of the Diamond-wire Saw Powder by Ni-catalyzed Nitridation to Prepare Si$_3$N$_4$. *Silicon*.

[122] Xie, W.-L., Zhang, X.-D., Liu, W.-H., Xie, Q., Wen, G.-W., Huang, X.-X., Zhu, J.-D., and Ma, F.-X. **2019**. Low-temperature synthesis of SiC nanowires with Ni catalyst. *Rare Met.* 38, 3, 206–209.

[123] Lü, J., Zhang, Y., Lü, Z., Huang, X., Wang, Z., Zhu, X., and Wei, B. **2015**. A preliminary study of the pseudo-capacitance features of strontium doped lanthanum manganite. *RSC Adv.* 5, 8, 5858–5862.

[124] Ren, J., Antonietti, M., and Fellinger, T.-P. **2015**. Efficient Water Splitting Using a Simple Ni/N/C Paper Electrocatalyst. *Adv. Energy Mater.* 5, 6, 1401660.

[125] Huang, L.-F., Hutchison, M. J., Santucci, R. J., Scully, J. R., and Rondinelli, J. M. **2017**. Improved Electrochemical Phase Diagrams from Theory and Experiment: The Ni–Water System and Its Complex Compounds. *J. Phys. Chem. C* 121, 18, 9782–9789.

[126] Bode, H., Dehmelt, K., and Witte, J. **1966**. Zur kenntnis der nickelhydroxidelektrode—I.Über das nickel (II)-hydroxidhydrat. *Electrochimica Acta* 11, 8, 1079–1087.

[127] Lyons, M. and Brandon, M. **2008**. The Oxygen Evolution Reaction on Passive Oxide Covered Transition Metal Electrodes in Aqueous Alkaline Solution. Part 1-Nickel. *Int. J. Electrochem. Sci. International Journal* 3, 1386–1424.

[128] Barnard, R., Randell, C. F., and Tye, F. L. **1981**. Studies concerning charged nickel hydroxide electrodes. *Journal of Electroanalytical Chemistry and Interfacial Electrochemistry* 119, 1, 17–24.

[129] Barnard, R., Randell, C. F., and Tye, F. L. **1980**. Studies concerning charged nickel hydroxide electrodes I. Measurement of reversible potentials. *J Appl Electrochem* 10, 1, 109–125.

[130] Hall, D. S., Lockwood, D. J., Bock, C., and MacDougall, B. R. **2015**. Nickel hydroxides and related materials: a review of their structures, synthesis and properties. *Proceedings. Mathematical, physical, and engineering sciences* 471, 2174, 20140792.

[131] Benck, J. D., Pinaud, B. A., Gorlin, Y., and Jaramillo, T. F. **2014**. Substrate selection for fundamental studies of electrocatalysts and photoelectrodes: inert potential windows in acidic, neutral, and basic electrolyte. *PloS one* 9, 10, e107942.

[132] Liu, X., Yin, X., Zheng, G., Liu, Y., Kong, L., Li, Q., and Yuan, X. **2014**. In-situ formation of carbon nanotubes in pyrolytic carbon–silicon nitride composite ceramics. *Ceramics International* 40, 1, 531–540.

[133] Ricohermoso, E., Klug, F., Schlaak, H., Riedel, R., and Ionescu, E. **2021**. Compressive thermal stress and microstructure-driven charge carrier transport in silicon oxycarbide thin films. *Journal of the European Ceramic Society* 41, 13, 6377–6384.

[134] Anne Marie Helmenstine**. 2019**. *Table of Electrical Resistivity and Conductivity*. https://www.thoughtco.com/table-of-electrical-resistivity-conductivity-608499. Accessed 2 August 2022.

[135] Hoekstra, J., Beale, A. M., Soulimani, F., Versluijs-Helder, M., Geus, J. W., and Jenneskens, L. W. **2015**. Base Metal Catalyzed Graphitization of Cellulose: A Combined Raman Spectroscopy, Temperature-Dependent X-ray Diffraction and High-Resolution Transmission Electron Microscopy Study. *J. Phys. Chem. C* 119, 19, 10653–10661.

[136] Wang, J., Gili, A., Grünbacher, M., Praetz, S., Epping, J. D., Görke, O., Schuck, G., Penner, S., Schlesiger, C., Schomäcker, R., Gurlo, A., and Bekheet, M. F. **2021**. Silicon oxycarbonitride ceramic containing nickel nanoparticles: from design to catalytic application. *Mater. Adv.* 2, 5, 1715–1730.

[137] Stangeland, K., Kalai, D., Li, H., and Yu, Z. **2017**. CO_2 Methanation: The Effect of Catalysts and Reaction Conditions. *Energy Procedia* 105, 2022–2027.